Roberta Manno

Microwave-Assisted Synthesis of Supported Nanocatalysts: A route from nanoparticles to nanoclusters, from batch to continuous.

Director/es

Sebastián Cabeza, Víctor
Mallada Viana, Reyes

Tesis Doctoral

MICROWAVE-ASSISTED SYNTHESIS OF SUPPORTED NANOCATALYSTS: A ROUTE FROM NANOPARTICLES TO NANOCLUSTERS, FROM BATCH TO CONTINUOUS.

Autor

Roberta Manno

Director/es

Sebastián Cabeza, Víctor
Mallada Viana, Reyes

UNIVERSIDAD DE ZARAGOZA
Escuela de Doctorado

2021

Departamento de Ingeniería
Química y Tecnologías
del Medio Ambiente

Universidad Zaragoza

1542

Department of Chemical Engineering and Environment Technologies

Microwave-Assisted Synthesis of Supported Nanocatalysts:

A route from nanoparticles to nanoclusters, from batch to continuous.

A thesis submitted in partial fulfilment of the requirements for the degree of Doctor

Roberta Manno

Zaragoza, 12-02-2021

INMA
INSTITUTO DE NANOCIENCIA
Y MATERIALES DE ARAGÓN

CSIC
CONSEJO SUPERIOR DE INVESTIGACIONES CIENTÍFICAS

NFP
nanostructured
films & particles

II

Doctor Reyes Mallada and Doctor Víctor Sebastián,

Associate Professors at the University of Zaragoza in the Department of Chemical Engineering and Environmental Technologies and members of the Nanostructured Films and Particles, NFP group.

Inform that:

The PhD thesis entitled:

"Microwave-Assisted Synthesis of Supported Nanocatalysts: A route from nanoparticles to nanoclusters, from batch to continuous."

has been written by the PhD student Roberta Manno under our supervision in the Department of Chemical Engineering and Environmental Technologies and has not been submitted in support of an application for another degree at this or any other university and we authorize and approve the presentation of this dissertation.

Reyes Mallada   **Víctor Sebastián**

To my family, to Carlos and to Maria…

My comfort zone

"Non temete i momenti difficili,

il bello viene da lí."

(Rita Levi Montalcini)

VI

I. FUNDING

II.   THESIS OUTLINE AND PROJECT FRAMEWORK

The European Training Network for Continuous Sonication and Microwave (ETN-COSMIC) aimed to train future researchers to accelerate the transition to continuous flow production with the use of alternative energy sources, i.e. microwaves and ultrasound. The project counted 15 early-stage researchers, 8 beneficiaries (with 2 industry) and 4 partner organizations, distributed in 7 European countries. 8 network-wide events were organized during the training period covering different environments (company visits, soft-skills training, expert lectures, summer school, etc.) and 6-months period revisions of the ESR progresses by the entire symposium.

The project was divided into four work packages (WP):

- WP1: Ultrasound and/or microwave-assisted organic synthesis for C-H, C=C and C≡C activation both in batch and continuous flow.
- WP2: Ultrasound and/or microwave-assisted particle formation, distinguishing between supported nanoparticles for catalytic applications, industrial continuous synthesis of submicron zeolite and nanoparticles for health applications.
- WP3: Innovative process technology development to investigate the aspects of millifluidics, clogging, scale-out and the combination of cavitation and microwave energy.
- WP4: Decision and assessment methodology to evaluate both the technical and sustainability performance of the developed technologies and benchmark them against the currently applied industrial processes.

The current thesis focused on the microwave-assisted synthesis of metal-containing nanocatalysts under flow conditions (Work Package 2 – Early Stage Researcher 6). The work has been carried out in the Chemical Engineering and Environmental Technologies Department at the University of Zaragoza, within the Nanostructured

Films and Particles (NFP) group which is a member of the *Instituto de Nanociencia y Materiales de Aragón* (INMA). The group has a large experience in the synthesis and characterization of nanostructures, and in the use of innovative microwave-heated catalytic systems (HECTOR and ADREM European projects). Furthermore, as part of Marie Skłodowska-Curie projects, interdisciplinary and intersectoral mobility and international collaboration have been performed to promote the creation of a solid framework between different partners. Two short-term secondments, for a total of six months, have been carried out at the Technical University of Valencia and University of Cordoba. The analysis of tuning systems and the measurement of the dielectric properties were performed in the ITACA Research Institute at the Technical University of Valencia, with the opportunity to deepen the simulation of monomode microwave heating cavity. Instead, during the second mobility in the *NANOVAL* group at the University of Cordoba alternative flow hydrogenation reactors were used, focusing on catalytic applications. In addition, there was a continuous collaboration between all the members of the symposium covering different aspects of the entire project.

The PhD thesis was completed in four years (January 2017 – January 2021).

III.   ACKNOWLEDGEMENT

Bueno ya ha llegado el momento de acabar también esta experiencia. Para este apartado, lo siento, pero mezclaré los tres idiomas (italiano, español e inglés) para que pueda utilizar las palabras más adecuadas para agradecer, desde el profundo de mi corazón, a todas las personas que han sido parte importante de estos años.

Como dijo Rita Levi Montalcini:

" La scelta di un giovane dipende dalla sua inclinazione, ma anche dalla fortuna di incontrare un grande maestro."

Ninguna palabra podría describir mejor el profundo afecto hacia mis tres jefes. Víctor fue la primera persona que conocí durante la entrevista en Leuven, y recuerdo todavía su pregunta "¿Estás lista para trabajar duro?". Pues en realidad no sabía lo duro que iba a ser, pero cuando una persona ama a tal punto su trabajo al final te acaba contagiando. Con Reyes he aprendido lo que quiere decir ser una verdadera maña, cabezona, intensa pero con un corazón muy grande. Así que gracias a los dos, por la formación técnica, las 58 reuniones, el haber estado siempre allí cuando tocaba a la puerta, el haberme enseñado a hacer ciencia y, sobre todo, gracias por el afecto y el constante apoyo que habéis demostrado en cada momento. Gracias a Jesús, por la oportunidad de ser parte del grupo y el constante interés y estímulo para obtener resultados mejores.

¿Qué decir de mis compañeros? Una familia gigante en tierra española. Gracias a todo el grupo: a Marti por las risas cotilleando en directo *Maestro de la Costura* (y por muchas razones más), a Bea que siempre ve lo bueno en cada día, a Cris tan directa, tan simple y tan buena amiga, a Isa por la cual nada es imposible, a Sara por sus charlas de Real Food y tonterías varias, a Fer que igual algún día me engañará para comer una pizza con piña, a Arturito por su música, a Cristóbalito por sus yemas de huevos, a Ainhoa por sus caramelos, a Diex y sus tortugas, a Javi por su paciencia, a Nacho por saber escuchar y aconsejar, a Laura un pilar del grupo, y a

IV. CONTENTS

V. List of Abbreviations and Acronyms

MEANING	SYMBOL
Nanoparticles	NPs
Nanoclusters	NCs
Highest Occupied Molecular Orbital	HOMO
Lowest Unoccupied Molecular Orbital	LUMO
Electro-Magnetic	EM
Classical Nucleation Theory	CNT
Conventional Heating	CH
Microwave Heating	MWH
Microwave	MW
Selective Cooling Microwave Heating	SCMWH
EXPERIMENTAL TECHNIQUES	
Transmission Electron Microscopy	TEM
High Resolution Transmission Electron Microscopy	HRTEM
High-Angle Annular Dark-Field Scanning Transmission Electron Microscopy	HAADF-STEM
Matrix-Assisted Laser Desorption Ionization	MALDI
Electrospray Ionization	ESI
Surface Plasmon Resonance	SPR
Microwave Plasma – Atomic Emission Spectroscopy	MP-AES
Scanning electron microscope	SEM
Dynamic Light Scattering	DLS
X-ray photoelectron spectroscopy	XPS
Photoluminescence	PL
Energy Dispersive X-ray Spectrometry	EDS
REACTOR DETAILS	
Inner diameter	I.D.
Outer diameter	O.D.
Infrared-Camera	IR-Camera
Optical Fiber	O.F.

1. INTRODUCTION

Goal: How to cover the gap between reversible low catalytically-active nanoparticles and unrecoverable highly-active single atoms?
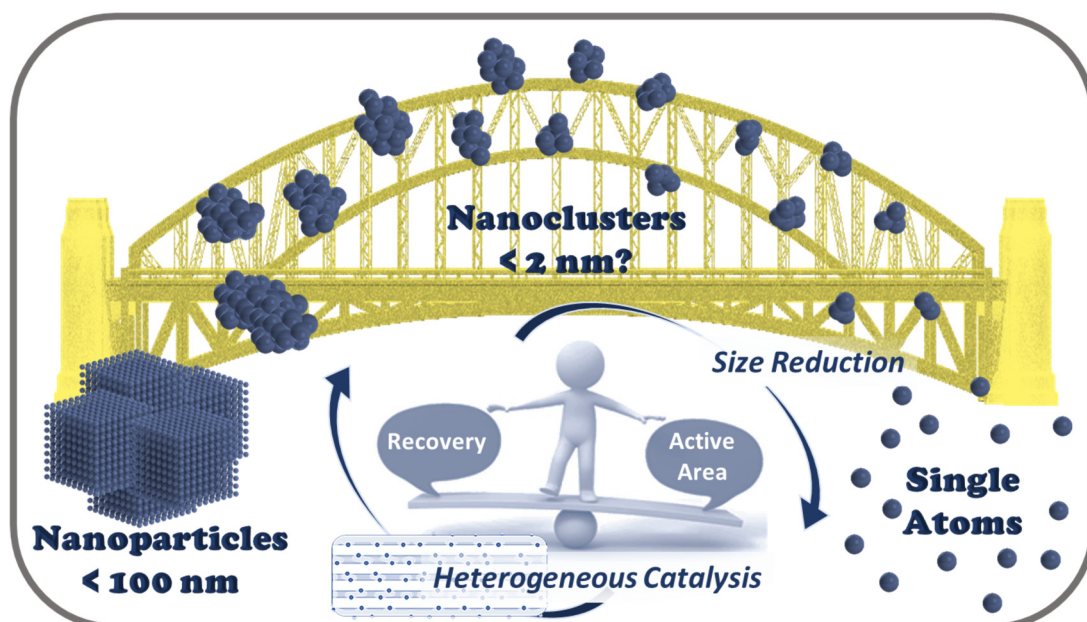
1. Introduction

"It is, then, proved that several simple or compound bodies, soluble and insoluble, have the property of exercising on other bodies an action very different from chemical affinity. By means of this action they produce, in these bodies, decompositions of their elements and different recombinations of these same elements to which they remain indifferent."

With this simple but brilliant statement, in 1836 the Swedish chemist Jöns Jacob Berzelius marked the beginning of catalysis science in the modern age[1]. In the following 50 years, Wilhelmy, Van't Hoff, Horstmann, Gibbs and Nernst made an important breakthrough by introducing a mathematical expression to quantify the reaction rate as a function of temperature and pressure[2]. The development of efficient catalytic processes began the staple of the industrial field. Since then, catalysis has rapidly and continuously evolved to satisfy the market demand. New explosives and the fluid catalytic cracking process drove the industries during the two World conflicts. The research on catalysis and its applications was conducted intensively and without interruption even during the post-war period, when the people's lifestyle was revolutionized thanks to polymeric and automotive innovations[2].

Nowadays, catalysis covers 30% of global gross domestic production (GDP) and 90% of chemicals are produced by catalytic processes[3]. In 2015 the *European Cluster on Catalysis* claimed that there is a pressing necessity to renovate the industrial production, because it is still widely based on technologies introduced at the end of the 1970s. The *European Cluster* identified the design of novel catalytic materials and the development of alternative preparation methods as part of the main challenges of the current R&D activities[3]. Conversion, reaction rate, catalyst stability and selectivity are considered as crucial aspects of an efficient catalyst, whereas the accessibility of the active sites and the reusability of the catalyst itself may lead to process intensification[4]. In homogeneous systems, direct contact is assured between

reactants and metallic atoms of dissolved salts or organometallic compounds, resulting in high synthesis yield and selectivity. Even so, the recovering step is still a critical point, by negatively impacting economic and environmental aspects. On the other side, the advances in nanostructured materials open plenty of rooms for the design of cutting-edge alternatives. The possibility to support the nanoparticles (NPs) allows their use for heterogeneous catalysis and may contrast agglomeration and ripening mechanisms, improving their long-time stability[5,6]. Centrifugation, magnetic decantation or filtration are some of the techniques commonly adopted to recover the nanocatalysts and reuse them for a large number of cycles. Unfortunately, the active sites lie exclusively on the external surface area of the nanomaterial, lowering their efficiency. However, when the particle diameter decreases from 100 to 1 nm, the total surface area becomes 100 times higher, the accessible active sites increase and, consequently, the catalytic activity[7]. Then, ultra-small nanocatalysts may represent a bridge between unrecoverable single atoms and low-efficient nanoparticles[8–10].

1.1. The Borderline between Nanoparticles and Nanoclusters

In 2008 the International Organization for Standardization (ISO) defined a nanoparticle as a "nano-object with all three external dimensions in the nanoscale" where the nanoscale ranges from 1 to 100 nm (ISO 27/687)[11]. The situation drastically changes when we talk about nanoclusters. Even if the interest in *nanoclusters* has grown exponentially in the last 30 years, there is still confusion on its definition. Just focusing on the publications of this year 2020, Farzin et al.[12] described a nanocluster as a nanoparticle with a diameter smaller than 10 nm, for Kauscher et al.[13] the threshold diameter for Au-NCs was 3 nm while for the majority the nanoclusters present a size smaller than 2 nm[7,9,10]. On the other hand, it is commonly recognized that for ultrasmall size the electronic energy levels become discrete, generating quantum size effects[9]. In view of this, to clarify where the threshold diameter to

observe quantum phenomena is, it is necessary to firstly familiarize with the quantization of the electronic energy levels[10].

In 1932, Robert Mulliken coined the term atomic orbital, as an abbreviation for *one-electron orbital wave function*, to identify the probability of finding any electron of an atom in any specific region around the nucleus of an atom. As described by the free-electron model, the atomic orbitals have discrete energy values. When two or more atoms interact, their atomic orbitals are split into a discrete number of molecular quantum levels (Highest Occupied Molecular Orbital (HOMO)-Lowest Unoccupied Molecular Orbital (LUMO) theory, Nobel prize 1981)[14]. For a large number of atoms ($N \sim 10^{23}$), even if the molecular orbitals still possess discrete values, the distance between adjacent orbital levels may be neglected approximating the states of energies to two continuous bands[15] known as valence and conduction bands, as schematically reported in Figure 1.1 a. At a bulk scale, insulators, semiconductors and conductors materials present a different relative position of the valence and the conduction bands, as reported in Figure 1.1 b, c and d respectively[16].
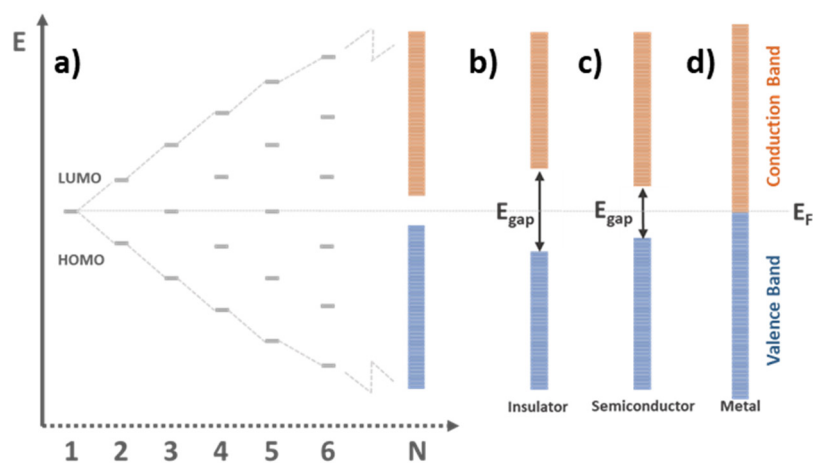
Figure 1.1 a) HOMO-LUMO molecular orbital as a function of the number of atoms (N). As N increases, the separation between adjacent molecular orbitals decreases. Valence and conduction bands for insulators (b), semiconductors (c) and metals (d), where E_{gap} and E_F indicate the bandgap and the Fermi energy respectively.

On the opposite side, when we move from bulk scale to nanoparticles and then to nanoclusters, the number of atoms that form the nanomaterial decreases. Consequently, the spacing between the electronic states becomes progressively higher, resulting in a discretization of the electronic energy states (Figure 1.2).
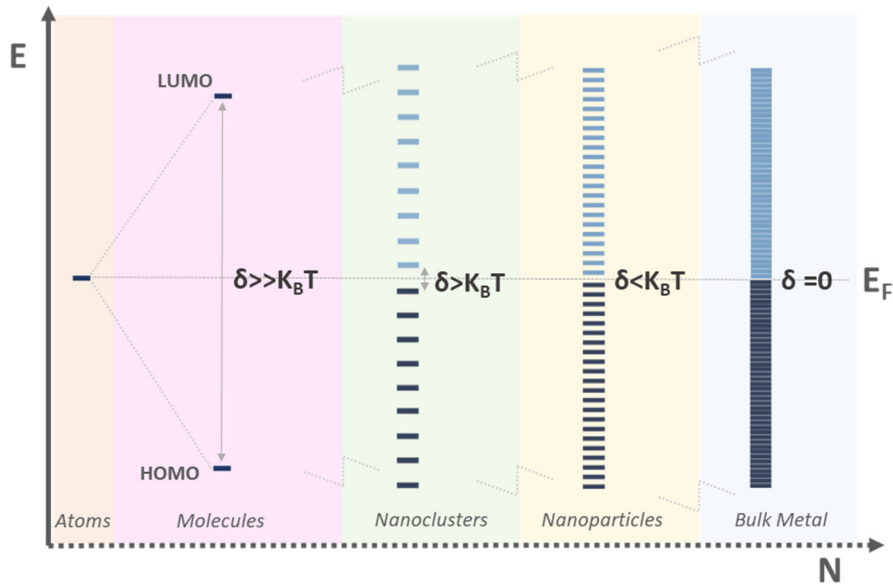
Figure 1.2 Differences of LUMO-HOMO molecular orbitals discretization between single atoms (pink area), molecules (purple area), nanoclusters (green area), nanoparticles (yellow area) and bulk metallic materials (blue area).

The Kubo criterion[17] (equation 1.1) estimates the average spacing δ, that exists between consecutive energy levels, as a function of the number of atoms N, as:

$$\delta \simeq \frac{E_F}{N} \qquad (1.1)$$

Where, for bulk metals, the Fermi energy (E_F) represents the highest occupied molecular orbital value (HOMO), measured at absolute zero temperature. In this state no conduction phenomena may occur. As the temperature increases, the electrons rapidly move from valence to conduction band, generating an electrical current. If the thermal energy ($K_B T$) is enough to create a mobile electron-hole pair, the electronic energy spacing δ is still small enough and the material presents metallic properties[18]. On the other hand, for the nanoclusters higher energy is required for the promotion of the electrons to the LUMO orbitals, similar to

semiconductor materials. On the basis of this theoretical observation, the nanoclusters' prerequisites may be summarized in two simple equations, as reported in the following system 1.2.

$$\begin{cases} \delta \simeq \dfrac{E_F}{N} \quad (Kubo\ Criterion) \\ \\ \delta > K_B T \quad (Quantum\ Size\ Effect\ Criterion) \end{cases} \qquad (1.2)$$

Furthermore, there is a direct proportion between the number of atoms N and the volume occupied, and consequently for spherical particles the radius itself[18]. For this reason, it is possible to generalize the equations of system 1.2 extrapolating the maximum number of atoms N and the minimum radius r required to observe quantum size effects, system 1.3.

$$\begin{cases} N < \dfrac{E_F}{K_B T} \\ \\ r > \sqrt[3]{\dfrac{3 E_F}{4 \pi \rho K_B T}} \end{cases} \qquad (1.3)$$

The separation between nanoclusters and nanoparticles is not a fixed value (Figure 1.3), as it is affected by the number of atoms per unit volume (ρ), the atomic electron configuration, the cluster melting temperature and the temperature of the system[19]. Despite that, the threshold diameter ranges between 1.5 and 2 nm for a wide range of metals commonly adopted (Ag, Au, Pd, Pt, Cu, and Fe). Then, a nanocluster may be classified as a nano-object with all three external dimensions smaller than 1.5 - 2 nm, which presents quantum size effects.

Tsukuda et al.[20] adopted the term ultrasmall nanoclusters when the number of atoms is smaller than 100. In this case, every single atom may strongly affect the material properties in a non-scalable regime[7]. When the number of atoms ranges between 100 and 500, the size confinement is less rigorous and the nanostructures, classified as *Large-Clusters*, progressively recover the metallic behaviour of nanoparticle regime, such as conductivity and surface plasmon resonance[21].
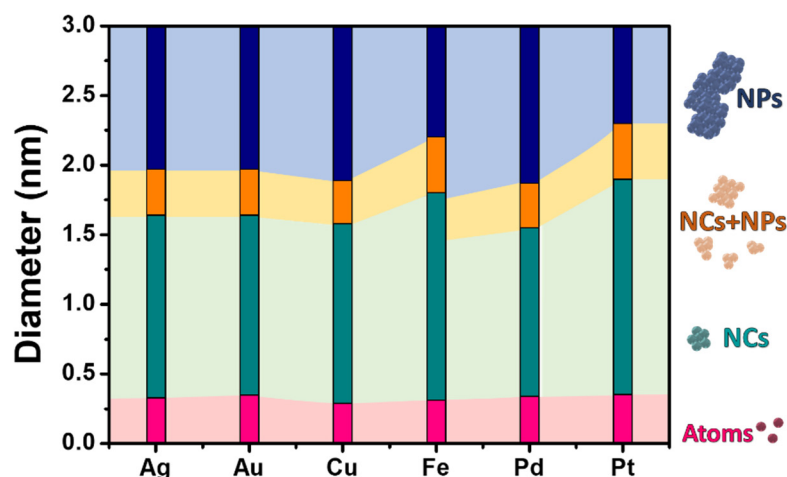
Figure 1.3 Schematic representation of the threshold diameter to distinguish between singles atoms, nanoclusters and nanoparticles for different metals (Ag, Au, Cu, Fe, Pd and Pt). The yellow area corresponds to a border zone where NCs and NPs may coexist. For the calculation, it was considered a maximum temperature of 100 °C and the physical properties of each metal as reported in literature[22,23].

1.2. **Size Dependent Properties**

The discretization of the electronic energy levels produces fascinating variations in chemical reactivity and physical properties such as electrical, thermal, optical and magnetic behaviour. The classification previously reported between large and small clusters is decisive for the interpretation of the system properties. For large clusters, Jortner[19] suggested that an indefinite cluster property G may be represented by a universal scaling law as a function of the number of atoms N (or for nearly spherical particles, the radius R), equation 1.4.

$$G(N) = G(\infty) + bN^{-\beta} \qquad (1.4)$$

As N increases, the system property G(N) varies with a regular trend (scalable regime), tending to a stable value typical of the bulk material G(∞), as schematically reported in Figure 1.4 a. On the other hand, a different scenario is presented for small clusters, where electronic effects dominate and the addition of every single atom provokes odd-even oscillations (non-scalable regime). Hou et al.[24] reported a detailed analysis of how ionization potential, electron affinity, chemical hardness

and magnetic moment randomly varied for Au nanoclusters when N ranges from 1 to 10 atoms. The analysis was continued by Nhat et al.[25] that determined the variation of the binding energy gap up to 20 Au-atoms. Instead, the limit between small and large clusters was investigated by Quijada et al.[26], who developed a theoretical model to estimate the lifetime of the electronic excitations in metallic clusters. As reported in Figure 1.4 b, small clusters (D<1.5 nm – N<340 atoms) presented a zig-zag function characterized by the alternation of maxima and minima peaks. A transitory phase is typical of larger clusters, where the variations produced by the addition of a single atom becomes progressively negligible.
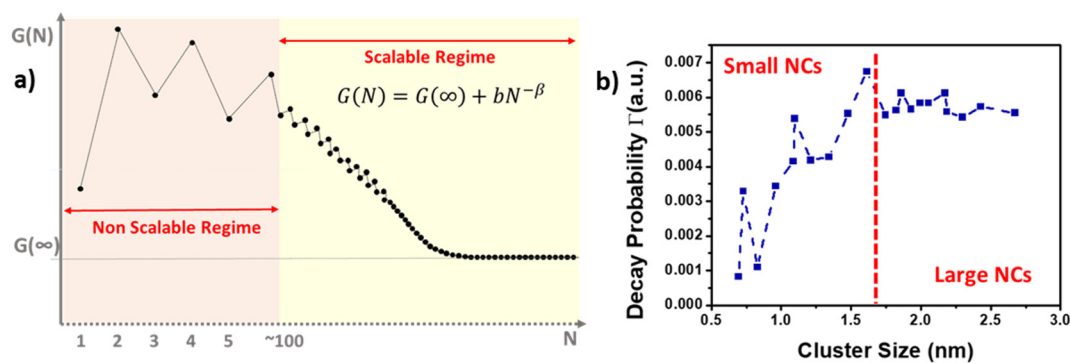
Figure 1.4 a) Variation of undefined system property G(N) as a function of the number of atoms N, distinguishing between non-scalable regime for small nanoclusters and scalable regime represented by Jortner's scaling law[19], adapted by permission of *The Royal Society of Chemistry*. b) Relation between decay probability Γ and clusters' size[26], adapted by permission of *IOP Publishing Ltd*.

1.2.1. *Geometrical Conformation*

As described by Wulff model[27], single atoms that form nanoparticles tend to occupy an equilibrium position that minimizes the total surface energy, resulting in crystalline order. Even if localized defects such as vacancies or dislocations may occur, common metals such as Ag, Au, Pd or Pt are usually characterized by a face-centered cubic (FCC) symmetry. The crystal planes and the lattice parameter *d* may be easily analysed by high-resolution microscopy and Fourier function transform (FFT). For FCC crystals, the packaging efficiency is usually higher than 70%. This means that nearly 34 million atoms are required to produce a nanoparticle of around 75 nm[28]. Unfortunately, the majority of the atoms will occupy the internal volume

of the crystalline structure, and consequently will not be accessible sites for catalytic reactions.

On the contrary, for the nanoclusters the number of atoms is lower than 500, the majority of them are active sites but the determination of their geometrical configuration is still a critical aspect. Theoretical models have been introduced by the combination of density functional theory (DFT) and mass spectroscopy[9]. In detail, matrix-assisted laser desorption ionization (MALDI) and electrospray ionization (ESI) are successful ionization techniques for small nanoclusters characterization, as they avoid excessive fragmentation[29].

In 1984, Knight et al.[30] presented a revolutionary and pioneering work on Na nanoclusters, introducing the concept of *magic numbers* (also known as *intensities anomalies*) to identify a series of stable metallic clusters (N=8, 18, 20, 34, 40, …). Besides electronic effects are the predominant stabilizing force for N lower than 10, geometric symmetry and atomic packing play a crucial role as the complexity of the system increases[31]. As confirmed by Imaoka et al.[32], no crystallinity was observed for Pt atomically precise clusters when N is lower than 13. The experimental size reported for Pt_{10} was 0.7±0.2 nm, following the theoretical value obtained by the previous equation 1.3 (d_{th}~0.5 nm). However, the packaging increased between Pt_{11} and Pt_{12}, Figure 1.5.
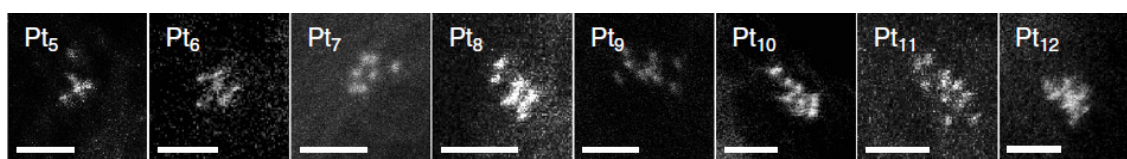
Figure 1.5 HR HAADF-STEM analysis of atomically precise nanoclusters Pt_N, where N ranges from 5 to 12[32], scale bar 1 nm (reproduced by permission of *Springer Nature*).

For high N values, Kabir et al.[33] demonstrated that high stability is assured by cuboctahedral or icosahedral geometries, which consist of a central atom surrounded by 12 neighbour atoms. This may explain why 13 and 55 atoms are the most common N values experimentally observed for small stable clusters[34–37]. The

evaluation of clusters stability becomes harder when stabilizing ligands are used to avoid agglomeration by electrostatic repulsion. As proposed by Walter et al.[38], the interaction between the metallic clusters and the ligand may originate an *electronically closed shell superatom complex*. The number of the electrons n^* that form the closed-shell may be estimated by the following equation 1.5.

$$n^* = Nv_A - M - z \tag{1.5}$$

Where N stays for the number of metal cores, v_A the relative valence electrons, M the electrons coordinated with the ligands and z the total charge of the complex. The technical limitation to produce stable and homogeneous metallic clusters and the large number of parameters that characterize the system, obstacle the investigation of ligand-stabilized nanoclusters[39]. Many of the works performed on NCs theorized that the central nucleus may present a stable configuration, i.e. icosahedral shape with N=13, surrounded by uncoordinated atoms without an apparent symmetry[18,40–42]. Despite the difficulties to obtain a clear characterization in an excess of organic ligands, the amorphous configuration is also confirmed by high-resolution transmission electron microscopy[9]. As clearly reported in Figure 1.6, the metallic nanoparticles present a crystalline order[43], on the left, while the nanoclusters are characterized by an amorphous configuration[44], on the right.
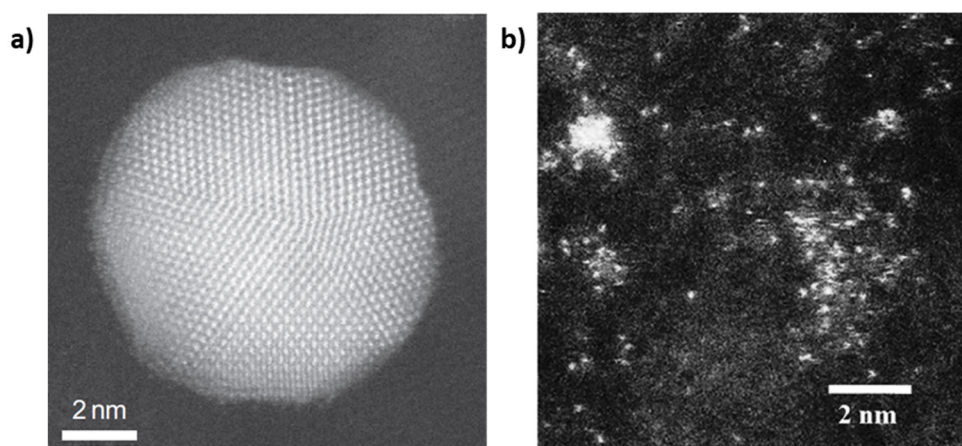
Figure 1.6 Comparison of HRSTEM analysis of Au nanoparticles (a) with an ordered crystalline structure[43] (adapted by permission of *Springer Nature*) and Au nanoclusters (b), characterized by an amorphous configuration[44] (adapted by permission of *The Royal Society of Chemistry*).

1.2.2. *Optical Properties*

One of the fastest and cheapest techniques to experimentally distinguish between metallic nanoparticles and nanoclusters dispersed in a colloidal solution is the UV-Vis spectroscopy, except for Pt and Pd NPs[39,45,46]. As described by the Mie theory, when the particle size is smaller than 100 nm a phenomenon called Localized Surface Plasmon Resonance (LSPR) occurs due to the collective oscillation of free electrons confined in the metallic nanostructures. Ag (grey line in Figure 1.7) and Au nanoparticles are characterized by a single plasmonic absorbance signal, which is a function of metal particle size and shape, and their concentration. As the size decreases, the metallic behaviour progressively disappeared, observing a molecular-like absorption spectra[10]. As confirmed by Figure 1.7, the characteristic spectroscopic fingerprints of small NCs present multiple absorbance signals that may be associated with the intraband (sp) HOMO-LUMO transmission, interband transition (d-sp) and a mixed of them[47].
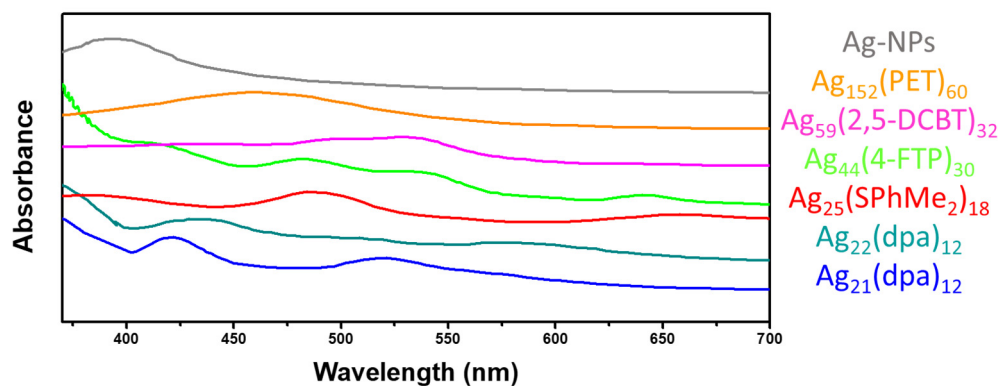
Figure 1.7 UV-Vis spectra for Ag NCs with 21[48], 22[48], 25[49], 44[50], 59[35], and 152[51] atoms and crystalline NPs[52].

The energy associated with the characteristic peaks may be adopted to approximate the value of the energy gap and, as demonstrated by Quintela et al.[53], the number of atoms that form the nanoclusters. ESI-MS and MALDI-MS are the most reliable techniques for the rigorous determination of the number of atoms in the case of monodispersed ligand-stabilized nanoclusters[10,27].

1.2.3. *Photoluminescence*

Similar results were observed by photoluminescence (PL) characterization. Small metallic nanoclusters may represent a winner alternative to largely used organic dyes, such as rhodamine or fluorescein[54]. As reported by Zheng et al.[55] for atomically precise Au nanoclusters, a direct proportion was observed between the number of atoms and the relative emission wavelength, Table 1.1. Photoluminescence is originated by HOMO-LUMO transitions of the electrons. In analogy with UV-VIS analysis previously reported, the energy gap may be correlated to the energy emitted. The smaller the clusters, the higher the energy gap, producing a shift of the emission band to a smaller wavelength. The quantum yield is strongly enhanced in clusters formed by less than 10 atoms, observing an increase of up to 95% for Ag_6 clusters[56]. Wu and Jin[57] evidenced that PL may be promoted by the interaction of uncoordinated atoms of the nanoclusters shell with the electron-rich groups of the stabilizing ligands. Furthermore, recent studies evidence that PL mechanism depends also on several other aspects, such as the solvent, the hydrophilicity and the temperature of the system[58].

Table 1.1 Photoluminescence properties of Au nanoclusters formed by a progressive high number of atoms[55], reproduced by permission of *Annual Reviews, Inc.*

Number of atoms (N)	Excitation wavelength (nm)	Emission wavelength (nm)	Quantum Yield (%)	Intrinsic Decay Rate (10^9 GHz)
5	330	385	70	0.200
8	385	455	42	0.056
13	433	510	25	0.048
23	670	760	15	0.042
31	765	866	10	-

1.2.4. *Catalytic Properties*

For catalytic applications, metallic nanoclusters may be considered a transitional material between single atoms and big nanoparticles. In a nanoparticle, only a small percentage of the metallic atoms interact with the external environment. Figuring the division of a "big" nanoparticle into an infinite number of ultra-small

nanoclusters, you may grasp that the majority of the atoms will be redistributed over the external surface. In catalysis, this results in an enhancement of the accessibility of the active sites, and consequently the efficiency of the catalyst itself. Moreover, as described by Janssen et al.[59] the coordination environment of the external atoms is modified. As reported in Figure 1.8, for large clusters the majority of the external atoms are distributed over the planar surfaces. As we enter to nanocluster regime (diameter < 2 nm), the number of the edges and corners atoms increased with a parabolic and a hyperbolic profile respectively. Edges and corners atoms present a lower coordination number, which implies a different interaction with catalytic reaction intermediates[60].
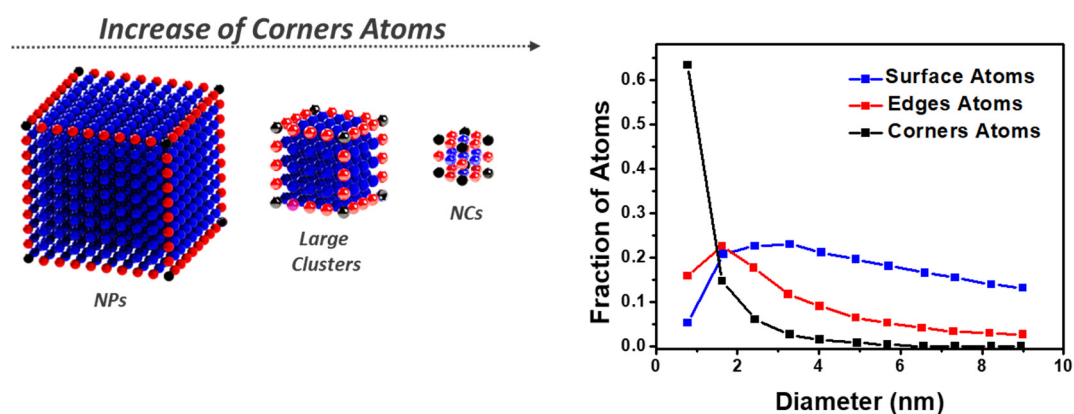
Figure 1.8 Distribution of external atoms distinguishing between surface (blue colour), edges (red colour) and corners atoms (black colour)[61]. (Adapted by permission of *Elsevier*)

Boudart classified catalytic reactions as structure sensitive and structure insensitive[62,63]. As confirmed by Guo et al.[64], switching from nanoparticles to nanoclusters or even single atoms is not always reflected in a higher catalytic activity. A detailed investigation of each reaction is required to determine which is the optimum combination of size, oxidation state, geometry and chemical/physical environment[65]. Calle-Vallejo et al.[66] observed that terrace Pt atoms are more active than edges and convex defects for oxygen reduction reaction. On the contrary, hydrogenation processes are usually accelerated by uncoordinated atoms of small nanocluster[7]. As demonstrated by Shimitu et al.[67], a conversion up to 100% with a

selectivity higher than 95% was obtained by (0.7-1.1) nm silver clusters, while no conversion was recorded adopting a weight amount 1000 times higher of Ag powder. Chang et al.[68] demonstrated that the reaction time may be halved moving from Ag_8 to Ag_4 for cycloaddition of Propargylamines. Furthermore, high stability was observed for Cu_5 clusters, reducing the drawback of copper oxidation that traditionally limits its application[69].

Finally, a key point to maintain activity is to stabilize small nanoclusters over a proper support[70], such as oxides (silica, zeolite, and alumina), magnetic nanoparticles or carbon materials, which may be easily recovered and reused for different cycles. To optimize the design of the catalyst, it is essential to focus on two main aspects. Firstly, the electrostatic cluster-support interaction may be strong enough to reduce the metallic leaching during the reaction[4]. Secondly, the clusters may be homogeneously distributed over the entire surface of the support, avoiding agglomeration and pore obstruction[71].

1.3. **Synthesis of Metallic Nanoclusters**

In the last twenty years, a considerable number of alternative procedures for the synthesis of supported metallic nanoclusters and small nanoparticles have been reported. As schematically summarized in Figure 1.9, it is possible to identify two main categories: *in-situ* generation and post-deposition. In the first case, the metallic nanoclusters are directly nucleated over the respective support. Even if the synthesis yield is usually higher than 80%, the majority of the synthesis routes reported so far are characterized by long synthesis time (1-24 hours[72–74]) and poor control of particle size distribution, with uncontrolled agglomeration[75] and particles growth[76]. H_2 cold plasma[77], laser pyrolysis[78] or a combination of gas-phase cluster ion sources, mass spectrometry, and soft-landing techniques[79] were successfully adopted to strictly control the cluster dimension. Unfortunately, these techniques require dedicated expensive equipment.
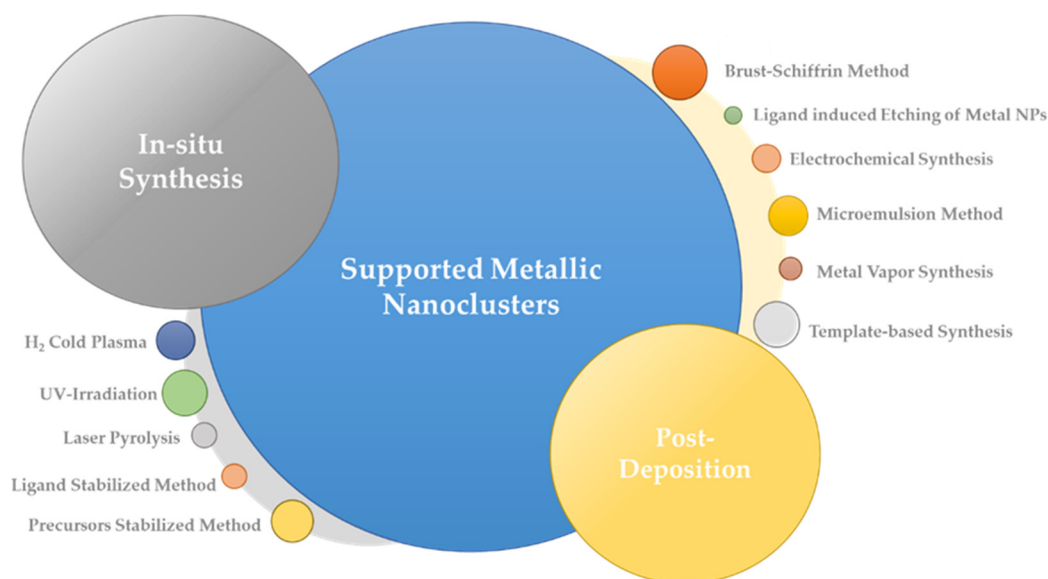
Figure 1.9 Scheme of the main procedures adopted in literature for the synthesis of supported metallic nanoclusters.

On the other hand, a low-cost and narrow size distribution may be obtained by the synthesis of colloidal NCs[60]. The most versatile procedure is the template-based method, where polymers, proteins, and dendrimers with different structures may act both as reducing and stabilizing agents. The majority of the works reported so far were conducted on a laboratory scale, producing between 10 and 70 mg of catalyst per batch[50,80–83]. Even if Zeng et al.[81] reported a conversion yield of 90% for a 10 mg synthesis of $Au_{28}(TBBT)_2$ NCs, usually the production efficiency is lower than 50%[35,40,82,84]. The clusters synthesized are usually surrounded by large quantities of the organic template which is essential to stabilize the sub-2 nm clusters but reduces the accessibility to the active sites. Furthermore, the recovery of unsupported small nanocatalysts is difficult and, as a result, they are usually used as homogeneous catalysts[85–87].

Then, the deposition of nanoparticles and nanoclusters over a proper substrate may facilitate the removal of part of the excess of stabilizing ligand, and make them suitable for heterogeneous catalysis.

1.3.1. *Synthesis Parameters Requirement*

Even if there is not a unique method to synthesize metallic nanoclusters, the Classical Nucleation Theory (CNT) may be adopted to critically identify some general rules for their production. In analogy with the nanoparticles, the mechanism for the nanoclusters production may be divided into nucleation, growth, and aggregation steps[88]. The nucleation occurs when an external stimulus provides enough energy to bypass the barrier value and form an initial nucleus, or in this case a nanocluster. Then, a self-nucleation mechanism starts, and the concentration of the small nuclei rapidly increases. The initial nuclei combine between them producing large clusters and then nanoparticles (Ostwald ripening), with the reorganization of the atoms in a crystalline structure. Furthermore, for longer storage time the nanoparticles tend to continue the aggregation process reducing the quality of the final product.

In view of this, it is possible to hypothesize that the ideal synthesis conditions to produce homogenous and stable nanoclusters are:

- A uniform and nearly instantaneous nucleation, which generates uniform nanoclusters[89];
- Rapid quenching of the reaction, to avoid that the unstable nuclei may reorganize in large nanostructures[90];
- A steric or electrostatic force to contrast clusters agglomeration, assuring long time stability[91,92], such as the interaction with a polymeric template or a supporting material.

Laser pyrolysis[78], H_2 cold plasma[77], UV-irradiation[93], ultrasound[94], and microwaves[95] have been proposed as some of the alternative technologies for the rapid heating of the reaction zone. Even if promising results have been reported, further investigation is still required to accurately measure the reaction temperature, a critical parameter, and to assure a homogeneous nucleation volume.

Furthermore, the fast cooling of the batch reactor is not trivial, with a high-temperature gradient that favours clusters growing and agglomeration.

The switching from batch to continuous flow microreactors may represent a winner alternative, guaranteeing fast heat transfer mechanisms and high control of the synthesis parameters.

1.4. Continuous Flow Technologies

A challenging engineering work is required to move a traditional batch process to a continuous flow production[96]. The first step is a detailed analysis of the process parameters, listing the critical ones, such as pressure, temperature or concentration of reagents, and how they may affect the quality of the final product, the production time and the final cost. Once the problem statement has been delimited, it is possible to work on the design of the reactor.

The reagents are injected by mechanical (low flow pumps, such as syringe, HPLC or peristaltic pumps are commonly used), electrostatic or magnetic forces into channels, whose diameters range from 50 to 1000 μm, allowing a precise control of the molecules residence time distribution. The geometry of the channels may be modelled to satisfy the reaction requirements, with the possibility to include subsequent configurations for multistep processes. Advanced multiphysics models strongly facilitate the operation, simulating an infinite number of layouts with economical, time, and environmental advantages. The small diameter of the reactor channels and the low flow rates employed generally result in laminar flow, limiting the mixing. For this reason, intersecting, zigzag, 3D serpentine, twisted or helical channels are commonly adopted as passive mixers[97–101]. For high viscous reagents, active mixers are preferred to avoid high pressure drop, enhancing the mixing by the application of an external force, such as ultrasonic waves, electric or magnetic fields[102]. The design of the reactor includes also the selection of a proper material and the manufacturing process.

The following step is the experimental testing of the reactor and the optimization of the process parameters (reagents, flow rate and temperature). The majority of the operations are automated, reducing human error and increasing the safety of the working conditions. Once the process is optimized, the reactor may be easily scaled, adopting the numbering-out (parallel production units) and scaling-up (increase of reactor volume) approaches.

As it is possible to observe, the switching to continuous flow requires a big effort in the initial steps and a complete renovation of the industrial plants. For this reason, many chemical companies still adopt traditional batch methods. On the other hand, a large number of promising nanoparticles have been developed in the research labs usually at a small scale, reporting excellent results of size distribution, and a wide variety of different structures[10,100,101]. Even though, the scale-up of batch nanoparticles protocols is difficult, due to the high sensitivity of the process to small temperature and mixing deviations. For this reason, continuous flow technologies are preferred, as also confirmed by the growing number of industrial continuous flow production of nanomaterials at large scale[24,103–105].

1.4.1. *Nanoclusters and Nanoparticles Synthesis in Microreactors*

Microfluidic reactors may satisfy all the requirements for the synthesis of stable metallic nanoclusters. Thanks to the reduced dimension of the reactor channels, the surface to volume ratio is really high, between 10000 and 50000 m^2/m^3 [106]. As a consequence, the heat transfer mechanisms are accelerated, allowing to rapidly heat or cool the inner volume. Furthermore, the reactor may be composed of different stages, as schematically reported in Figure 1.10. This opens the possibility to design a multistep reactor, flexible to different synthesis procedures.
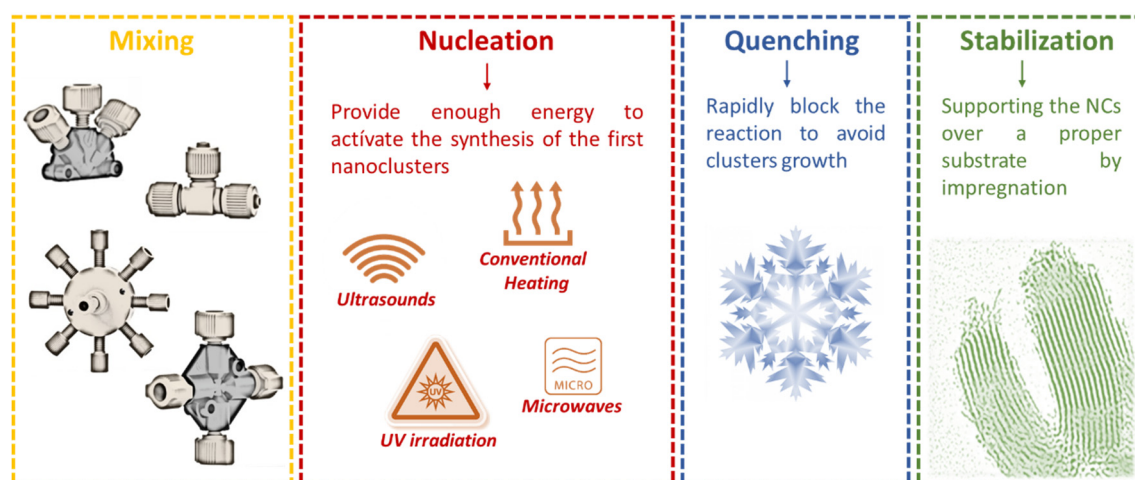
Figure 1.10 Schematic representation of a multistep microfluidic reactor considered in this PhD Thesis for the synthesis of metallic NCs.

For the mixing, a wide range of commercial options is available, allowing up to 9 simultaneous inlets[107]. Albeit it is commonly identified as the first step of the process, intermediate mixing processes may be implemented. In this way, reagents may be added with precise control of the inlet temperature and time, offering, for example, a simple way to produce bimetallic nanoclusters.

The nucleation may be restricted in a limited and homogeneous region with precise control of the synthesis parameters. As reported by Sebastian et al.[108], a stable temperature gradient of 75 °C may be guaranteed between mixing and reaction zone by the combination of a thermal isolation halo etch and a recirculating coolant flow, avoiding nonhomogeneous nucleation. Huang et al.[89] investigated how the residence time and the temperature may influence the quality of Au NCs in a continuous flow microreactor. The best results were obtained for high temperatures and short residence times, confirming that the nucleation may occur nearly instantaneously. Once the nucleation occurs, the flow may be quickly cooled down. The lower the temperature, the lower the energy of the system and the movements of the clusters. Biswas et al.[90] demonstrated the efficiency of the quenching step, reducing the size of Cu nanoclusters from (2.0±0.5) nm to (1.2±0.3) nm in a dual step continuous flow reactor.

After the cooling zone, the colloidal solution of metallic nanoclusters may be easily characterized by UV-VIS spectroscopy or photoluminesce analysis, even by in-line monitoring[100]. Finally, for catalytic applications the nanoclusters may be deposited by wet-impregnation over a proper support, guaranteeing longer shelf-life and recovery of the catalyst after application.

Regrettably, metallic nanostructures may deposit over the wall reactor for long working period, reducing the quality of the product or even blocking the production[109]. The fouling is particularly evident in the nucleation zone, where a hot-wall reactor promotes the growth of the nanoclusters over the wall surfaces[110]. The mechanism is reduced by the use of segmented or annular flow, where the nucleation is confined within the droplets[102]. Unfortunately, for slug flow reactors the stabilization of the flow is complicated and the residence time is reduced, which implies longer reaction time and the need of a subsequent separation of the two immiscible solvents. In this work, microwave heating was suggested as a valid alternative to selectively promote the nucleation in the inner volume, maintaining the wall reactor at lower temperature and then reducing the fouling in microfluidic channels. More details of microfluidic reactors will be provided in the following chapter 2.

1.5. **Microwave Heating**

In 1945, the engineer Percy LeBaron Spencer was visiting his lab at Raytheon Company, where magnetrons were being tested for military applications. Suddenly, he noticed that a peanut bar in his pocket begun to melt[111]. This strange and accidental event signs the discovering of the microwave heating mechanism. Even if Spencer patented the first domestic microwave oven just one year later, at the beginning it was not really appreciated by the consumers. The worries derived from the erroneous idea that microwave heated food may become radioactive.

From a physical point of view, microwaves occupy a small portion of the electromagnetic spectrum that ranges from 300 MHz to 300 GHz. When an external

electric field is applied to a dielectric compound, its molecules start to rotate, reaching a stable configuration when the electric dipoles moments are parallel to the electric field, Figure 1.11 a. The same happens with an electromagnetic wave, where the electric field **E** and the magnetic field **H** are perpendicular to each other and the propagation direction. As the field is oscillating, the molecules continuously rotate to follow the electric field with a rotation every 3 ns – 3 ps depending on the working frequency[112], as schematically represented in Figure 1.11 b.
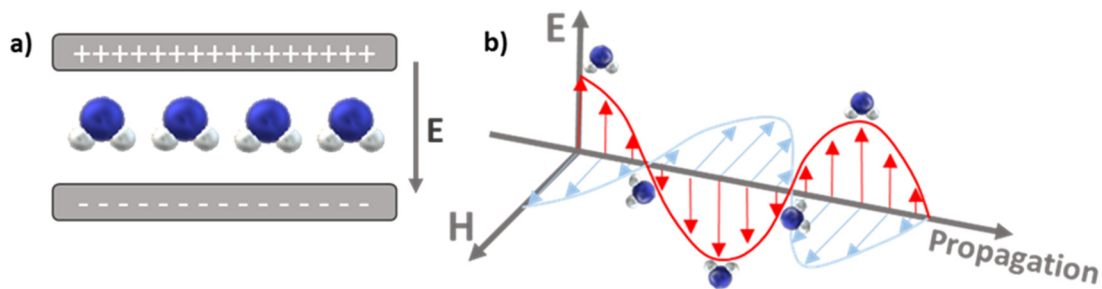
Figure 1.11 a) Orientation of dipole moments of a molecule of water in a static electric field and b) in an oscillating electromagnetic-wave.

The rapid rotations and the random collisions between molecules generate the temperature increase, technically known as polarization loss.

1.5.1. *Dielectric Properties*

The ability of a material to be heated in the presence of the MWH field is defined by its dielectric loss tangent: $\tan\delta=\varepsilon''/\varepsilon'$. The dielectric constant (ε') determines the energy storage in the dielectric, while the dielectric loss factor (ε'') measures the dissipation of electric energy in form of heat within the material[113]. Another important parameter is the penetration depth, defined as the distance at which the intensity of electromagnetic radiation falls to 1/e of its initial value, reported in equation 1.6[114].

$$D_p = \frac{\lambda}{4\pi}\left[\frac{2}{\varepsilon'(\sqrt{1+(\varepsilon_r''/\varepsilon_r')^2}-1)}\right]^{1/2} \tag{1.6}$$

Based on the dielectric constant and the penetration depth, the different materials can be divided into three groups[112]:

+ Microwave reflectors, e.g. metals. The radiation cannot penetrate inside of the material (skin penetration depth) and is reflected inside of the MW cavity. However, superficial electrons may be attracted by the electromagnetic field. For this reason, metallic walls may get hot (electric current dissipation) and produce sparks in case of thin and sharp borders.

+ Microwave absorbers, those able to take up energy from the microwave field and heat rapidly; $\tan \delta > 0.1$[115]. The dielectric properties are function of the working frequency and the temperature of the system, as reported in Table 1.2.

Table 1.2 Dielectric properties calculated at 20, 50 and 80 °C for 2.45 GHz[114].

Solvent	Loss Tangent (tan δ) – 2.45 GHz		
	20 °C	50 °C	80 °C
Ethylene Glycol	1.0137	0.6994	0.3606
Ethanol	0.9499	0.8027	0.5537
Tetrahydrofurfuryl alcohol	0.4608	0.3350	0.1909
1-Pentanol	0.3036	0.4968	0.5995
o-Dichloro benzene	0.2451	0.1839	0.1289
1-Hexanol	0.2325	0.3773	0.4998
Water	0.17	0.10	0.07
Acetone	0.0256	0.0181	Over b.p.
Octane	0.0197	0.0535	0.0763
Ethyl Acetate	0.0106	0.0045	Over b.p.

+ Microwave transmitters, e.g. fused quartz, ceramics, zirconia, etc. ($\tan \delta < 0.1$). In this case, the materials are transparent to microwaves, which means a very high penetration depth, Table 1.3. Even if liquid water is a good absorbent material, ice and water vapor act as transmitters. In the first case, the atoms present a rigid structure with strong hydrogen bonds that prevent atoms vibration. Instead, for water vapor the molecules are randomly dispersed, and the density of intermolecular interactions rapidly slows down.

Table 1.3 Penetration depth of different materials[116].

Solvent	Penetration Depth (mm) at 2.45 GHz
Water – 20 °C	14
Water – 95 °C	57
Ice – (-12 °C)	11000
Quartz	160000
Teflon	92000

1.5.1. *Microwaves-Assisted Synthesis of Nanocatalysts in Microreactors*

Fast nucleation, instantaneous quenching and reduced fouling are the main advantages of microwave-heated microreactors[110]. These benefits are only achievable if the reactor is microwave transparent, the inner flow is a high microwave absorbent and the channel size is smaller than the penetration depth in the liquid phase. The majority of nanoclusters synthesis is performed using water or ethanol as a solvent[91], which at 2.45 GHz possess a penetration depth of few centimeters. Despite this aspect limits the use of microwaves for batch reactors, it does not represent a restriction for microfluidic reactors (channel size ranges from 50 to 1000 µm). Microwave transparent materials have to be adopted for the reactor manufacturing, allowing the transmission of the MW irradiation in the channel volume. For this reason, quartz and Teflon® are preferred while metals and high-absorbent polymers are banned.

Horikoshi et al.[117,118] pioneered the switch from batch to continuous flow, comparing traditional jacketed reactor to alternative microwave heating system. Relevant results were also reported by the set-up introduced by Nishioka et al.[109], Figure 1.12 a. A linear Teflon® pipe (I.D. = 1 mm) was fixed in the center of a single-mode cavity, which guarantees higher reproducibility and efficiency[119]. Higher conversion was obtained by microwave heating (Figure 1.12 b) with a lower wall deposition, Figure 1.12 c and d. Even if the results are encouraging, the development of innovative techniques for an accurate estimation of the working temperature is crucial to discern between electromagnetic wave effects (non-thermal effects) and

temperature effects (thermal effects)[119]. Dziko et al.[120] reported an accurate analysis of the effects of different precursors, but the temperature was measured exclusively at the outlet point. Radial and longitudinal temperature gradient may occur in the heating zone, as the inner diameter (I.D.) of the polytetrafluoroethylene (PTFE) pipe adopted was 8 mm and the total length was 42 mm. The experimental measurement of the inner flow temperature is still one of the key points to address. The use of a thermographic camera, to estimate the temperature of the external wall surface of the reactor, results particularly useful for channels of few millimetres, where the radial gradient may be neglected[109,121,122].
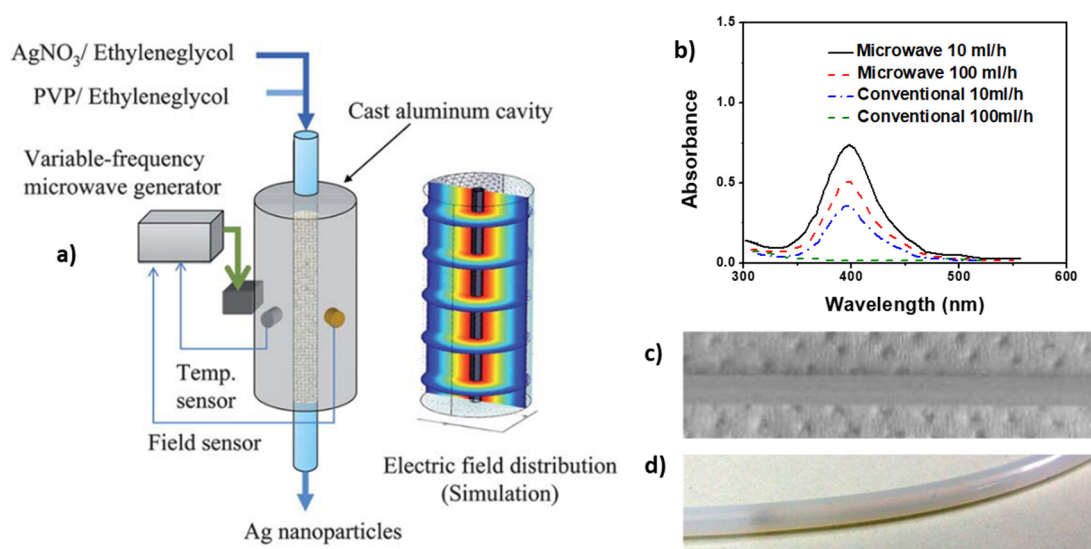
Figure 1.12 a) Microwave-assisted microfluidic reactor for NPs synthesis. b) UV-VIS spectra of silver nanoparticles comparing between microwave and conventional heating at different flow rates. c) and d) wall fouling after 2 h reaction for microwave and conventional heating respectively. (Adapted by permission of *The Royal Society of Chemistry*[109])

1.6. **PhD Thesis Objectives**

The main drawbacks of the traditional batch chemical processes are the excessive energy consumption, the variable product quality, the limited scaled-up and the poor efficiency. The European Training Network for Continuous Sonication and Microwave Reactors (ETN-COSMIC) aims to support the transition of the chemical industry from batch to continuous flow technologies with the investigation of alternative no contact energy sources, such as ultrasounds and microwaves.

The current PhD work targets the development of high efficient nanocatalysts suitable for heterogeneous catalytic reactions, focusing on the effects of microwaves and continuous flow reactors. The final goal is to develop an appropriate synthesis procedure for a recoverable heterogeneous catalyst that consists of supported metallic nanoclusters. The procedure should be robust, reproducible and easy to scale-up.

Considering the synthesis mechanism of metallic nanoclusters previously described, this thesis proposes a continuous microreactor heated up by microwaves as an optimum reactor for the synthesis of metallic nanoclusters. Finally, the metallic nanoclusters could be deposited on the catalytic support either by in-situ synthesis (direct procedure) or in a second step (indirect procedure).

This thesis covers the following aspects to successfully design the synthesis reactor and the final high efficient nanocatalysts:

- Study of microwave heating in a continuous microreactor for the synthesis of metallic nanoparticles, including simulation of the electromagnetic field and temperature distribution, and validation with experimental results.

- Definition of the optimum microwave heating patterns for the synthesis of metallic nanoclusters.

- Development of a synthesis procedure, based on microwave heating, for the in-situ synthesis of metallic nanoclusters on catalytic supports.

- The catalytic activity of nanoparticles and nanoclusters synthesized will be evaluated in the 4-Nitrophenol reduction as a reaction test and in hydrogenation of C≡C bonds which are of great interest for the synthesis of heterocyclic compounds, largely used in pharmaceutical and photochemistry as building blocks of higher complex molecules.

1.7. **Thesis Structure**

This thesis is structured in five experimental chapters. In chapter 2, it is introduced the microwave-heated continuous flow reactor used in this PhD research, benchmarking its efficiency with a common silver nanoparticles procedure that is carried out in a batch-type reactor comparing a conventional heating mode, such as an oil bath, and the alternative electromagnetic heating. An accurate investigation of the temperature mapping, performed by integrating simulated and experimental results, confirmed that microwaves guarantee a higher heating rate and consequently higher synthesis yield. Furthermore, the different heating profile contrasts the wall fouling and then, improves the quality of the final product. Once validated the pros of the reactor, it was explored an innovative template-assisted synthesis for the production of silver nanoclusters.

Firstly, the analysis was conducted in a batch-type process (chapter 3), evidencing the effects of the nucleation rate on the size distribution of the resulting nanoparticles. A detailed analysis of the temperature profile evidenced that the quality of the final product may increase by adopting a rapid selective heating rate, function of the microwave irradiation power. The quality of the produced nanomaterials was remarkable not only for their high activity in the tested conditions but also for their long-term stability which is more than 18-months. In a following step, the nanoparticles produced were deposited into mesoporous SBA-15 and their activity was tested using the hydrogenation of 4-Nitrophenol with sodium borohydride, comparing the developed nanosystem with literature results.

Then, the production process was switched in chapter 4 to a continuous flow reactor where the nearly instantaneous nucleation and the rapid quenching lowered the average clusters size and their relative size deviation. The nanoclusters were uniformly supported over the mesoporous channels of SBA-15, and the catalyst was tested for alkynes' hydrogenation. The high density of uncoordinated Ag atoms was responsible for the high activity observed, confirming that supported nanoclusters may represent a bridge between low active nanoparticles and unrecoverable silver salts. Furthermore, sometimes the coexistence of metallic and ionic state of the metal results in higher catalytic activity.

In chapter 5, an alternative reactor for *in-situ* nucleation of silver nanoclusters was introduced with the purpose of increasing the synthesis yield, lowering the metal loss. Microwave heating assured instantaneous nucleation of metallic clusters directly inside the substrate pores and an ice-water shell, transparent to microwaves, instantaneously cooling the system and inhibiting a further clusters growth. The clusters size was still reduced and the synthesis yield was higher than 90%. The higher metal loading may play a crucial role in accelerate some catalytic reaction, as demonstrated by the hydrogenation of 4-Nitrophenol. Furthermore, the nanocatalyst synthesized confirmed its usefulness for a wide range of C≡C cyclization and its morphological and catalytic stability was proved after one year of storage. To conclude, the scalability of the batch method was evaluated moving from 100 mg to 1 g of catalyst, in 2 minutes synthesis time.

Finally, chapter 6 is focused on the production of bimetallic nanoclusters, which may present interesting and fascinating properties. The continuous flow reactor was properly modified to allow a dual-step reducing process, and bimetallic structures were synthesized, investigating the effects of residence time and temperature profile. The bimetallic nanoclusters were directly synthesized on the carbon support in the continuous flow, maximizing the synthesis yield and optimizing clusters distribution.

2. MICROWAVES VERSUS CONVENTIONAL HEATING: Nanoparticles Synthesis

Goal: *Which are the main advantages of combining microwave heating and continuous flow reactors?*
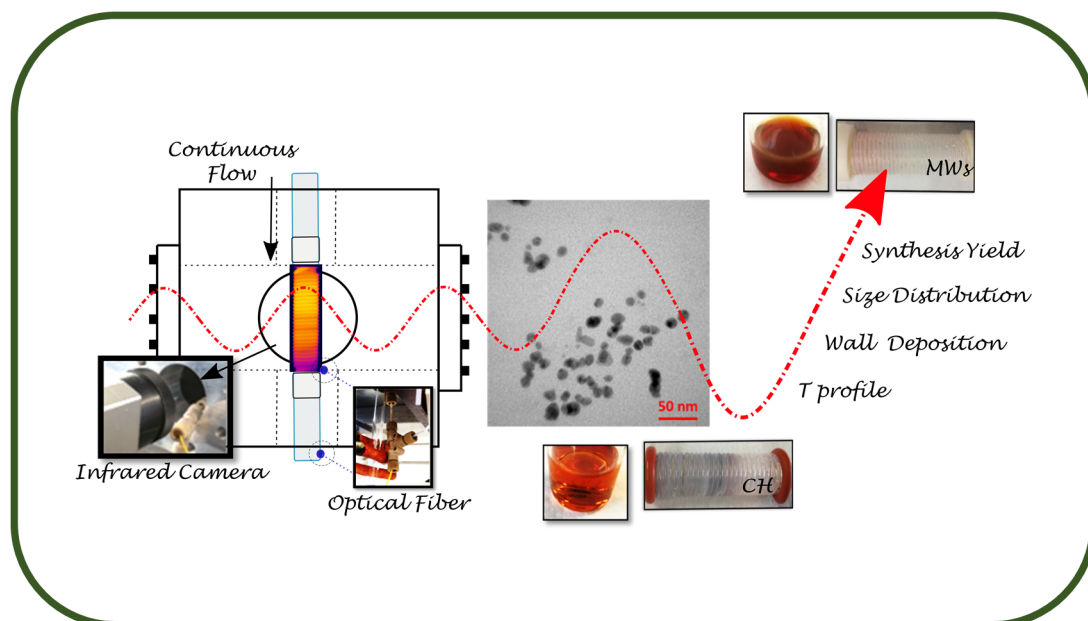
The contents of this chapter were adapted from the following published work:

"110th Anniversary: Nucleation of Ag Nanoparticles in Helical Microfluidic Reactor. Comparison between Microwave and Conventional Heating"

Roberta Manno, Víctor Sebastián*, Reyes Mallada*, Jesús Santamaría

Ind. Eng. Chem. Res. 2019, 58, 28, 12702-12711

Copyright 2019 American Chemical Society

2. MICROWAVES VERSUS CONVENTIONAL HEATING: Nanoparticles Synthesis

2.1. Introduction

The high flexibility and high control of residence time distribution afforded by microfluidic reactors make them especially suitable for nanomaterials synthesis, and thus they have been used for the fabrication of several nanostructures, such as monodisperse monometallic and bimetallic nanoparticles, nanocubes, nanorods, nanosheets, core-shell, Janus structures, and so on[123–129]. In comparison with traditional techniques, the result is usually a reduction of reagents waste, side reactions, synthesis time, temperature and narrower nanoparticle size distribution, as well as increase the synthesis yield[127,130]. Unfortunately, microchannel obstruction by deposited nanoparticles still represents a serious challenge for the synthesis of nanomaterials in continuous flow[131].

Microwave heating (MWH) may represent a winner alternative to invert the radial temperature profile, diminishing the nucleation of nanoparticles over the reactor wall. Tsuji et al.[132] suggested that microwaves promote the formation of hot spots on the surface of aprotic polar molecules, like PVP, which remarkably accelerates the formation of metallic nanoparticles. Moreover, polar solvents, characterized by high values of dielectric loss, can convert electromagnetic (EM) energy into thermal energy very fast. The localized rapid rise of temperature enhances the product yield, decreasing the reaction time required to produce nanomaterials with similar quality[133,134]. On the other hand, MWH is limited by the penetration depth of the EM wave in the heated medium, which is very low in the case of polar solvents[114]. Although this could limit its use for batch reactors, no physical limitations may interfere with its application for continuous flow reactors, where the structural dimension is below millimetre scale[117,134–136]. As a result, if the flowing medium is microwave absorbent and the external wall is microwave transparent, the

maximum temperature appears in the center of the channel, reducing the wall deposition[117,118].

Among the methods for the synthesis of silver nanoparticles, the polyol-based procedure has been selected as a test reaction due to several studies reported[124,137]. Commonly ethylene glycol is used as solvent and reducing agent of silver nitrate, (or other silver salts) and PVP acts as stabilizing agent of the formed nanoparticles. This synthesis has been previously reported under MWH in a batch reactor[109,124], observing in all the cases high conversion at low reaction times due to the rapidity of the heating mechanism. In 2011, Nishioka et al.[109] demonstrated the advantages of combining microwaves and flow chemistry in the polyol method by working at residences times between 2.8 and 28.3 s and a nominal temperature of 160 °C. The particles synthesized presented a narrower size distribution, compared to conventional heating and the deposition on the internal wall of the reactor drastically decreased. The faster reaction observed with MWH is usually related to the different temperature profile induced. Although the cylindrical monomode cavity employed presented a uniform distribution of the EM field, the temperature profile observed with a thermographic sensor along the length of the reactor varied from 80 to 160 °C. Dzido et al.[120] also reported a continuous synthesis method under MWH, observing in this case, a bimodal size distribution of nanoparticles attributed to the non-isothermal nature of the realized continuous flow process. The accurate estimation of the working temperature is crucial to discern between electromagnetic wave effects (non-thermal effects) and temperature effects (thermal effects). However, the experimental measurement of the inner flow temperature is still a challenging problem for microfluidic reactors, where infrared camera (IR-camera) is usually adopted to estimate the temperature of the external wall surface checking exclusively the outlet temperature point by an optical fiber (O.F.)[109,122].

This chapter aims to explore the advantages of adopting MWH versus conventional heating (CH) for a continuous flow microreactor, using systems that otherwise

present the same characteristics concerning reactor design, residence time and chemical reagents. In both systems, Ag nanoparticles have been synthesized and characterized at different flow rates, comparing size distribution, synthesis yield, and accumulation of nanoparticles onto the microchannel surface (wall deposition). For the first time a detailed temperature mapping, combining experimental and simulated measurements, has been presented. Experimental data were obtained both by a thermographic camera in the MW heated microreactor and an optical fiber at the heating zone outlet. On the other hand, simulated results were obtained by the multiphysics modelling of the reactor designed in the framework of this PhD.

2.2. **Materials and Methods**

2.2.1. *Synthesis Procedure of Ag Nanoparticles and Microfluidic Reactor*

Silver Nitrate (Aldrich 99.9999%), acted as precursor of silver nanoparticles and was mixed under mechanical stirring, at room temperature, with deionized water (0.157 g into 10 mL). Polyvinylpyrrolidone (PVP-Sigma Aldrich MWH 55,000) acted as a stabilizer, reducing the agglomeration of the nanoparticles. PVP was mixed under mechanical stirring at 80 °C with ethylene glycol (Aldrich 99.9%) (2.4 g into 10 mL). Ethylene glycol (Sigma Aldrich 99.8%) worked as the reducing agent and as the reaction solvent. The reaction occurred according to the following steps[109]

$$CH_2OH - CH_2OH \rightarrow CH_3CHO + H_2O$$
$$2CH_3CHO + 2Ag^+ \rightarrow 2Ag + 2H^+ + CH_3COCOCH_3$$
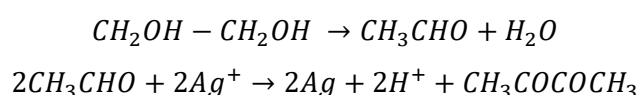
The silver nitrate and PVP solutions were pumped through two separate syringes using high precision syringe pumps (PHD ULTRA by Harvard Apparatus), mixed in a Y-mixer and fed to the reactor. The two inlets, indicated by I_1 and I_2 in Figure 2.1, presented the same flow rate and the resulting flow ranged between 0.1 and 0.6 mL/min. The continuous synthesis of Ag NPs was performed in polytetrafluoroethylene (Teflon®, Iberfluid Instruments) helical tubular reactors with an inner diameter (I.D.) of 0.39 mm and an outer diameter (O.D.) of 1.59 mm. All the Peek connections adopted (ferrules, nuts, luer adapter, and Y-mixers) have

been provided by IDEX. In detail, the Y-mixer presents a thru-hole of 0.02'' and a swept volume of 1.7 μL. The Teflon® pipe was rolled on top of a quartz tube (O.D. 9 mm) and precisely fixed by Teflon® tape, see Figure 2.1. The total length of the Teflon® tube in the heating zone was 77 cm, which corresponds to 27 turns of the helix and a total reactor volume of 91 μL.

After synthesis, the colloidal solutions of nanoparticles collected were centrifuged at 21,000 rpm for 15 minutes and washed with acetone to purify them.
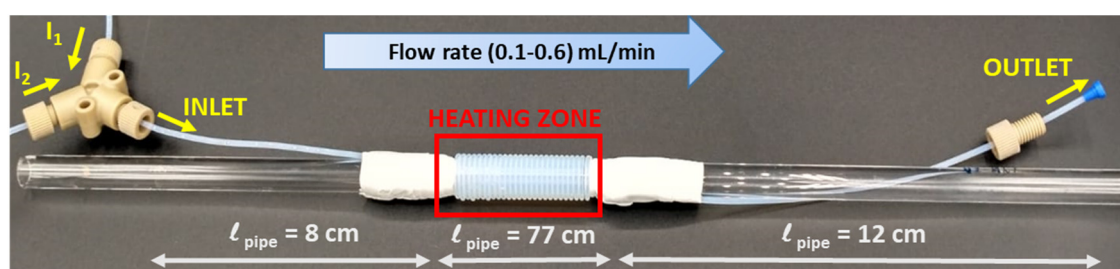
Figure 2.1 Microfluidic reactor adopted for the synthesis of Ag nanoparticles. The two flows of the precursors (I_1 and I_2) were mixed in a commercial Y-mixer. After a length of 8 cm, the precursors were fastly heated by MWH or CH.

2.2.2. *Characterization of Ag Nanoparticles*

Transmission Electron Microscopy (TEM): The synthesized silver NPs were observed by Transmission Electron Microscopy (TEM) in a FEI TECNAI T20 microscope with a maximum energy of 200 keV. A 10 μL suspension of the NPs was pipetted onto a TEM copper grid having a continuous carbon film. After complete evaporation, the sample was analyzed by TEM. The particle size distribution of the synthesized nanoparticles was obtained by analysis of at least 120 nanoparticles.

Scanning electron microscope (SEM) in a FEI-INSPECT-F50 was employed for the examination of the internal surface of the Teflon® pipe.

Dynamic Light Scattering (Zeta Plus; Brookhaven Instruments Corporation, NY, USA) was performed of each sample after appropriate dilution in Milli-Q water and sonication of the sample for 5 minutes, evaluating polydispersity and size distribution. At least five replicate measurements were recorded in each case.

UV-Vis Spectroscopy (Agilent 8453 UV-Visible spectrophotometer) was employed to measure surface plasmon resonance (SPR), which is a qualitative measure of size distribution and synthesis yield of silver nanoparticles. The spectrophotometric test was performed diluting 100 µL of the sample into 1500 µL of ethylene glycol and 1500 µL of distilled water.

Microwave Plasma – Atomic Emission Spectroscopy (MP-AES): The silver content of liquid samples and suspensions was determined by Microwave Plasma – Atomic Emission Spectroscopy (MP-AES) (Agilent 4100 MP-AES). 3 mL of NPs produced sample were centrifuged into 20 mL of pure Acetone at 21,000 rpm for 30 minutes. Supernatant and pellet were analyzed as followed to assess the appropriateness of the analytical method:

- Supernatant: 100 µL of the supernatant was digested into 2 mL with the addition of nitric acid (HNO_3) and hydrochloric acid (HCl) in a volume ratio of 1:3. The resultant digested sample was diluted with Milli-Q water to a final volume of 10 mL for the MP-AES analysis.

- Pellet: The pellet was dispersed in Milli-Q water to a final volume of 10 mL for the analysis. 100 µL of the sample was digested into 2 mL with the addition of nitric acid (HNO_3) and hydrochloric acid (HCl) in a volume ratio of 1:3. The resultant digested sample was diluted with Milli-Q water to a final volume of 10 mL for the MP-AES analysis.

All the characterization experiments presented were repeated at least with three different independent experiments, and average results are presented in the following section.

2.2.3. _Microwave and Conventionally Heated Systems and Temperature Measurements_

The rectangular MW cavity adopted consisted of:

- A solid-state microwave generator operating in a range of 2.43-2.47 GHz, with a 0.1 MHz step and a maximum working power of 150 W, provided by Sairem Iberica.

- A TE10 monomode microwave cavity and a WR340 waveguide, provided by Sairem Iberica.

- A three stub-tuner, model GA1002, provided by Gerling Applied Engineering. The three capacitive, non-contacting stubs were spaced at a quarter guide wavelength intervals and offset a sixteenth guide wavelength from the center.

The microwave power was supplied continuously. More details about the design of the MW cavity were provided in previous works published in our group by Nigar et al.[138,139]. The input of the MW irradiation was represented by a coaxial port connected with a metallic loop. Its function was to convert a coaxial transverse electromagnetic mode (TEM) to a transverse electric mode (TE10) typical of a rectangular cavity[140]. A Vector Network Analyzer was adopted to optimize the position of the three stub tuners minimizing the reflection S_{11} parameter. During the synthesis, constant values of power and frequency, 20 W and 2.45 GHz respectively, were applied. For MWH experiments the reactor was vertically located in the microwave rectangular cavity, the reagents flowed downwards, as reported in Figure 2.2. A commercial T-fitting was modified to locate a Neoptix Optical Fiber sensor (range 193-523 K, Ø: 1 mm) to measure the temperature of the liquid near the exit of the PTFE tubing. The temperature was measured in two points, in Figure 2.2: A, which corresponded to the last turn of the helical reactor in the heating zone, and B, located immediately outside of the cavity at around 50 mm of the last turn. Moreover, a thermographic camera (Optris PI-400038T900) recorded the temperature distribution on the outer surface of the PTFE tubing.

In CH experiments, the microfluidic reactor was immersed in a thermostatic bath. The temperature was measured experimentally using an optical fiber at four

different points inside the tubing corresponding to the end of the 5th, 10th, 20th, and 25th turn. In this case, the hot liquid that surrounds the reactor prevents the use of the thermographic camera for the measurement of the temperature distribution along the reactor.
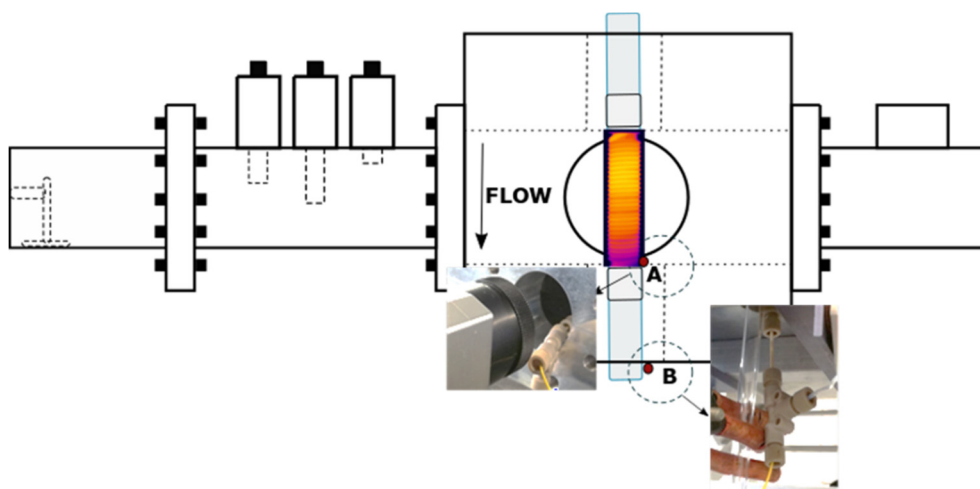
Figure 2.2 Representation of the rectangular microwave cavity and the location of the reactor. On the left of the cavity, the metallic loop connected with the coaxial input port and the three stub tuners. The microreactor was vertically fixed in the center of the cavity. The IR-camera recorded a thermograph of the entire external surface of the reactor and the optical fiber measured the temperature in two points: A inside the cavity to measure the temperature of the last turn and B for the outlet temperature.

2.3. Multiphysics Model

The multiphysics model allowed to simultaneously analyse the laminar flow inside of the microfluidic reactor, the heat transfer balance of the entire set-up and, in the case of MWH, the EM wave propagation inside of the rectangular cavity. The common hypothesis of stationary state has been considered. For MWH analysis, the numerical simulation was adopted to estimate the radial temperature deviation between the inner flow domain and the external wall reactor. Furthermore, it allowed to study the EM wave distribution and to corroborate the selective heating of the inner flow. In the case of CH, the model was mainly adopted to estimate the temperature profile along the reactor as a function of the residence time. Experimental results validated the model for both of the heating mechanisms. More

details on physical properties, dimensionless parameters (Re, Nu, Pr and De numbers), and mesh analysis have been summarized in appendix 1.

2.3.1. *Laminar Flow Analysis*

For the incompressible fluid flow of the microfluidic reactor, it was considered steady-state momentum and mass conservation respectively by solving Navier-Stokes and continuity equations, as reported in equations 2.1 and 2.2.

$$\rho(\boldsymbol{u} \cdot \boldsymbol{\nabla})\boldsymbol{u} = \boldsymbol{\nabla} \cdot [-\rho\boldsymbol{l} + \mu(\nabla\boldsymbol{u} + (\nabla\boldsymbol{u})^T)] + \boldsymbol{F} \qquad (2.1)$$

$$\rho\boldsymbol{\nabla} \cdot (\boldsymbol{u}) = 0 \qquad (2.2)$$

The pressure transmitted from the syringe pump to the fluid was represented by the external force $\boldsymbol{F}$ of equation 2.1. Physical properties such as density ρ and viscosity μ have been considered as a function of temperature.

2.3.2. *Heat Transfer*

The steady-state energy balance was reflected in equation 2.3

$$\rho C_p \boldsymbol{u} \cdot \boldsymbol{\nabla}T + \boldsymbol{\nabla} \cdot \boldsymbol{q} = Q \qquad (2.3)$$

Thermal conductivity and heat capacity of water and air domains have been considered temperature-dependent. Instead, constant values have been considered for quartz and Teflon® domains. For both of the heating mechanisms, continuity condition was applied between the interface of two adjacent domains 1 and 2, as resumed by equation 2.4.

$$\boldsymbol{q} = -k\boldsymbol{\nabla}T \qquad (2.4)$$

For MWH, the heat transfer mechanism has been correlated to the EM wave propagation in four different domains (inner flow, Teflon® wall reactor, surrounded air and quartz support) and, consequently, the dielectric properties of each domain were expressed as a function of temperature itself. Instead, for the CH, the analysis was reduced to two domains (inner flow and Teflon® wall reactor), fixing the temperature of the external surface in contact with the oil bath.

2.3.3. *EM wave*

The solving of Maxwell equations, 2.5 and 2.6, were applied to estimate the propagation of the EM wave in the rectangular cavity and the external heat contribution, indicated as *Q* value in previous eq. 2.3.

$$\nabla^2 \mathbf{E} + \omega^2 \varepsilon \mu \mathbf{E} = 0 \tag{2.5}$$

$$Q_{MW} = \pi f \varepsilon_0 \varepsilon_r'' \mathbf{E} \cdot \mathbf{E}^* \tag{2.6}$$

To solve the equations, the following hypothesis have been considered:

- Impedance boundary condition was assigned to the metallic walls of the reactor, to approximate a skin effect linked to the generation of dissipative electric surface currents.

- The relative permeability μr was considered equal to 1, avoiding the contribution of magnetic field on power dissipation.

- No magnetic materials have been considered, μ≈0.

- Dielectric properties have been considered temperature dependent only for water and air domains. For quartz and Teflon® domains have been kept constant.

- The EM wave was transmitted by a one feed coaxial input port.

The simulations were conducted for a geometry of 10 turns instead of 27 for the helix construction to reduce the computational time, as represented in Figure 2.3. The liquid flowing along the reactor was pure water at different flow rates. Considering the reduced volume of absorbent material, the input power was reduced to 10 W to preserve the equipment from high reflected power during experimental validation.
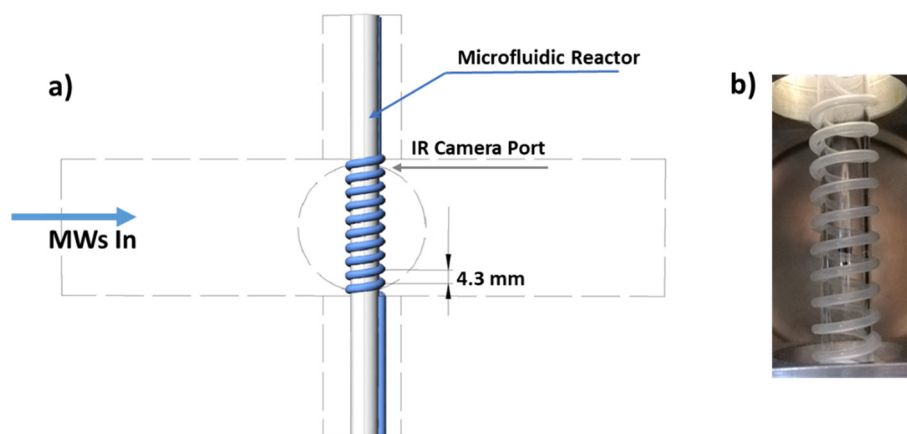
Figure 2.3 Microreactor placed in the center of the rectangular MW cavity. In figure a) the schematical representation and the geometrical details, while in figure b) the experimental set-up adopted for the simulation of EM wave analysis.

2.4. Results and Discussions

2.4.1. *Radial Temperature Mapping and Velocity Profiles in the Microfluidic System*

The combination of microwave technologies with microfluidic reactors tangles the accurate measurement of temperature profile inside of small reactor channels. The use of a numerical model represents a useful tool to overpass the technical limitation of experimental measurements. As represented in Figure 2.4 a, the EM wave travels unhindered in the air domain, transparent to MW, then the EM field decreases to a certain extent due to MW absorption in the Teflon® (tanδ=0.002857at 2.45 GHz and 25 °C) wall and finally a rapid decrease of the EM intensity occurs in the inner flow domain (tanδ=0.12 at 2.45 GHz and 25 °C for water[141]), which is the unique high MW absorbent material of the set-up presented. As a result of the conversion of electric energy to thermal energy, the temperature of the flow domain increases and a radial heat flux come out of the flow reactor where heating dissipation occurred due to conduction and convection phenomena, as presented in Figure 2.4 b.
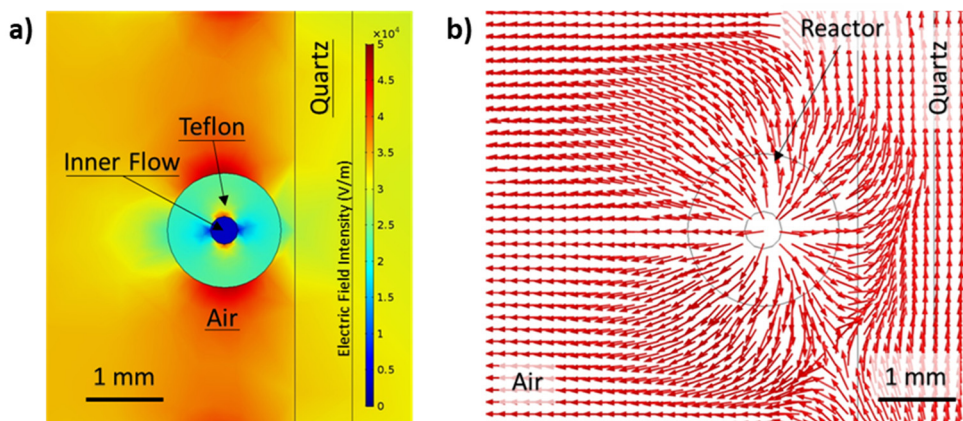
Figure 2.4 Electromagnetic field distribution a) and heat flux b) in quartz support, microreactor and air domain obtained by COMSOL Multiphysics® Simulation.

A good agreeement of temperature distribution was observed between experimental and simulated results, (see Figure 2.5 a and Table 2.1) validating the numerical model. Analysing a cross-section of the reactor (d=0.39 mm), a slight radial variation of temperature was observed, reporting a deviation of approximately 1.4% (ΔT=0.7 °C) for the wall in contact with air and 2.2% (ΔT=1.1 °C) for the wall in contact with the quartz surface, in Figure 2.5 b. Instead, a more heterogeneous profile was reported by Zhu et al.[142] with differences of more than 20 °C when the reactor presents a diameter of 40 mm, as a result of the decrease of EM wave intensity during the penetration of the absorbent domains.

On the other hand, the variation of the flow rate mainly affects the temperature gradient along the reactor length (i.e "number of turn" see Figure 2.5), without relevant variations in the radial direction (Table 2.1). Then, it is possible to conclude that for the flow rate range analysed, the difference of temperature between the inner flow and the experimental surface profile, recorded by the IR camera, was nearly negligible in the stationary step. For this reason, the experimental data obtained by the IR camera will be adopted as a reference value for the MWH experiments.
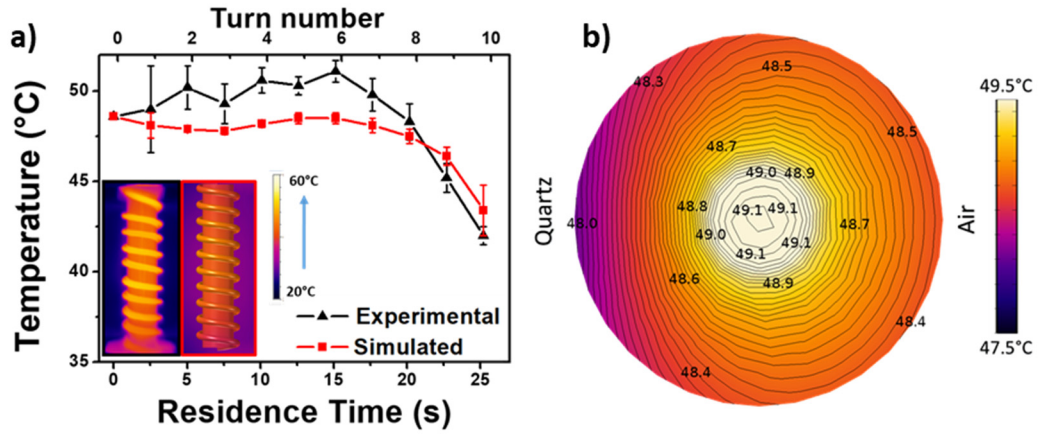
Figure 2.5 a) Experimental and simulated longitudinal temperature profile for a microfluidic reactor considering a residence time of 25 s, highlighted respectively in red and black border of optical inserts. b) Radial T mapping in the cross-section of the microfluidic reactor calculated on the surface with the maximum temperature. Simulated results were obtained by COMSOL Multiphysics® Simulation.

Table 2.1 Experimental (on the left) and simulated (on the right) longitudinal temperature gradient and radial temperature gradient at different flow rates, from 0.2 mL/min to 0.6 mL/min. Simulated results were obtained by COMSOL Multiphysics® Simulation.
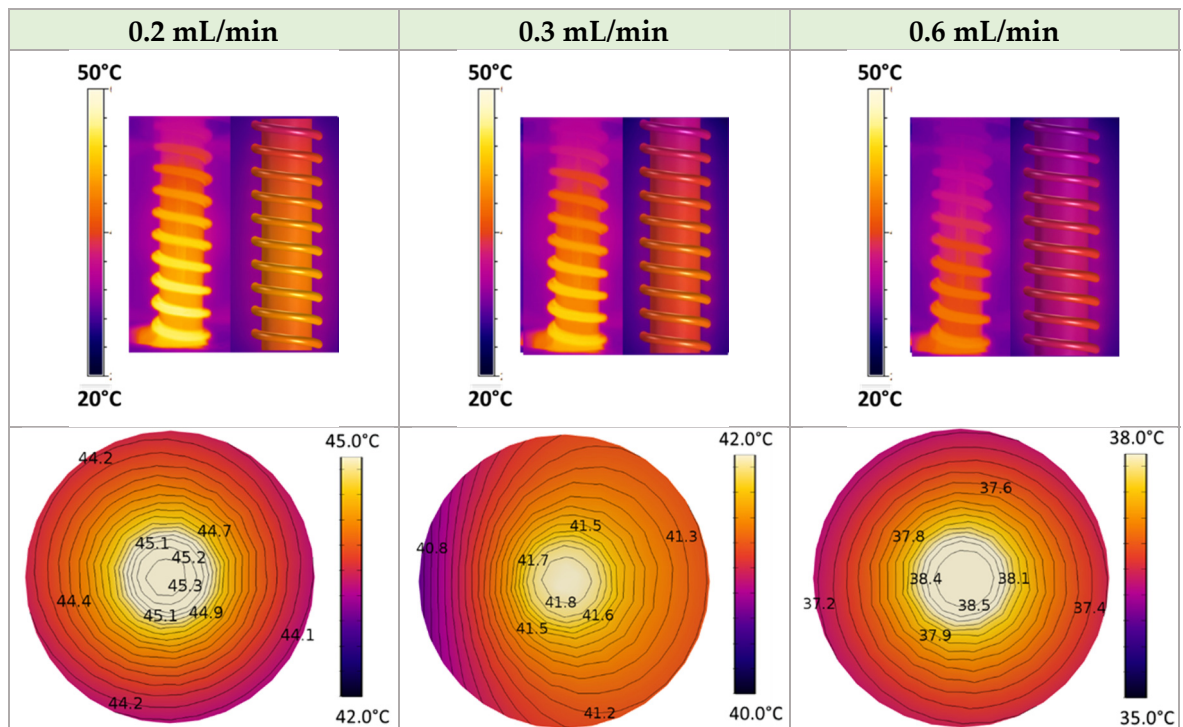
Furthermore, the numerical model was useful to estimate the velocity profile in the helical reactor for conventional heating mode. For this analysis, a more complex geometry was adopted for the following synthesis experiments (n=27 turns) fixing the temperature of wall surface. In accordance with Srinivasan et al.[113], the estimation of the critical Reynold number (Re_{cr}) for a helical shape reactor is strictly dependent on the curvature ratio. For the configuration here presented, the threshold value is close to 6600 and the Reynold number ranges between 91.5 and 548.7 for 0.1 mL/min and 0.6 mL/min respectively. For this reason, the velocity distribution presents a parabolic profile without turbulences, typical of microfluidic systems that usually work with laminar flow conditions[143]. Furthermore, the mass transport depends only on diffusion mechanism[130]. Chen and Meiners[144] demonstrated how a helical channel, that continuously folds the flow, enhances the mixing between the reagents. Nevertheless, Kumar et al.[145] underlined that for so small values of the Re number, the curvature ratio rather than the helical shape influences the diffusivity of the reagents. In curved pipes the centrifugal force disturbs the parabolic profile of the flow, generating recirculation of fluid from the center to the outer channel wall, known as Dean effect[146]. The higher the ratio of the pipe diameter to the pipe bending radius, the higher the effects of secondary flow. These vortices cause mixing in the cross-section, enhancing heating and mixing mechanisms. As previously described by Parameswaran et al.[147], an unstable flow is observed when Dean number is beyond 200-300. However, as a result of the variation of the stream velocity, the Dean number progressively switches from 16.3 to 97.9, for 0.1 and 0.6 mL/min respectively (more details in appendix 1). Then, an increase of the effects of secondary flows was observed and the fluid was forced from the center to the outer channel wall, as reported in Table 2.2.

Table 2.2: Map of inner flow at different flow rates obtained by COMSOL Multiphysics® Simulation.

FLOW RATE			
0.1 mL/min	0.2 mL/min	0.3 mL/min	0.6 mL/min
Velocity Field _ Streamlines			
Vorticity Field			
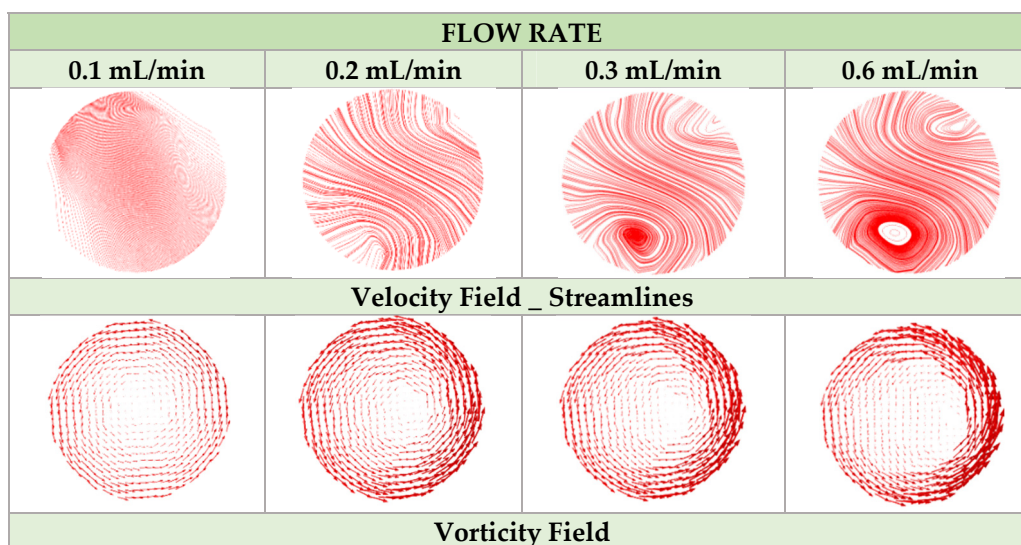
2.4.2. *Synthesis of Ag NPs*

The polyol assisted synthesis of Ag NPs is usually performed at 140-160 °C, temperature required to oxidize the ethylene glycol, facilitating the complexation of the polyol with the metal centre. This step is crucial to activate the nucleation phase. It is still difficult to establish if the first nuclei were generated by solvated metal species or unreduced metal species. Once formed, Ag nanoparticles promote polyol oxidation via an autocatalytic process[148,149]. Despite that, the oxidation of ethylene glycol starts at 40 °C[150] and, as reported by Dziko et al.[137], Ag nanoparticles may be produced at temperatures lower than 100 °C in continuous flow. In this work, a preliminary analysis was conducted to determine the average temperatures under MWH at different flow rates, with a constant power of 20 W, using the IR camera to record the temperature profile. Figure 2.6 a shows an example of the thermographic images employed to determine the average temperature of the external wall of the reactor, T_w. As expected, an increase in the flow rate produces a decrease in the average temperature (Figure 2.6 b), being in all the cases higher than 80 °C. The average temperatures calculated were selected as set point temperatures for the oil bath during CH experiments (see $T_{oil\ bath}$ in Table 2.3). In this way, the outer surface temperature of the reactor presented the same average temperature for the two

heating modes. Table 2.3 summarizes all the experiments carried out, indicating the heating source, the flow rate Q, the residence time t_{res}, and temperatures of conventional heating $T_{oil\ bath}$ and microwave-heated T_w modes, together with a photograph of the resulting solution after synthesis. It can readily be seen that the solution containing the nanoparticles synthesized with MWH presented a more intense colour compared to CH, indicating a higher concentration of Ag nanoparticles.
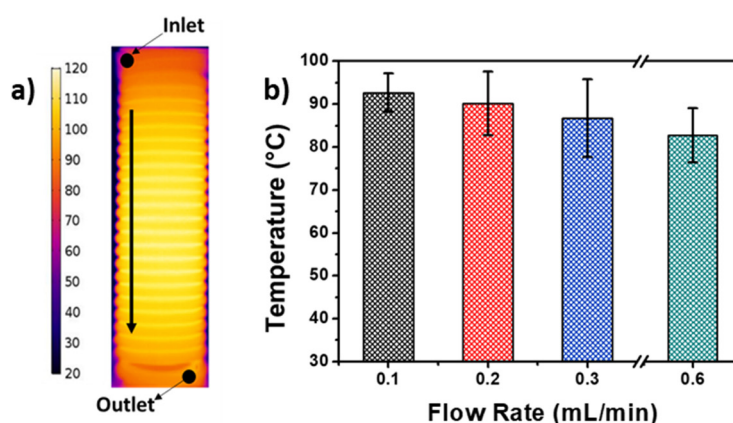
Figure 2.6. a) Image of the thermographic camera showing the outer reactor wall. Temperature readings were used to determine average surface temperatures under MWH for different flow rates. b) Average IR temperature obtained under MWH for different flow rates, P_{MWs}=20 W, f=2.45 GHz.

Table 2.3: Summary of experiments and experimental conditions for MWH and CH.

Heating Source		Q	t_{res}	$T_{oil\ bath}$	T_w
CH	MWH	mL/min	s	°C	°C
		0.1	54	92.7	(92.7±4.5)
		0.2	27	90.2	(90.2±7.4)
		0.3	18	86.7	(86.7±9.1)
		0.6	9	82.7	(82.7±6.3)

The analysis of the UV-Vis spectra, in Figure 2.7, showed a typical absorption at around 419 nm associated with the surface plasmon resonance SPR of Ag NPs. The SPR absorption peak intensity decreased for CH and high flow rates, i.e. low residence times. A similar trend was reported by Nishioka et al.[109] at 160 °C outlet reaction temperature, where the intensity of the SPR peak decreased from around 0.8 to 0.5 (without dilution of the sample) as the residence time decreased from 28 to 2.8 s. The absorbance was nearly zero for a residence time of 0.5 s. Several factors may affect the differences reported on the absorbance spectra, mainly connected with alterations in the morphology of the nanoparticles and their concentration. The broad shape observed may indicate the presence of a wide distribution of silver nanoparticles following Mie theory[151]. This phenomenon is especially relevant in Ag nanoparticles produced under a residence time of 54 s, where the bandwidth of MWH produced nanoparticles is larger than the CH ones. According to Mie theory, the bandwidth of silver nanoparticles is very sensitive to particle radius in the range of 1.5-10 nm and 20-40 nm[152]. This agrees with the particle size histograms reported in Figure 2.8 where it can be observed that mean size of Ag nanoparticles produced by MWH at 54 s residence time are in the size range of (19±4.3) nm, whereas the ones produced by CH are in the range of (10.8±4.7) nm. In any case, the SPR absorption is always more intense under MWH which may indicate a faster conversion of the reaction. This is due to the volumetric heating achieved under microwaves: a fast heating of the inner fluid occurs, resulting in faster nucleation and growth.

MP-AES, TEM and DLS analysis were adopted to further investigate the influence of residence time and heating mode on the synthesis mechanism. The MP-AES analysis confirmed an increase of synthesis yield of around 13%, (from 41% to 54%) when comparing MWH and CH, for the highest residence time of 54 s. This value agrees well with the 42% reported by Grzegorz Dzido[120] working at 90 °C outlet

temperature of the MWH reactor and a residence time of 12 s. Full conversion was reported only when the reaction temperature was higher than 150 °C.
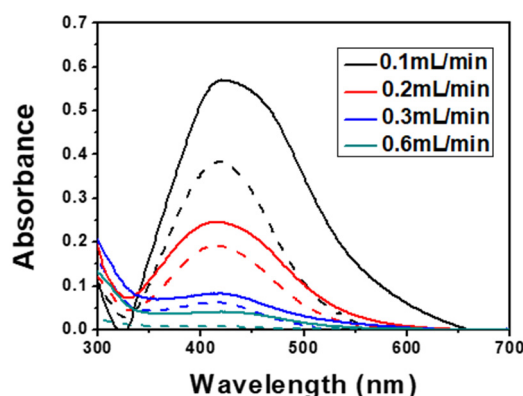
Figure 2.7 UV-Vis spectra analysis of Ag NPs synthesized at different flow rates. Continuous and dashed lines represent MWH and CH, respectively.

TEM and DLS analysis allowed us to determine the particle size distribution of the different experiments. The polydispersity index obtained in DLS was always higher than 0.15 indicating a relatively broad distribution of the particle size, also confirmed by the shape of UV-Vis analysis. This broad size distribution is partly a consequence of the velocity profiles under laminar flow regime. Figure 2.8 and Table 2.4 show the analysis of size distribution obtained from TEM images for microwaves and conventional heating at the different flow rates. The software ImageJ was adopted to determine the size distribution. A clear correlation of residence time and size of the particles is observed. For both of the systems, an increase in flow rate shifts the size distribution to lower diameter values. Moreover, the particle diameter is dependent on the heating source. Particles synthesized by microwaves are almost twice as big as particles obtained by CH indicating a more intense reaction under MWH. On the other hand, the size distribution was broader for conventional heating, as indicated by the relative standard deviation in Table 2.4, which is roughly double when comparing CH vs. MWH. Less pronounced difference was observed by Hongjin Jiang[153], who noticed a shift of relative standard from 0.46 to 0.36 respectively for CH and MWH.
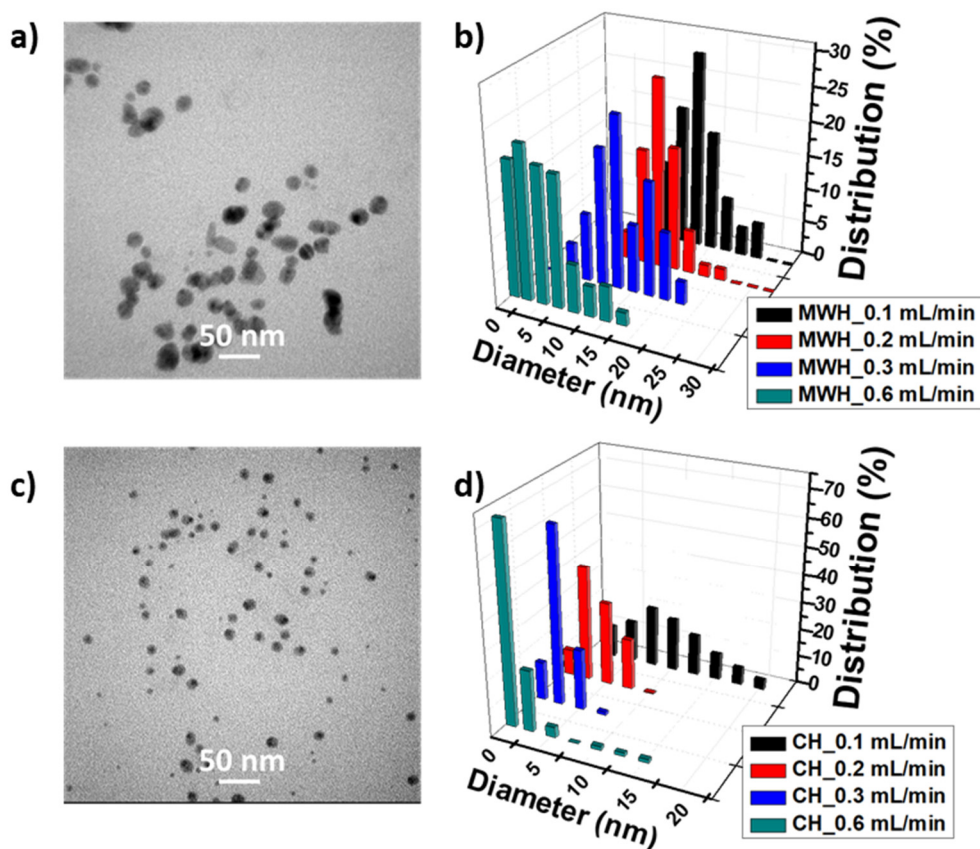
Figure 2.8 Particle size distribution at different flow rates and representative TEM images for a flow rate of 0.2 mL/min for MWH (a and b) and CH (c and d) heating modes.

Table 2.4: TEM analysis distribution for MWH and CH. N stands for the number of nanoparticles measured to obtain the nanoparticles size distribution histogram.

TEM Analysis						
Q	MWH			CH		
(mL/min)	Mean Value (nm)	Rel. Stan. Dev.	N meas.	Mean Value (nm)	Rel. Stan. Dev.	N meas.
0.1	19.0±4.3	0.23	226	10.8±4.7	0.44	269
0.2	14.3±2.9	0.20	182	5.1±2.1	0.41	233
0.3	14.0±4.3	0.31	185	3.8±1.7	0.45	121
0.6	5.8±3.4	0.59	195	2.7±2.4	0.88	128

Ag synthesized NPs were highly crystalline, as it inferred from HRTEM images of two representative nanoparticles (Figure 2.9 a and b). Fourier transform analysis

revealed a face-centered cubic symmetry, characteristic of the Ag packing in NPs with Fm3m crystallographic space group (Figure 2.9 c-f).
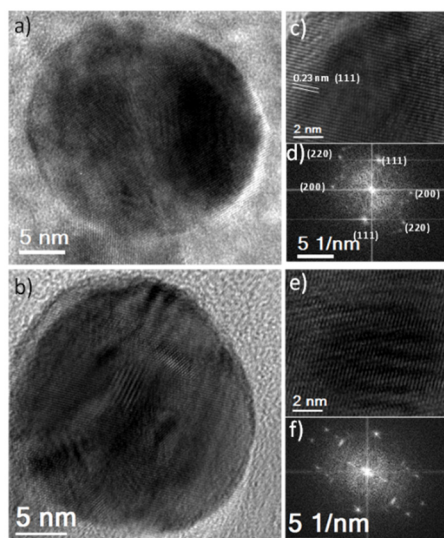
Figure 2.9 a)-b) High-resolution TEM analysis of Ag-NPs produced by MWH, flow rate 0.1 mL/min. c-e) Micrographs showing fine detail of a single Ag-NP; d)-f) Fourier function transform (FFT) analysis of a) and b); where crystal planes and d-spacing corresponds to Fm3m space group.

2.4.3. *Comparison of Temperature Profile between MWH and CH*

A detailed evaluation of the temperature profile was performed to justify the differences in synthesis yield and size distribution obtained with the two heating systems. A slow nucleation mechanism may occur even at room temperature between the Y-mixer and the heating zone (l_{pipe}=8 cm, as reported in Figure 2.1). However, considering the small volume of the concerned section of the reactor (nominal residence times in that zone would be at least 5.6 seconds) and the slow kinetics for this low temperature, the extent of particles nucleation before the heating step can be neglected in this work. For MWH, a preliminary study allowed to compare data of IR-camera, recording the wall temperature of the Teflon® pipe, and the readings of the O.F. inserted inside the tubing. The temperature recorded with the IR-camera in the last turn was very close to the temperature recorded with the O.F. (position A of Figure 2.2), with a difference always lower than 2 °C. This fact confirmed that the temperature drops along the thickness of the Teflon® tube (0.6 mm) is negligible and the IR-camera temperature is a good approximation of

the internal flow temperature. Thus, the temperature profile along the tube could be determined by calculating the average temperature of the area of each pipe turn, recorded by thermographs of IR-camera. In the case of CH, the internal flow temperature was simulated by COMSOL Multiphysics®, as described in the previous section.

Figure 2.10 presents the temperature profiles for the 4 different residence times studied, in red for thermographic camera measurements for MWH and in black simulation for CH. The black star symbols correspond to the experimental measurement of the optical fiber in CH at 4 different points (5th, 10th, 20th and 25th turns), measured for a flow rate of 0.1 mL/min and 0.6 mL/min. The experimental values agree well with the simulated line, validating the model parameters and the calculated heat transfer coefficient for CH. Looking at the two temperature profiles, it is clear that the temperature reached by the fluid under CH is always lower compared to the fluid heated by MW. This is mainly due to the strong reduction of the heating length achieved under MWH conditions, where reaction temperature is achieved earlier, as shown in Figure 2.10 under any of the conditions employed. This observation correlates with the lower synthesis yield obtained in CH and explains the differences observed in terms of nanoparticle size and concentration, in agreement with previous analysis suggesting that thermal effects are responsible for the higher synthesis yield obtained by microwave heating[154]. In the case of the lowest flow 0.1 mL/min the temperature of the fluid is above 75 °C for 95% of the length of the reactor. However, this is only true for around 80% in the case of CH, leading to a lower synthesis yield. As flow rate increased, the differences in the temperature profile are less pronounced which also explains that the UV-VIS spectra intensity is more similar in both heating rates for the cases of 0.3 and 0.6 mL/min although a more intense reaction is always observed for MWH.
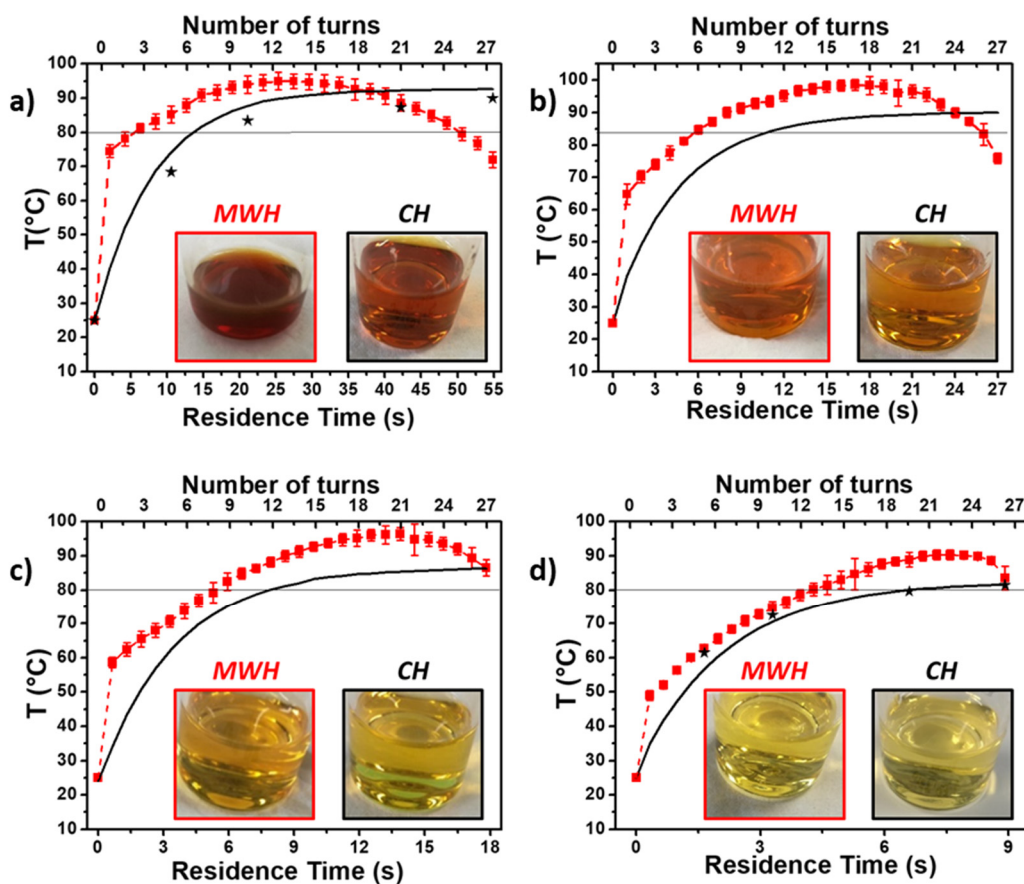
Figure 2.10 Temperature profiles for 20 W-MWH (red color-experimental values) and CH (black colour line – simulated data, black stars – experimental values) at different flow rates: a) 0.1 mL/min, b) 0.2 mL/min, c) 0.3 mL/min and d) 0.6 mL/min. Simulated data were obtained by Comsol Multiphysics® Simulation.

Finally, the measurement of the temperature in the position B of Figure 2.2 demonstrated the fast cooling: from a temperature higher than 80 °C at the end of the reactor, the fluid temperature dropped to 30 °C immediately outside of the cavity. This fast decrease of temperature helped to quench the reaction preventing further uncontrolled growth (as confirmed by the narrower particle size distribution), and also increased rapidly fluid viscosity, hindering the subsequent aggregation of the nanoparticles.

2.4.4. *Deposition of NPs on the Tubing Surface*

Another advantage of using microwaves was the strong decrease of nanoparticle wall deposition (see Figure 2.11). This could be directly observed thanks to the

transparent reactor wall used. Thus, for instance, in the case of the highest residence time the deposition of nanoparticles on the wall of the reactor under CH is evident and contrasts to the almost clear surface observed for the MWH heated system. Only in the case of 0.6 mL/min the wall was completely clean under CH (Table A5.5 in appendix 1).

To quantitatively analyze the difference of silver deposition, the portion of the Teflon® pipe showing higher fouling was analyzed by SEM for the samples MWH_0.1mL/min and CH_0.1mL/min, where the contact time between particles and reactor wall was maximum. The longitudinal section analyzed confirmed the first visual impression (Figure 2.11), a much higher concentration of silver was observed for the CH. In detail, the deposition value, defined as the ratio of the surface covered by silver respect to the total Teflon® pipe surface, shifted from 18% of CH to 3% for MWs, determined from the quantitative color contrast of SEM images by the software ImageJ. The observed wall fouling agreed well with the temperature profile simulations under CH conditions since no deposition was observed in the first seven turns, where the temperature was lower than 80 °C, as reported in Figure 2.11 a). These effects were drastically reduced by the parabolic temperature profile observed for MWH. The mixture presented a temperature higher than 90 °C exclusively in the central zone of the reactor. Once the nucleation occurred, the temperature gradually decreased. Focusing on the last 15 turns of the reactor, where a critical deposition was observed, 93% of the reactor presented a temperature higher than 90 °C for CH experiments. In contrast, for MWH the temperature decreased between (80 – 90) °C for 27% of the analyzed volume and was even lower than 80 °C for 20% of the last 15 turns. The high constant temperature, observed in the second portion of the reactor for CH, increased both the subsequent aggregation of the particles and the wetting of the Teflon® surface, resulting in a higher wall deposition. Furthermore, there is a strict correlation between the wall deposition and the particle size distribution observed. As the

growth occurs through an autocatalytic process, the particles concentration decreases leading to a slower growth rate.
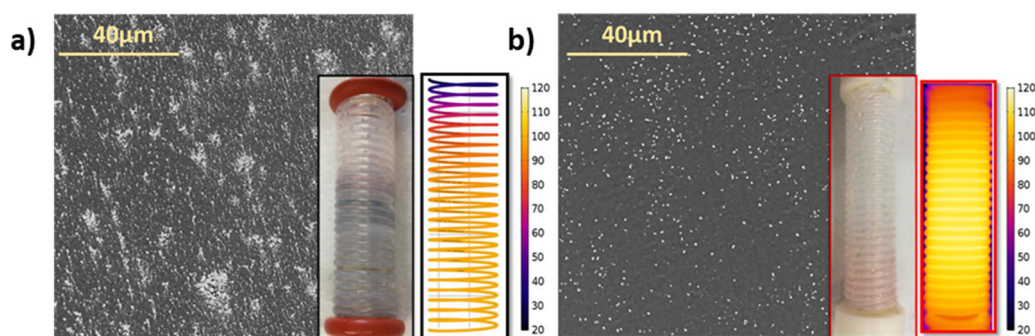
Figure 2.11 HR-SEM pictures showing representative views of the areas of the reactor wall with the highest fouling under MWH (right) and CH (left) for a flow rate of 0.1 mL/min, after 200 minutes of continuous working time. For CH the COMSOL Multiphysics® simulation of temperature profile is also presented on the CH figure, while IR thermograph of the reactor is shown for MWH.

2.5. Conclusions

Microfluidic synthesis of silver nanoparticles allows the continuous production of small non-aggregated silver nanoparticles with tuneable particle sizes. Comparing the different results obtained by UV-Vis, MP-AES, DLS, and TEM, the syntheses of Ag NPs obtained under MWH demonstrated a faster heating rate and a longer growing rate than the CH. Furthermore, the fast decrease of temperature, that characterized MWH, allowed to better control particle size growth, reducing the relative standard deviation of size distribution. Moreover, a considerable reduction of the wall deposition was observed with MWH, due to a selective heating mechanism which clearly affected the temperature profile. For this reason, the combination of microfluidic processing and homogeneous MWH may represent an ideal system for the synthesis of silver nanoparticles. The differences in temperature distribution for CH and MWH systems reflect the different heating patterns responsible for the higher reaction yields and lower wall fouling observed. Finally, the faster cooling achieved under MWH reduced the possibility of agglomeration of the nanoparticles and helped to narrow the particle size distribution.

3. ULTRA-SMALL Ag-NPs:
Microwave Heated Batch Reactor

Goal: *How the heating rate may affect the particle size distribution and the long-term stability of nanoparticles?*
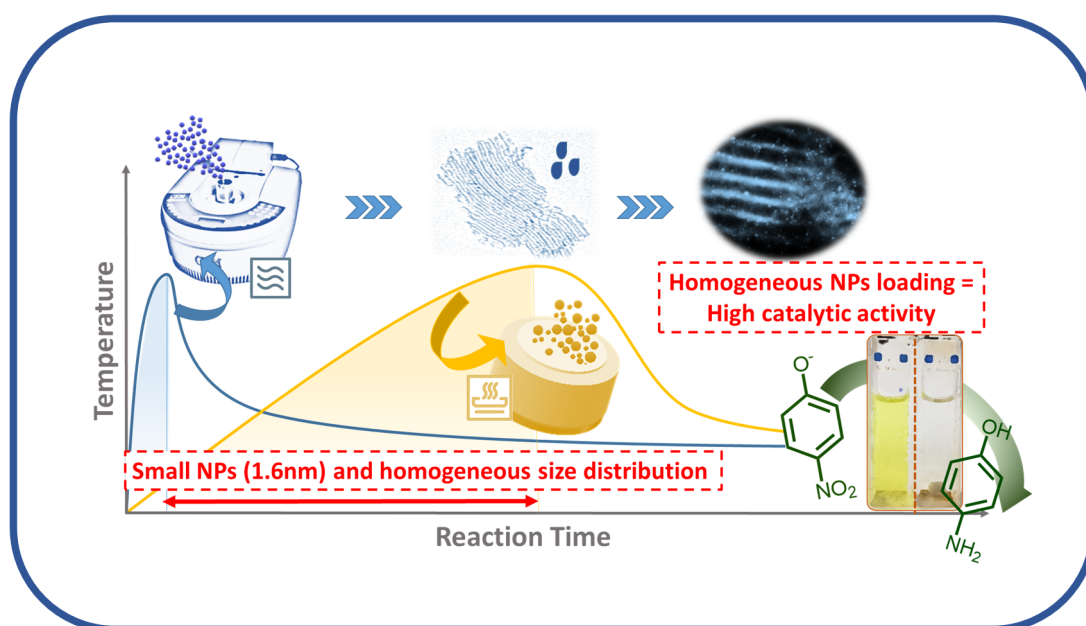
The contents of this chapter were adapted from the following published work:

3.   ULTRAS-SMALL Ag-NPs: Microwave Heated Batch Reactor

3.1. Introduction

A crucial problem of the synthesis of nanostructured catalytic materials is still the control of their size distribution[155,156], as it was also highlighted in the experimental results reported in previous chapter 2. The generation of secondary products or particles with different diameters may strongly affect not only their long-time stability but also their catalytic properties[9,157]. In 1935, Becker and Döring introduced a thermodynamic model, known as Classical Nucleation Theory (CNT), which expresses the Gibbs free energy of a spherical particle as a function of its radius. If the radius is higher than a critical value r_c, which depends on the ratio of the surface energy per unit area and the Gibbs free energy per unit volume, the energy of the system exceeds the activation energy and enhances the particle growth[158,159]. The nucleation rate can be described by the Arrhenius equation as a function of the Gibbs free energy and the temperature of the system. As reported by Keating et al.[160], long nucleation time or high temperature may promote the simultaneity of nucleation and coalescence mechanisms, reducing the homogeneity of the particle size distribution. This is especially important when monodisperse ultra-small nanoparticles (NPs) with a diameter smaller than 2 nm are the objective. The production of this type of ultra-small nanoparticles is desirable because its high surface to volume ratio, together with unusual quantum size effects, are the hallmarks of an innovative category of highly active nanocatalysts[7,88,161].

The way the energy needed for particle nucleation is supplied is key in the growth process. A wide range of alternative energy sources has been proposed for the controlled production of ultra-small Ag-NPs. Generally, the aim is to achieve a rapid nucleation step, and sources such as earlier studies with γ-irradiation[162–164], microwave heating[95,165], UV-irradiation[166] or sonochemical methods[94] have been studied. Analysing these studies, microwaves (MW) seem to be a winner procedure, giving a noticeable reduction of the synthesis time down to 70 s and a strong

improvement of the size distribution[95]. Despite these encouraging results, considerable room for improvement exists, especially concerning the analysis of the heating patterns and the possibility of temperature gradients in the system that could promote the presence of several nucleation/growth events. Furthermore, the deposition of small nanoparticles on a suitable substrate needs further study as it may both stabilize the NPs and facilitate their application in heterogeneous catalytic reactions, allowing its reusability[75,167,168].

In this chapter, a silica mesoporous substrate whose pores would range between 2 and 15 nm was selected. For this reason, small particles may be grafted inside and outside of the pores without their obstruction, assuring the accessibility of the active sites during catalytic reactions[76]. Furthermore, they present a high surface to volume ratio, endowing these materials of excellent properties for catalysis. The morphology, i.e. pore size, surface area and/or wall thickness, may be tuned to specific requirements, as confirmed by the wide library of synthesis procedures so far reported[169–171]. The surface may be easily functionalized by hydrophobic/hydrophilic or positive/negative-charged molecules, guaranteeing a high versatility of use[171–173]. In addition, mechanical separation techniques, such as filtration or centrifugation, do not damage the mesoporous framework, allowing to recover the catalyst in heterogeneous reactions and reuse it[174].

As reported in chapter 2, the combination of microwaves and continuous flow may reduce both particle polydispersity and wall fouling. However, the minimum size observed with the polyol mechanism was 5.8±3.4 nm with a relevant size deviation and a very low synthesis yield, as confirmed by UV-Vis spectroscopy. In this chapter, an alternative mechanism, based on polyacrylic acid reducing and stabilizing agent, for the synthesis of homogeneous ultra-small Ag-NPs was introduced. To focus exclusively on the impact of microwave heating, all the experiments have been performed firstly in a batch reactor. In detail, it was analyzed the effects of the heating mechanism (MWH versus CH), for different

irradiation time (70, 35 and 17 s) and heating slopes (2.8, 1.3, 0.4 and 0.2 °C/s), switching the MW power from 200 to 10 W. Furthermore, the relation between size distribution and NPs stability was studied upon long-term storage, i.e. 18 months. Finally, the homogeneous ultra-small Ag-NPs were deposited on amino-functionalized SBA-15 with a pore size of around 10 nm. The negative-charged polyacrylic acid was electrostatically attracted by the positive-charged amino groups, playing a crucial role in the catalyst stability.

To conclude, the activity of the Ag@SBA-15 catalyst was investigated by the reduction of 4-Nitrophenol (4-NP) in water, in an excess of NaBH$_4$. This reaction is often used as a test reaction since 4-NP reduction does not occur at ambient conditions in the absence of a proper catalyst and may be easily monitored by UV-VIS spectroscopy[175,176].

3.2. **Materials and Methods**

3.2.1. *Synthesis of Amino-Functionalized SBA-15 Nanorods*

SBA-15 nanorods, used as support of metallic nanoclusters, were synthesized by a traditional sol-gel protocol reported in literature[76,177]. Firstly, 1.2 g of the symmetric triblock copolymer poly(ethylene Glycol) – block – poly(propylene glycol) – block – poly(ethylene glycol) (Pluronic P-123, Sigma-Aldrich) were dissolved into 40 mL of HCl 1.75 M (AnalaR NORMAPUR 37%) with the addition of 14 mg of ammonium fluoride NH$_4$F (Sigma Aldrich, ≥ 98%). The Pluronic P-123 is a non-ionic surfactant. Once dissolved in water, it rearranges to generate spherical micelles. In detail, the hydrophilic polyethylene glycol (PEG) blocks, which have high affinity for water, surround the hydrophobic polypropylene glycol (PPG) block as reported in Figure 3.1 a. This step was carried out in a 250 mL HDPE-jar with a screw cap, maintained at 20 °C and 1,500 rpm stirring rate (magnetic stirrer bar of Ø6 mm x 25 mm) until the complete dissolution of the copolymer.

Then, a fresh mixture of heptane (Sigma-Aldrich, 99%) (8.5 mL) and TEOS (Fluka, 98%) (2.75 mL) was added, keeping the reaction at 1,500 rpm stirring rate for 4 min.

Once dissolved in the acidic medium, a sol-gel mechanism occurs, as schematically reported in scheme 3.1. Firstly, the alkoxy groups of TEOS undergo a hydrolysis process, which results in the formation of the relative alcohols. After that two silanols condense, with the formation of a gel phase. The silicate oligomers interact by hydrogen bonds with the PEO hydrophilic chain of the surfactant, Figure 3.1 b[178]. Fluoride ions act as catalyst, accelerating their interaction even at low temperature.

Scheme 3.1: Sol-Gel mechanism of TEOS in acidic medium.
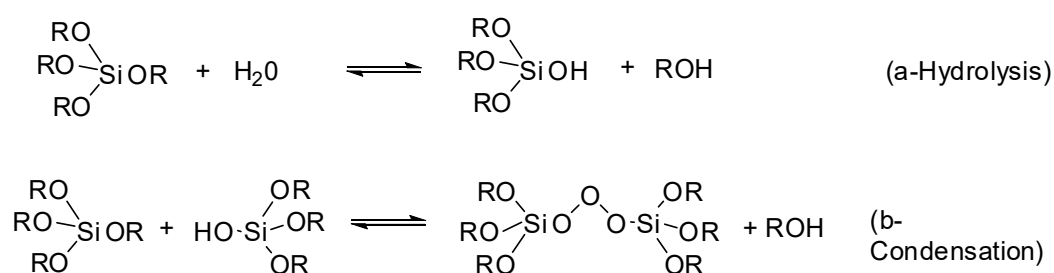
The initial 2D organic-inorganic structures start to interact between them, generating micellar rods and then assembling in hexagonal arrays (Figure 3.1 c and d respectively)[179]. The heptane acts as swelling agent[180]. After 10 minutes in a static condition, the solution was transferred to a PTFE-lined autoclave for hydrothermal treatment at 100 °C for 24 h. During this step, the diameter of the pore size increases due to a low hydrophilicity of PEG at high temperature[181].
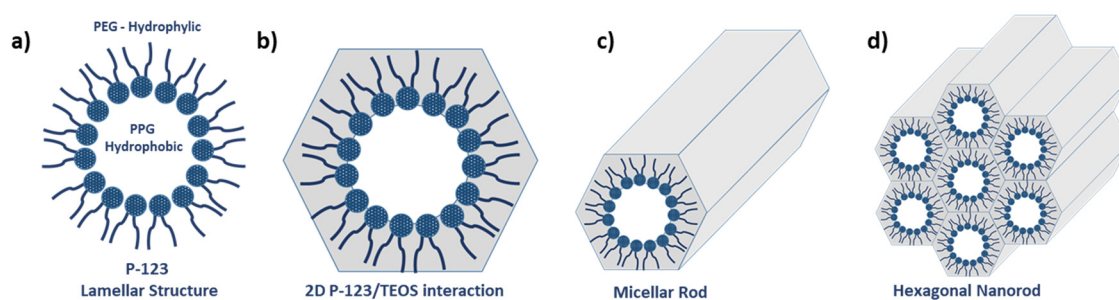
Figure 3.1 Mechanism of SBA-15 nanorods formation by solvothermal mechanism. a) P-123 micellar structure, b) 2-D interaction between silica precursor and surfactant, c) micellar nanorod and finally d) hexagonal SBA-15 nanorod.

Next, the product was washed, filtered and calcined in a muffle furnace at 550 °C for 5 h with a heating rate of 1 °C/min. In this way, the surfactant was completely

removed from the mesoporous channels, without damage of the silica framework. To conclude, the empty rod-shaped channels of SBA-15 were amino-functionalized. A mass of 1 g of calcined rod-shape SBA-15 was dispersed into 20 mL of toluene (Fisher Chemical, General Purpose Grade). After 15 minutes of Ar-purging, 400 μL of (3-aminopropyl)triethoxysilane (Sigma-Aldrich, ≥ 98%) were added maintaining the system at 110 °C for 1 h. Finally, the product was filtered, washed with a mixture of dichloromethane/ diethyl ether (1:1 in volume) and dried at 80 °C overnight.

3.2.2. *Microwave-Assisted Synthesis of Ag Nanoparticles*

Microwave-assisted synthesis of Ag NPs was conducted in a CEM Microwave Discover® Cavity. The quartz reactor (I.D. 20.8 mm, O.D. 24.0 mm) was precisely fixed in the centre of the open vessel cavity, as schematically represented in Figure 3.2. For the synthesis of Ag NPs, 85 mg of silver nitrate (Aldrich 99.9999%) were dissolved under mechanical stirring at room temperature in 10 mL of deionized water (50 mM) and covered with aluminium foil. Then, 500 μL of poly (acrylic acid, sodium salt) solution (Na-PAA Sigma Aldrich MW 1,200, 45 wt.% in water) was added and the solution was premixed to obtain a homogeneous starting solution. The mixture was irradiated by microwaves, with an input power varied between 10 W and 200 W, for three different time-lapses (17 s, 35 s, and 70 s) under high stirring conditions (magnetic stirrer bar of Ø4 mm x 10 mm). Na-PAA played the dual role of reducing and stabilizing agent. Accurate monitoring of reaction temperature was performed both by a thermographic camera (Optris PI-400038T900), that recorded the radial temperature profile on the top surface, and by an optical fiber at three different axial points (10, 20 and 30 mm) of the 35 mm height occupied by the liquid volume, as reported in Figure 3.2 (b) and (c) respectively. For CH experiment, a traditional oil bath previously set at the desired working temperature, i.e. 74.6 °C (based on preliminary MWH experiments), was adopted.

To stabilize the synthesized NPs and to allow their application for heterogeneous catalytic reactions, 100 mg of amino-functionalized SBA-15 nanorods were

impregnated by 400 µL of the as-made PAA-Ag colloid (1 h x 1,500 rpm). Afterwards, the catalyst was centrifuged with distilled water (12,000 rpm x 20 min), eliminating non-grafted NPs, and dried in an oven at 50 °C overnight.
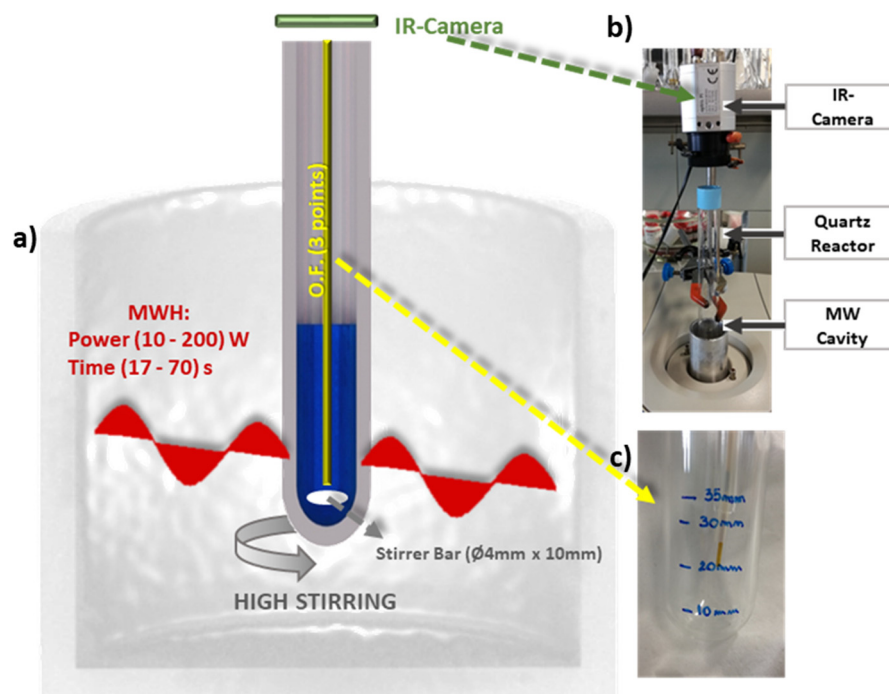
Figure 3.2 (a) Schematic representation of MWH batch reactor. The experiments were performed in CEM Microwave Discover® Cavity, in open vessel configuration. (b) Optical image to represent the configuration of the IR-camera. (c) Optical image which indicates the different positions of the optical fiber (O.F.) 10, 20 and 30 mm from the bottom part, ensuring total immersion of the fiber since the total height of the liquid corresponds to 35 mm.

3.2.3. *Characterization Techniques*

Nitrogen Adsorption: The effects of ultra-small Ag NPs grafting on specific surface area and pore size distribution of amine-functionalized SBA-15 were evaluated by nitrogen adsorption analysis at 77 K in a Micrometrics ASAP 2020. The samples were out-gassed at 26.7 Pa and 110 °C for 5 h before the measurement. The analysis of the desorption branch by Brunauer-Joyner-Halenda (BJH) method was adopted for the calculation of mean pore diameter (MPD) and pore size distribution. Brunauer-Emmett-Teller (BET) method was applied for the determination of

specific surface area from the adsorption isotherm in the range of relative pressure 0.06-0.19.

Zeta Potential: To confirm the electrostatic interaction between amino-functionalized SBA-15 and PAA-Ag NPs Zeta Potential measurement (Zeta Plus; Brookhaven Instruments Corporation, NY, USA) was performed of each sample after appropriate dilution in Milli-Q-water and sonication of the sample for 5 minutes. At least ten replicate measurements were recorded in each case.

Transmission Electron Microscopy (TEM) and High-Angle Annular Dark-Field Scanning Transmission Electron Microscopy (HAADF-STEM) was conducted to characterize the synthesized Ag nanoparticles and their dispersion on Ag-NPs@SBA-15 nanorods. A 10 µL drop of colloidal nanoparticles was deposited onto a Formvar TEM copper grid covered by a continuous carbon film. After complete evaporation, the sample was analysed in a FEI TECNAI T20 microscope with an operating voltage of 200 keV. A similar procedure was adopted for the characterization of ultra-small Ag-NPs before and after grafting on silica substrate, dropping 10 µL suspension of the ultra-small Ag NPs onto a holey carbon TEM grid. In this case, a high-angle annular dark-field scanning transmission electron microscope FEI Titan™ (80–300 kV) was adopted and elemental analysis was carried out with an Energy Dispersive X-ray Spectrometry (EDS) detector that allows performing EDS experiments in the scanning mode.

UV-Vis Spectroscopy: The optical properties of ultra-small Ag particles were evaluated by UV-Vis Spectroscopy (Agilent 8453 UV-Visible Spectrophotometer). 500 µL of the sample was diluted into 2.5 mL of deionized water. The measurement range adopted was from 1000 to 200 nm with a scan speed of 400 nm/min.

Microwave Plasma Atomic Emission Spectroscopy (MP-AES): The quantification of Ag metal loading in the mesoporous channels was determined by Microwave Plasma Atomic Emission Spectroscopy (MP-AES) (Agilent 4100 MP-AES). Firstly, 30 mg of

the catalyst were microwave digested (200 °C for 20 min in Milestone Ethos Plus microwave cavity) in 5 mL of nitric acid (HNO_3) and hydrochloric acid (HCl) in a volume ratio of 1:3. Then, the digested sample was diluted with Milli-Q water obtaining a final volume of 30 mL. To discard any fragmented particle, the sample was centrifuged (12,000 rpm x 20 min) and the supernatant was filtered by hydrophilic syringe filters of 0.2 μm.

X-ray photoelectron spectroscopy (XPS): The presence of $Ag_{(m+n)}^{m+}$ species was verified by X-ray photoelectron spectroscopy (XPS), performed with an Axis Supra spectrometer (Kratos Tech). The samples were mounted on a sample rod placed in the pre-treatment chamber of the spectrometer and then evacuated at room temperature. The samples were excited by a monochromatized AlK_α source at 1486.6 eV and subsequently run at 12 kV and 10 mA. Survey spectrum was measured at 160 eV pass energy and for the individual peak regions, spectra were recorded with a pass energy of 20 eV. CasaXPS software was adopted to analyse the peaks adopting a weighted sum of Lorentzian and Gaussian component curves after Shirley background subtraction. The binding energies were referenced to the internal C_{1s} standard at 284.9 eV.

3.2.4. *Catalytic Application*

Reduction of 4-nitrophenol by an excess of $NaBH_4$ in water was selected to test the catalytic activity of PAA-Ag nanoparticles supported on SBA-15. In a typical reaction, 1.44 mmol of $NaBH_4$ was added into 30 mL of a fresh solution of 4-Nitrophenol (0.125 mM). After collecting the UV-Vis spectrum as a reference of time zero, 1 mg/L of the catalyst was added keeping the reaction in stirring condition, covered with Aluminium foil. The absorbance peak was analysed every 40 s in a continuous UV-Vis Spectrophotometer (Agilent 8453). For reusability test, the solution was centrifuged after each cycle, observing the deposition of the nanocatalyst as a pellet. The supernatant solution was eliminated, the residue was dried and then reused with fresh reagents for a different catalytic cycle.

3.3. **Results and Discussions**

      3.3.1. *Effects of Different Heating Patterns*

Low temperature syntheses of stable metallic nanoclusters may be assured by the use of anionic templates in short times, i.e. polyacrylic acid (PAA). As reported by Pradeep[52], radiolytic reduction of Ag^+ ions occurs in the presence of sodium polyacrylate generating atomic Ag. Then, Ag atoms rapidly react with Ag^+ forming diatomic clusters Ag^{2+}, which continue to grow and are stabilized by electrostatic repulsion of the supporting polymeric chains. In this investigation, firstly a detailed analysis of the microwave-assisted synthesis of PAA-Ag NPs was performed, evaluating the effects of three different irradiation times (17 s, 35 s, and 70 s). Reagents concentrations, reactor configuration, heating rate and the procedure for the characterization of the samples were kept constant, focusing exclusively on the temperature effects.

The heating rate was independent on the irradiation time for a given irradiated power, reporting a common value of 2.8 °C/s (Figure 3.3). The temperature gradient, observed between the different points of the reactor (see Figure 3.2), is due to a non-uniform distribution of the electromagnetic field, already reported by other authors with the same cavity[182]. For an irradiation time of 17 s the maximum temperature reached was lower than 80 °C (Figure 3.3 a). Instead, for 35 s the mixture reached 100 °C and was maintained at the maximum temperature for 5 s, Figure 3.3 b. Finally, for 70 s (Figure 3.3 c), the mixture reached the boiling temperature of water after around 30 s. Then, the temperature was nearly constant, observing a slight decrease, T=(98.8±1.1) °C, due to the homogeneity assured by the high stirring condition.
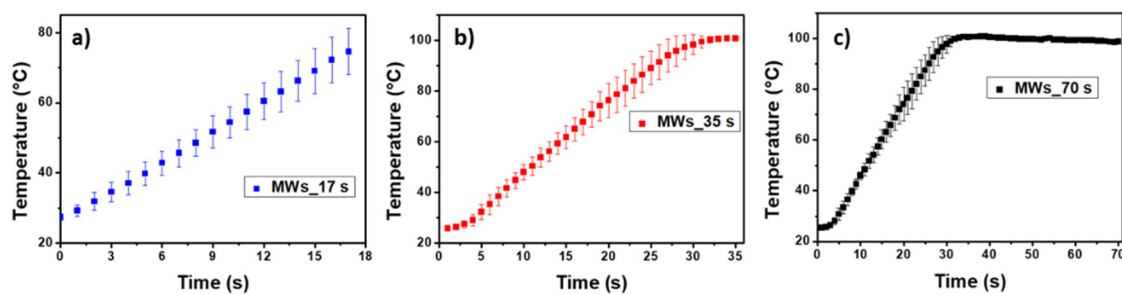
Figure 3.3 Average temperature evolution (average synthesis temperature of three different points and its corresponding deviation) for MWs-assisted synthesis at different heating times (17 s, 35 s, and 70 s) and fixed power (200 W).

Poor control of particle size distribution was observed for nanoparticles synthesized at 70 s and 35 s, as reported in Figure 3.4 a) and c), respectively. While more than 85% of nanoparticles presented a diameter smaller than 3 nm, a significant proportion of particles with a size around 10 nm were observed in both cases. Instead, uniform size distribution of (1.6±0.7) nm was observed for NPs produced with an irradiation time of 17 s, Figure 3.4 e. By LaMer model, the fast microwave heating (2.8 °C/s as reported in Figure 3.3 a-c) enhanced uniform nucleation of small particles. However, the subsequent, or even simultaneous, Ostwald ripening and diffusion mechanisms are responsible for the growth of the initial nuclei which may be strongly accelerated by higher temperatures[159]. At a heating time of 17 s, the maximum temperature reached was (74.6 ± 6.6) °C, 23% lower than the maximum temperature observed for 35 s and 70 s (Figure 3.3). According to studies using in-situ SAXS at a millisecond time resolution, colloidal silver nanoparticles grow via the cluster-aggregative nucleation pathway[183]. This pathway implies that silver ions are reduced to produce Ag_{13} clusters that subsequently form small silver nanoparticles by agglomeration of Ag_{13} clusters. Temperature significantly influences the nucleation event, modifying the maximum concentration supersaturation and the diffusion mobility of Ag_{13} clusters. Considering this fact, it was observed that increasing the temperature from 60 °C to 92 °C resulted in the presence of successive nucleation events. This uncontrolled nucleation introduced

non-uniformity in the growth kinetics of Ag NPs due to unavoidable random coagulations/aggregations events[184]. In fact, the aggregation kinetics increase with temperature[185]. In this analysis, no relevant aggregation was reported until around 75 °C, where a unique population was observed, Figure 3.4 e. Instead, a consistent cluster-aggregation nucleation mechanism occurred as temperature increased (100 °C as reported in Figure 3.3 a-b), as confirmed by the heterogeneous distribution of Ag NPs obtained after 70 s and 35 s of MWH (Figure 3.4 a and c). It is also likely that an increase of reaction temperature gives rise to the desorption of the negatively charged ligand chains[186], promoting aggregation and polydispersity.

Furthermore, the uniformity of Ag NPs synthesized under 17 s of MW irradiation was reflected in higher stability for longer storage time, due to a reduction of Ostwald ripening and coalescence mechanisms[6]. The evolution of ultra-small particles in water suspension is still a common critical factor[187,188]. In fact, after a storage period as long as 18 months an evident alteration of the colloidal solution colour was observed for all the colloids synthesized. TEM analysis confirmed that a drastic variation of particle size distribution was observed for 70 s and 35 s respectively, where particle size shifted in a wide range from 2 to 26 nm (Figure 3.4 b and d respectively). Instead, a high uniformity was observed for the 17 s sample as clearly seen in Figure 3.4 f, where still 51% of the particles presented a diameter smaller than 3 nm and no particles bigger than 7 nm were observed. Higher the homogeneity lower the particles growth, confirming the theoretical model reported by Reiss[189], who theorized that the smallest particles may grow fast in the presence of large particles.
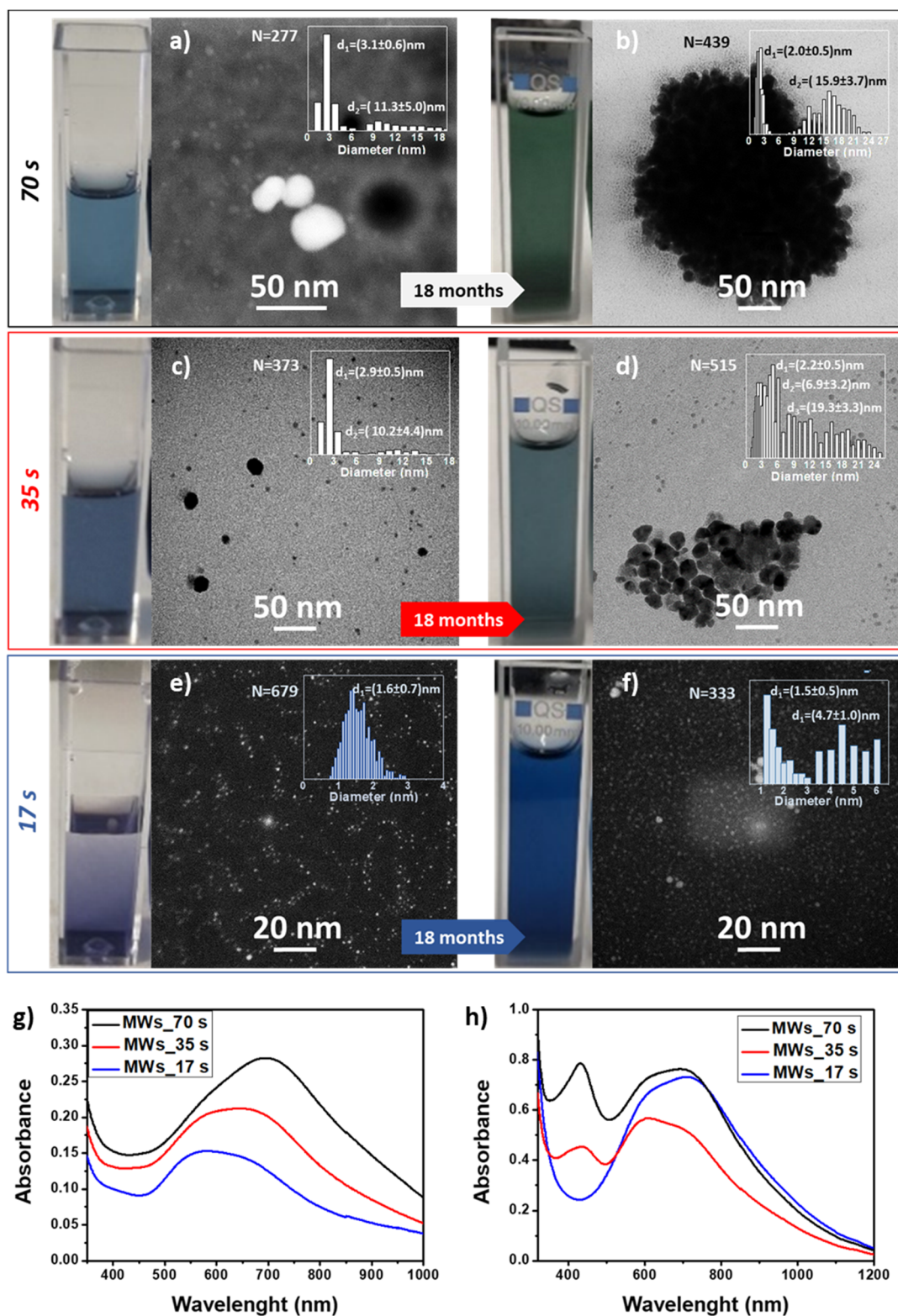
Figure 3.4 TEM, HAADF-STEM and optical images of Ag nanoparticles for three different MW irradiation times (70 s, 35 s and 17 s) monitoring the evolution between time zero (respectively a, c and e) and after 18 months (b, d and f). Insets, optical images of the colloids and particle size histograms. Finally, the comparison of UV-VIS spectroscopy for three different MW irradiation times (17 s, 35 s and 70 s) at time zero (g) and after 18 months (h).

However, while at 35 s and 70 s a gradual transition to green colour was observed, the NPs produced in 17 s still presented a blue tone (optical images in Figure 3.4). The green color comes because of the combination of blue ultra-small NPs and yellow silver NPs with SPR at 425 nm. The increase in the intensity of blue tone corresponds to an increase in the conversion of ultra-small nanoparticles, also evident in TEM and UV-VIS signal. After synthesis (Figure 3.4 g) there was a unique long-wave absorption band at $\lambda > 600$ nm indicating the complexes of small particles with the carboxylate group of the polymer[186], without significant differences between the three samples. No variations were observed after 3 days. On the other hand, after 18 months a secondary Ag-NPs signal at a wavelength of 430 nm appeared exclusively for 70 s and 35 s, characteristic of crystalline Ag nanoparticles[137].

3.3.2. *Influence of the Heating Mode: MWH vs CH.*

As expected, the temperature and the synthesis time strongly affected the quality of the final product. According to this study, the best synthesis conditions to assure the homogenous production of ultra-small Ag-NPs were obtained at 200 W-MWH for 17s. However, a further analysis was required to establish if non-thermal effects may be associated to the alternative EM heating mechanism. For this reason, it was adopted the reference temperature of 74.6 °C using an oil bath (CH) to evaluate the influence of the heating mechanism adopted. The evolution of the average synthesis temperature and its corresponding deviation is presented in Figure 3.5 both for CH and MWH. It shows different heating patterns and heating rates for the two heating modes to reach the same final set point. MWH not only reached the final temperature 10 times faster, but a completely different heating pattern was observed. For CH (see Figure 3.5 c), it was possible to observe how the heating proceeded from the wall of the quartz reactor towards the centre with the hottest region close to the vessel wall. Instead, an opposite gradient was observed for MWH in Figure 3.5 f, where the centre of the sample was rapidly heated and then the rest

of the liquid underwent fast heating, with the high-temperature wave moving towards the reactor wall.

From LaMer theory[160], a control of the nucleation step, without the presence of successive nucleation, can be considered essential to better control the homogeneity of the resulting NPs. This gives a clear advantage to MW-heated systems, where the whole system is heated up to the required temperature in about 15 s, while under CH the centre of the vessel is still at (58.7±5.7) °C after one minute of reaction. The fast nucleation under MW irradiation indeed results in a more homogeneous product, with a reduction of 70% of the NPs size deviation and a decrease of 58% of the NPs average diameter, as reported in Figure 3.5 b and e respectively. It can be concluded that fast, volumetric heating is able to produce almost simultaneous nucleation in the whole reactor volume, while the slow conventional heating process gives rise to a heating wave that moves towards the centre of the vessel, producing new nucleation events as the heat front reaches inner regions. In the meantime, the nuclei formed at the outer regions continue to grow, consuming precursors and giving rise to a non-homogeneous growth in the vessel. These results are in agreement with the previous work of Liu et al.[190], confirming the thermal advantages of microwave heating. Indeed, the ability of MWH to provide fast heating throughout the sample volume can be the key to control nanoparticle production in systems where fast kinetics are involved, such as in the production of noble metal nanoparticles where it is estimated that nucleation occurs in less than 100 ms[191].
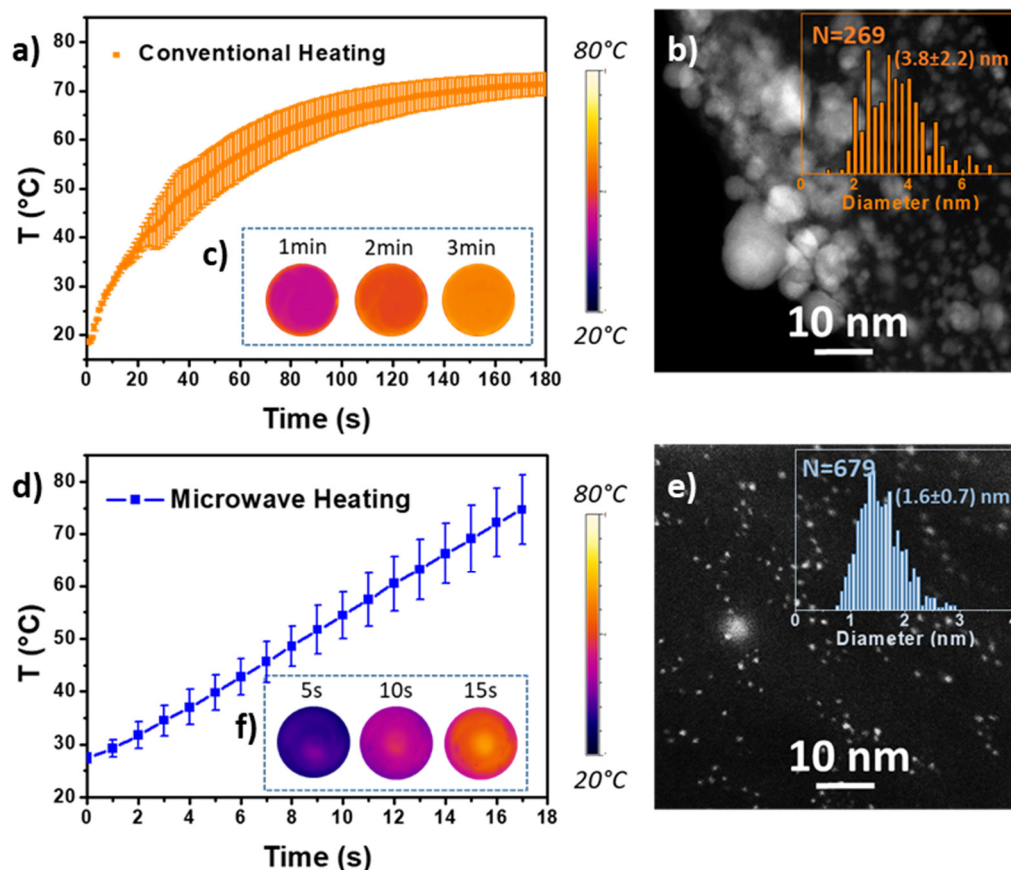
Figure 3.5. Evolution of temperature profile with time and IR images of temperatures at the top surface of the liquid respectively for CH (a and c) and MWH (d and f). HAADF-STEM images and particle size histogram of Ag NPs for CH (b) and MWH (e) respectively.

3.3.3. *Analysis of the Heating Rate*

In order to confirm the influence of the heating rate, the working microwave power was gradually reduced from 200 W to 10 W, decreasing the heating rate from 2.8 to 0.2 °C/s as reported in Figure 3.6 a. For MWH, the temperature may be expressed as a function of the power applied, observing a linear correlation between them, in accordance with previous results reported by Zhang et al.[192]. When the input power was changed from 200 W to 100 W, the heating rate was nearly halved, decreasing from 2.8 °C/s to 1.3 °C/s. If the input power was still reduced to one tenth (10 W), the heating rate progressively decreased to 0.2 °C/s. The effect of different heating rates was confirmed by UV-VIS spectroscopy in Figure 3.6 b, where a gradual increase of secondary signal of large silver nanoparticles was observed at a

wavelength of 425 nm. The presence of big agglomerates was also confirmed by TEM analysis in Figure 3.6, where it was observed that the slower is the heating rate, the higher is the polydispersity. Although at 100 W, the sample was mainly formed by particles smaller than 3 nm, bigger isolated particles started to appear with an overall average size of (3.1±2.1) nm (Figure 3.6 c). The isolated particles gradually tend to agglomerate as the heating rate decrease down to 0.4 °C/s and 0.2 °C/s, respectively reported in Figure 3.6 d and f. As a result, the average diameter and the relative standard deviation increased to 3.8±1.8 nm and 3.8±2.6 nm respectively, lowering the quality of the final product. It is interesting to underlying the similarity with the previous CH experiment (3.8±1.8 nm), where the heating rate of the first 60 seconds was 0.55 °C/s. These results may confirm that the enhancement of the homogeneity of ultra-small nanoparticles reported by MWH was exclusively due to a thermal effect. An instantaneous uniform heating promotes the simultaneous nucleation of ultra-small Ag NPs in the entire synthesis volume, improving the quality of the resultant product.
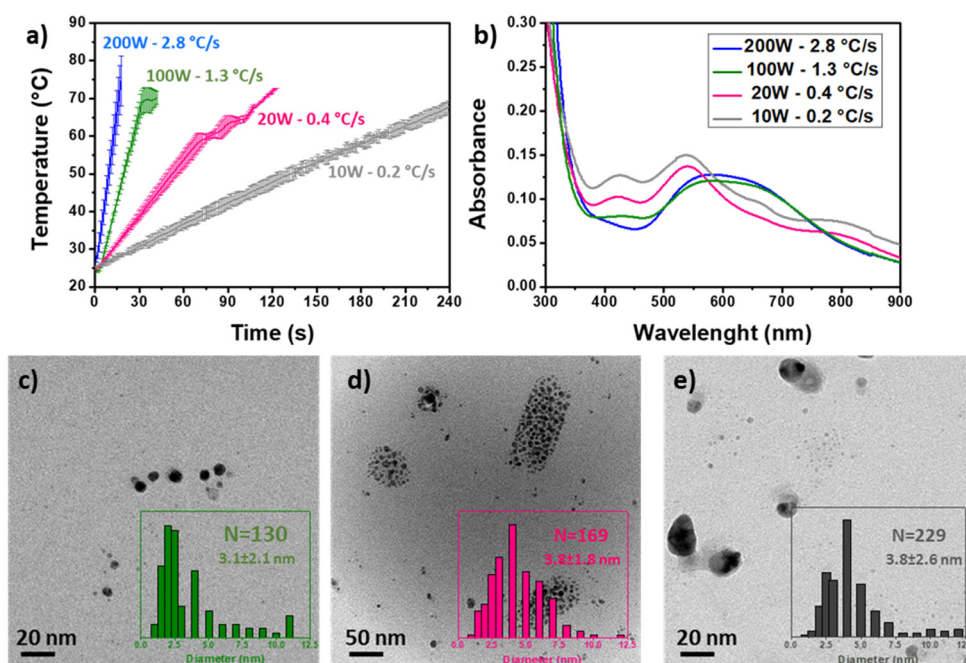
Figure 3.6 (a) Microwave temperature profile at different heating rates, from 2.8 to 0.2 °C/s. (b) Comparison of UV-VIS spectroscopy for four different MW irradiation powers (200 W, 100 W, 20 W and 10 W). (c) TEM images at 100 W, (d) TEM images at 20 W and (e) TEM images at 10 W.

3.3.4. *Supported Ultra-Small Ag NPs on a Mesoporous Substrate*

The deposition of the metallic NPs over a proper substrate is essential to increase their stability and also to facilitate their recovery and application for heterogeneous catalysis. In this case, Ag-NPs produced under 200 W - MWH at 17 s, were deposited on amino-functionalized SBA-15 by incipient wetness impregnation. The catalyst was indicated as B-AgNPs@SBA-15, where B stays for batch reactor. As evidenced by HAADF-STEM analysis in Figure 3.7 a-b, the particles were homogeneously distributed along the channels of the porous substrate, without relevant variation of their size distribution. In fact, the particle size distribution was (1.6±0.7) nm before and (1.5±0.3) nm after deposition as reported in Figure 3.7. As confirmed by zeta-potential, Figure 3.7 c - analysis at pH of 7.4, a strong electrostatic interaction occurred between amino-functionalized SBA-15 and the negatively charged PAA chains. The percentage of metal loading was quantified by MP-AES analysis as a total of (0.98±0.05) wt.%, which corresponded to a deposition yield of 41-48%. Furthermore, a slight obstruction of the pores was evidenced in the type IV-isotherm with H1 hysteresis , Figure 3.7 e, and the corresponding analysis of the N_2 adsorption listed in Table 3.1. The total pore volume in the sample containing the Ag NPs (0.76 cm^3/g) decreased only by 15% respect to the original amine-grafted SBA-15 support (Table 3.1), and the pore diameter was still higher than 8 nm. A uniform organization of the ultra-small Ag NPs, together with pore size large enough is highly desirable to ensure the access of a wide range of organic molecules to the active sites. The XPS analysis (Figure 3.7 f) confirmed the presence of a core structure (55% of Ag(0)) surrounded by a high concentration of uncoordinated atoms (45% of Ag(I)) . The presence of a large proportion of atoms with an oxidation state higher than 0 around a noble metal core is not surprising, given the high surface to volume ratio of the NPs prepared in this case, and has been observed for other noble metals, e.g. Pt[193].

Table 3.1. N_2 adsorption analysis data for SBA-15 and B-AgNPs@SBA-15

Sample	S_{BET} (m²g⁻¹)	V_t (cm³g⁻¹)	D_{BJH} (nm)
SBA-15	317	0.89	9.3
B-AgNPs@ SBA-15	266	0.76	8.6
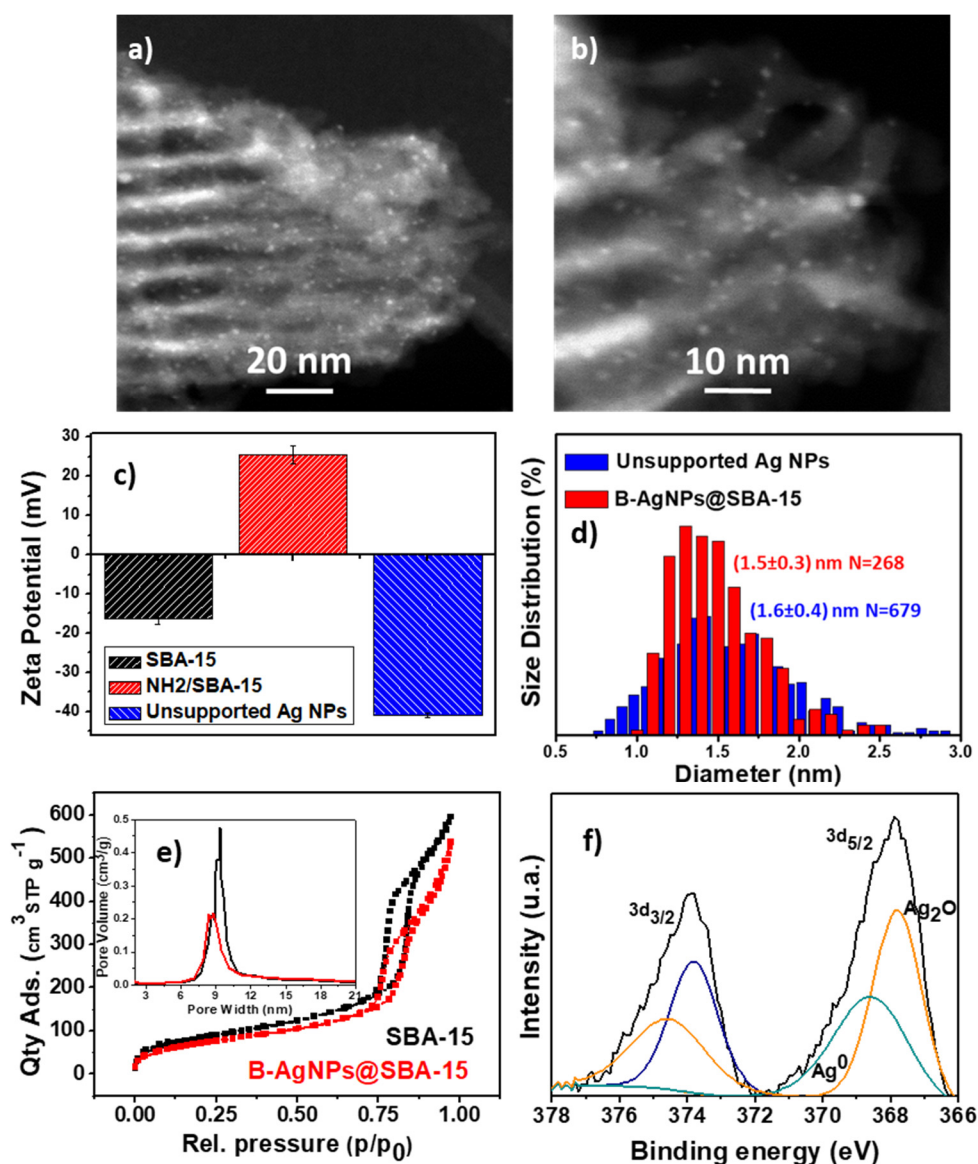
Figure 3.7 A uniform distribution of ultra-small Ag NPs over the channels of mesoporous SBA-15 substrate was evidenced by HAADF-STEM analysis (a and b). The grafting of the ultra-small nanoparticles was due to electrostatic forces as observed by zeta potential analysis (c), without altering the size distribution (d). No relevant variations of pore diameter were observed after the grafting of Ag-NPs (e). Furthermore, XPS analysis confirmed the presence of both Ag(0) and Ag(I), complexed by the polycarboxylate group of PAA (f).

3.3.5. *4-Nitrophenol Reduction*

Considering the adverse effects on human beings and aquatic life of the carcinogenic pollutant 4-nitrophenol, the catalytic activity of ultra-small Ag-NPs was tested for the reduction of 4-nitrophenol in an excess of $NaBH_4$. This reaction is commonly used to test and compare the catalytic activity of new-designed catalysts, as it occurs in water at ambient temperature/pressure and can be easily monitored by UV-VIS spectroscopy.

In accordance with the recent work of Sebastian et al.[175], the reaction mechanism is schematically reported in Scheme 3.2. The 4-nitrophenol was firstly deprotonated by the hydrolysis of sodium borohydride in aqueous solution, generating the 4-nitrophenolate ion (4NP$^-$) (Scheme 3.2) which presents a characteristic wavelength absorbance at 400 nm (Figure 3.8 a - time 0 s). The silver catalyst accelerates the 4-NP reduction, through a redox mechanism. In detail, the Ag nanoparticles interact with the borohydride ions, receiving 4 e$^-$ and liberating 4 H$^+$ due to reduction of water to H_2. Then, the 4-NP$^-$ is absorbed on the catalyst surface and reduction R_I occurs, with the production of the intermediate 4-hydroxylaminophenol (4-HAP) and a molecule of H_2O. In a following step, it was observe a reversible two-electron transfer mechanism, with the production of 4-AP. Finally, the product is released to the water solution and the active site is ready to start a new activation. The system is stable in the absence of the catalyst, because an electrostatic repulsion forbid the interaction between the 4NP$^-$ and the BH_4^-. Only after the addition of the nanocatalyst the characteristic absorbance peak of 4-nitrophenolate gradually decreased while the peak of 4-aminophenol (294 nm) increased[194].

Scheme 3.1: Reaction mechanism of 4-NP reduction in an excess of NaBH₄.
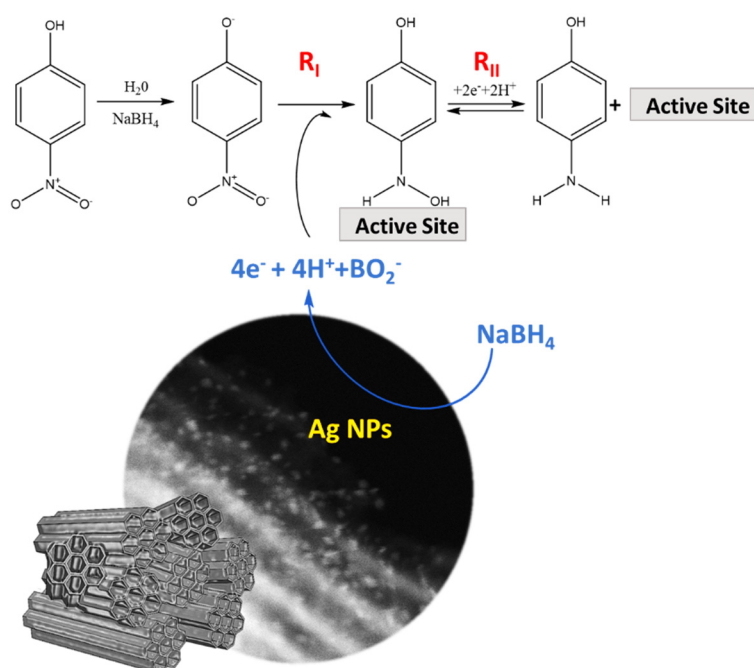
In this analysis, the reaction was concluded after 440 s, as confirmed by the disappearance of the absorbance signal of sodium phenolate and the transparency of the solution, optical insets in Figure 3.8 a. No reactions occurred in the absence of catalyst or with the pure mesoporous substrate SBA-15 (red curve in Figure 3.8 d), confirming that ultra-small Ag-NPs are responsible for the catalytic reaction. Langmuir-Hinshelwood kinetics were employed to quantify the catalytic performance[73]. The catalytic reduction of 4-nitrophenol to 4-aminophenol has been well studied and, considering that NaBH₄ is in excess ($C_{NaBH4}/C_{4\text{-nitrophenol}} = 400$), it can be considered constant during the reaction process, and the reaction kinetics can be treated as pseudo-first-order with respect to 4-nitrophenol. The apparent kinetic constant corresponded to the slope of the linear relation between the $\ln(A_t/A_0)$ and the reaction time. The apparent kinetic constant was normalized with respect to catalyst weight and reaction volume, identified as normalized kinetic constant. The linear correlation was excellent, with a fitting regression coefficient r^2 higher than 0.9935 for the three different batches, confirming the pseudo-first-order reaction kinetics (Figure 3.8 c). In the reusability test, the catalyst presented a good activity even after 8 cycles as reported in Figure 3.8 b. It was observed a reduction of 33% of

kinetic constant compared to the fresh catalyst, with a kinetic constant of $(5.91\pm0.07)\cdot10^{-3}$ ($l\cdot mg^{-1}\cdot s^{-1}$) (Figure 3.8 d). The slight decrease of catalytic activity observed after 8 cycles may be attributed to a gradual loss of catalyst amount due to the centrifugation step between the different cycles.
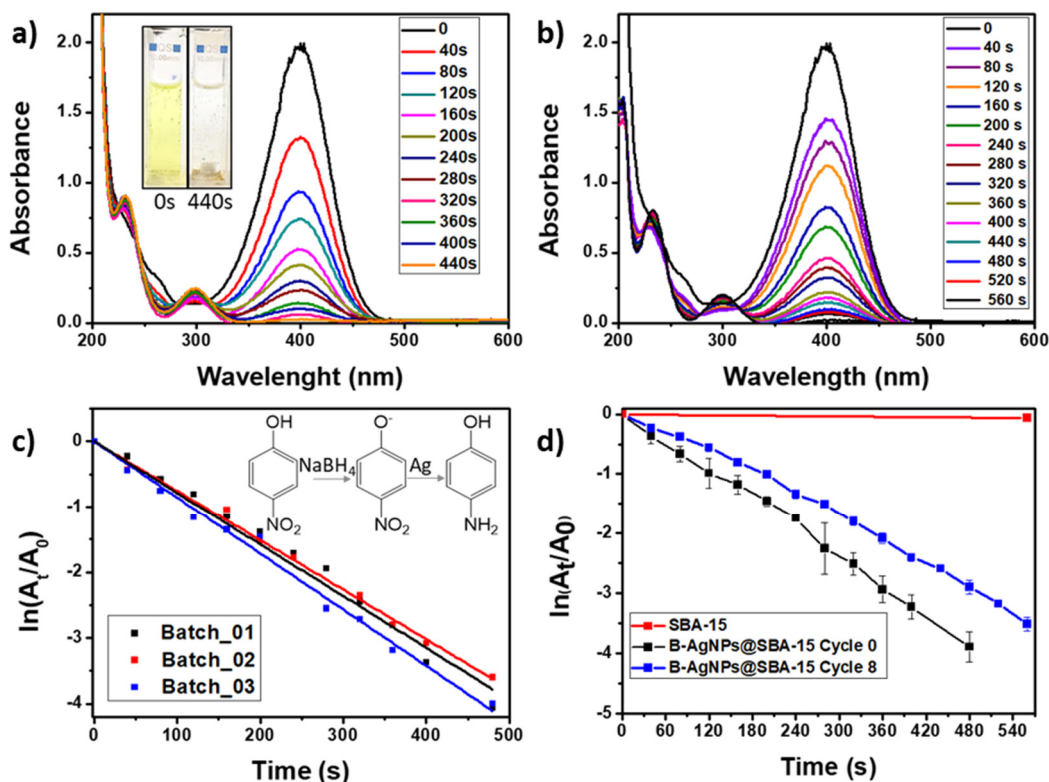
Figure 3.8 (a) Gradual decrease of 4-nitrophenolate ion (400 nm) concentration and formation of 4-aminophenol at a wavelength of 298 nm for cycle 0. The inset shows optical images that evidence the difference of colour between 4-nitrophenolate ion (dark yellow for t=0 s) and 4-aminophenol (transparent solution at 440 s). (b) Gradual decrease of 4-nitrophenolate ion (400nm) concentration and formation of 4-aminophenol at a wavelength of 298 nm for cycle 8. (c) Catalytic activity tests performed for different batches. (d) Linear fitting curve of pseudo-first order kinetics of 4-NP reduction for pure support, B-AgNPs@SBA-15 cycle 0 and B-AgNPs@SBA-15 cycle 8.

Table 3.2 compares the normalized kinetic constant of several works reported in literature where Ag-NPs were used as a catalyst for 4-nitrophenol abatement. The small diameter (1.6 ± 0.7) nm and the uniform distribution of the Ag NPs on the surfaces of the mesoporous substrate strongly impacted on the catalytic activity, which was around two times higher than the best Ag-based catalyst listed in Table

3.2[195]. However, the size distribution is the not the unique parameter that affects the catalytic activity. A kinetic constant lower than $4.73 \cdot 10^{-5}$ (l mg^{-1} s^{-1}) was reported by particles smaller than 5 nm (entries 4 and 9 of Table 3.2). For Murugadoss et al.[196], lower the molar fraction of chitosan higher the catalytic activity, confirming that the polymeric template may reduce the accessibility of the active sites. Zheng et al.[197] evidenced a strong inter- and intra- molecular interaction between exopolysaccharide and Ag NPs. On one hand, it decreases the catalytic efficiency, but on the other hand, it guarantees a higher stability and the reusability of the small nanoparticles. Furthermore, the support itself may play an active role in the catalytic mechanism. As demonstrated by Zhang et al.[195] the epoxy groups of PGMA-SH microspheres acts as electron acceptor, resulting in a charge distribution between the support and the metallic nanoparticles. A similar phenomena occurs with graphene oxide, observing both electron transfer mechanism and naked surfaces of NPs on GO sheets[198]. Focusing on the SBA-15, the worst result was reported for silver nanowires (entry 7 of Table 3.2) mainly due to the pore obstruction of the mesoporous substrate. The catalytic behaviour strongly improved for 7 nm-spherical nanoparticles[199], which were homogenously distributed inside and outside of the SBA channels. The catalyst developed in this chapter (entry 20) presented a surface area around 4 times higher, which is reflected in a 4.5 higher kinetic constant. Better results have been reported by Huo et al.[200] with 2.1-Ag nanoparticles stabilized on mesoporous SBA-15 with a higher metal loading (3.5 wt.%). This in turn allowed to operate with a considerable reduction of metal loading, leading to enviromental and economical advantages[201].

Table 3.2 A summary of Normalized Kinetic Constant for the reduction of 4-NP catalysed by Ag nanoparticles.

Entry	Catalyst	Diameter (nm)	[Ag] (mg l^{-1})	K (l mg^{-1} s^{-1})	Ref.
1	Ag/CaCO$_3$	20.0-30.0	1250	2.54·10^{-6}	[202]
2	Ag NPs	10.0-35.0	616	4.30·10^{-6}	[194]
3	Ag NP/C	10.0±2.0	184	9.18·10^{-6}	[203]
4	Chitosan-Ag NPs	~3.0	273	9.82·10^{-6}	[196]
5	Ag NPs-CP25	30.0-40.0	975	1.60·10^{-5}	[204]
6	Ag NPs	540.0-640.0	500	2.00·10^{-5}	[205]
7	0.7Ag-SBA-15	Nanowires	500	2.27·10^{-5}	[206]
8	PI/Ag NPs	5.0-20.0	344	2.75·10^{-5}	[207]
9	Ag/rGO NPs*	8.6±3.5	250	4.06·10^{-5}	[198]
10	EPS-Ag	~5.0	27	4.73·10^{-5}	[197]
11	TA@Fe$_3$O$_4$-AgNPs	~10.0	200	5.35·10^{-5}	[208]
12	Ag-OMS-C	-	390	7.77·10^{-5}	[170]
13	Ag/SiO2/PNIPAM	15.0-20.0	46	8.99·10^{-5}	[209]
14	Ag@C	6.0-8.0	78	1.81·10^{-4}	[73]
15	SPAG	~50.0	8.5	9.45·10^{-4}	[210]
16	Ag@mTiO2@CF	~10.0	13	1.44·10^{-3}	[5]
17	Ag/SBA-15	~7.0	2.3	1.56·10^{-3}	[199]
18	AgNP-PG-25K	85.0±2.0	3.5	1.57·10^{-3}	[211]
19	AgNPs@PGMA-SH	17.0±3.2	0.9	4.38·10^{-3}	[195]
20	**B-AgNPs@SBA-15**	**1.6±0.7**	**1**	**(7.90±0.58)·10^{-3}**	*This work*
21	MSAg-50	2.1 nm	35	33.71·10^{-3}	[200]

3.4. Conclusions

The fast heating rate and volumetric character of MWH were essential for the synthesis of ultra-small Ag-NPs with the PAA acting both as reducing and stabilizing agent. A uniform size distribution of (1.6±0.7) nm was obtained after 17 s synthesis time and temperature below 74.6 °C. An increase of the synthesis temperature led to a low homogeneity of the product which is likely due to a high number of clusters coalescing, resulting in a broad particle size distribution, as observed for longer heating times than 17 s, 35 s and 70 s.

MWH resulted in a 10 times faster heating rate, compared to CH in an oil bath. This resulted in high homogeneity of NPs with a 70% reduction of the particle size deviation and also a reduction of 58% of the average diameter. It was experimentally verified that an instantaneous nucleation is crucial to improve the

quality of the final product, as observed by varying the heating rate from 2.8 to 0.2 °C/s.

Furthermore, the homogeneity of the suspension formed with ultra-small nanoparticles stabilized by PAA assured an extended storage life-time of the product, without the observation of the characteristic plasmon peak of silver nanoparticles at 400 nm, after 18 months storage.

Finally, the ultra-small Ag-NPs were deposited on the porous surface of SBA-15 (1 wt.%) by wet impregnation, giving rise to a homogeneous particle distribution both inside and outside the pores, while preserving accessibility of the reactants to the mesoporous structure. The catalytic activity of the B-AgNPs@SBA-15 was tested in the reduction of 4-nitrophenol. A high value of the kinetic constant for the pseudo-first order reaction was observed of $(7.90\pm0.58)\cdot10^{-3}$ ($l\cdot mg^{-1}\cdot s^{-1}$), which is above the literature values previously reported for this reaction.

80

FROM BATCH TO CONTINUOUS FLOW PROCESSING: Ag NCs

Goal: Is it possible to improve the particle size distribution switching to a continuous flow reactor with a strict control not only on heating but also on quenching steps?
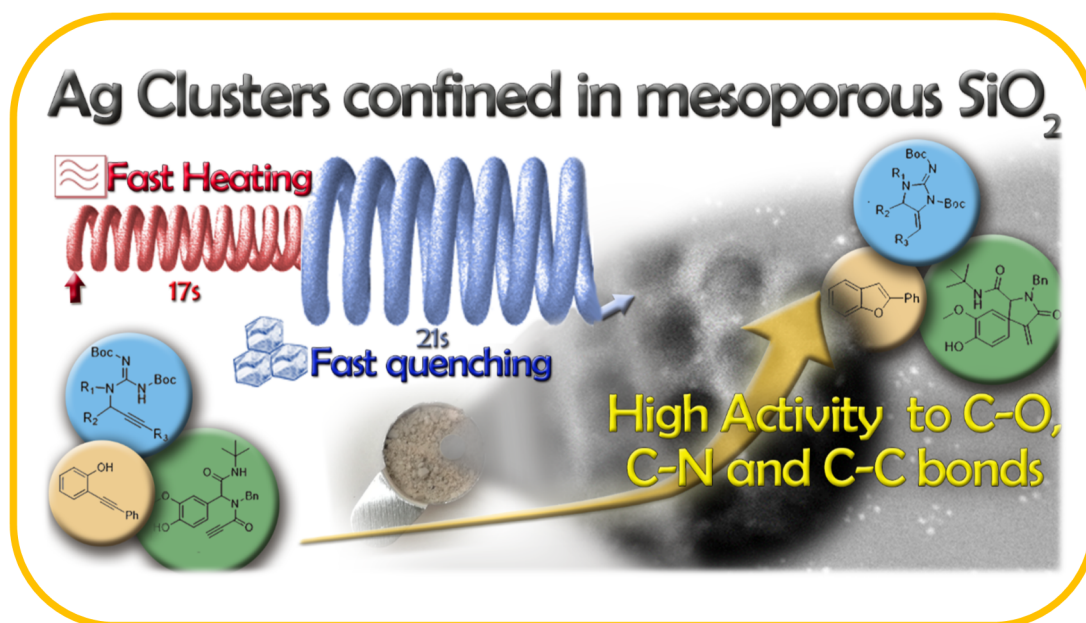
The contents of this chapter were adapted from the following published work:

"Continuous Microwave-Assisted Synthesis of Silver Nanoclusters Confined in Mesoporous SBA-15: Application in Alkyne Cyclizations."

Roberta Manno[‖], Prabhat Ranjan[‖], Víctor Sebastian*, Reyes Mallada, Silvia Irusta, Upendra K. Sharma, Erik V. Van der Eycken*, and Jesús Santamaría

Chemistry of Materials 2020, 32, 7, 2874-2883

[‖] These authors contributed equally.

4. FROM BATCH TO CONTINUOUS FLOW PROCESSING: Ag NCs

4.1. Introduction

The experimental results reported in previous chapter showed that a remarkable reduction of the synthesis time down to 17 s by microwave heating results in a homogeneous size distribution of ultra-small Ag-NPs with an average diameter of (1.6±0.7) nm on the border between nanoparticle and nanocluster classification. The speed of microwave heating may represent an efficient alternative to reduce induction times and control the nucleation of small clusters with more accuracy. Furthermore, its combination with continuous flow microfluidics not only may help to improve the control of the temperature gradient, increasing the rates of heating and mixing, but also enabling a fast quench, stopping further nucleation events[165]. In this chapter, the synthesis of Ag nanoclusters stabilized by PAA template was switched to the MW-heated continuous flow microreactor, previously described in chapter 2.

Silver nanoclusters have been intensively investigated since the early work by Ershov et al.[212] generating a wide library of synthesis procedures, particularly about Ag-NCs stabilized by anion templates[213] or thiolate groups[52,214]. The works of Belloni and Mostafavi[162–164] were of extreme interest to further investigate the mechanism of Ag nucleation in a polyacrylic acid (PAA) template by γ-irradiation. The hydrated electrons generated by the energy of irradiation activated the reduction of Ag(I), which were then complexed by the COO$^-$ anionic groups of the polymer.

The catalytic activity of the supported NCs has been tested in collaboration with the Laboratory of Organic and Microwave Assisted Chemistry (LOMAC) group of KU Leuven. The activity of Ag atoms is largely reported for alkynylation, cycloaddition and cycloisomerization of functionalized alkynes. Its high activity is strictly connected with its d_{10} electronic configuration which allowed the formation of π-complexes[215]. Silver salts have been reported as excellent catalysts for the synthesis

of biologically relevant molecule viz. furoquinolines[216], imidazolones[169], spiroindolines[217], o-alkynylbenzohydroxamic acid cycloisomerizations[218], cycloaddition of propargylamines[68], 2-aminoimidazole alkaloids[219], etc... . Despite the high yield and selectivity usually observed, a high concentration of silver-salts has been used, with many drawbacks related to their recovery after reaction. Small supported metal clusters, characterized by a $M_{(n+m)}^{m+}$ structure, represent an innovative and more efficient alternative, not only due to the high surface to volume ratio but also due to the population of highly active uncoordinated atoms that usually surround the metal core structure[220]. Furthermore, to facilitate the catalytic use and the reusability of the Ag-NCs synthesized, the clusters were stabilized on amino-functionalized SBA-15.

4.2. **Materials and Methods**

4.2.1. *Microwave-Assisted Synthesis of Ag Nanoclusters*

A MW-heated continuous flow reactor, schematized in Figure 4.1, was adopted for the synthesis of the C-AgNCs@SBA-15 catalyst, where C stays for continuous process. The entire reactor, made by polytetrafluoroethylene (Teflon®, Iberfluid Instruments, outer diameter 1/16" and inner diameter 0.39 mm), consisted of three different zones: mixing, heating and, quenching. In the mixing stage (l_{mixing}=8 cm, and V_{mixing}=0.91 μL), a 50 mM solution of $AgNO_3$ (Aldrich 99.9999%) and poly (acrylic acid, sodium salt) solution (500 μL of Na-PAA Sigma Aldrich MW 1200, 45 wt.% in water, dispersed in 9.5 mL of D.W.) were pumped at a flow rate of 0.146 mL/min by a syringe pump (High precision PHD ULTRA by Harvard Apparatus) and mixed in a commercial Y-mixer (material PEEK, IDEX Corporation, thru-hole of 0.02'' and swept volume of 1.7 μL). After rapid mixing, the precursors reached the heating zone (Figure 4.1), where 71 cm of Teflon® pipe was rolled on a quartz tube (O.D. 9 mm) to obtain a helical tubular reactor ($V_{heating}$=83 μL). For MWH, the rectangular microwave cavity previously described in chapter 2 was adopted, fixing the frequency and the power at 2.45 GHz and 15 W, respectively. As reported in

chapter 2, the temperature profile was recorded as a function of the residence time exclusively by the thermographic camera (Optris PI-400038T900). Finally, undesired further nucleation and cluster growth were prevented by the quenching step. The quenching stage was performed in a coil PTFE tubing ($l_{quenching}$=89 cm, $V_{quenching}$=104 μL) immersed in an ice bath and maintained at a constant range of temperature of 0-4 °C (Figure 4.1). The temperature decrease was simulated by COMSOL Multiphysics® (model described in chapter 2, keeping constant the external wall temperature to 4 °C) and experimentally measured at the outlet point by an optical fiber.

After synthesis, the clusters were immobilized over the SBA-15 rods (synthesis procedure detailed in chapter 3) by wet-impregnation mechanism, injecting 800 μL at 1,500 rpm for 1 hour. Finally, the catalyst was centrifuged with distilled water at 12,000 rpm for 20 min to separate both the non-grafted Ag-NCs and the PAA excess, and dried overnight at 50 °C. Two catalysts with lower loading (0.16 wt.% and 0.62 wt.%) were obtained reducing the injecting volume to 400 μL and 200 μL respectively.
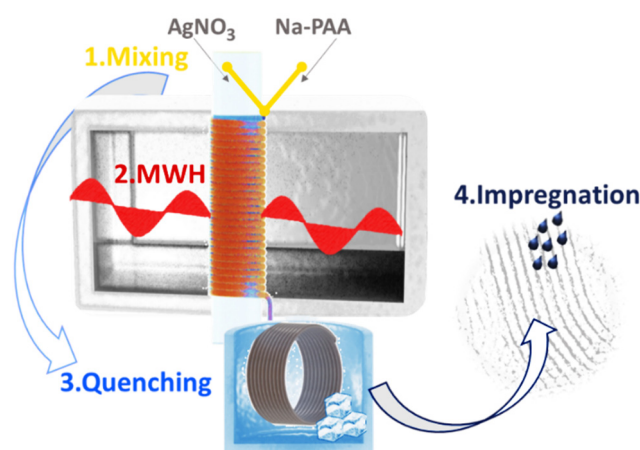
Figure 4.1 Continuous flow microreactor adopted for the synthesis of the catalyst C-AgNCs@SBA-15. The set-up consisted of mixing, microwave heating and quenching stages for the synthesis of Ag-NCs, which were subsequently grafted over SBA-15 by wet-impregnation.

4.2.2. *Catalyst Characterization Techniques*

The catalysts were characterized following the respective procedures reported in chapter 3, section 3.2, and paragraph 3.2.3.

4.2.3. *Catalytic Activity*

Both reagents and solvents were used as received without further purification unless stated otherwise. Reagents and solvents were supplied by Sigma Aldrich and Tokyo Chemical Industry (TCI) and, if applicable, kept under Ar atmosphere. Technical solvents were bought from VWR International and Biosolve. Product isolation was performed using silica (60, F254, Merck™), and thin-layer chromatography (TLC) analysis was performed using Silica on aluminum foils TLC plates (F254, Supelco Sigma-Aldrich™) with visualization under ultraviolet light (254 nm and 365 nm) or appropriate TLC staining. Infrared (IR) spectra were recorded on Bruker Alpha FTIR spectrometer, analysing the maximal peaks. ^{1}H (400 MHz or 600 MHz), ^{13}C (100 MHz) NMR spectra were recorded on ambient temperature using a Bruker-Avance 400. ^{1}H NMR spectra are reported in parts per million (ppm) downfield relative to $CDCl_3$ (7.26 ppm) and all ^{13}C NMR spectra are reported in ppm relative to $CDCl_3$ (77.2 ppm). NMR spectra uses the following abbreviations to describe the multiplicity: s = singlet, d = doublet, t = triplet, q = quartet, p = pentet, h = hextet, hept = heptet, m = multiplet, dd = double doublet, td = triple doublet. Known products were characterized by comparing to the corresponding ^{1}H NMR and ^{13}C NMR from literature[217,219,221,222]. High-resolution mass spectra were acquired on a quadrupole orthogonal acceleration time-of-flight mass spectrometer (Synapt G2 HDMS, Waters, Milford, MA). Samples were infused at 3 μL/min and spectra were obtained in positive (or negative) ionization mode with a resolution of 15,000 (Full width at half maximum - FWHM) using leucine enkephalin as lock mass.

4.2.3.1   *Cyclization of N-Propargylguanidines*

Propargylamine (0.3 mmol), 1,3-bis(tert-butoxycarbonyl)thiourea (DBTU, 115 mg, 0.41 mmol), and diisopropylethylamine (112 mg, 0.9 mmol) were dissolved in anhydrous MeCN (2 mL). After stirring at room temperature, it was cooled to 0 °C followed by addition of EDCI (115 mg, 0.6 mmol). Then, reaction was stirred at RT overnight, diluted with EtOAc (50 mL), and washed with water (3×100 mL), followed by brine and dried over anhydrous Na_2SO_4. The solvent was evaporated under vacuum followed by column chromatography on silica using 20% EtOAc in heptane as eluent (R_f 0.25-0.3)[217223].

A proper amount of C-AgNCs@SBA-15 was added to 0.32 mmol of N-propargylguanidine in 3.2 mL of organic solvent (DCM, Toluene or DCE), previously dispersed at 50 °C until complete dispersion. The reaction vial was immersed in an oil bath preheated at set-point temperature and stirred at 500 rpm. Then, the reaction mixture was centrifuged to recover the catalyst, which was washed three times with DCM. The resulting organic layer was evaporated under reduced pressure, and the residue was purified by silica gel column chromatography.

4.2.3.2   *Cyclization of 2-(Phenylethynyl Phenol)*

Firstly, 0.05 mmol of 2-(phenylethynyl)phenol of as-made precursor[87] were dissolved in 1 mL of toluene at 80 °C. The reactor was immersed in an oil bath preheated at set-point temperature and stirred at 500 rpm, adding the proper amount of silver catalyst. After the reaction time, the reaction mixture was centrifuged and the catalyst was washed three times with toluene. The resulting organic layer was evaporated under reduced pressure, and the residue was analyzed by ^{1}H-NMR spectroscopy and GC-MS.

4.2.3.3   *Spirocyclization of Phenol-based Propargylamide*

In an oven-dried 10 mL screw-cap vial, a proper amount of C-AgNCs@SBA-15 and N-benzyl-N-(2-(tert-butylamino)-1-(4-hydroxy-3-methoxyphenyl)-2-oxoethyl)

propiolamide (40 mg, 0.1 mmol) was dissolved in 0.1 M dry DCM. After 12 h of heating at 50 °C, the mixture was diluted with DCM. The solvent was evaporated and the crude product was purified by column chromatography on silica (EtOAc : Heptane = 1 : 2 to 1: 1).

4.3. Results and Discussions

4.3.1. *Characterization of C-AgNCs@SBA-15*

The results presented in chapter 3, in batch reactor, showed that the mean size and the standard deviation increases as the irradiation time is extended from 17 s to 70 s. The most monodisperse distribution of ultra-small Ag-NPs (1.6±0.7) nm was obtained at the shortest irradiation time (17 s). This achievement slightly improves some previous results reducing the average size distribution, halving the synthesis time and improving the size deviation[95]. However, as reported in Figure 4.2 a, the switching off of MW did not lead to a fast cooling of the system. In fact, a temperature higher than 50 °C was recorded for more than 300 s which may promote subsequent aggregation of Ag atoms, and size evolution of the clusters.

In the case of continuous flow reactor a cooling stage to rapid quench the reaction after the heating step was included, minimizing the further evolution of the metallic nanoclusters. The temperature profile along the residence time in the microfluidic reactor (Figure 4.2 b) was totally different compared to the evolution of temperature with time in the batch reactor (Figure 4.2 a). In the batch system the average temperature was (50.4±22.4) °C. On the other hand, in the microfluidic reactor the (71.7±8.7) °C reaction temperature was reached during the 17 s residence time in the heating step and the temperature dropped down to 4 °C in the fast 21 s quenching step (Figure 4.2 b). The narrower temperature along the reactor together with the fast cooling in the flow reactor yielded a reduction of the average diameter and the standard deviation (1.2±0.3) nm compared to the batch type-reactor (1.6±0.7) nm (Figure 4.2 c and d). The Ag-NCs size distribution was remarkably reduced around 60% with the use of the continuous microfluidic platform. The HAADF-STEM

analysis of clusters confirmed the absence of a crystalline structure (Figure 4.3 b)[164,224]. A clear difference in the color of the solution was observed between the two synthesis procedures (Figure 4.2 e). In detail, J. Belloni et al.[162,163] reported the mechanism of clusters formation by γ-irradiation with a detailed STM analysis. The carboxylate group in PAA had a dual function: anchoring of clusters like a ligand and protecting them from coalescing through electrostatic repulsion.

The clusters may present a structure like $Ag_{(4+m)}^{m+}$, with silver atoms and silver ions stabilized by the carboxylate groups of the polyelectrolyte[225,226]. On the basis of their analysis, it may be plausible to associate a structure of $Ag_4^{2+}+PA^-$ to the pink colloidal solution, obtained with continuous flow synthesis, and of larger clusters to blue complexes, reported for batch reactions[212,225]. The differences between the plasmonic resonance peaks confirmed the absence of larger crystallized Ag-NPs and the synthesis of Ag-NCs[224,227,228]. The control of synthesis conditions is usually challenging and has a strong effect on the resulting nanomaterials. This issue is even more critical in fast kinetic reactions[229], such as the one considered in this work. The microfluidic synthesis of nanomaterials can enhance the controllability and reproducibility of the resulting Ag-NCs due to the excellent control at the mixing and reaction levels[229].
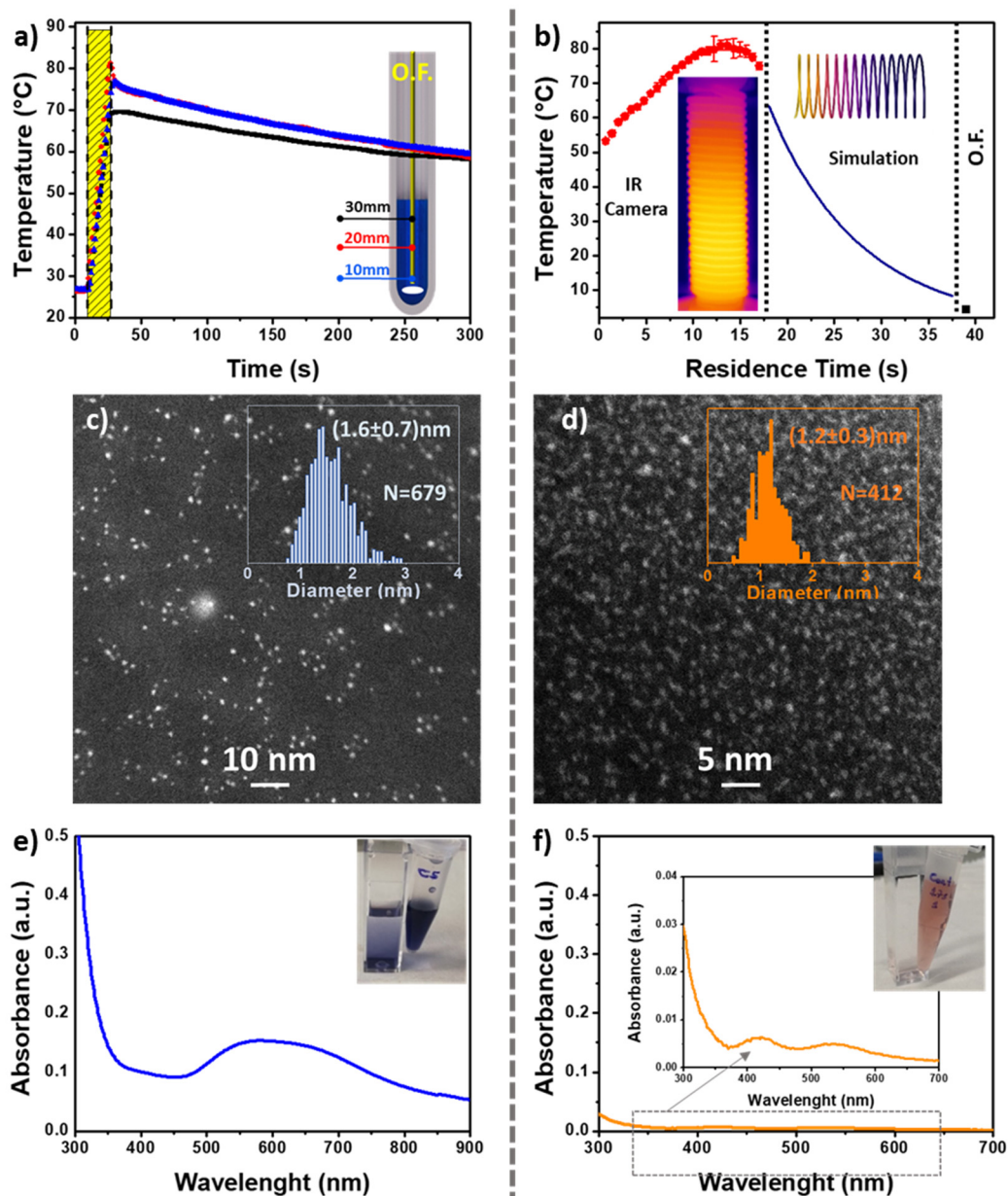
Figure 4.2 a) Experimental temperature profile for the batch-type reactor measured with an optical fiber in three different points as indicated in the schematic representation on the right; b) Temperature profile in a continuous-flow reactor measured by an IR Camera (red points), Comsol Multiphysics® (blue line) and an optical fiber (black point); c) Size distribution of ultra-small Ag-NPs (N=679) produced by a batch-type reactor; d) Size distribution of Ag-NCs (N=412) produced in a microfluidic system; e) UV-Vis Spectroscopy of ultra-small Ag-NPs produced in a batch-type reactor, synthesis time 17 s. Inset, optical image of resulted Ag-NCs (dilution in the quartz cuvette 0.5 mL of sample in 2.5 mL of DW); f) UV-Vis Spectroscopy of Ag-NCs produced in the continuous microfluidic system. Inset, optical image of resulted Ag-NCs (dilution in the quartz cuvette 0.5 mL of sample in 2.5 mL of DW). *Copyright 2020 American Chemical Society*

The improved clusters synthesized by continuous synthesis were stabilized through deposition on a mesoporous substrate, ensuring a long lifetime and their use as heterogeneous catalyst. The morphological characterization of SBA-15 nanorods is reported in Figure 4.3 a and the HAADF-STEM images of the nanochannels with different metal loadings, from 0.16 to 0.96 wt.% (c-e). Overall the NCs are uniformly distributed along the entire surface of the mesoporous substrate, without evident agglomeration.
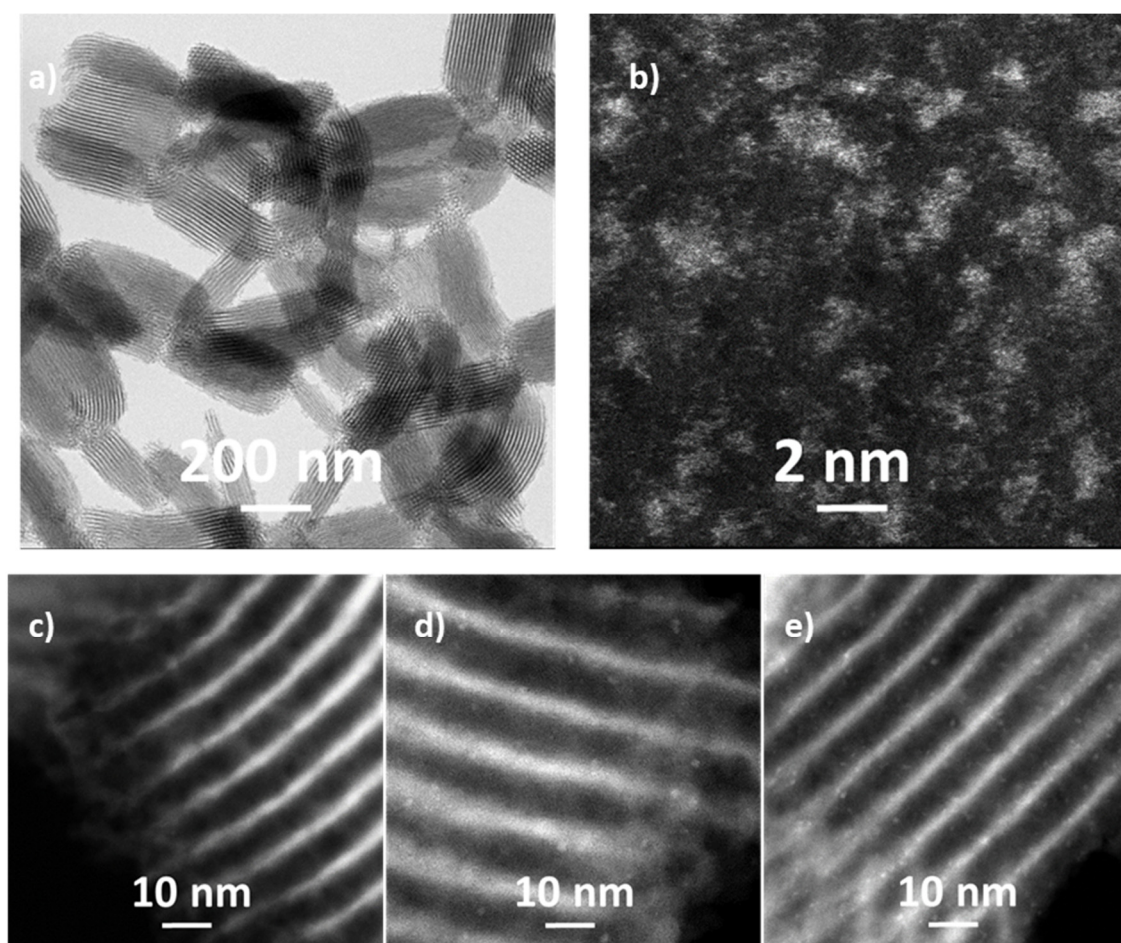
Figure 4.3. TEM and HAADF-STEM analysis for SBA-15 grafted with APTES (a), unsupported Ag NCs (b), C-AgNCs@SBA-15 with three different metal loading: 0.16 wt.% (c), 0.62 wt.% (d) and 0.96 wt.% (e). *Copyright 2020 American Chemical Society*

For the 0.96 wt.% metal loading, no size alteration was observed after the deposition step, in Figure 4.2 d) and Figure 4.4 c-e). The clusters occupied the internal and the external surfaces of the mesoporous channels and the entrances of the pores were not obstructed by clusters' grafting (Figure 4.4 a). It is important to note a very good

reproducibility of interbatch nanoparticle size distributions, presented in Figure 4.4 c, d and e.
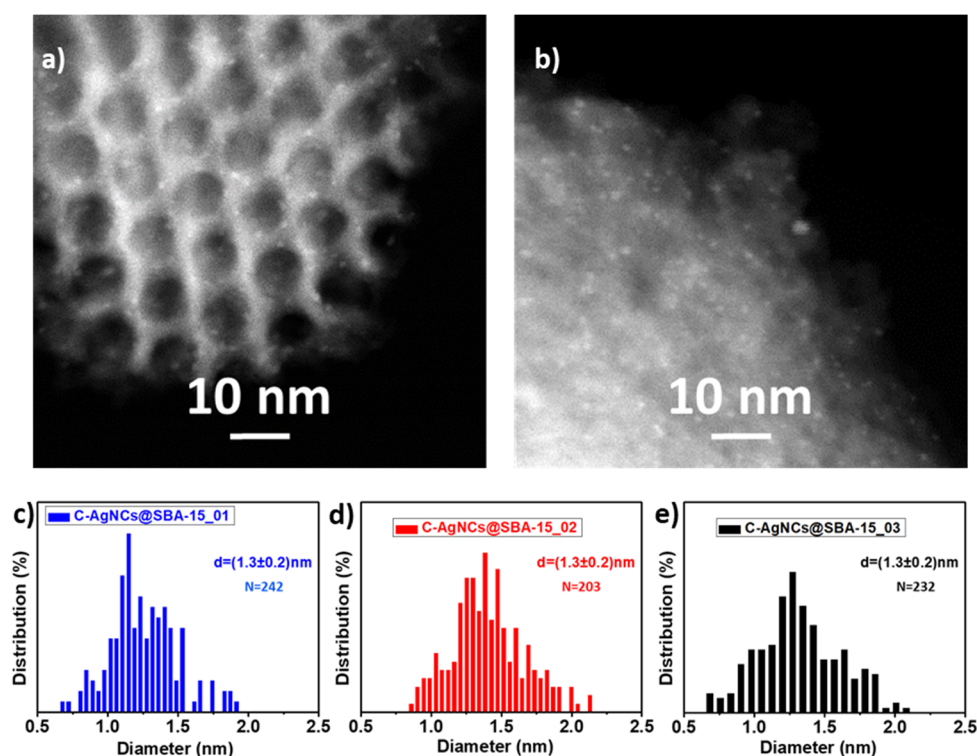
Figure 4.4 a) and b) HAADF-STEM analysis C-AgNCs@SBA-15 (0.96 wt.%) evidencing the homogeneous distribution of the metallic clusters inside and outside of the pores. c), d) and f) reproducibility tests of size distribution. *Copyright 2020 American Chemical Society*

The N_2 adsorption analysis evidenced a decrease of 33% of pore volume as a result of the clusters deposition. In spite of this, the analysis of the type-IV isotherm with H1 hysteresis obtained after deposition (Figure 4.5 a) confirmed the presence of clusters both inside and outside of the nanorods. In fact, the pores presented a bimodal size distribution with few pores in 3.2 nm while the majority in 9.2 nm (Figure 4.5 b), with an average pore volume of 0.59 cm^3/g (Table 4.1). Even though, the functionalized mesoporous support can be used as a suitable catalyst, since the molecular size of the reactants is lower than 2 nm. Finally XPS analysis confirmed the copresence of 50% of Ag(0), that presumably forms the core of Ag-NCs, and 50% of Ag(I), complexed by the polycarboxylate group of PAA (Figure 4.5 c and Table 4.1)[225].

Table 4.1: N_2 adsorption and XPS analysis details of amino-functionalized SBA-15 before and after Ag-NCs grafting.

Sample	S_{BET} (m^2g^{-1})	V_t (cm^3g^{-1})	D_{BJH} (nm)	Ag(0)	Ag(I)
SBA-15	317	0.89	9.3	-	-
C-AgNPs@SBA-15	255	0.59	9.2	50%	50%
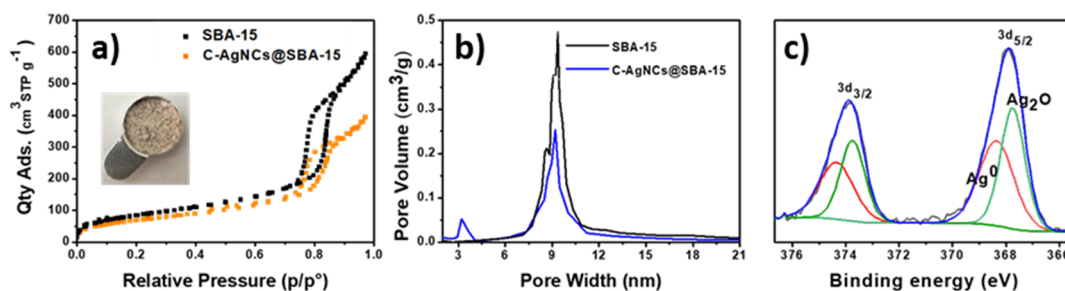
Figure 4.5 a) and b) The grafting of SBA-15 at first with APTES and subsequent with Ag-NCs is evidenced by the reduction of pore diameter, which still continues to be higher than 9.0 nm, allowing its catalytic application. C-AgNCs@SBA-15 sample in the optical inset. c) XPS test evidenced the presence of Ag(0) and Ag(I), *Copyright 2020 American Chemical Society*.

4.3.2. *Heterogeneous Catalytic Activity*

Silver salts may represent an excellent catalyst for hydroamination of propargylguanidines[219]. The mechanism is presented in Scheme 4.1, silver (I) catalyzes the activation of the triple bond (C≡C), followed by nucleophilic attack of nitrogen and subsequent proto-demetallation together with the regeneration of the catalyst, and the liberation of product b. Unlike crystallized nanoparticles, Ag-NCs present a high concentration of uncoordinated atoms, the presence of Ag(I) and Ag(0) presents a favourable situation to increase the catalytic activity of Ag. In view of recent reports on silver catalysis, a preliminary analysis was conducted to optimize the reaction conditions in standard solvents commonly used for silver and gold catalysts. Ag-NCs (0.15 mol% in overall Ag content) gave 2a in 90% yield (Table 1, entry 2). Among the tested solvents, DCM worked well (Table 1, entries 2, 3 and 4). A slight increase in temperature resulted in a 99% yield of 2a after 3 h (Table 1, entry 5).

Scheme 4.1 Proposed mechanism for hydroamination of propargylguanidines, from reactant a to product b[219].
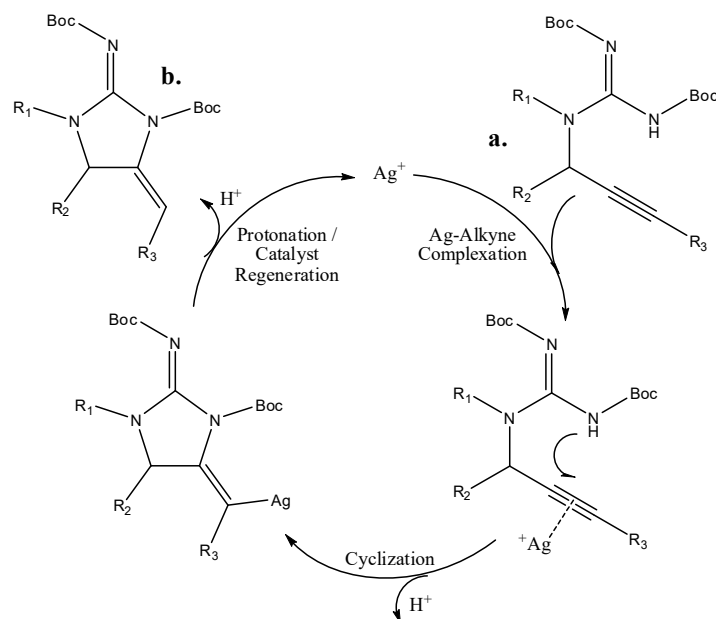
This is remarkable, since compared with the traditionally used silver salts, the catalyst loading is about 33 times lower (compared to $AgNO_3$)[230] and about 7 times lower compared to the Ag-NCs used by Duan et al.[68]. The effect of metal loading on the SBA-15 support (0.16, 0.62 and 0.96 wt.%) was studied for a total constant catalyst loading of 0.15%mol of Ag (Table 4.2 entries 5 and 7). The highest yield was obtained for the highest load in the SBA-15 support. The catalytic study evidenced that a major density of the clusters on the porous substrate (reported in Figure 4.3 c-e) may increase the stochastic probability of the substrate to reach the active site.

A hot-filtration test was performed by removing the catalyst after 90 min of reaction. No further conversion was observed after the removal of the catalyst, confirming the heterogeneous nature of the reaction. Furthermore, the catalytic activity remained higher than 90% even after 4 cycles (Figure 4.6 a) and no leaching of the Ag content could be detected by MP-AES analysis (Table 4.3). Finally, to verify the possible alterations in size distribution, HAADF-STEM analysis was performed on the recovered catalyst used for the reaction at different temperatures and in different solvents. As reported in Figure 4.6 b) and c), no relevant variations of size

distribution were observed confirming the absence of modifications on the catalyst itself.

Table 4.2 Optimization studies of propargylguanidine cyclization, catalyzed by C-AgNCs@SBA-15 [a].
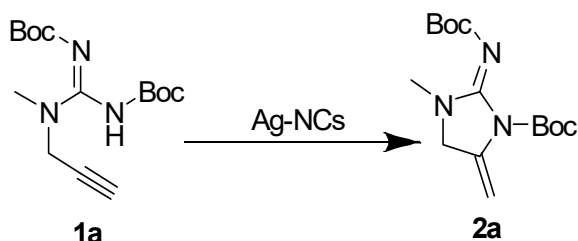
Entry	Metal Loading wt.%	Mol % Ag	Solvent	Temperature (°C)	time (h)	Conversion (%)[b]	Yield (%)[b]
1	-	-	DCM	40	12	< 5	< 5
2	0.96	0.15	DCM	40	2	90	90
3	0.96	0.15	DCE	40	2	50	50
4	0.96	0.15	Toluene	40	3	85	83
5	0.96	0.15	DCM	50	3	100	99
6	0.62	0.15	DCM	50	3	84	81
7	0.16	0.15	DCM	50	3	53	53

[a]Reaction conditions: All reaction were run with 1a (0.12 mmol) in the indicated solvent (1.2 mL) in a screw cap vial. [b] Conversion and yield were determined by the NMR-integration method using 3,4,5-trimethoxybenzaldehyde as an internal standard.
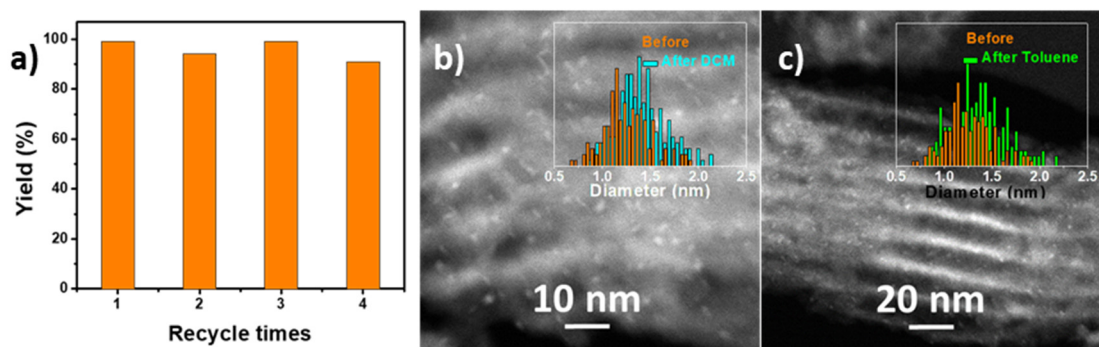
Figure 4.6 a) Activity tested up to 4 cycles for propargylguanidine cyclization. b) and c) HAADF-STEM analysis for C-AgNCs@SBA-15 catalyst after reaction at 50 °C for 3 h in DCM and in Toluene respectively. *Copyright 2020 American Chemical Society*

Table 4.3 Metal catalyst evaluation before and after the use of the C-AgNCs@SBA-15.

	Fresh Catalyst	Used Catalyst
[Ag] wt.%	(0.96+0.04)%	(0.93+0.05)%
[Ag] wt.%	(0.62+0.03)%	(0.61+0.02)%

The substrate scope for the hydroamination of propargylguanidines, employing the optimized conditions, was subsequently investigated and listed in Table 4.4. A yield higher than 90% was reported by substrates a and e, which presented the smaller R_1 group. On the other hand, the catalytic activity gradually decreases to 80, 70 and 5% when the R_1 group is represented by polymethylpentene (2c-PMP), benzyl (2d-Bn) and biphenyl (2b) respectively. The phenyl groups, characterized by a high electronic delocalization, may both confer a higher stability to the reagent molecule and contrast the Ag complexation. In that case, an optimization of catalyst amount, catalyst-support pore size or time/temperature condition of the process may guarantee a higher conversion.

Table 4.4 Scope of the reaction by C-AgNCs@SBA-15 catalyst in batch conditions [a].

Product no.	Product	Time (h)	Temperature (°C)	Yield (%)
2a		3	50	99
2b[b]		3	50	50
2c		3	50	80
2d		3	50	70
2e		3	50	92

To further extend the applicability of our catalyst, it was examined the synthesis of 2-phenylbenzofuran by employing Ag-NCs, which is usually performed under homogeneous catalysis or with Pt-, Pd- and Au-NCs[87,193,231]. In line with the literature it was assumed that the activation of the triple bond by Ag-NCs would result in O-cyclization[232,233]. Lower yield was observed with $AgNO_3$, AgOAc and Ag_2O, respectively of 15%, 5% and 5% (Table 4.5, entries 1, 2 and 3). Furthermore, no conversion was observed with larger silver nanoparticles previously used for the synthesis of imidazolones (Table 4.5, entry 4)[169]. On the contrary, Ag-NCs gave a nearly quantitative conversion of 3a (Table 4.5, entry 5). Satisfyingly, increasing the temperature to 70 °C reduced the reaction time to 3 h (Table 4.5, entry 7). Somorjai and co-workers[87] have reported same reaction with 4 mol% of Pd_{40}/SBA-15 but in this work the same conversion was achieved with a lower amount of Ag-NCs (1.5 mol%) at lower reaction temperature (Table 4.5, entry 7).

Table 4.5 Optimization of the cyclization of 2-(phenylethynyl)phenol catalyzed by different Ag catalysts.[a]
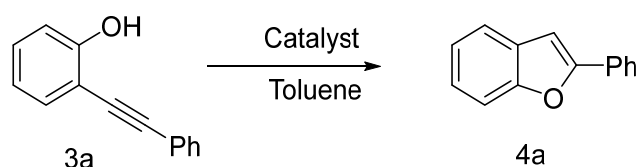
Entry	Type of Catalyst	Ag (mol%)	Temperature (°C)	Time (h)	Yield[b] (%)	Conversion (%)
1	$AgNO_3$	5	50	24	15	15
2	AgOAc	5	50	24	5	5
3	Ag_2O	5	50	24	5	5
4	Ag-NPs@SBA-15[c,169]	5	50	24	0	0
5	C-AgNCs@SBA-15	1.5	30	20	91	91
6	C-AgNCs@SBA-15	1.5	50	6	93	95
7	C-AgNCs@SBA-15	1.5	70	3	93	100

[a]Reaction conditions: All reaction were run with substrate 3a (0.05 mmol) in toluene (1 mL) in a screw cap vial. [b] Conversion and yield were determined by the GC-MS using hexamethylbenzene as an internal standard, [c] Ag-NPs@SBA15 = 2 wt.%[169].

A deactivation of the catalyst was observed after each application, diminishing the yield to 20% after the third cycle at 70 °C, as reported in Figure 4.7 a. This result

might be due to the reduction of Ag(I) to Ag(0), as confirmed by XPS analysis after the reaction (Figure 4.7 b). In an attempt to reactivate the catalyst, the H_2O_2 oxidation reaction in water was used to increase the surface of Ag(I) ions[234,235]. This procedure effectively restore the catalytic activity, giving 90% yield of 4a after the oxidation step (Figure 4.7 a). Furthermore, HAADF-STEM analysis confirmed that the morphology of the catalyst remained almost invariable after H_2O_2 treatment (Figure 4.7 c).
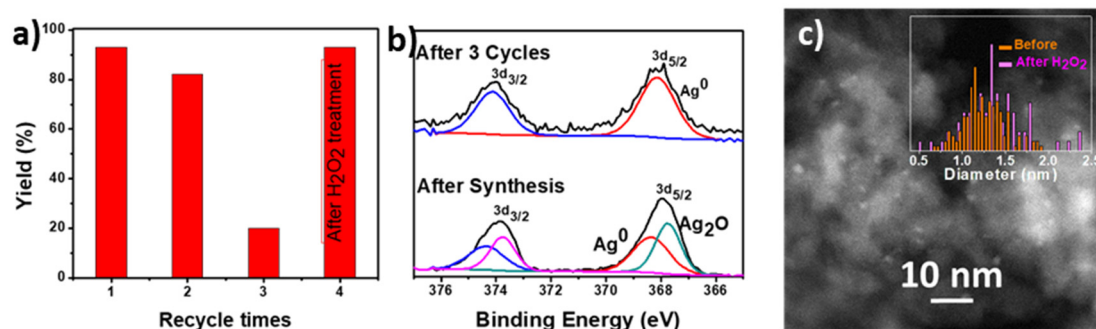
Figure 4.7 a) Reusability activity tested up to 4 cycles of cyclization of 2-(phenylethynyl)phenol, with a H_2O_2 regeneration step. b) XPS Analysis after 3 cycles, where it is possible to notice the complete reduction of Ag. c) HAADF-STEM after the H_2O_2 treatment. *Copyright 2020 American Chemical Society*

To conclude, the C-AgNCs@SBA-15 catalyst was used on post-MCR spirocyclizations. In particular for dearomatization/ipso-cyclization of substrate 5a (Scheme 4.2), because of the lower selectivity reported with triphenylphosphine[217] in a previous report. Ag-NCs gave a high and selective conversion of 70% for 6a, without traces of product 6b which is a further confirmation of the peculiar reactivity and applicability of Ag-NCs[236].

Scheme 4.2 Spirocyclization of phenol based propargylamide 5a by Ag-NCs.[a]
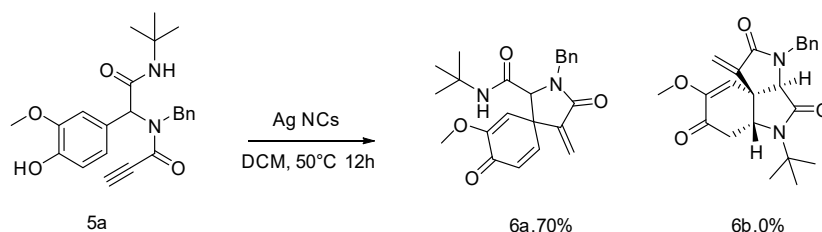
[a]Reaction condition: Reaction was run with substrate 5a (0.1 mmol) in DCM (1 mL) and Ag-NCs (0.3 mol%, 0.96 wt.% C-AgNCs@SBA-15) in a screw cap vial.

4.4. **Conclusions**

The innovative design of a microfluidic system for the synthesis of Ag NCs including Y-mixing section of reagents, MWH during reaction and fast quenching in ice bath, allowed to precisely control all the synthesis steps, resulting in homogeneous Ag NCs, which were further stabilized in SBA-15 porous support, C-AgNCs@SBA-15 catalyst. The small clusters with a dimension lower than 2 nm were homogeneously distributed on the porous hexagonal channels of the mesoporous substrate, as confirmed by HAADF-STEM analysis, with a resulting loading yield lower than 50%.

The resulting catalysts presented good accessibility for the substrates employed, could be easily separated and recycled and were stable (in terms of particle size) under the reaction conditions employed. The catalytic test evidenced the high performances of cyclization of alkyne bonds for Ag-NCs, due to the formation of π-complexes. The cycloisomerization of propargylguanidine resulted in the formation of C-N bonds, with a yield of 99% in less than 3 h at 50 °C. Furthermore, a reduction of 30 times of the metal loading was obtained in comparison to commonly used non recoverable Ag salts.

Furthermore, a clear advantage, in terms of catalytic activity, 93% yield was observed for the cyclization 2-(phenylethynyl)phenol in comparison to the application of Ag-salts (15% yield) and bigger nanoparticles (0% yield). This extraordinary enhancement of catalytic activity for Ag-NCs should be assigned to a good π-accepting behavior due to the co-presence of Ag(0) and Ag(I). This is also supported by the fact that, for the cases where deactivation was observed, a complete reactivation of the catalyst was possible through H_2O_2 treatment that induced the partial oxidation of Ag(0).

To conclude, the Ag-based catalyst here presented may result a competitive alternative for alkynes activation as demonstrated by its versatility for C-N, C-O and C-C bonds, covering a wide range of organic applications.

SIMULTANEOUS COOLING-MICROWAVE HEATING:

In-situ clusters nucleation and deposition

Goal: *What about to nucleate, quench and support the nanoclusters at the same time?*
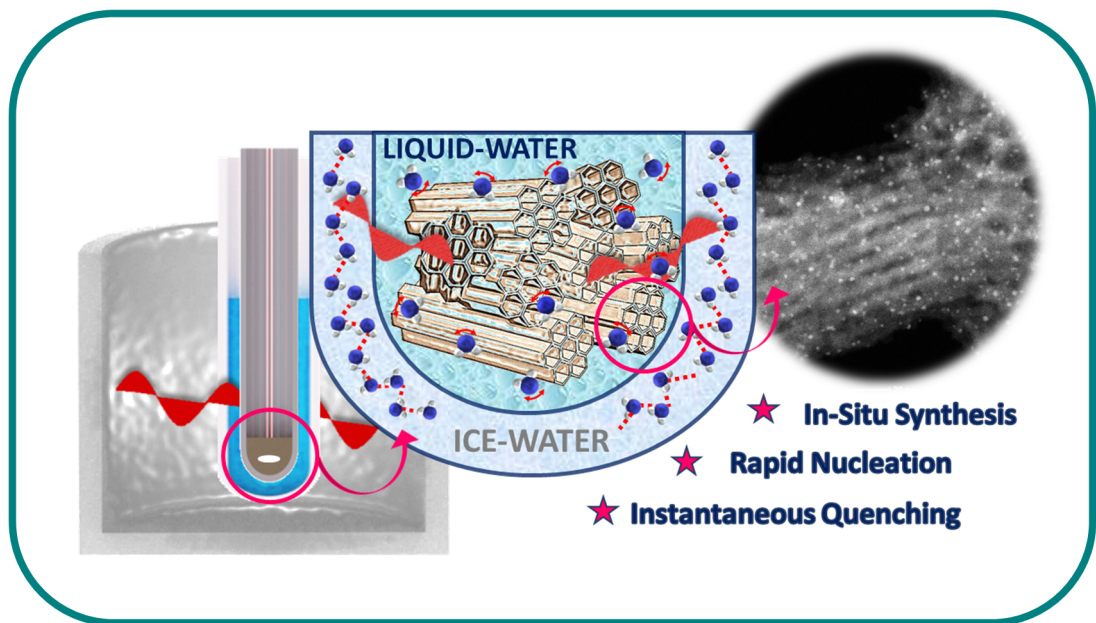
5. SIMULTANEOUS COOLING-MICROWAVE HEATING: In-situ Clusters Nucleation and Deposition

5.1. Introduction

Traditional template-assisted methods are characterized by high reproducibility and an atomic control of the structure of the final clusters[85,91]. However, the post-grafting may result in no uniform clusters distribution[168,237] and, as confirmed in the previous chapters, a loading yield lower than 50%[238]. Even if the maximum loading may be increased by the in-situ synthesis, the control of the nucleation step is still a critical aspect[75,76].

Focusing on the three key aspects for the ideal synthesis conditions, an external stimulus is required to instantaneously and homogeneously yield small nanoclusters. So far, this was considered the main critical aspect, as reflected by several publications recently reported[47,91,94,239]. The implementation of alternative and localized energy sources, such as ultrasound, microwaves or plasma, may surely represent winner techniques but are not enough to assure subsequent clusters stabilization. The quenching step is as important as the heating one. By thermal laser pulsed experiments reported by Yang et al.[240], one of the main advantages of alternative energy sources is the quick removal of the external stimulus once the activation limit was bypassed. Wei et al.[241] demonstrated that even single-atoms catalysts may be produced by low-temperature metallic atoms reduction. In the iced-photochemical process, liquid nitrogen was used as a key quenching step to stabilize the reaction temperature during the 1-hour exposure to UV irradiation, observing a uniform distribution until a maximum concentration of 2 wt.%. On the contrary, a mixture of nanoclusters, single atoms and nanoparticles were observed by 120 fs ultrashort-light pulses in the absence of a quenching step[242]. A rapid cooling and the heterogeneization of the nanoclusters may guarantee long-time stability and higher quality of the final product[9,90,243].

In this chapter, an innovative one-pot procedure was designed for the confinement of Ag NCs directly on the mesoporous substrate based on the selectivity of microwave heating. The water-based NCs precursors are high microwave absorbers but the reactor was surrounded by a thin layer of ice, which is a microwave transparent material[116]. In this way, a simultaneous cooling microwave heating occurred, guaranteeing both rapid localized nucleation and a nearly instantaneous blocking of undesired sintering events. To the best of my knowledge, simultaneous cooling-microwave heating has been widely applied for organic chemical reactions[244–246], but there are no reports on its application for the in-situ nanoclusters and/or nanoparticles synthesis.

The catalyst developed by this innovative method was compared with the previous batch and continuous methods, described in chapter 3 and 4 respectively. In detail, the differences in terms of temperature profile, size distribution, oxidation state, synthesis yield and catalytic activity in the 4-nitrophenol test reduction were evaluated. Then, the activity of heterogeneous Ag-NCs was tested for a wide range of alkynes cyclization. To conclude, the analysis was focused on the scalability of the reactor, adopting a synthesis volume 2, 5 and 10 times higher, and on its versatility for the synthesis of different metallic clusters, such as Cu NCs and on different support, such as commercial Vulcan XC-72.

5.2. **Materials and Methods**

5.2.1. *Simultaneous Cooling-Microwave Heating synthesis of AgNCs@SBA-15*

A cross section of the set-up adopted was schematically reported in Figure 5.1 a. The reactor was formed by two coaxial cylinders, an external Teflon® tube (O.D. 24.5 mm, I.D. 20.7 mm) and an inner coaxial cylinder made of Pyrex (O.D. 16.4 mm, I.D. 13.3 mm), indicated by numbers 1 and 3 in Figure 5.1 b. The annular space between them was occupied by ice (number 2 in Figure 5.1 b). The system was precisely fixed in the centre of the open vessel CEM Microwave Discover® Cavity, immediately before the irradiation, and a thermographic camera (Optris PI-400038T900)

recorded the temperature profile on the top surface. The emissivity of each material was considered for the temperature evaluation (ε_{Teflon}=0.85, ε_{Ice}0.98, ε_{Pyrex}=0.92 and ε_{SBA}=0.79).

100 mg of amino-functionalized SBA-15 (synthesis procedure detailed in chapter 3) were located in the central volume of the inner tube (number 4 in Figure 5.1 b) and were impregnated by 400 µL of fresh precursors' mixture (50 mM of $AgNO_3$ and 20 µL of Na-PAA Sigma Aldrich MW 1,200, 45 wt.% in water). After a vigorous stirring for 30 s to assure a homogeneous impregnation, the sample was MW irradiated for 17 s, heating selectively the water-based precursors located at the ordered pores of SBA-15 and in-situ activating the nucleation-growth mechanism (Figure 5.1 b). The liquid water-based precursors were the preferential microwave absorber material of the set-up presented, as demonstrated by the comparison of the loss tangent which is 0.157 for liquid water while lower than 0.005 for the remaining materials (Figure 5.1 c). The CEM Discover® manual recommended a maximum power of 50 W for the heating of 35 mL vessel of low absorber materials to limit the energy reflected back to the magnetron. Considering the small absorbent volume of the set-up (the brown area in Figure 5.1 a), containing a small volume of water the working power was set at 20 W. The short-time of the entire process (lower than 5 minutes) allowed the use of ice-water, as the defrosting effect may be neglected. However, commercial solutions may guarantee longer reaction times with the integration of higher expensive systems based on the use of liquid Nitrogen or dry-ice as cooling medium[247].

As the MWs were switched-off, the ice-water immediately cooled the reactor, generating a quenching effect. After synthesis, the catalyst was washed by centrifugation at 12,000 rpm for 20 minutes with distilled water and finally dried at 50 °C overnight. The sample was covered with aluminium foil and stored at 4 °C for 12 months. The sample was identified as SCMWH-AgNCs@SBA-15, where SCMWH stayed for Simultaneous Cooling-Microwave Heating.
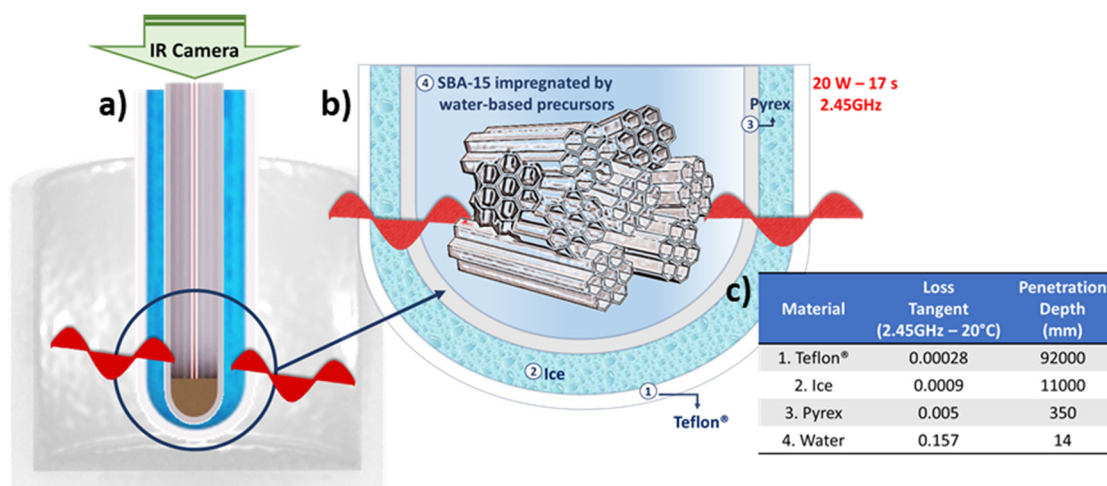
Figure 5.1 a) Cross section of simultaneous cooling microwave heating reactor in the commercial CEM Microwave Discover® Cavity. In detail b) a schematic representation of the different zones of the reactor and c) the relative penetration depth at 2.45 GHz and 20 °C[114,116].

5.2.2. *Scale-Up Analysis: Synthesis of AgNCs@PAA-C*

For the scalability of the synthesis procedure, a cheaper commercial non porous substrate with high surface area, Vulcan XC-72 (Cabot – USA), was adopted. Firstly, the substrate was functionalized directly with PAA. 1 g of Vulcan XC-72 was dispersed in 10 mL of deionized water under ultrasound irradiation for 5 minutes. Then, it was covered with aluminium foil and 1.2 mL of Na-PAA Sigma Aldrich MW 1,200, 45 wt.% in water, were drop wised. The mixture was stirred at 1,200 rpm for 1 hour. The ungrafted polymer was eliminated by 3 following centrifugations in water (12,000 rpm for 20 minutes), removing the supernatant and drying the pellet at 50 °C overnight. Finally, the carbon substrate was ground in a ceramic mortar, obtaining the support PAA-C.

For the synthesis of AgNCs@PAA-C, the PAA-C was impregnated with a proper volume of Ag precursor (50 mM $AgNO_3$ water solution) varying the theoretical metal loading from 1 wt.% to 2.15 wt.%, and vigorously stirred for 30 s to assure a homogeneous mixture. The MWH and the washing steps were performed following the same procedure previously described for SCMWH-AgNCs@SBA-15 in section

5.2.1. In the scale-up synthesis, it was possible to measure the longitudinal temperature profile by Neoptix Optical Fiber sensor (range 193-523 K, Ø: 1 mm).

5.2.3. *Versatility Analysis: Cu NCs synthesis on SBA and PAA-C*

The same procedures previously reported to produce Ag NCs were applied for the synthesis of Cu-based catalysts. In detail for the catalysts CuNCs@SBA-15 and CuNCs@PAA-C, 5 mg of $Cu(NO_3)_2 \cdot 3H_2O$ (Sigma-Aldrich) was dissolved in 400 μL of deionized water with the addition of 123 μL of Na-PAA Sigma Aldrich MW 1200, 45 wt.% in water. Then, 100 mg of the catalytic support was loaded in the central volume of the coaxial reactor, following the same procedure as in the case of SCMWH-AgNCs@SBA-15.

5.2.4. *Characterization Techniques*

All the synthesized catalyst AgNCs@SBA-15, AgNCs@PAA-C, CuNCs@SBA-15 and Cu@PAA-C were characterized following the respective procedures reported in chapters 3, section 3.2, and paragraph 3.2.3. All the characterization experiments presented were repeated at least with three different independent experiments, and average results are presented in the following section.

5.2.5. *Catalytic Activity*

The 4-Nitrophenol reduction was adopted as a reference reaction for the comparison of batch, continuous and one-pot techniques. Further details of the method and reaction settings are summarized in chapter 3, section 3.2, and paragraph 3.2.4.

An alternative chemical reaction was also proposed to explore the feasibility of these NCs based catalysts in the production of valuable chemicals. The catalytic activity for C≡C alkynes group was tested by the LOMAC group of KU Leuven. The procedures for propalgylguanidine (substrate 2b of Table 4.4) and 2-(phenylethynyl phenol) cyclization were previously described in chapter 4, section 4.2, and paragraph 4.2.3.

Furthermore, the catalyst SCMWH-AgNCs@SBA-15 was adopted for oxazolidinones synthesis. In oven-dried 10 mL screw-cap vial propargylic amine (0.24 mmol), DBU (20 mol%) and Ag NCs (1 mol%) were suspended in 0.01 M of different solvents (Toluene, DCE or DMSO). The reaction mixture was placed in a preheated oil bath under CO_2 environment by using a balloon. After 3 h of heating at 50 °C, the mixture was diluted with EtOAc and filter through a syringe filter (Chromafil – PET 0.2 μm). The solvent was evaporated and crude product was purified by column chromatography on silica (EtOAc : Heptane = 1 : 6 to 1: 4) . The final product was characterized by ^{1}H (400 MHz or 600 MHz) and ^{13}C (100 MHz) NMR.

5.3. **Results and Discussions**

5.3.1. *Characterization of SCMWH-AgNCs@SBA-15*

The AgNCs were in-situ synthesized directly on the mesoporous substrate of SBA-15. Once the microwaves were switched on, a fast localized heating was experimentally observed by IR mapping (Figure 5.2 a). According to IR mapping, a maximum temperature of (16.8±3.2) °C was achieved after 15 s of irradiation (average T of the circular area indicated by a red rhombus in Figure 5.2 c.). The ice-shell, the Teflon® and the pyrex were not affected by the electromagnetic radiation, as confirmed by the respective stationary temperature profiles in Figure 5.2 b. As the microwaves were switched off, the system rapidly cooled down reaching a temperature of (5.7±1.1) °C at t= 60 s.
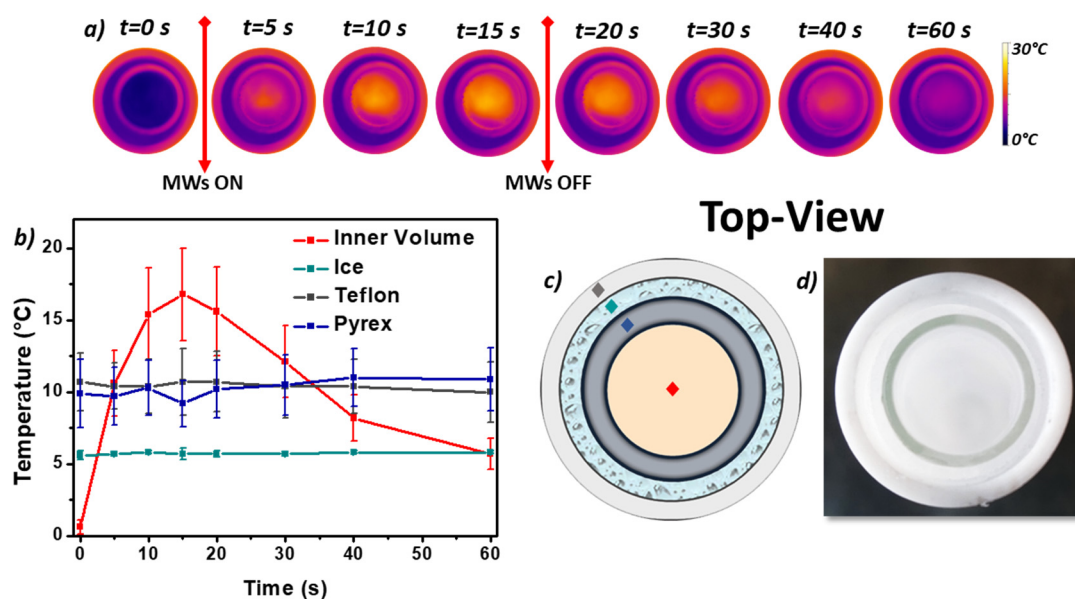
Figure 5.2 a) IR thermographs of the top surface of the reactor. b) and c) temperature profile and schematic representation of the reactor made by inner volume (in red), ice (in green), Teflon® (in grey) and pyrex (in blue). d) In the optical inset, the top view of the reactor.

Comparing the resulting nanomaterials with previous batch and continuous methods, the differences in the heating/cooling patterns were reflected in a variation of the size distribution. The batch catalyst B-AgNPs@SBA-15 presented an average size of (1.5±0.3) nm with few particles of bigger dimensions (Figure 5.3 a and d) representing a percentage smaller than 2% of the total particles. The distribution improved with the dual step continuous flow reactor, C-AgNCs@SBA-15, halving the relative size deviation thanks to the higher control of the heating and quenching steps[248]. Even so, the higher temperature of the heating step, considering that the average of the temperature during the overall residence time was (71.7±8.7) °C, promoted the clusters growth with a final diameter of (1.4±0.2) nm (Figure 5.3 b, e and h). The simultaneous cooling microwave heating protocol allowed to obtain a particle size distribution with a final size of (1.1±0.3) nm (Figure 5.3 c, f and i), 27% lower than batch and continuous ones.

Furthermore, the catalysts presented higher synthesis yield and density of anchored clusters. Although the same theoretical metal was loaded (2.15 wt.%), the catalyst SCMWH-AgNPs@SBA-15 presented double load of Ag compared to batch and

continuous methods, as confirmed by MP-AES quantification in Table 5.1. The loading yield was lower than 50% for the impregnation method, while higher than 80% for the in-situ synthesis, without undesired particles growing. The increase of the density of anchored clusters could be observed in the HAADF-STEM images (Figure 5.3) and may favour the contact between the active site and the molecules of interest[67]. However, a critical equilibrium exists between high metal loading and the quality of the sub-nanometer nanoclusters[249]. Haruta et al.[250] reported a higher 90% loading yield by solid grinding method, but compared to SCMWH-AgNCs@SBA-15 the final product presented a size deviation higher than 50%, the minimum size obtained was (1.8±0.9) nm and the maximum loading of 1 wt.%. Then, from an economical and environmental point of view, the loss of high expensive silver precursors and the required amount of SBA-15 support were both reduced. Similar results, in the same loading range (1-2 wt.%), were obtained by higher-expensive techniques, such as chemical vapour deposition[251], H_2 cold plasma[77] or laser pyrolysis[78].

Table 5.1: Metal loading, synthesis yield, textural properties and oxidation state of the catalysts designed.

Catalyst	Ag Load. wt.%	Load. Yield (%)	S_{BET} (m²g⁻¹)	V_t (cm³g⁻¹)	D_{BJH} (nm)	Ag^0	Ag^{+1}
SBA-15	-	-	317	0.89	9.3	-	-
B-AgNPs@SBA-15	0.98±0.05	43-48	266	0.76	8.6	45%	55%
C-AgNCs@SBA-15	0.96±0.07	41-48	255	0.59	9.2	50%	50%
SCMWH-AgNCs@SBA-15	1.80±0.08	80-87	245	0.69	9.2	49%	51%
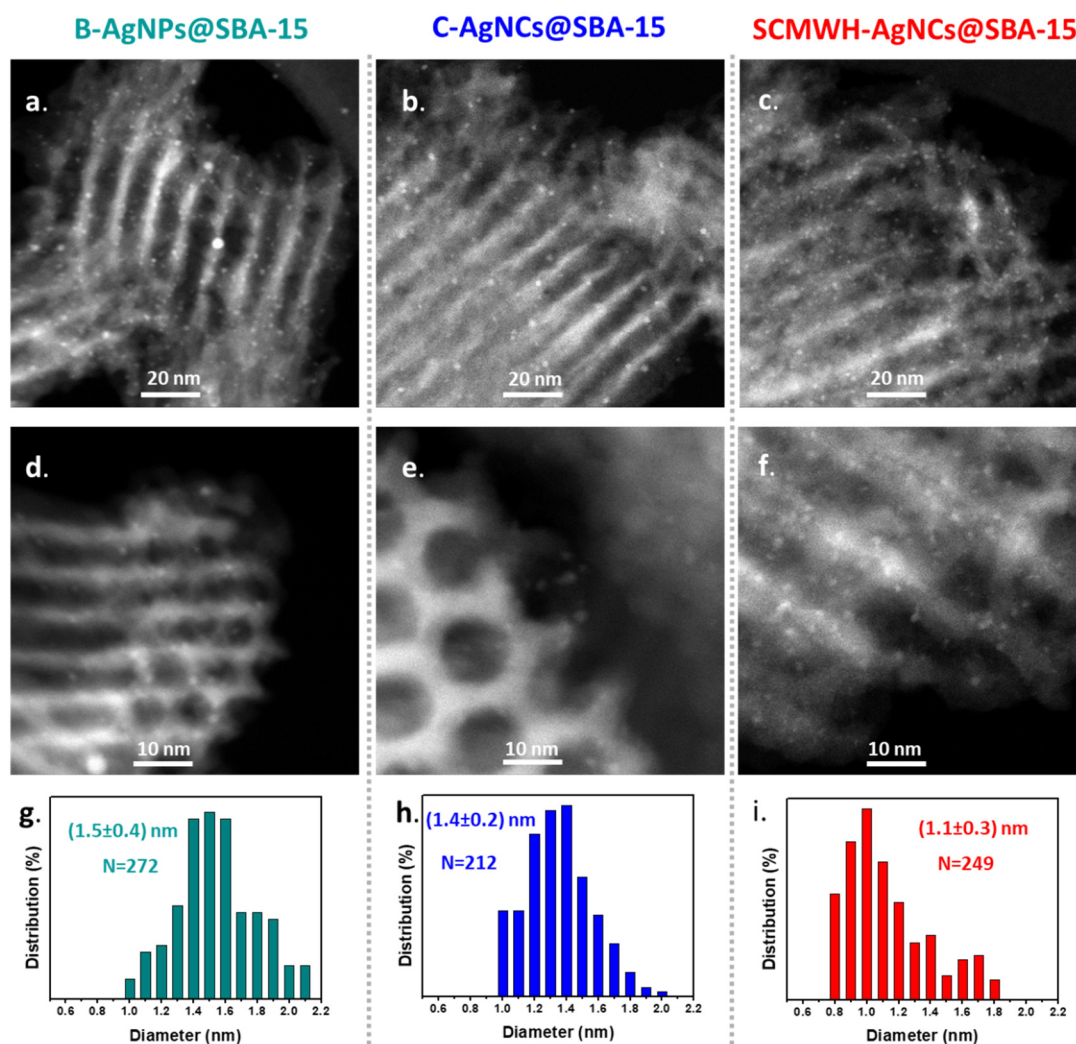
Figure 5.3 HAADF-STEM analysis of the three different nanocatalysts, B-AgNPs@SBA-15 (on the left – green color) and C-AgNCs@SBA-15 (in the center– blue color) and SCMWH-AgNCs@SBA-15 (on the right – red color). In figures a, b, and c it is possible to highlight the uniform distribution of silver NPs/NCs along the entire surface of SBA-15 rods. In figures d, e, and f a detail of the entrance of the pores, without evident sign of pore obstruction. In figures g, h, and i the relative size distribution.

Interesting results were also obtained by N₂ adsorption analysis, in Table 5.1 and Figure 5.4. For the catalyst B-AgNCs@SBA-15, the 8% reduction of the pore width (Figure 5.3 a) and the slight variation of the pore volume (15%) confirmed that the majority of the nanoclusters were deposited over the external surface of the SBA channels, and that large agglomerates may partially reduce the pore accessibility, in accordance with microscopy analysis (Figure 5.3 a and d). On the contrary, for the catalyst C-AgNCs@SBA-15 the total pore volume decreased by 33% due to a

high deposition of the smaller clusters inside of the mesopores. In fact, a dual-size distribution of the pores was observed: unvaried 9.2 nm and smaller 3.2 nm width-channels, (see Figure 5.3 b). In the case of catalyst SCMWH-AgNCs@SBA-15 the clusters were distributed also inside and outside of the channels (24% pore volume decrease). However, thanks to the smaller diameter of the metallic nanoclusters the pore obstruction was lower as confirmed the pore width analysis (monodistribution at 9.2 nm).

Finally, the effect of the synthesis procedure on the oxidation state were determined, as reported in Figure 5.4 and Table 5.1. The XPS analysis confirmed that the small Ag nanoclusters presented an inner Ag(0) core surrounded by uncoordinated Ag(I) ions stabilized by electrostatic interactions with the PAA template, without relevant variation between them.
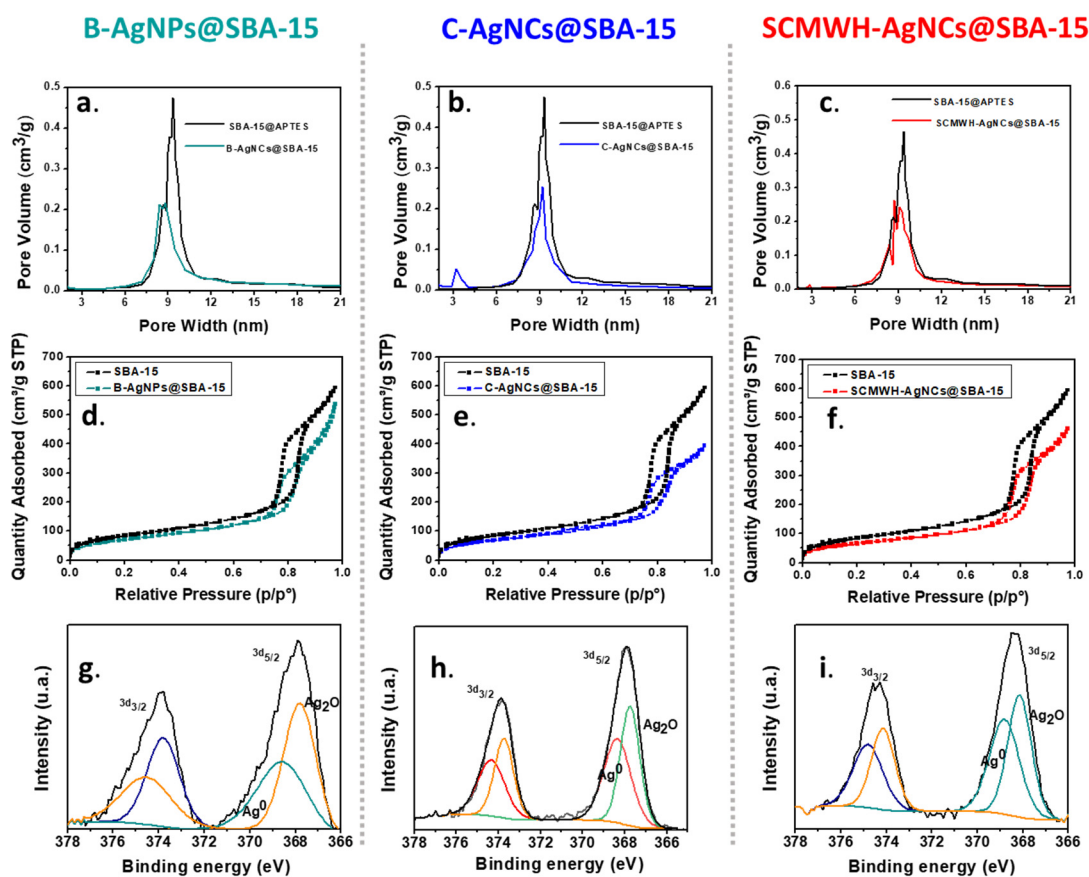
Figure 5.4 N_2-adsoprtion and XPS analysis for B-AgNCs@SBA-15 (a, d and g), C-AgNCs@SBA-15 (b, e and h) and SCMWH-AgNCs@SBA-15 (c, f and i).

The catalyst SCMWH-AgNCs@SBA-15 presented a high concentration of sub-2nm clusters, homogeneously dispersed inside and outside of the SBA-15 channels, even after 12 months of storage (Figure 5.5). Few agglomerations, less than 11% of the total particles counted, presented a diameter higher than 2 nm due to slow and uncontrolled Ostwald ripening mechanism[6]. Then, the heterogenization may both guarantee the reusability of the nanocatalyst and increase its stability[252].
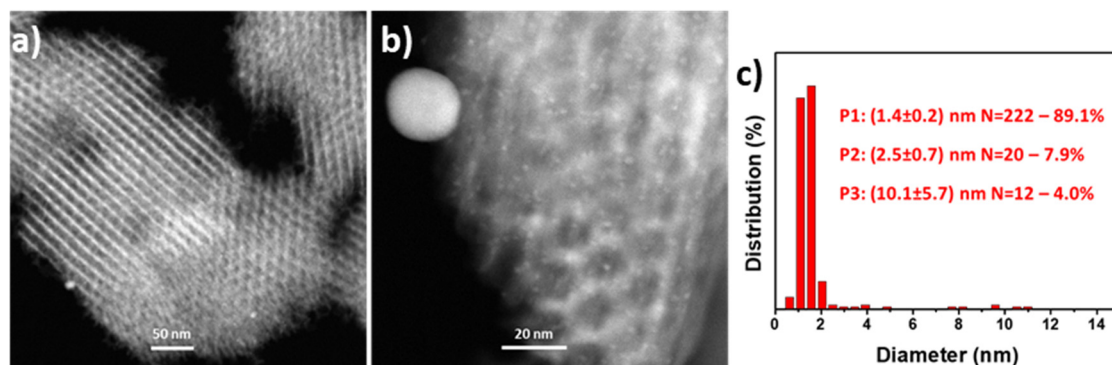
Figure 5.5 a) and b) HRSTEM and c) size distribution of catalyst SCMWH-AgNCs@SBA-15 after one year of storage, characterized by the presence of three size-populations.

5.3.2. *Comparison of Catalytic Activity: 4-Nitrophenol Reduction*

As underlined by Maschmeyer et al.[176], the 4-Nitrophenol reduction in aqueous solution is widely reported as a reference reaction to compare different nanocatalysts. Table 5.2 presents a summary of the pseudo-first order kinetic constant reported for several Ag based catalysts, ranging from silver nanowires to NPs and NCs, together with the NCs prepared by different methods in this thesis. The Ag nanowires in-situ generated by Kong et al.[206] presented a very low activity, which may be correlated to the partially pore obstruction and the low surface to volume ratio of nanowires if compared with smaller spherical nanoparticles (entries 1-4 of Table 5.2). The activity strongly improved for small silver nanoparticles with an average diameter of 7 nm, where the kinetic constant increased up to $1.56 \cdot 10^{-3}$ s$^{-1} \cdot$L$\cdot$mg^{-1} (entry 5 of Table 5.2)[199]. A further increase of the catalytic activity was observed when the particles diameter was smaller than 2.1 nm, observing the same kinetic order of the small nanoclusters here produced (Table 5.2 entries 10-12)[200]. No

relevant differences were observed between batch and continuous catalysts, confirming that the minimum variations in clusters size may not be considered the discerning parameters.

The catalyst SCMWH-AgNCs@SBA-15 with a kinetic constant of $(15.98\pm0.42)\cdot10^{-3}$ $s^{-1}\cdot L\cdot mg^{-1}$ is more than 2 times higher than B-AgNPs@SBA-15 and C-AgNCs@SBA-15. The density of anchored clusters represented a critical aspect. As confirmed by Lin et al.[200], the higher is the loading density, the higher is the probability of contact between the 4-nitrophenolate, the hydrogen and the metallic surface. The catalyst SCMWH-AgNCs@SBA-15 presented a kinetic value close to the entries 7 and 8 of Table 5.2, obtained by 2.1 nm-AgNPs with a metal loading of 2.6-3.0 wt.%. By Langmuir−Hinshelwood (LH) model, the higher activity of SCMWH-AgNCs@SBA-15 may be explained by the faster adsorption/desorption on closest Ag active sites and the shorter diffusion distance required for 4-nitrophenolate ions to interact with H_2 at the Ag catalytic surface[211].

Table 5.2 A summary of Normalized Kinetic Constant for the reduction of 4-NP catalysed by Ag nanowires, Ag nanoparticles and Ag nanoclusters at different metal loading.

Entry	Sample	Ag Morphology	Ag Loading (wt.%)	K ($s^{-1}\cdot L\cdot mg^{-1}$)
1	0.7Ag-SBA-15 [206]	Nanowires	9.26	$2.27\cdot10^{-5}$
2	0.5Ag-SBA-15 [206]	Nanowires	7.89	$2.17\cdot10^{-5}$
3	0.3Ag-SBA-15 [206]	Nanowires	6.52	$1.73\cdot10^{-5}$
4	0.1Ag-SBA-15 [206]	Nanowires	5.45	$1.53\cdot10^{-5}$
5	Ag10@SBA-15 [200]	NPs-7 nm	10	$1.56\cdot10^{-3}$
6	MSAg-50 [200]	NPs/NCs (< 2.1 nm)	3.5	$33.71\cdot10^{-3}$
7	MSAg-70 [200]	NPs/NCs (< 2.1 nm)	3.2	$19.06\cdot10^{-3}$
8	MSAg-90 [200]	NPs/NCs (< 2.1 nm)	3	$15.70\cdot10^{-3}$
9	MSAg-110 [200]	NPs/NCs (< 2.1 nm)	2.6	$15.38\cdot10^{-3}$
10	B-AgNPs@SBA-15	(1.5±0.4) nm	(0.98±0.05)	$(7.90\pm0.58)\cdot10^{-3}$
11	C-AgNPs@SBA-15	(1.4±0.2) nm	(0.96±0.07)	$(6.70\pm0.22)\cdot10^{-3}$
12	SCMWH-AgNPs@SBA-15	(1.1±0.3) nm	(1.80±0.08)	$(15.98\pm0.42)\cdot10^{-3}$

After 8 cycles, as reported in Figure 5.6 h, the kinetic activity decreased by 43%, 25%, and 17% respectively for SCMWH-AgCs@SBA-15, B-AgNPs@SBA-15 and C-AgNCs@SBA-15. The drop in the activity may be mainly due to a gradual inevitable loss of catalyst during the recovery process by centrifugation, as previously reported also by Fu et al.[253]. The hypothesis was experimentally verified by the evaluation of the catalytic activity of SCMWH-AgCs@SBA-15 after 7 consecutive centrifugations in deionized water, reporting a kinetic constant of $10.41 \cdot 10^{-3}$ $s^{-1} \cdot L \cdot mg^{-1}$, 35% lower than the initial value. Furthermore, the effect of gradual loss of the catalyst in the recovering step may be higher for the catalyst SCMWH-AgNCs@SBA-15 compared to B-AgNPs@SBA-15 and C-AgNCs@SBA-15 catalysts, due to difference in terms of metal loading.
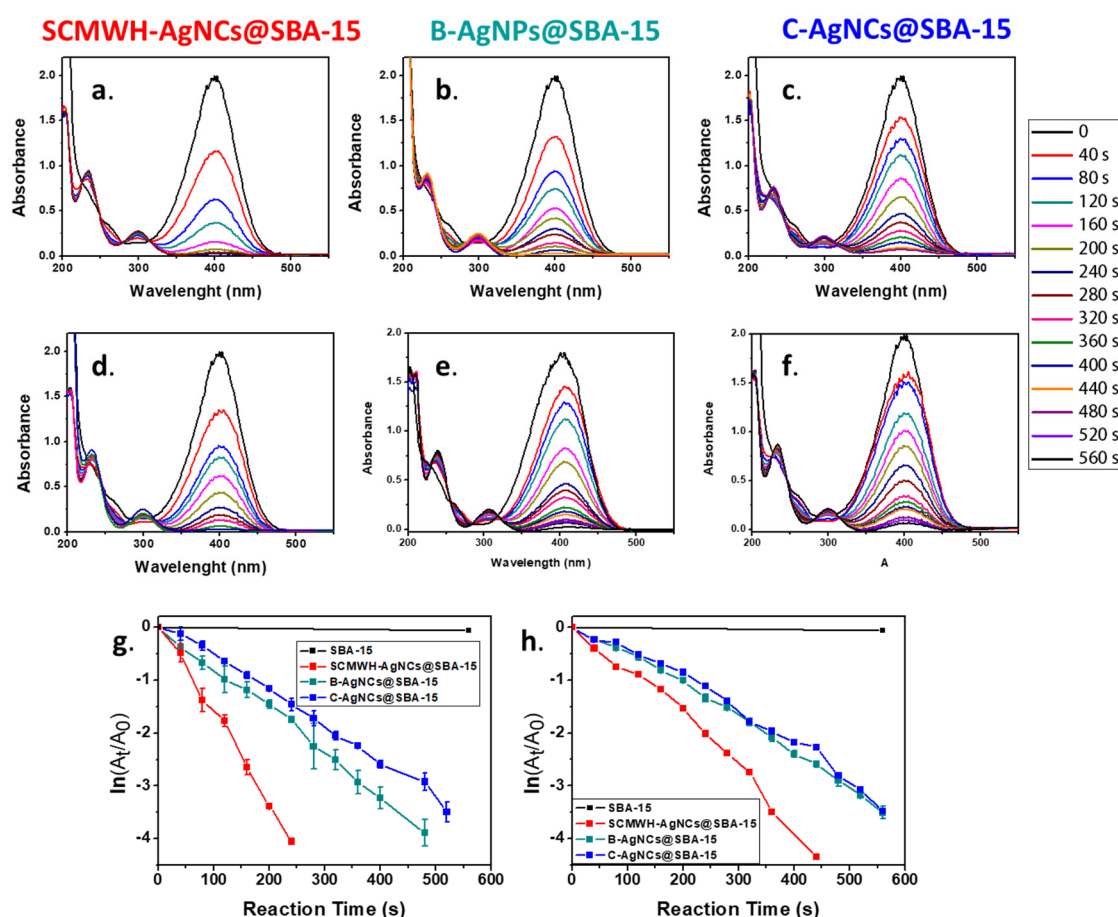
Figure 5.6 UV-Vis spectrophotometer 4-Nitrophenol reduction study for different catalysts at cycle 0 (a, b and c) and cycle 8 (d, e and f). Kinetic analysis at cycle 0 and cycle 8, g and h respectively. All the measurements were performed with the addition of 1 mg/L of Ag concentration.

5.3.3. *Catalytic Activity: Alkynes Cyclization*

In a following step, the catalytic activity of SCMWH-AgNCs@SBA-15 for a wide range of alkynes cyclization reactions was studied in collaboration with the LOMAC group of KU Leuven. For substrate 2 b of Table 4.4 the catalyst C-AgNCs@SBA-15 presented a maximum yield of 50% after 3 h at 50 °C (silver content 0.3 mol.%). Referring to the previous work of Stratakis[254] and LOMAC group[255] this was predictable due to the sterically hindered substituents on the internal triple bond. By the use of SCMWH-AgNCs@SBA-15, the yield was enhanced up to 73%, Table 5.3 entry 1. For catalyst C-AgNCs@SBA-15, the cluster-cluster distance was of around (6.1±2.1) nm with 0.011 NCs per nm², while for catalyst SCMWH-AgNCs@SBA-15 it was 26% smaller (0.026 NCs per nm²) possibly favouring the interaction of alkyne bond with Ag and then the catalytic reaction. In accordance with Fang et al.[256], the main challenges of sub-2 nm heterogeneous catalysts preparation are the control of size distribution and the increase of metal loading, with the possibility to observe synergic interactions between closer active sites.

Table 5.3 Propargylguanidine cyclization (substrate 2b of Table 4.4), catalyzed by SCMWH-AgNCs@SBA-15.
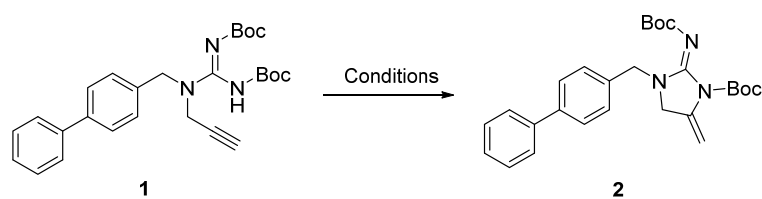
Entry	Mol % Ag	Solvent	Temp (°C)	Time (h)	Yield (%)
1	0.3	DCM	50	3	73
2	0.5	DCM	50	3	94

The dual nature of Ag NCs (Ag(0)/Ag(I)) resulted particularly active for the cyclization of 2-(phenylethynyl)phenol in contrast to silver salts or big nanoparticles (Table 4.5). The catalyst was still active after one year of storage, with a yield decrease lower than 4%, as it is depicted in Figure 5.7 (t=450 s). Furthermore, the

heterogeneous catalyst SCMWH-AgNCs@SBA-15 was approximately 3.5 times more active than homogeneous catalytic conditions, which were performed at 80 °C with 1.0 mol% of Ag. The excellent catalytic results, the reusability and the long-time stability of the catalyst are key-aspects for its industrial potential application.
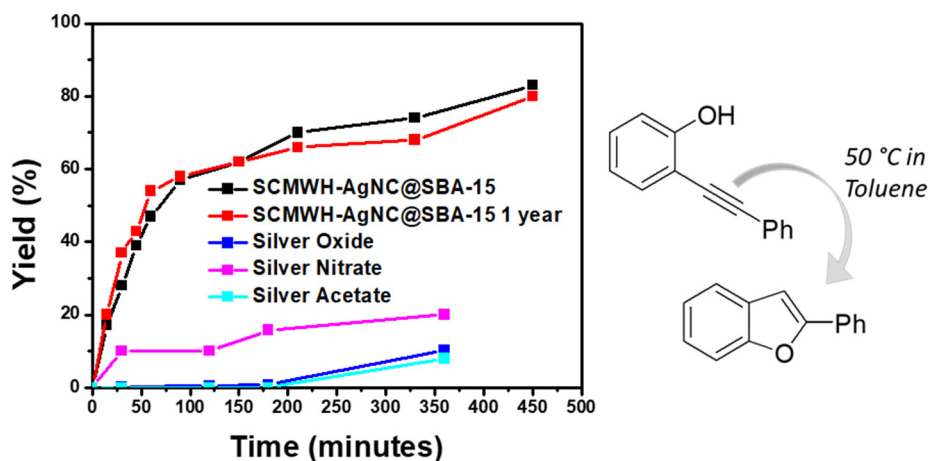
Figure 5.7 Test of long-time stability of the catalytic activity of SCMWH-AgNCs@SBA-15 (1.5 mol %) for cyclization of 2-(phenylethynyl)phenol.

To conclude, Ag NCs were adopted for the synthesis of Oxazolidinone in the presence of CO_2, firstly reported in literature for Ag salts by Yamada in 2009[257]. As reported in Scheme 5.1, the synthesis of Oxazolidinones required both the presence of 1,8-diazobicyclo undec-7-ene (DBU) to trap the CO_2 and Ag catalyst to activate the triple bond of propargylic amine[258]. Entries 1 and 6 of Table 5.4 confirmed the dual-constituent nature of the reaction mechanism[258].

Scheme 5.1: Reaction mechanism of Oxazolidinones synthesis by CO_2 capture[258,259].
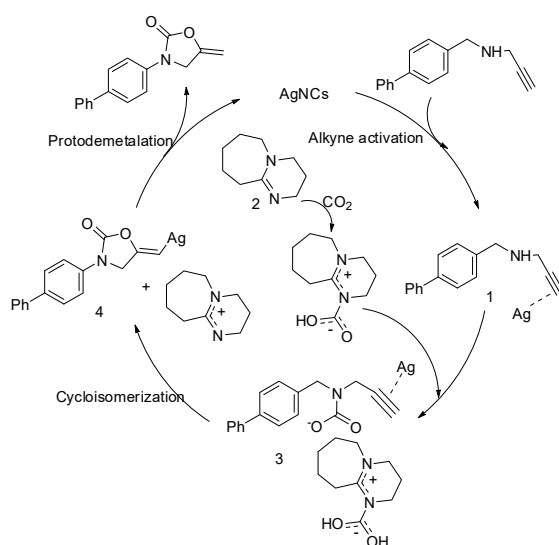
The optimum reaction conditions are presented by entry 5, reporting a yield of 94% after 3 hours at 50 °C with 0.5 mol.% of Ag and 0.2 equivalents of DBU. This resulted in 13 hours time-reduction compared to homogeneous data[258] (AgO_2 yield of 92% after 16 hours with 0.5 mol% of Ag). Long reaction time was required for $AgNO_3$ (95% - 20 h) and AgOAc (90% - 18 h). On the contrary, Ag NPs of 20-35 nm supported on covalent organic frameworks (COF)[259] presented a slight better result with a yield of 95% after 3 hours at RT, adopting a molar concentration 24 times higher than silver clusters catalyst. In both cases, the supporting of the catalysts allowed the easy recovery of the catalysts and their reuse. The reaction time was reduced to 30 min by 10 mol.% of high precious Pd nanoparticles of 6 nm stabilized on porous organic polymer (T_r = 80 °C)[260]. On the opposite side, 12 hours were required to 95% - yield with COF@Cu nanoclusters (39 mol.%)[261], confirming that silver may still cover the gap between low active copper and expensive palladium solutions.

The substrate scope, reported in Table 5.5 evidenced the versatility of the mechanism proposed, observing a lower yield (66%) exclusively for substrate 2d. The results are in accordance with previous substrate scope reported in Table 4.4

for propalgylguanidines, confirming that polymethylpentene (2c-PMP) and benzyl (2d-Bn) groups obstaculate the interaction with Ag clusters.

Table 5.4 Optimization of synthesis of Oxazolidinones via CO_2 capture catalysed by SCMWH-AgNCs@SBA-15 with the different concentration of DBU additive.
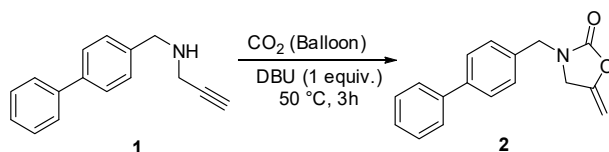
Entry	Mol % Ag	Additive	Solvent	Temp. (°C)	Time (h)	Yield (%)
1	-	DBU (1equiv.)	DCE	50	3	0
2	1	DBU (1equiv.)	DCE	50	3	94
3	0.5	DBU (1equiv.)	DCE	50	3	94
4	0.5	DBU (0.5 equiv.)	DCE	50	3	94
5	0.5	DBU (0.2 equiv.)	DCE	50	3	94
6	0.5	DBU (0 equiv.)	DCE	50	3	13

[a]Reaction conditions: All reaction were run with 1 (0.12 mmol) in the indicated solvent (1.2 mL) in a screw cap vial. Yield were determined by the NMR-integration method using 1,3,5-trimethoxybenzaldehyde as an internal standard.

Table 5.5 Substrate scope for Oxazolidinones synthesis.

Product no.	Product	Time (h)	Temp. (°C)	Yield (%)
2a		3	50	99
2b		3	50	90
2c		3	50	80
2d		3	50	66
2e		3	50	99

5.3.4. *Scalability Analysis: Synthesis of AgNCs@PAA-C*

SBA-15 and Vulcan XC-72 substrates are characterized by a different dielectric behaviour. The dielectric tangent of silica substrate is lower than 0.05, which means that the material is almost MW transparent[262]. On the contrary, black carbon is an excellent microwave absorber (tanδ=0.28)[263,264]. This was reflected in a maximum temperature achieved, approximately 2 times higher, for PAA-C 40.3 °C (Figure 5.8 b) compared to SBA-15 (16.8±3.2) °C (Figure 5.2). The high nucleation-growth temperature achieved, was responsible for the different size distribution between previous SCMWH-AgNCs@SBA-15 and AgNCs@PAA-C catalysts, which changed respectively from (1.1±0.3) nm to (1.6±0.3) nm.

In accordance with the previous work reported by Sturm et al.[182], the EM distribution in the commercial CEM Discover® Cavity is not homogenous producing a relevant longitudinal temperature gradient, which was particularly evident for higher sample volumes, Figure 5.8 b, e, h and k. The average particle size progressively decreased as the mass of irradiated catalyst increased from 100 mg ((1.6±0.3) nm) to 500 mg scale ((1.3±0.2) nm), due to the gradual decrease of the synthesis temperature with the maximum temperature 22% lower. However, the longitudinal temperature gradient was particularly evident for 1000 mg where 38% of the reactor volume presented a temperature higher than 15 °C in the central zone, 13% between 10 °C and 15 °C, while for approximately 50% the temperature was lower than 10 °C as reported in Figure 5.8 k. In this case, more than 95% of the clusters nucleated presented a size smaller than 1 nm due to the lower synthesis temperature, but the heterogeneity of the nucleation was responsible for agglomerates of 4-5 nm and a metal loading deviation of 21%, as clearly visible in Figure 5.8 l and Table 5.6.

Regarding the carbon substrate, the maximum loading was of approximately 1 wt.% with a loading yield of 93.2%, as confirmed by Table 5.7. Wang et al.[265] presented a large scale production of single-atom catalysts with the production of 1.5 kg of

carbon-based catalyst every 2 hours of pyrolysis at 600 °C under an Argon atmosphere. In this work, considering the production volume of 500 mg and an average time of 5 minutes between each synthesis, the simultaneous cooling microwave heating method may produce up to 4 g per hour.

Table 5.6 Metal loading and size distribution for different scales of simultaneous cooling-microwave synthesis of AgNCs@PAA-C catalysts.

Sample	Metal Loading (wt.%)	Size Distribution (nm)
AgNCs@PAA-C_100mg	0.96±0.04	1.6±0.3
AgNCs@PAA-C_200mg	0.96±0.05	1.4±0.3
AgNCs@PAA-C_500mg	0.93±0.07	1.3±0.2
AgNCs@PAA-C_1000mg	1.02±0.22	0.9±0.3

Table 5.7 Maximum metal loading analysis.

Sample	$[Ag]_{th}$ (wt.%)	$[Ag]_r$ (wt.%)	Loading Yield (%)
AgNCs@PAA-C_2.16	2.16	0.96± 0.04	44.5
AgNCs@PAA-C_1.50	1.50	0.97± 0.07	64.4
AgNCs@PAA-C_1.00	1.00	0.93± 0.01	93.2
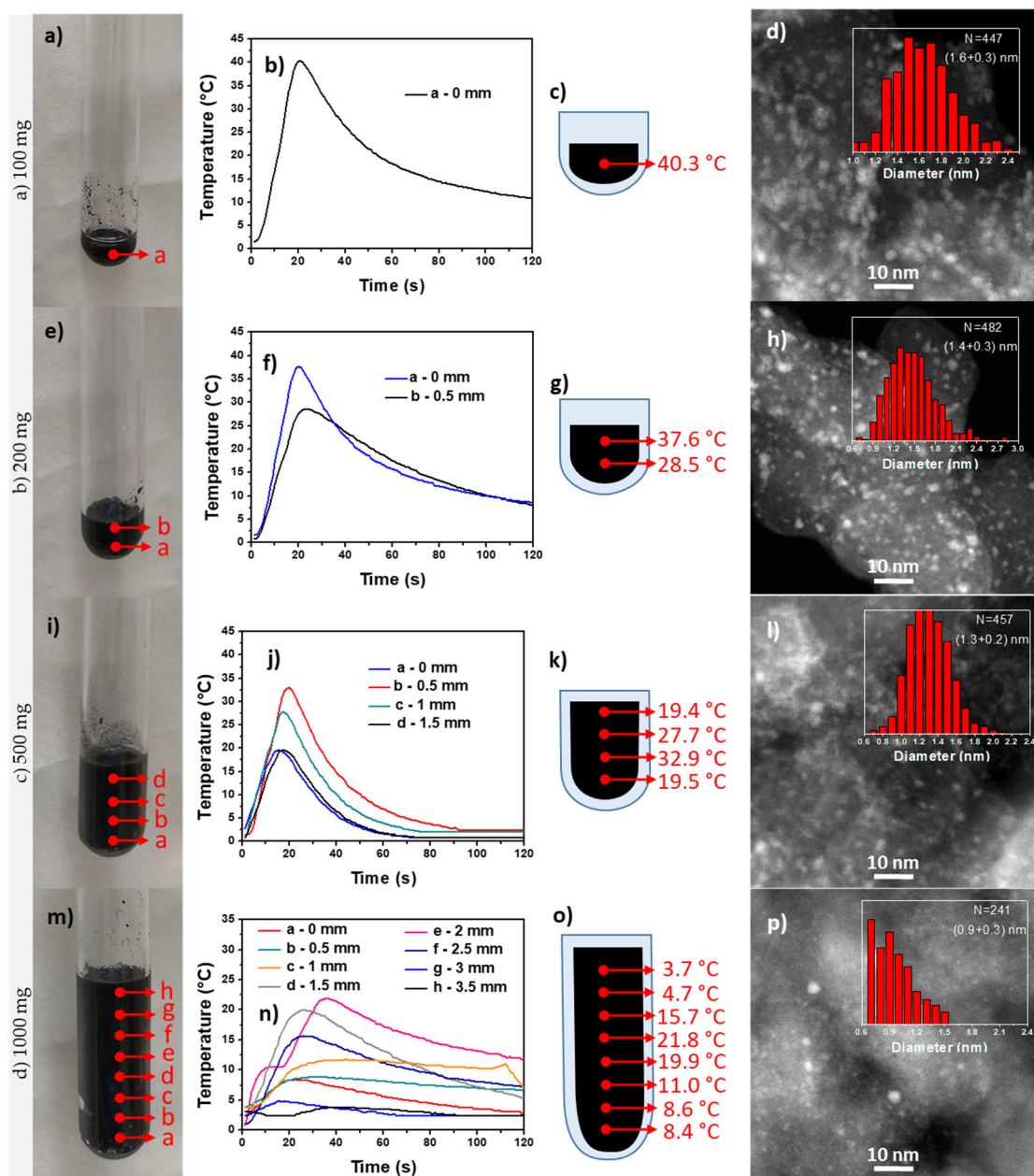
Figure 5.8 Optical inset, temperature profile, longitudinal maximum temperature measured by an optical fiber in different positions and HAADF-STEM size distribution for 100 mg (a, b, c and d), 200 mg (e, f, g and h), 500 mg (i, j, k and l) and 1000 mg (m, n, o and p).

5.3.5. *Versatility Analysis: Synthesis of CuNCs@SBA-15 and CuNCs@PAA-C*

Finallly, this PhD thesis has intended to validate the versatility of the one-pot procedure by the production of clusters made of other type of metal than Ag. One of the main challenges is the synthesis of highly stable and small Cu(I)/Cu(0) nanomaterials. Kawasaki's group[266] reported the microwave-assisted synthesis of 2 nm of Cu(I)/Cu(0) NCs, obtained after 30 minutes of MW irradiation and a

maximum synthesis temperature of 185 °C in inert atmosphere. On the opposite side, Vilar-Vidal and coworkers[267] synthesized aggregates of stable and small Cu NCs of (0.61±0.13) nm which presented a core-shell structure, with a thin layer of Cu(II) ions over the external surface. By the use of simultaneous cooling-microwave heating reactor, both situations were observed. For the SBA-15 substrate, Cu NCs smaller than 1.5 nm were homogeneously distributed over the silica surface (Figure 5.9 b). The detection of Cu clusters on SBA-15 functionalized surface was achieved using the HAADF detector, since the contrast is approximately proportional to square of atomic number of the elements. EDS analysis confirmed a uniform distribution of the metallic clusters over the entire surface of the mesoporous substrate, Figure 5.9 a and c. The pore volume and the surface S_{BET} decreased respectively of 22% and 3.5% but the final pore diameter was 8.1 nm, which assured the accessibility of the mesoporous channels for heterogeneous catalytic applications (Figure 5.9 h and i). No Cu(II) satellites were detected by XPS analysis (Figure 5.9 g). This insight is in accordance with the recent results reported by Abiraman et al.[268] of unsupported sub-1 nm Cu(I)–NCs stabilized by PAA template. On the other hand an evident Cu(II) satellite peak was observed for CuNCs@PAA-C catalyst (Figure 5.9 g), which presented 23% of Cu oxidized. The presence of approximately 14% of particles in the range (1.5-2) nm, transition size between quantum and metallic regime, and the lower interaction with PAA, which was wrapped over the carbon surface reducing its mobility, may be responsible for the higher oxidation rate.
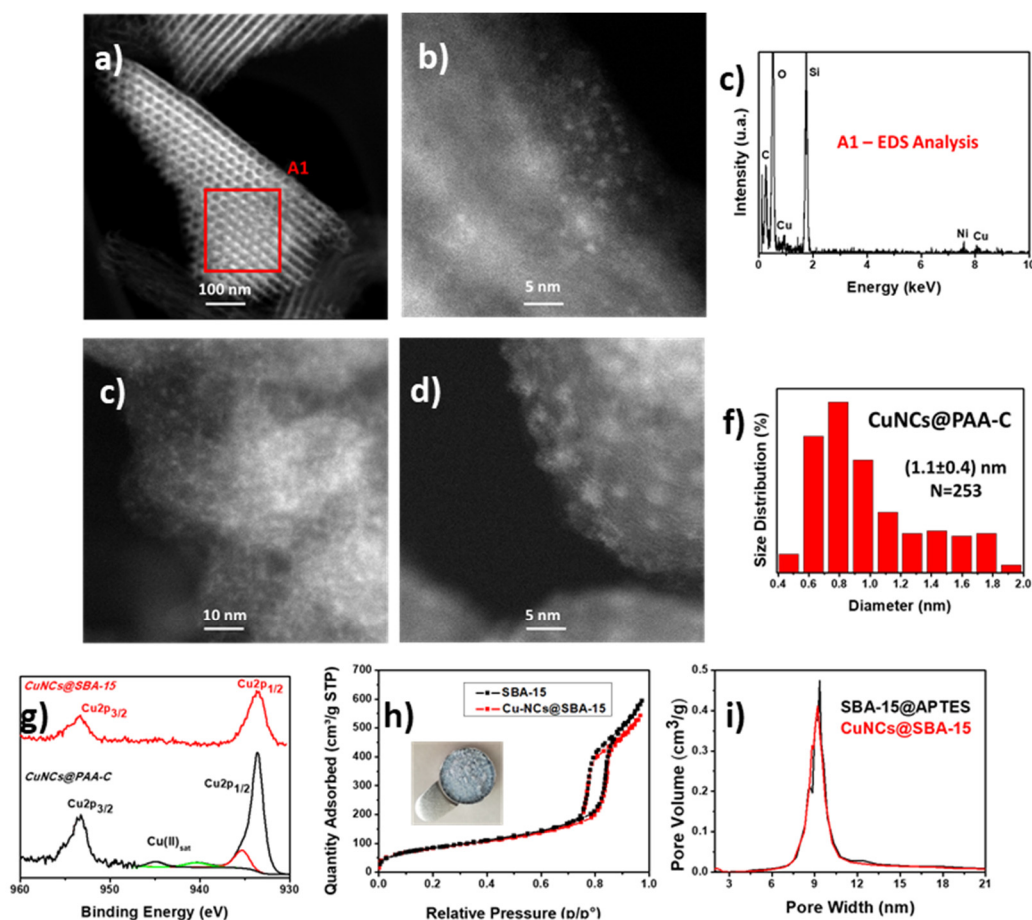
Figure 5.9 a) HAADF-HRSTEM analysis of CuNCs@SBA-15 with the selection of an area of 4 μm² and (c) its relative EDS analysis. b) CuNCs smaller than 2 nm. c) and d) HRSTEM analysis of CuNCs@PAA-C and f) relative size distribution. g) XPS analysis reported in red the catalyst CuNC@SBA-15 and in black the catalyst CuNCs@PAA-C. h) and i) N₂ adsorption curve for the mesoporous substrate and the CuNC@SBA-15 catalyst. Optical inset with the CuNC@SBA-15 catalyst.

5.4. **Conclusions**

The rapidity and the selectivity of microwave heating have been exploited for the design of a simultaneous cooling-microwave heating reactor. The in-situ nucleation by MW heating and the fast quenching resulted in a lower average synthesis temperature during the synthesis process giving rise to smaller clusters size, (1.1±0.3) nm, 27% lower than batch and continuous ones. Furthermore, the loading yield increased up to 80%, due to the in-situ synthesis combined with smaller particle size. There is no relevant variation of the oxidation state, confirming the copresence of Ag(I) and Ag(0). The cluster-cluster distance was nearly 30% smaller

than catalyst C-AgNCs@SBA-15, which resulted in a faster adsorption/desorption on closest Ag active sites and a shorter diffusion distance, as confirmed by 4-Nitrophenol reduction tests. Furthermore, the use of silver nanoclusters guaranteed high conversion at low temperature, reusability and reduction of the metal amount required for Oxazolidinones synthesis.

The synthesis was scaled-up on commercial Vulcan XC-72 substrate following the same procedure and conditions as SBA-15 support. Due to the higher dielectric loss of carbon, higher temperature was achieved and consequently bigger particle size was obtained. In spite of the non-homogeneous temperature distribution in the MW cavity, clusters smaller than 2 nm were also observed by scaling the production volume up to 500 mg, which means a production of approximately 4 g per hour. A proper design of a MW cavity with homogeneous MW field distribution and consequently temperature distribution would be required for up-scaling the synthesis resulting in smaller and narrower particles size distribution.

Furthermore, the method was easily adapted for the synthesis of different metallic nanoclusters, as confirmed by the production of copper nanoclusters on two different substrates SBA-15 and PAA-C. Thanks to scalability, versatility and long-time stability of high-quality nanocatalysts, the simultaneous cooling-microwave heating reactor may be considered a valid alternative to continuous production of heterogenous catalysts.

BIMETALLIC Ag@Cu NANOCLUSTERS:

In-situ Flow Nucleation

Goal: *How to adapt the continuous flow reactor for the one-pot synthesis of bimetallic Ag@Cu nanoclusters?*
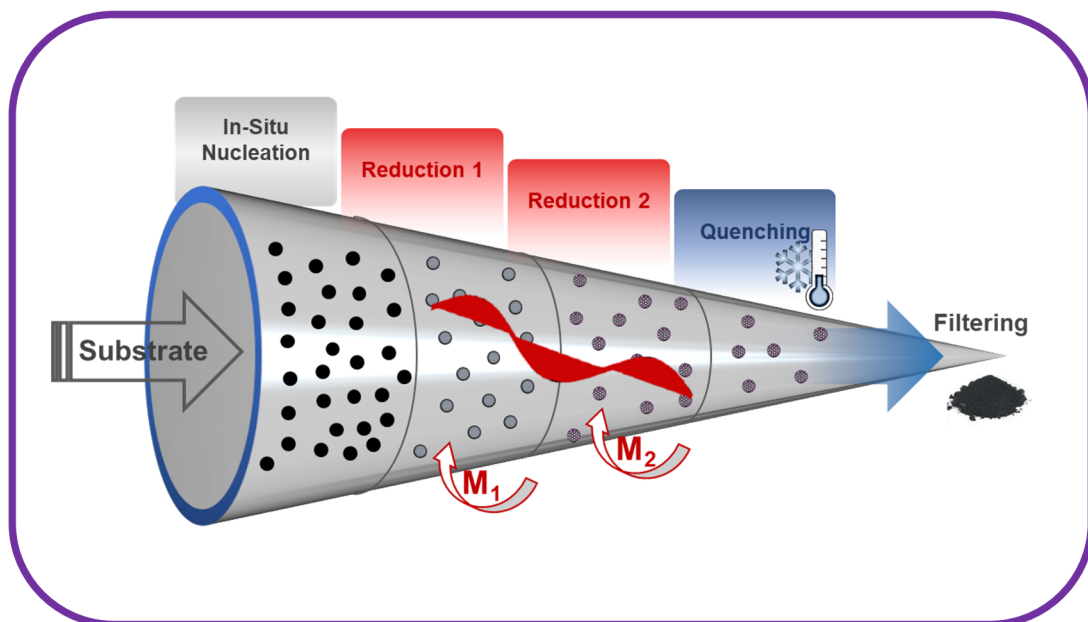
6. BIMETALLIC NANOCLUSTERS: In-Situ Flow Nucleation

6.1. Introduction

Considering that a great challenge for future chemical production is the exploitation of novel catalysts to improve existing ones, in this chapter multielement clusters and in-situ reduction were simultaneously performed in a MW-heated flow reactor. While the progress reported on monometallic structures mainly evidenced the advantages of their size reduction, Feynman's statement of 1959 ("There's Plenty of Room at the Bottom") summarizes the importance of heterometallic systems. Infinite combinations derive from the variation of size, composition and structure[269,270]. Furthermore, the combination of two or more metals does not just result in the sum of their individual properties, as synergistic effects have also been observed[271–274].

Recently, bimetallic Ag@Cu NCs begin to receive increasing attention as the Ag shell may reduce Cu oxidation[275,276], resulting in an increase of photoluminescence[271] and catalytic properties[269,277–279]. Furthermore, copper is earth-abundant (around four orders of magnitude more than Au, Ru or Pt), low cost and environmentally benign[280]. For the production of bimetallic nanosystems, there are two possible synthesis routes: the simultaneous reduction (*co-reduction*) and the dual-step reduction (*galvanic replacement, anti-galvanic replacement, under-potential deposition, thiol etching or re-organization*)[281,282]. Gold and silver atoms are excellent candidates for the co-reduction mechanism, as they possess the same atomic radius (1.44 Å), the same valence electrons ($d^{10} s^1$) and the difference in their potential reduction ($E^0_{Ag+/Ag}$=0.79 eV / $E^0_{AuCl4-/Au}$=1.0 eV) may be partially compensated by the higher affinity of Au for thiolate groups[281,283–286]. On the opposite side, copper atoms are characterized by a smaller radius (1.28 Å) and the differences in bond energies between Cu-Ag and Ag-Ag atoms generate distortions of the geometrical structure. Furthermore, copper is more difficult to be reduced ($E^0_{Cu2+/Cu}$=0.34 eV), resulting in a preferential silver reduction[269,281]. In that case, the galvanic replacement may

represent a valid alternative. In the first step, the metal with the lower potential reduction M_1 was reduced, creating a sacrificial structure. Then, in a sequential step the metal with a higher oxidation power M_2 was added and, through a redox mechanism, the M_1 is oxidized and dissolved in the solution while the M_2 was reduced and deposited over the sacrificial structure[271,287]. Multistage reactions may be easily shifted to continuous flow processes, guaranteeing high control and reproducibility[175288289].

Herein, two sequential reduction stages in a continuous flow reactor for the MW-assisted synthesis of bimetallic Ag@Cu nanoclusters have been proposed. In a preliminary analysis it was evaluated the relationship between residence time and temperature. Then, a colloidal stable suspension of PAA functionalized-Carbon nanoparticles (PAA-C NPs) was adopted to in-situ anchor bimetallic clusters in continuous flow, analysing the effect of different metal loading. According to the literature, the anchoring of nanoparticles to the support is generally performed in a different stage of catalysts manufacturing, to control the active phase morphology and loading[290–292]. On the contrary, the reactor presented includes a fast nucleation, a nearly instantaneous quenching and the simultaneous nucleation-growth directly over the carbon surface.

6.2. **Materials and Methods**

6.2.1. *Dual-Nucleation Stage Reactor for Bimetallic Nanoclusters Synthesis.*

For the in-situ synthesis of bimetallic nanoclusters, the MW continuous flow reactor (see Chapter 4) was modified as schematically reported in Figure 6.1.
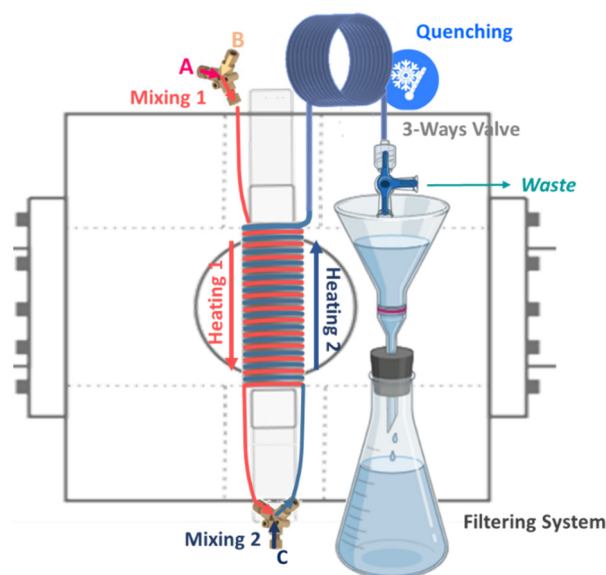
Figure 6.1 Set-up adopted for the continuous flow reactor, which consisted of: Mixing 1 (A+B), Heating 1 (flow downwards), Mixing 2 (addition of C), Heating 2 (flow upward) and Quenching. For reactions with substrate PAA-C, the set-up included a three-ways valve to discard the product of the transitory step and a filtering system to eliminate unreacted metallic salts.

Three different inlets (A, B and C) were considered. The polyacrylic acid (100 μL of Na-PAA Sigma Aldrich MW 1200, 45 wt.% in water, dispersed in 10 mL of D.W.) was always added in inlet B, while inlets A and C were used either for silver (AgNO$_3$, Aldrich 99.9999%, 10 mM in D.W.) or copper (Cu(NO$_3$)$_2$·3H$_2$O, Aldrich ≥ 99%, 10 mM in D.W.) precursors. The entire reactor was made of Teflon® pipe (Teflon®, IDEX Corporation, outer diameter 1/16" and inner diameter 1.016 mm). Precursors A and B were pumped at a certain flow rate by a syringe pump (High precision PHD ULTRA by Harvard Apparatus) and were mixed in a commercial Y-mixer (material PEEK, IDEX Corporation, thru-hole of 0.02'' and swept volume of 1.7 μL). After rapid mixing, the precursors reached the heating zone 1 ($V_{heating,1}$=350 μL). Then, the product of the first nucleation-growth was mixed with precursor C through a second Y-mixer and, consequently, the second nucleation-growth stage occurred ($V_{heating,2}$=350 μL). The two heating zones presented the same geometric parameters but opposite flow directions, as reported in Figure 6.1. The relationship between the residence time, the irradiation power and the mixing order was evaluated, as listed in Table 6.1.

Table 6.1 Preliminary analysis of continuous synthesis of unsupported monometallic and bimetallic nanoclusters. Parameters of study the microwave power and the residence time, distinguishing between heating 1 ($t_{res,H1}$), heating 2 ($t_{res,H2}$) and the sum of them ($t_{res,t}$).

Inlet A	Inlet B	Inlet C	Power (W)	Flow Per Inlet (mL/min)	$t_{res,H1}$ (s)	$t_{res,H2}$ (s)	$t_{res,t}$ (s)
AgNO$_3$	PAA	-	20 – 15 - 10 - 5	0.248	42	28	70
AgNO$_3$	PAA	-	15 - 10 - 5	0.167	63	42	105
AgNO$_3$	PAA	-	10 - 5	0.124	84	56	140
Cu(NO$_3$)$_2$	PAA	-	20 – 15 - 10 - 5	0.248	42	28	70
Cu(NO$_3$)$_2$	PAA	-	15 - 10 - 5	0.167	63	42	105
Cu(NO$_3$)$_2$	PAA	-	10 - 5	0.124	84	56	140
Cu(NO$_3$)$_2$	PAA	AgNO$_3$	20 – 15 - 10 - 5	0.248	42	28	70
Cu(NO$_3$)$_2$	PAA	AgNO$_3$	15 - 10 - 5	0.167	63	42	105
Cu(NO$_3$)$_2$	PAA	AgNO$_3$	10 - 5	0.124	84	56	140

The rectangular microwave cavity previously described in chapter 2 was applied fixing the frequency at 2.45 GHz and varying the applied power, Table 6.1. The temperature profile was recorded by the thermographic camera (Optris PI-400038T900). Immediately outside of the MW cavity, the product was quenched in an ice-bath and directly analysed by UV-VIS spectroscopy.

For the in-situ generation of bimetallic nanoclusters, the substrate PAA-C (preparation procedure in chapter 5, section 5.2, and paragraph 5.2.2) was dispersed in D.W. (1 mg/mL), and introduced at inlet B. The concentration of copper (inlet A) and silver (inlet C) precursors were varied as indicated in Table 6.2, while the residence time and the MW power were fixed at 70 s and 5 W respectively. The solution was collected once the temperature profile was stabilized, eliminating the initial volume by a three-way valve, and the final product was in-line vacuum filtered with 0.1 µm PC membrane (Isopore™, hydrophilic, non-sterile, diameter 47 mm), Figure 6.1. After synthesis, the product was washed by filtering 100 mL of D.W and dried at 50 °C overnight.

Table 6.2 Bimetallic synthesis conditions applied for the in-situ generation of bimetallic NCs supported on PAA-C (MW power 5 W, flow rate 0.248 mL/min and residence time 70 s).

Sample Name	Inlet A Cu load$_{th}$ (wt.%)	Inlet B	Inlet C Ag load$_{th}$ (wt.%)
V@10Cu	10	PAA-C	-
V@6Cu@0.9Ag	6	PAA-C	0.9
V@10Cu@1.5Ag	10	PAA-C	1.5
V@15Cu@2.0Ag	15	PAA-C	2.0

6.2.1. *Characterization Techniques*

The PAA-C supported clusters were characterized following the respective procedures reported in chapters 3. The unsupported clusters were characterized by UV-VIS spectroscopy, without dilution of the sample.

Fourier-transform infrared spectroscopy (FTIR): The substrate PAA-C was characterized by Fourier-transform infrared spectroscopy (Vertex-70 FTIR spectrophotometer, Brucker, USA).

6.3. **Results and Discussions**

6.3.1. *Preliminary studies: power, residence time and precursors mixing.*

Considering the set-up reported in Figure 6.1, the final result is mainly affected by the concentration of the precursors, the mixing between them, and the reduction/ cooling stages (6 time-temperature parameters $t_{heating,1}$, $T_{heating,1}$, $t_{heating,2}$, $T_{heating,2}$, $t_{cooling}$ and $T_{cooling}$). To simplify the analysis, the salts concentration was fixed at 10 mM for each metal, which may reduce undesired agglomeration or segregation mechanisms[159]. In this way, the analysis was focused exclusively on the differences of the time-temperature profiles.

The temperature profile exhibited overall a swallow-shape (Figure 6.2). The two parabolic branches represented the time-temperature profiles of each nucleation-growth step, heating 1 and heating 2 of Figure 6.1 respectively. The heating mechanism was nearly instantaneous[121,293], with similar temperature profile in the

two branches. As reported in chapter 2, the EM field distribution was responsible for the parabolic profile, as the electric field intensity was maxima in the central zone of the rectangular cavity[138,139]. In fact, the main absorber of the set-up was the mixture of deionized water with polyacrylic acid, and minimum variations of its dielectric properties were expected for so low salts deviations (more details in annex 2)[294,295].

In accordance with the power analysis reported in chapter 3, the maximum temperature observed was directly influenced by the power applied. In detail, for the slower flow rate (t_{res}=140 s) the maximum temperature varied from (57.3±0.3) °C up to (90.9±1.2) °C when the input power changed from 5 W to 10 W, Figure 6.2 a. Similar results were observed for higher flow rates (Figure 6.2 b and c), where the maximum gradient was observed between 5 W and 20 W for a residence time of 70 s, where the maximum temperature ranged from (43.0±0.2) °C to (91.0±0.5) °C (see Figure 6.2 c). Furthermore, for higher flow rates the contact time between the heating source and the fluid decreased. The longer the irradiation exposure time the higher the energy absorbed by the liquid volume, and then higher the maximum temperature. For this reason, lower working powers were required for slower flow rates to achieve the same temperature profile. Comparing the temperature profile at 10 W for 140 s, 105 s and 70 s of residence time, the maximum temperature varied from (90.9±1.2) °C to (69.2±1.5) °C and to (55.0±0.3) °C respectively (Figure 6.2 a, b and c).

The UV-VIS spectroscopic analysis of the resulting colloidal solutions is presented in Figure 6.2. For temperatures lower than 90 °C, no relevant variations were observed, i.e. between 140 s at 5 W and 70 s at 5 or 10 W. In accordance with results reported in previous chapters, the product may contain a mixture of nanoclusters and ultra-small nanoparticles. On the contrary, whenever the temperature was higher than 90 °C, (i.e. 10 W, 15 W and 20 W for 140 s, 105 s and 70 s respectively),

Ag nanoparticles predominated in the final product, confirmed by the plasmonic peak close to 420 nm.
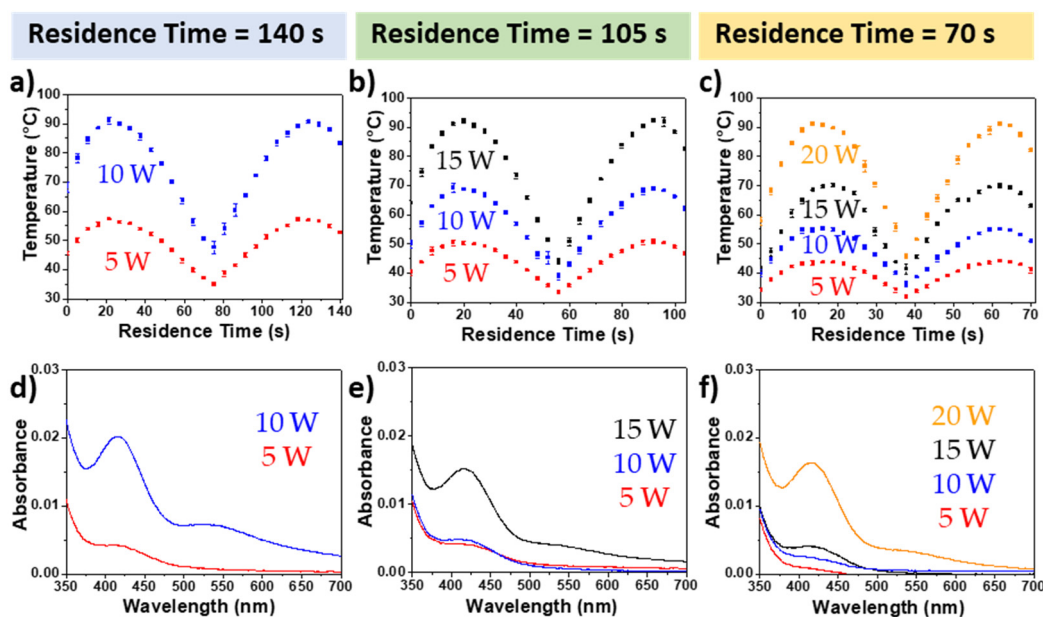
Figure 6.2 Temperature profile (a, b and c) and UV-VIS Spectra (d, e and f) for Ag microwave-assisted continuous flow synthesis as a function of power applied (5, 10, 15 and 20 W) and total residence time (70, 105 and 140 s).

As demonstrated by Pande et al.[296] the $Cu(NO_3)_2$ presents a broad signal at approximately 810 nm, attributed to d-d transitions of $[Cu(H_2O)_6]^{2+}$. The interaction between PAA and Cu^{2+} ions originated both mononuclear and binuclear complexes, as proved by the shift of the characteristic peak at 720 nm[297,298], as observed in Figure 6.3 a-c. Instead, the broad peak in the range 400-500 nm appeared exclusively for bimetallic nanostructures (d, e and f in Figure 6.3)[299,300]. The differences observed were due to several parameters, such as the synthesis yield, the silver/copper weight fractions and the dimension of the particles produced. Also in this case for temperature higher than 90 °C (Figure 6.3 d – 10 W, e – 15 W and f – 20 W) the silver reduction was favoured as confirmed by the SPR signal at 426 nm. The absence of separated peaks may discard the presence of two segregated particle populations, but it was no possible to discern between alloy or core-shell structure[301]. However,

in all the cases there was still a high signal of unreacted Cu^{2+}-PAA^- complexes close to 720 nm.
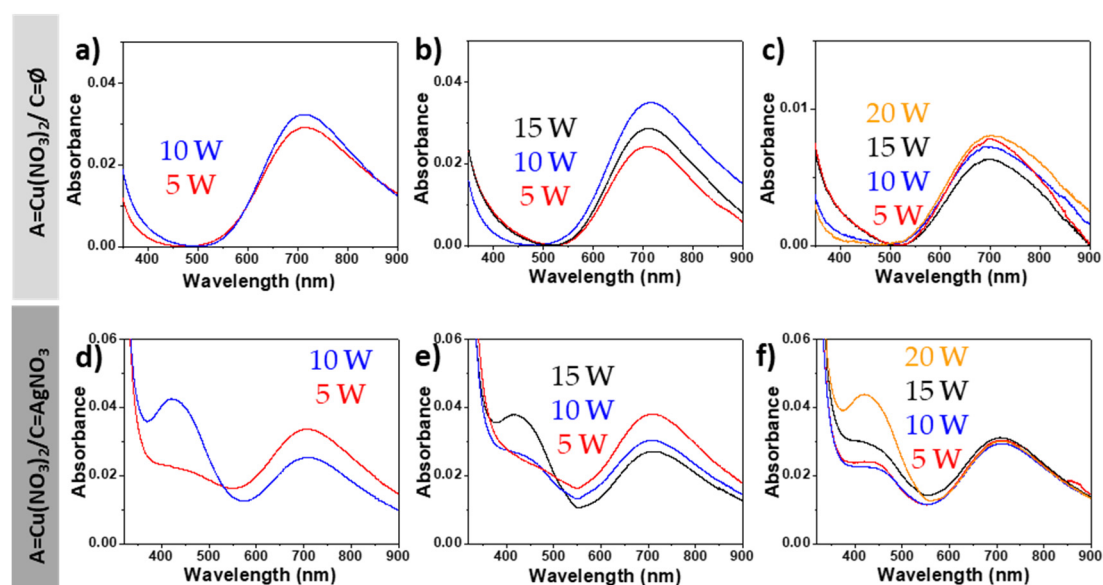
Figure 6.3 UV-VIS Spectra for Cu (a, b and c) and Ag@Cu (d, e and f) of microwave-assisted continuous flow synthesis as a function of power applied (5, 10, 15 and 20 W) and total residence time (70, 105 and 140 s).

6.3.2. *In-situ Flow Nucleation of Cu@PAA-C Nanoclusters*

In the following analysis, the PAA precursor was replaced with a colloidal solution of PAA-C particles (1 mg/L) to nucleate-growth the clusters directly over the carbon substrate. As reported by Liu et al.[302], the PAA wrapped the carbon surface with a strong hydrophobic interaction between the polymer backbone and the carbon surface enhancing the dispersion of the nanoparticles and allowing their use as a support for in-situ continuous flow synthesis. The Vulcan XC-72 nanoparticles presented a spherical shape with an average diameter of 30 nm, as confirmed by TEM images in Figure 6.4 a. The PAA functionalization was demonstrated by FTIR analysis, in Figure 6.4 b. The functionalized carbon substrate presented the characteristic peaks for COO^- functional groups of PAA. The PAA-C spectrum shows a peak at 1649 cm^{-1}, assigned to the carboxylate C=O stretching mode, a weak asymmetric stretching of COO^- peak at 1544 cm^{-1}, a weak band at 995 – 973 cm^{-1} of C-O-C stretching and the rocking mode of CH_2 was observed at 823 cm^{-1} [303–305].
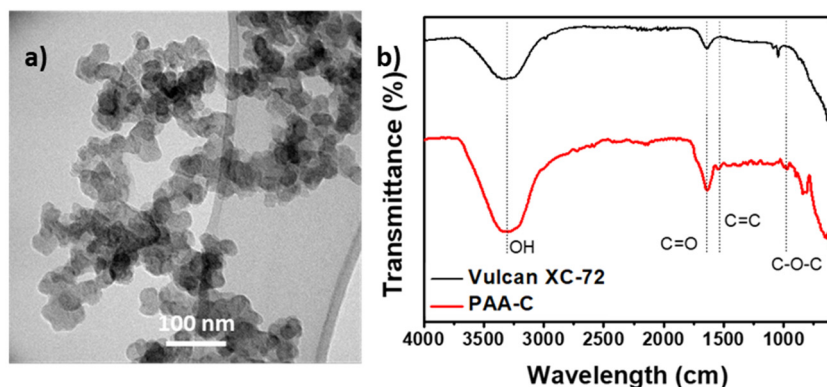
Figure 6.4 a) and b) TEM images FTIR analysis of PAA-C substrate.

Copper is characterized by a low potential reduction ($E^0_{Cu2+/Cu}$=0.34 eV) and its complexation with the PAA functional groups is slower than Ag ions[306]. As a starting point pure copper clusters were synthesized, V@10Cu sample of Table 6.2. The temperature was 12% higher than the temperature achieved without the carbon substrate due to its better microwave absorption properties[265,307], see Figure 6.5 d. HAADF-STEM analysis in Figure 6.5 evidenced that the catalyst V@10Cu is comprised of (1.1±0.3) nm Cu clusters homogenously distributed over the surface, without the presence of aggregates. The Cu content in the catalyst V@10Cu was analyzed by MP-AES and corresponds to 2 wt.%. Cu(II) ions (68%) were coordinated with the PAA template, as confirmed both by XPS analysis (Figure 6.5 e) and previous UV-VIS data (Figure 6.3 i). The peak at 940.7 eV was assigned to the shake-up satellite of Cu NCs, which suggested a strong bond between the Cu^{2+} and the COO^- of the PAA chains. By a previous work reported by Liang et al.[306], the copper ions preferentially interact with the chain-ends of the PAA template which, at sub-1 nm scale, prevent copper oxidation[268]. For the catalyst here developed, the bonding between the PAA chains and the carbon substrate may reduce the protecting power of PAA to Cu oxidation. This may explain the presence of Cu^+ ions both for VC and CuNCs@PAA-C (chapter 5), while no oxidation was observed for CuNCs@SBA-15 (chapter 5) where the PAA was not previously deposited over the mesoporous substrate.
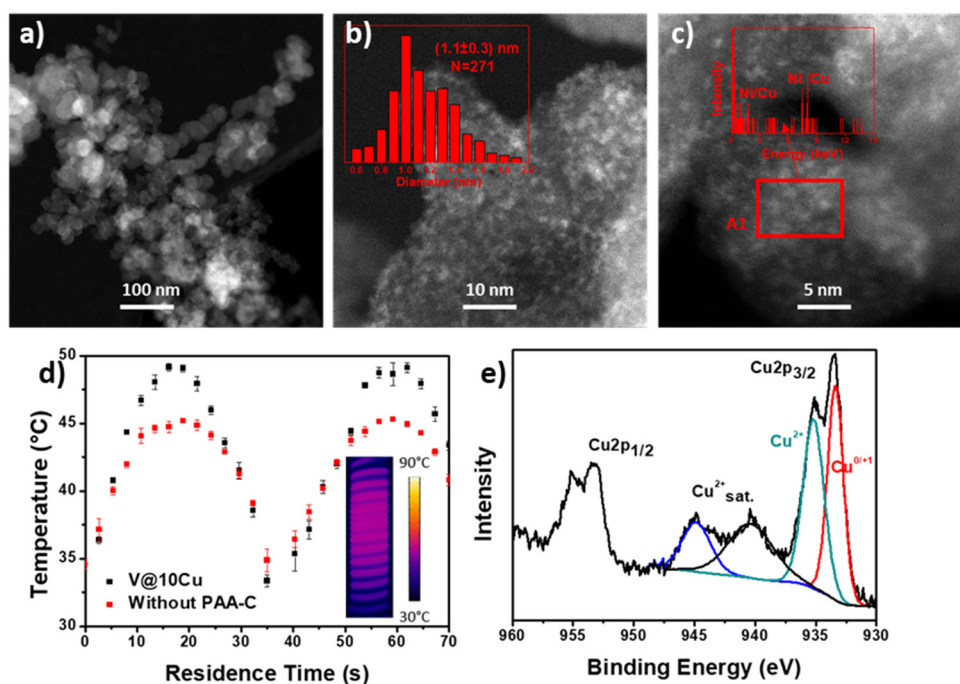
Figure 6.5 a)-c) HAADF-STEM analysis of V@10Cu sample (flow rate 0.248 mL/min, power 5W, residence time 70 s, theoretical Cu loading 10 wt.%), with the uniform (1.1±0.3) nm Cu NCs distribution and EDS analysis of area A1 evidenced in c). d) Temperature profile and IR thermograph of the millifluidic reactor without the carbon substrate (in red) and for V@10Cu sample (in black) e) XPS evidence of different oxidation states, Cu^{+2} satellites and $Cu^{0/+1}$ peak.

6.3.3. *In-situ Flow Nucleation of Cu@Ag Nanoclusters*

Once verified the efficiency of the set-up for the in-situ nucleation of Cu-NCs, the subsequent Ag reduction was evaluated to produce bimetallic catalysts, varying the theoretical metal loading (Cu_{th} and Ag_{th}) from 6 to 15 wt.% for Cu and from 0.9 to 2 wt.% for Ag. The temperature profile was not affected by the addition of different concentration of metal salts.

The HAADF-STEM analysis evidenced that the carbon substrate was overall covered by 1.0-1.3 nm clusters, whose bimetallic nature was confirmed by EDS analysis (Figure 6.6 b, e and h). However, irregular Ag particles progressively grew from 5 nm (Ag_{th} 1.5 wt.% - V@10Cu@1.5Ag, Figure 6.6 f) to 10 nm (Ag_{th} 2.0 wt.% - V@15Cu@2.0Ag, Figure 6.6 i) in an excess of Ag precursor. On the contrary, no individual Ag particles were observed for catalyst V@6Cu@0.9Ag (Ag_{th} 0.9 wt.%)

which presented two populations, bimetallic nanoclusters (Figure 6.6 b) and monometallic Cu clusters (Figure 6.6 c).

The Cu/Ag atomic ratio of reagents calculated for these catalysts was 9.7, 11.3 and 12.8 for V@6Cu@0.9Ag, V@10Cu@1.5Ag and V@15Cu@2.0Ag respectively. Then, it seems that the high concentration of Ag reagent promotes the fast homogenous nucleation of silver atoms and their uncontrolled aggregation to form Ag nanoparticles. This phenomenon has been well studied, since a low concentration of metallic reagents is required to produce clusters and avoid an uncontrolled growth into nanoparticles[167]. On the other hand, it is desirable a high density of anchored clusters on the carbon support to improve the catalytic performance, as reported in chapter 5.
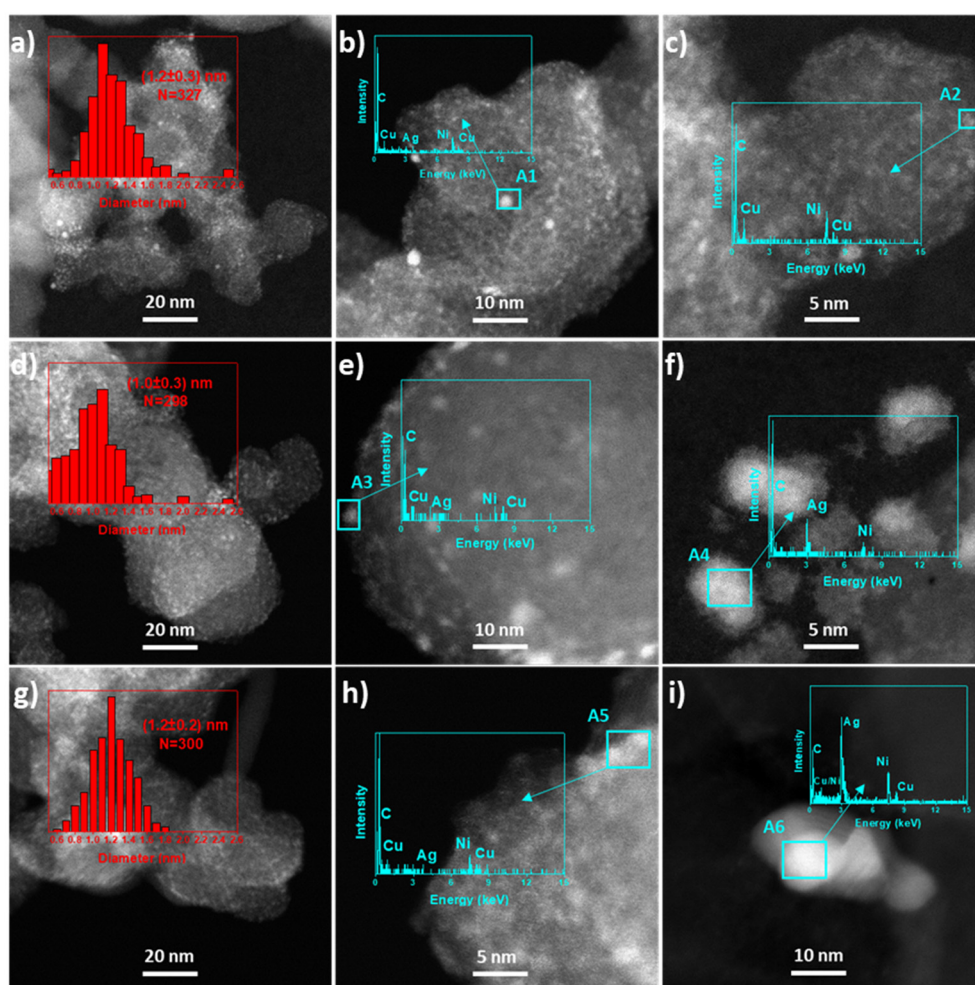
Figure 6.6 HAADF-STEM images, EDS spectra and size distribution of V@6Cu@0.9Ag (a-c), V@10Cu@1.5Ag (d-f) and V@15Cu@2.0Ag (g-i).

The maximum loading observed was of approximately 4.00 wt.% and 0.5 wt.%, which corresponds to a loading yield of around 80% and 50% for Cu and Ag, respectively (Sample V@6Cu@0.9Ag in Table 6.3). An increase of the concentration of the metal precursors did not result in an increase of the metal deposition. This result can be rationalized by the saturation of the COO^- available sites of the PAA template, which could promote a drastic dropping of the synthesis yield.

The enhancement of copper loading between V@Cu and V@Cu@Ag catalysts, around two times higher in V@Cu@Ag (Table 6.3), pointed out that there are several copper nucleations.

Table 6.3 Theoretical and experimental metal loading, loading yield and oxidation state for bimetallic nanocatalysts.

Sample Name	Cu Load.$_{th}$ (wt.%)	Cu Load.$_{exp}$ (wt.%)	Load. Yield Cu (%)	Ag Load.$_{th}$ (wt.%)	Ag Load.$_{exp}$ (wt.%)	Load. Yield Ag (%)
V@10Cu	10	2.16±0.02	20.8-22.9		-	-
V@6Cu@0.9Ag	6	4.05±0.08	79.5-82.7	0.9	0.64±0.03	44.7-46.9
V@10Cu@1.5 Ag	10	3.79±0.09	37.0-38.8	1.5	0.52±0.02	20.8-22.1
V@15Cu@2.0 Ag	15	4.08±0.11	26.5-27.9	2.0	0.32±0.01	24.8-26.8

In the first heating stage Cu nucleation occurred directly over the carbon surface, while in the second heating stage, where the Ag precursor was added, two concurrent mechanisms may occur. From one side, the electrostatic attraction between Ag^+ and PAA^- is thermodynamically favoured[308] and stronger than the copper one[309,310]. The double displacement reaction between Na^+PAA^- and $AgNO_3$ generates $NaNO_3$, characterized by lower acidic behaviour. The pH variation was experimentally verified in a batch condition, moving from 5.44 for the aqueous solution of silver nitrate to a value of 7.85 after Na-PAA addition. On the contrary, a smaller variation was observed for copper nitrate, where the pH varied from 4.27 to 5.97. Thus, an increase of the pH occurs along the reactor volume for the bimetallic configuration, which may enhance the Cu complexation due to a local variation of the deprotonation degree of the PAA[306].

Silver, characterized by a higher reduction potential than copper, could partially oxidize the formed Cu clusters to generate alloyed AgCu clusters by a galvanic replacement reaction. Cu^0 can partially be replaced by a galvanic redox process, where two Ag atoms can replace one Cu atom. This process was confirmed by the increase of Ag^0 and Cu^{+2} in Table 6.5 and Figure 6.8. 100% of Ag^0 was observed for V@6Cu@0.9Ag and V@10Cu@1.5Ag catalysts, which presented the higher concentration of Cu^{2+} fraction (82%). The redox replacement rate decreased in an excess of copper precursor, as confirmed by V@15Cu@2.0Ag characterization where the Ag^0 fraction decreased to 56% and 38% respectively (Table 6.4 and Figure 6.7 f and g).

Table 6.4 XPS Analysis of monometallic and bimetallic samples.

Sample Name	$Cu^{0/+1}$	Cu^{+2}	Ag^0	Ag^+
V@10Cu	32 %	68 %	-	-
V@6Cu@0.9Ag	18 %	82 %	100 %	0 %
V@10Cu@1.5Ag	18 %	82 %	100 %	0 %
V@15Cu@2.0Ag	23 %	77 %	56 %	44 %
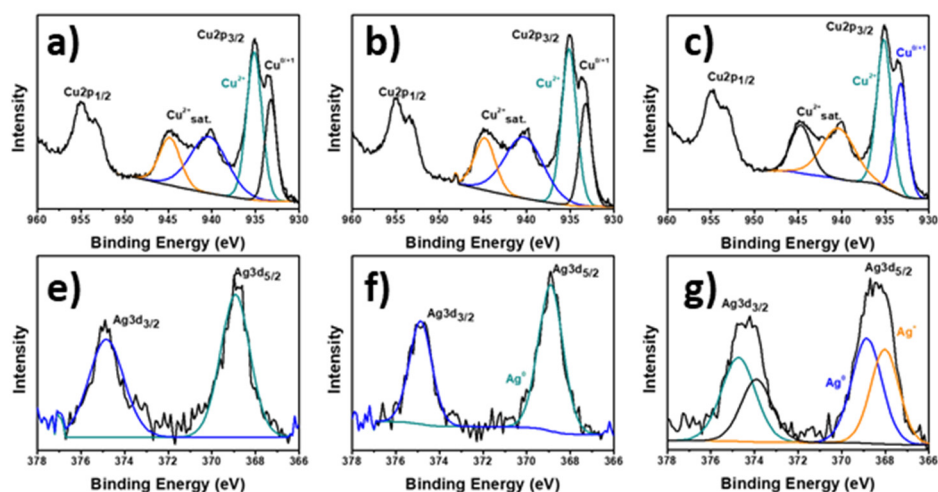
Figure 6.7 XPS analysis for Cu and Ag species of V@6Cu@0.9Ag (a-e), V@10Cu@1.5Ag (b-f) and V@15Cu@2.0Ag (c-g).

On the other hand, considering that Cu is in excess, the initial Cu/Ag ratio was close to 10 or even higher in V@10Cu@1.5Ag and V@15Cu@2.0Ag, Cu cations could also heterogeneously nucleate over Ag/Cu clusters by PAA reduction effect[311]. The

elemental mapping may help to discern between the two different mechanisms proposed. Unfortunately, the clusters presented a diameter smaller than 1.5 nm and the high PAA content promotes the formation of C deposition under the TEM electron beam, which unable an accurate EDS analysis.

6.1.   Conclusions

The PAA wrapping of Vulcan XC-72 nanoparticles resulted in an increase of the dispersion of the carbon substrate in an aqueous stream, which represented an excellent option for the in-situ flow nucleation of Cu and Ag@Cu NCs. The continuous flow reactor was properly modified, implementing two following mixing-heating stages which allowed the successive reduction of Cu and Ag ions for the production of bimetallic nanostructures. Furthermore, the longer the residence time the higher the maximum temperature, due to a longer exposure time to MW heating. Undesired Ag NPs were observed for temperature higher than 90 °C, while neglected variations were observed for the remaining configurations giving the possibility to maximize the flow rate and reduce the input power. The spectroscopic analysis evidenced that Ag@Cu complexes and Cu^{2+}-PAA complexes predominated in the colloidal product.

Furthermore, the clusters were synthesized directly over the PAA-C substrate, with a loading yield of around 80% and 50% for Cu and Ag respectively. The XPS characterization evidenced that 100% of Ag^0 was observed for V@6Cu@0.9Ag and V@10Cu@1.5Ag catalysts, which presented the higher concentration of Cu^{2+} fraction. On the other hand, Ag impurities of bigger dimensions and lower rate of the redox replacement were observed in an excess of Ag and Cu precursors. The best result were obtained for the sample V@6Cu@0.9Ag, where the clusters were overall uniformly distributed, and their bimetallic nature was proved by EDS analysis.

OVERALL CONCLUSIONS

Resume: *Nanocatalysts design: Where are we now?*
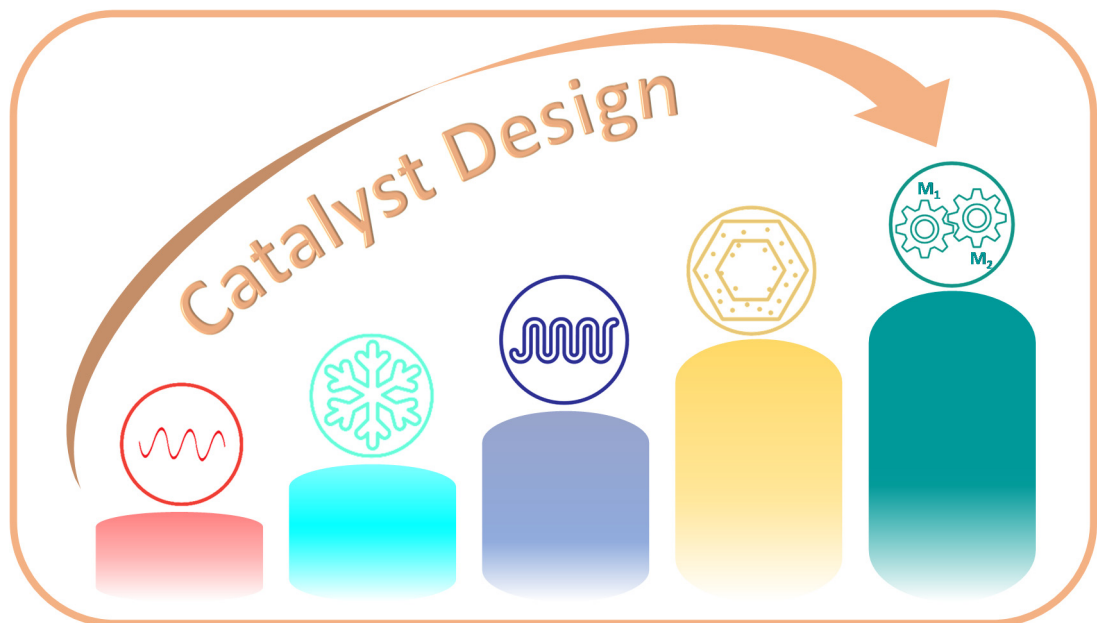
7. OVERALL CONCLUSIONS

MICROWAVE VERSUS CONVENTIONAL HEATING: Nanoparticles Synthesis. The simulation and experimental temperature measurements of a helical microfluidic system for continuous liquid synthesis of nanoparticles, heated in a monomode microwave cavity, showed a distinct temperature distribution compared with the same system heated in an oil bath, i.e conventional heating (CH). The temperature profile is narrower in the MW heating (85.2±13.9) °C compared to CH (83.9±40.6) °C, for 0.1mL/min. Furthermore, the different heating mechanism results in a parabolic temperature profile, with lower temperature in the microfluidic wall in MWH, which is inverse than the one obtained in CH by conduction mechanism.

The effects of this temperature distribution in the synthesis of Ag nanoparticles by the polyol method are two, first the narrower T^a profile results in a narrower particle size distribution (19.0±4.3) nm vs (10.8±4.7) nm and secondly, the inverse temperature profile and the different heating pattern, gives rise to a low deposition of nanoparticles on the microfluidic wall, an important drawback in the synthesis of NPs in microfluidic systems conventionally heated by conduction.

ULTRA-SMALL Ag-NPs: Microwave Heated Batch Approach.

The Classical Nucleation Theory (CNT) of nanoparticle synthesis affirms that a fast activation is required to produce a homogeneous nucleation. The MWH in a batch reactor system is linear and 10 times faster compared to an asymptotic profile in the slower CH.

A comprehensive study of different heating rates under MWH from 0.2 to 2.8 °C/s was conducted for the synthesis of ultrasmall Ag nanoparticles, using polyacrylic acid as reducing and stabilizing agent. The highest heating rate during 17s, reaching a final temperature of 75 °C, resulted in a uniform size distribution of ultrasmall Ag NPs (1.6±0.7)nm. In this case no surface plasmon resonance at 426nm corresponding

to crystalline Ag nanoparticles was observed, whereas with the other heating rates and same final temperature, the SPR peak was always visible and a much broader particle size distribution was obtained.

Thanks to the stabilization with PAA and the narrow particle size distribution, with the absence of crystalline Ag NPs, Ostwald ripening mechanism was avoided and the ultrasmall NPs could be considered as stable under storage at 4 °C covered by aluminium foil. The apparition of a new distribution of NPs of (4.7±1.0) nm was observed, but the UV-Vis spectra did not show peak at 426nm after the storage period of 18 months.

The deposition of the ultra-small Ag-NPs on mesoporous SBA-15 by wet impregnation, with a metallic loading yield of 0.98 wt.%. This catalysis was identified as B-AgNPs@SBA-15, and tested for the heterogeneous 4-nitrophenol reduction reporting a catalytic activity 4.5 times higher than the 7 nm Ag NPs also supported on SBA-15.

FROM BATCH TO CONTINUOUS FLOW PROCESSING: Ag NCs.

The Ag synthesis procedure with PAA was switched from batch to continuous flow reactor including a rapid cooling step to quench the reaction and avoid subsequent undesired clusters growth. The Ag nanoclusters of (1.2±0.3) nm were homogeneously dispersed over the SBA-15 channels, with a remarkable 60% size reduction if compared to the batch process without cooling. Furthermore, HAADF-STEM analysis of clusters confirmed the absence of the crystalline structure.

The catalyst, named C-AgNCs@SBA-15, was successfully used for alkynes cyclization, demonstrating a high versatility for C-N, C-O and C-C bonds. The heterogeneous catalyst allowed a reduction of 30 times of metal loading in comparison to homogeneous processes, and at the same time guaranteeing the reusability of the catalyst for different cycles. This extraordinary enhancement of catalytic activity for Ag-NCs should be assigned both to size reduction and to a good π-accepting behavior due to the co-presence of Ag(0) and Ag(I).

SIMULTANEOUS COOLING-MICROWAVE HEATING: In-situ Clusters Nucleation and Deposition.

The main drawback of post-synthesis impregnation methods is the low loading yield usually lower than 50%. By the use of the alternative in-situ synthesis with simultaneous microwave heating and cooling reactor, the clusters were rapidly nucleated directly over the support and the instantaneous cooling blocked every undesired sintering. The resulting AgNCs also showed the copresence of Ag(I) and Ag(0) and the size was reduced to (1.1±0.3) nm, with loading yield on the porous support enhanced up to 80%, increasing the density of AgNCs on the support with a uniform distribution and a total metal load of 1.8 wt.%.

The 4-Nitrophenol test demonstrated that higher intrinsic catalytic activity was observed by the increase of the density of anchored clusters, due to the faster adsorption/desorption on closer Ag active sites. Furthermore, it was confirmed that Ag catalysts represent an excellent alternative for alkynes cyclization, reporting a high stability even after one year of storage.

Furthermore, this procedure was reproducible, versatile for different metals Ag and Cu and supports SBA-15 and commercial carbon Vulcan XC-72. The synthesis on the carbon support was scaled-up from 100 mg to 1 g in the same MW monomode cavity, being successful up to 500 mg. When the load in this cavity was 1 g, the temperature distribution was not homogeneous and as a result the nucleation was not fully controlled. Further investigations in design cavity for scaling-up the synthesis are necessary.

BIMETALLIC Ag@Cu NANOCLUSTERS: In-Situ Flow Nucleation.

The MW-heated continuous flow reactor was properly modified to allow a dual-stage nucleation process, followed by an instantaneous cooling step. As expected, the longer the residence time and the power applied, the higher the maximum temperature observed. Due to differences in the redox potential, undesired bigger Ag NPs predominate for temperatures higher than 90 °C and for higher Ag concentrations. For the catalyst V@6Cu@0.9Ag, the carbon substrate was uniformly

covered by two populations of nanoparticles smaller than 2 nm, bimetallic Ag@Cu NPs and monometallic Cu NPs.

To conclude, the reduction of the catalyst size down to nanoclusters, the stabilization over different substrates, the improvement of the loading yield and the enhancement of the catalytic activity were some of the outcomes achieved in this thesis. Microwave heating and microfluidic reactors may still be considered a winner alternative to synthesize mono- and/or hetero- metallic NPs and/or NCs.

VI. APPENDIX

1. DETAILS OF MULTIPHYSICS SIMULATION

1.1. Physical Parameters

Table A1.1 Physical parameters for COMSOL Multiphysics® Simulation

Water Physical Parameters		
C_P (Specific Heat)	$A-BT+CT^2-DT^3+ET^4$ $A=12010,\ B=80,\ C=0.31,\ D=5.38*10^{-4},\ E=3.63*10^{-7}$	$J/(kg \cdot K)$
k (Thermal Conductivity)	$-F+GT-HT^2+IT^3$ $F=0.87,\ G=0.0089,\ H=1.58*10^{-5},\ I=7.97*10^{-9}$	$W/(m \cdot K)$
μ (Viscosity)	$L-MT+NT^2-OT^3+PT^4-QT^5+RT^6$ $L=1.38,\ M=0.021,\ N=1.36*10^{-4},\ O=4.65*10^{-7},\ P=8.90*10^{-10},\ Q=9.08*10^{-13},\ R=3.85*10^{-16}$	$(Pa \cdot s)$
ϱ (Density)	$S+UT-VT^2+ZT^3$ $S=838.47,\ U=1.40,\ V=0.003,\ Z=3.72*10^{-7}$	(kg/m^3)
Air Physical Parameters		
C_P (Specific Heat)	$a-bT+cT^2-dT^3+eT^4$ $a=1047,\ b=0.37,\ c=9.45*10^{-4},\ d=6.02*10^{-7},\ e=1.29*10^{-10}$	$J/(kg \cdot K)$
k (Thermal Conductivity)	$-f+gT-hT^2+iT^3$ $f=0.227*10^{-2},\ g=1.155*10^{-4},\ h=7.902*10^{-8},\ i=4.12*10^{-11}$	$W/(m \cdot K)$
μ (Viscosity)	$-l+mT-nT^2+oT^3-pT^4$ $l=8.38*10^{-7},\ m=8.36*10^{-8},\ n=7.69*10^{-11},\ o=4.64*10^{-14},\ p=1.07*10^{-17}$	$(Pa \cdot s)$
ϱ (Density)	$pA*0.02897/8.314/T$	(kg/m^3)
Teflon® Physical Parameters		
C_P (Specific Heat)	1050	$J/(kg \cdot K)$
k (Thermal Conductivity)	0.23	$W/(m \cdot K)$
ϱ (Density)	2160	(kg/m^3)

1.2. Heat and Mass Flow Balance

The heat transfer coefficient was calculated according to equation (A1) developed by Purandare et al.[312] for heat transfer in helical tubes in heat exchangers:

$$Nu = 0.858\left\{(De)^{0.7202}(Pr)^{-1.8224}\left(\frac{a}{2\pi R}\right)^{0.0119}\right\} = \frac{hD_h}{k} \tag{A1}$$

The hydraulic diameter D_h was calculated with equation (A2)

$$D_h = 4A/P \tag{A2}$$

Where A and P represent the area and the perimeter of a circular cross section of the pipe respectively. This value was also used to determine the dimensionless numbers used to describe heating and flow conditions, as per the definition reported in the following formulas[312–314]

$$Re = \frac{\rho v D_h}{\mu} \tag{A3}$$

$$Pr = \frac{c_p \mu}{k} \tag{A4}$$

$$De = Re\sqrt{\frac{r}{R}} \tag{A5}$$

The dimensionless numbers were evaluated at the different flow rates and summarized in Table A1.2. Furthermore, the critical value of Re was calculated as reported in equation A6[315].

$$Re_{cr} = 2100 * \left[1 + 12\left(\frac{r}{R}\right)^{0.5}\right] = 6595 \tag{A6}$$

Table A1.2: Dimensionless numbers and Heat Transfer Coefficient for different flow rates.

Flow Rate (ml/min)	Re	De	Nu	h (W/m²K)
0.1	91.5	16.3	0.33	454
0.2	182.9	32.6	0.54	748
0.3	274.4	48.9	0.72	1001
0.6	548.7	97.9	1.18	1650

1.3. Mesh analysis

In the previous work reported by Nigar et al.[139], we reported a detailed analysis of the mesh selection to verify the accuracy of the cavity model and the optimization of the computational time. Herein, we focused on the optimization of the meshing for the microfluidic reactor. For the meshing of the helical reactor, we used the sweep function of the triangular meshed base surface along the helical profile. In Figure A1.1, a progressive increment of the number of triangular elements varying

from 20 to 442 was considered. In Table A1.3, an improvement of the mesh produced a relative increase of computational memory and time required.
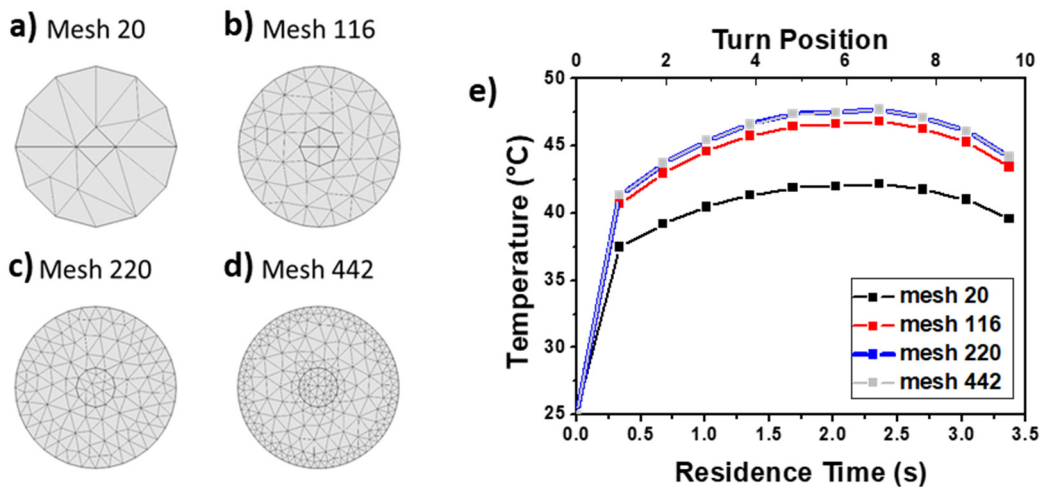
Figure A1.1: Triangular mesh elements of the cross section of the microfluidic reactor (a-d) and effects of triangular mesh elements of the cross-section of the helical reactor on the temperature profile (e).

Table A1.3: Computational memory and time as function of mesh elements.
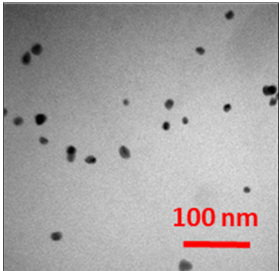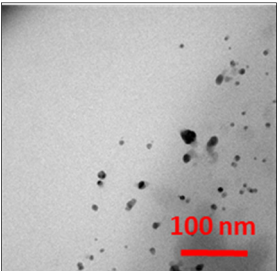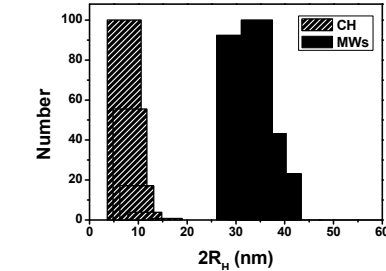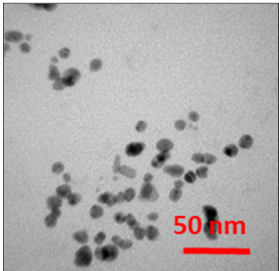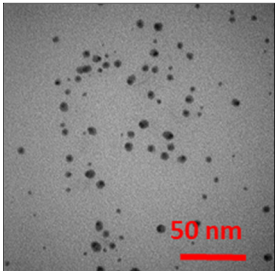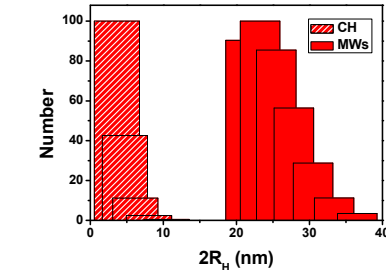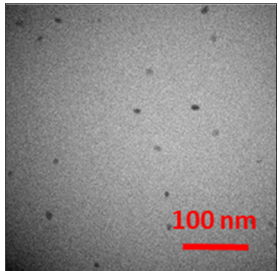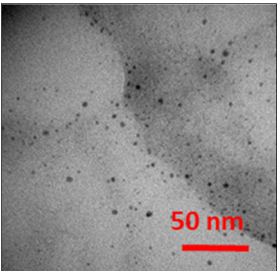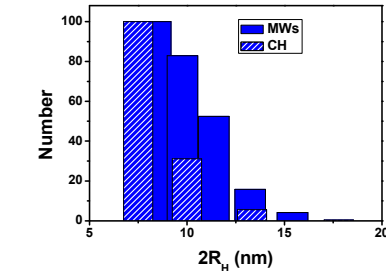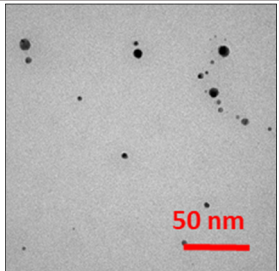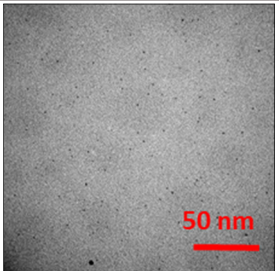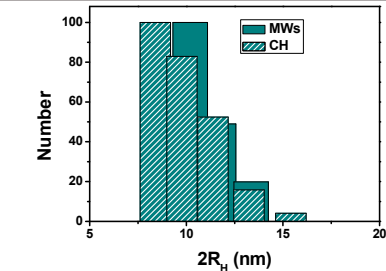
Mesh Elements	Memory (GB)	Sol. Time (s)
20	12.92	2528
116	23.40	6197
220	27.95	8783
442	38.25	13058

In order to determine the optimum point between processing time and accuracy of the data, we reported the temperature profile obtained in each situation in Figure A. Due to extremely simplification of mesh 20, we observed a deviation of temperature higher than 10 degrees. A higher precision was obtained dividing the inner circle in 24 triangular elements. No relevant differences were observed between 220 and 442 elements. For this reason, we decided to adopt the subdivision in 220 triangular mesh of base surface as optimum point, considering the reduction of computational time as listed in Table A1.3.

2. MICROSCOPY AND WALL DEPOSITION DETAILS
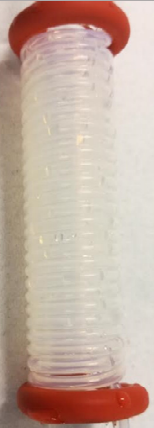
2.1. TEM and DLS analysis

Table A2.1: TEM and DLS Analysis at different flow rates for microwaves and conventional heating.

Flow Rate	TEM analysis		DLS analysis
	MWH	CH	
0.1			
0.2			
0.3			
0.6			

2.2. Tubing Surface Deposition at Various Flow Rates

Table A2.2: Tubing surface deposition at different flow rates for microwaves and conventional heating.

Sample	0.1 mL/min	0.2 mL/min	0.3 mL/min	0.6 mL/min
Microwaves Heating				
Conventional Heating				
Working Time (min)	200	100	66.7	33.3
Volume Produced (ml)	20	20	20	20

3. TIME-TEMPERATURE PROFILES
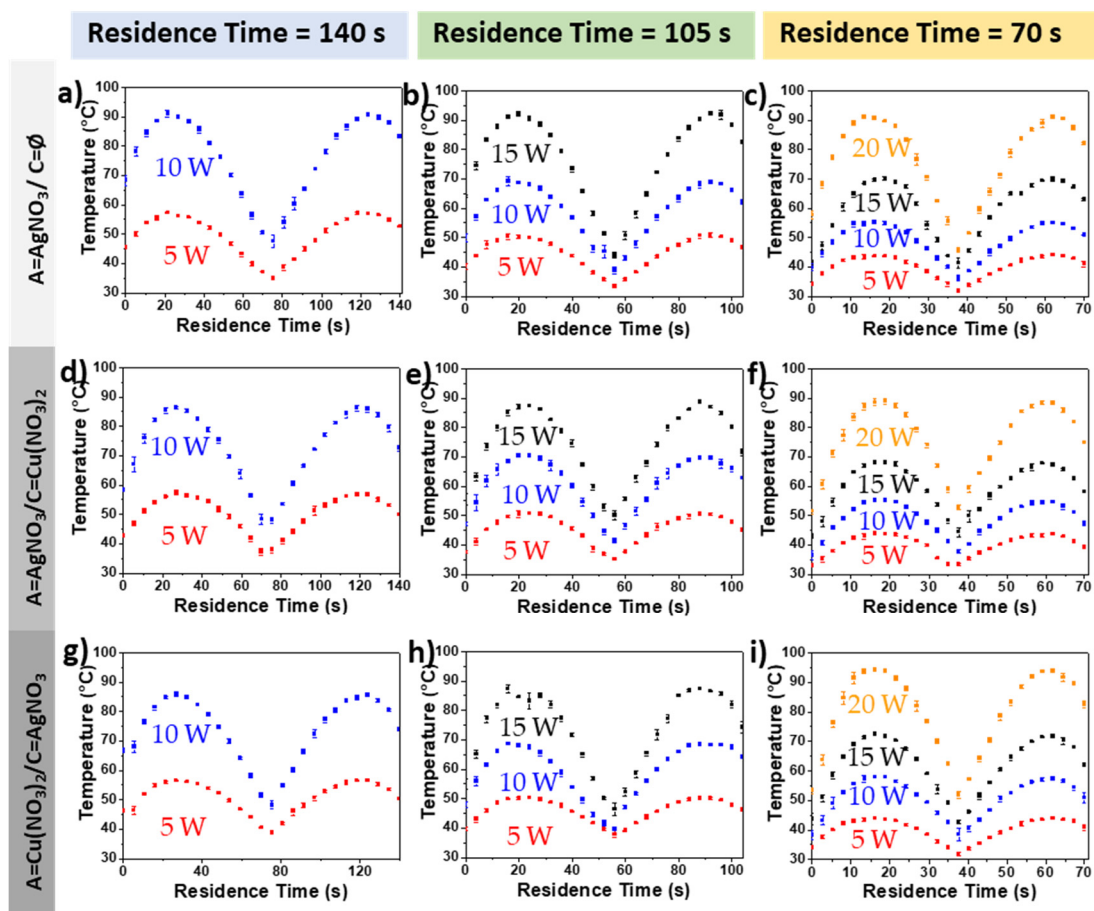
Figure A3.1: Temperature profile for Ag (a, b and c), Cu (d, e and f), and Cu@Ag (g, h and i) microwave-assisted continuous flow synthesis as a function of power applied (5, 10, 15 and 20 W) and total residence time (70, 105 and 140 s).

VII. REFERENCIES

(1)   Robertson, A. J. B. The Early History of Catalysis. *Platin. Met. Rev.* **1975**, *19* (2), 64–69.

(2)   Lindströma, B.; Pettersson, J., L. A Brief History of Catalysis. *Cattech* **2003**, *7* (4), 130–138. https://doi.org/10.1023/A:1025001809516.

(3)   Lanzafame, P.; Perathoner, S.; Centi, G.; Gross, S.; Hensen, E. J. M. Grand Challenges for Catalysis in the Science and Technology Roadmap on Catalysis for Europe: Moving Ahead for a Sustainable Future. *Catal. Sci. Technol.* **2017**, *7* (22), 5182–5194. https://doi.org/10.1039/c7cy01067b.

(4)   Dumesic, J. A.; Huber, G. W.; Boudart, M. Principles of Heterogeneous Catalysis. In *Handbook of Heterogeneous Catalysis*; Wiley-VCH Verlag GmbH & Co. KGaA., Ed.; 2008; pp 1–15. https://doi.org/10.1002/9783527610044.

(5)   Ghosh, B. K.; Moitra, D.; Chandel, M.; Lulla, H.; Ghosh, N. N. Ag Nanoparticle Immobilized Mesoporous TiO2-Cobalt Ferrite Nanocatalyst: A Highly Active, Versatile, Magnetically Separable and Reusable Catalyst. *Mater. Res. Bull.* **2017**, *94*, 361–370. https://doi.org/10.1016/j.materresbull.2017.06.015.

(6)   Hu, S.; Li, W.-X. Influence of Particle Size Distribution on Lifetime and Thermal Stability of Ostwald Ripening of Supported Particles. *ChemCatChem* **2018**, *10* (13), 2900–2907. https://doi.org/10.1002/cctc.201800331.

(7)   Liu, L.; Corma, A. Metal Catalysts for Heterogeneous Catalysis: From Single Atoms to Nanoclusters and Nanoparticles. *Chem. Rev.* **2018**, *118* (10), 4981–5079. https://doi.org/10.1021/acs.chemrev.7b00776.

(8)   Tyo, E. C.; Vajda, S. Catalysis by Clusters with Precise Numbers of Atoms. *Nat. Nanotechnol.* **2015**, *10* (7), 577–588. https://doi.org/10.1038/NNANO.2015.140.

(9)   Jin, R.; Zeng, C.; Zhou, M.; Chen, Y. Atomically Precise Colloidal Metal Nanoclusters and Nanoparticles: Fundamentals and Opportunities. *Chem. Rev.* **2016**, *116* (18), 10346–10413. https://doi.org/10.1021/acs.chemrev.5b00703.

(10)   Du, Y.; Sheng, H.; Astruc, D.; Zhu, M. Atomically Precise Noble Metal Nanoclusters as Efficient Catalysts: A Bridge between Structure and Properties. *Chem. Rev.* **2020**, *120* (2), 526–622. https://doi.org/10.1021/acs.chemrev.8b00726.

(11)   ISO. ISO/TS 27687: Nanotechnologies — Terminology and Definitions for Nano-Objects — Nanoparticle, Nanofibre and Nanoplate. *Int. Organ. Stand.* **2009**, *1*, 14.

(12)   Farzin, L.; Shamsipur, M.; Samandari, L.; Sadjadi, S.; Sheibani, S. Biosensing Strategies Based on Organic-Scaffolded Metal Nanoclusters for Ultrasensitive Detection of Tumor Markers. *Talanta* **2020**, *214*, 120886–120898. https://doi.org/10.1016/j.talanta.2020.120886.

(13)   Kauscher, U.; Penders, J.; Nagelkerke, A.; Holme, M. N.; Nele, V.; Massi, L.; Gopal, S.; Whittaker, T. E.; Stevens, M. M. Gold Nanocluster Extracellular Vesicle Supraparticles: Self-Assembled Nanostructures for Three-Dimensional Uptake Visualization. *Langmuir* **2020**, *36* (14), 3912–3923. https://doi.org/10.1021/acs.langmuir.9b03479.

(14)   Ashcroft, N. W.; Mermin, N. D. *Solid State Physics*, 33rd ed.; New York, Holt, R. and W., Ed.; New York, 1976.

(15)   Petrucci, R. H.; Madura, J. D.; Bissonnette, C. *General Chemistry: Principles and Modern Applications*, 10th ed.; Hall, P., Ed.; 2011.

(16)   Rockett, A. *The Materials Science of Semiconductors*, 1st ed.; Springer US, 2008. https://doi.org/10.1007/978-0-387-68650-9.

(17)   Johnston, R. L. *Atomic and Molecular Clusters*, 1st ed.; Taylor & Francis, Ed.; London, 2002. https://doi.org/10.1201/9780367805814.

(18)   Qian, H.; Zhu, M.; Wu, Z.; Jin, R. Quantum Sized Gold Nanoclusters with Atomic Precision. *Acc. Chem. Res.* **2012**, *45* (9), 1470–1479. https://doi.org/10.1021/ar200331z.

(19)   Johnston, R. L. The Development of Metallic Behaviour in Clusters. *Philos. Trans. R. Soc. London A* **1998**, *356* (1735), 211–230. https://doi.org/10.1098/rsta.1998.0158.

(20)   Tsukuda, T.; Häkkinen, H. *Protected Metal Clusters: From Fundamentals to Applications*, 1st ed.; Elsevier, 2015.

(21)   Piñeiro, Y.; Rivas, J.; López-Quintela, M. A. The Emergence of Quantum Confinement in Atomic Quantum Clusters. In *Colloidal Foundantions of Nanoscience*; Elsevier, 2014; pp 81–105. https://doi.org/10.1016/B978-0-444-59541-6.00004-7.

(22)   Krogh Andersen, O. Electronic Structure of the Fcc Transition Metals Ir, Rh, Pt, and Pd. *Phys. Rev. B* **1970**, *2* (4), 883–906. https://doi.org/10.1103/PhysRevB.2.883.

(23)   Roth, S.; Carroll, D. *Foundations of Solid State Physics: Dimensionality and Simmetry*; Wiley-VCH Verlag GmbH & Co. KGaA, Ed.; 2019. https://doi.org/10.1002/9783527816590.

(24)   Hou, X.-F.; Yan, L.-L.; Huang, T.; Hong, Y.; Miao, S.-K.; Peng, X.-Q.; Liu, Y.-R.; Huang, W. A Density Functional Theory Study on Structures, Stabilities, and Electronic and Magnetic Properties of AunC (n = 1–9) Clusters. *Chem. Phys.* **2016**, *472*, 50–60. https://doi.org/10.1016/J.CHEMPHYS.2016.03.009.

(25)   Nhat, P. V.; Si, N. T.; Leszczynski, J.; Nguyen, M. T. Another Look at Structure of Gold Clusters Aun from Perspective of Phenomenological Shell Model. *Chem. Phys.* **2017**, *493*, 140–148. https://doi.org/10.1016/j.chemphys.2017.06.009.

(26)   Quijada, M.; Muiño, R. D.; Echenique, P. M. The Lifetime of Electronic Excitations in Metal Clusters. *Nanotechnology* **2005**, *16* (5), 176–180. https://doi.org/10.1088/0957-4484/16/5/008.

(27)   Rambukwella, M.; Sakthivel, N. A.; Delcamp, J. H.; Sementa, L.; Fortunelli, A.; Dass, A. Ligand Structure Determines Nanoparticles' Atomic Structure, Metal-Ligand Interface and Properties. *Front. Chem.* **2018**, *6*, 330–347. https://doi.org/10.3389/fchem.2018.00330.

(28)   O'Brien, M. N.; Jones, M. R.; Mirkin, C. A. The Nature and Implications of Uniformity in the Hierarchical Organization of Nanomaterials. *Proc. Natl. Acad. Sci. U. S. A.* **2016**, *113* (42), 11717–11725. https://doi.org/10.1073/pnas.1605289113.

(29)   Lu, Y.; Chen, W. Application of Mass Spectrometry in the Synthesis and Characterization of Metal Nanoclusters. *Anal. Chem.* **2015**, *87* (21), 10659–10667. https://doi.org/10.1021/acs.analchem.5b00848.

(30)   Clemenger, K.; Heer, W. A. De; Saunders, W. A. Electronic Shell Structure and Abundance of Sodium Clusters. *Phys. Rev. Lett.* **1984**, *52* (24), 2141–2143. https://doi.org/10.1103/PhysRevLett.52.2141.

(31)   Jug, K.; Zimmermann, B. Structure and Stability of Small Copper Clusters. *J. Chem. Phys.* **2002**, *116* (11), 4497–4507. https://doi.org/10.1063/1.1436465.

(32)   Imaoka, T.; Akanuma, Y.; Haruta, N.; Tsuchiya, S.; Ishihara, K.; Okayasu, T.; Chun, W. J.; Takahashi, M.; Yamamoto, K. Platinum Clusters with Precise Numbers of Atoms for

Preparative-Scale Catalysis. *Nat. Commun.* **2017**, *8* (1), 1–8. https://doi.org/10.1038/s41467-017-00800-4.

(33) Kabir, M.; Mookerjee, A.; Bhattacharya, A. K. Structure and Stability of Copper Clusters: A Tight-Binding Molecular Dynamics Study. *Phys. Rev. A* **2004**, *69* (4), 43203–43213. https://doi.org/10.1103/PhysRevA.69.043203.

(34) Bromley, S. T.; Woodley, S. M. *Computational Modelling of Nanoparticles*, 1st ed.; Elsevier, 2018.

(35) Zou, X.; Jin, S.; Du, W.; Li, Y.; Li, P.; Wang, S.; Zhu, M. Multi-Ligand-Directed Synthesis of Chiral Silver Nanoclusters. *Nanoscale* **2017**, *9* (43), 16800–16805. https://doi.org/10.1039/c7nr06338e.

(36) Joshi, C. P.; Bootharaju, M. S.; Alhilaly, M. J.; Bakr, O. M. [Ag25(SR)18]-: The "Golden"Silver Nanoparticle Silver Nanoparticle. *J. Am. Chem. Soc.* **2015**, *137* (36), 11578–11581. https://doi.org/10.1021/jacs.5b07088.

(37) Jin, R. Atomically Precise Metal Nanoclusters: Stable Sizes and Optical Properties. *Nanoscale* **2015**, *7* (5), 1549–1565. https://doi.org/10.1039/c4nr05794e.

(38) Walter, M.; Akola, J.; Lopez-Acevedo, O.; Jadzinsky, P. D.; Calero, G.; Ackerson, C. J.; Whetten, R. L.; Grönbeck, H.; Häkkinen, H. A Unified View of Ligand-Protected Gold Clusters as Superatom Complexes. *Proceeding Natl. Acad. Sci. United States Am.* **2008**, *105* (27), 9157–9162. https://doi.org/10.1073/pnas.0801001105.

(39) Zeng, C.; Chen, Y.; Das, A.; Jin, R. Transformation Chemistry of Gold Nanoclusters: From One Stable Size to Another. *J. Phys. Chem. Lett.* **2015**, *6* (15), 2976–2986. https://doi.org/10.1021/acs.jpclett.5b01150.

(40) Abdulhalim, L. G.; Ashraf, S.; Katsiev, K.; Kirmani, A. R.; Kothalawala, N.; Anjum, D. H.; Abbas, S.; Amassian, A.; Stellacci, F.; Dass, A.; et al. A Scalable Synthesis of Highly Stable and Water Dispersible Ag 44(SR)30 Nanoclusters. *J. Mater. Chem. A* **2013**, *1* (35), 10148–10154. https://doi.org/10.1039/c3ta11785e.

(41) Yang, J.; Jin, R. New Advances in Atomically Precise Silver Nanoclusters. *ACS Mater. Lett.* **2019**, *1* (4), 482–489. https://doi.org/10.1021/acsmaterialslett.9b00246.

(42) Jadzinsky, P. D.; Calero, G.; Ackerson, C. J.; Bushnell, D. A.; Kornberg, R. D. Structure of a Thiol Monolayer-Protected Gold Nanoparticle at 1.1 A Resolution. *Science.* **2007**, *318* (5849), 430–433. https://doi.org/10.1126/science.1148624.

(43) Lopez-Sanchez, J. A.; Dimitratos, N.; Hammond, C.; Brett, G. L.; Kesavan, L.; White, S.; Miedziak, P.; Tiruvalam, R.; Jenkins, R. L.; Carley, A. F.; et al. Facile Removal of Stabilizer-Ligands from Supported Gold Nanoparticles. *Nat. Chem.* **2011**, *3* (7), 551–556. https://doi.org/10.1038/nchem.1066.

(44) Corpuz, R. D.; Ishida, Y.; Yonezawa, T. Controlling an Electrostatic Repulsion by Oppositely Charged Surfactants towards Positively Charged Fluorescent Gold Nanoclusters. *Phys. Chem. Chem. Phys.* **2016**, *18* (13), 8773–8776. https://doi.org/10.1039/c6cp00538a.

(45) Gharibshahi, E.; Elias Saion. Influence of Dose on Particle Size and Optical Properties of Colloidal Platinum Nanoparticles. *Int. J. Mol. Sci.* **2012**, *13* (11), 14723–14741. https://doi.org/10.3390/ijms131114723.

(46) Langhammer, C.; Yuan, Z.; Zoric, I.; Kasemo, B. Plasmonic Properties of Supported Pt and Pd Nanostructures. *Nano Lett.* **2006**, *6* (4), 833–838. https://doi.org/10.1021/nl060219x.

(47)   Pei, Y.; Wang, P.; Ma, Z.; Xiong, L. Growth-Rule-Guided Structural Exploration of Thiolate-Protected Gold Nanoclusters. *Acc. Chem. Res.* **2019**, *52* (1), 23–33. https://doi.org/10.1021/acs.accounts.8b00385.

(48)   Yuan, S. F.; Guan, Z. J.; Liu, W. Di; Wang, Q. M. Solvent-Triggered Reversible Interconversion of All-Nitrogen-Donor-Protected Silver Nanoclusters and Their Responsive Optical Properties. *Nat. Commun.* **2019**, *10* (1), 1–7. https://doi.org/10.1038/s41467-019-11988-y.

(49)   Bootharaju, M. S.; Joshi, C. P.; Parida, M. R.; Mohammed, O. F.; Bakr, O. M. Templated Atom-Precise Galvanic Synthesis and Structure Elucidation of a [Ag24Au(SR)18]- Nanocluster. *Angew. Chemie - Int. Ed.* **2016**, *55* (3), 922–926. https://doi.org/10.1002/anie.201509381.

(50)   Bootharaju, M. S.; Burlakov, V. M.; Besong, T. M. D.; Joshi, C. P.; Abdulhalim, L. G.; Black, D. M.; Whetten, R. L.; Goriely, A.; Bakr, O. M. Reversible Size Control of Silver Nanoclusters via Ligand-Exchange. *Chem. Mater.* **2015**, *27* (12), 4289–4297. https://doi.org/10.1021/acs.chemmater.5b00650.

(51)   Back, S.; Yeom, M. S.; Jung, Y. Active Sites of Au and Ag Nanoparticle Catalysts for CO2 Electroreduction to CO. *ACS Catal.* **2015**, *5* (9), 5089–5096. https://doi.org/10.1021/acscatal.5b00462.

(52)   Udayabhaskararao, T.; Pradeep, T. New Protocols for the Synthesis of Stable Ag and Au Nanocluster Molecules. *J. Phys. Chem. Lett.* **2013**, *4* (9), 1553–1564. https://doi.org/10.1021/jz400332g.

(53)   Santiago-Gonzàlez, B.; Vázquez-Vázquez, C.; Blanco-Varela, M. C.; Martinho, J. M. G.; Ramallo-López, J. M.; Requejo, F. G.; M.A. López-Quintela. Synthesis of Water-Soluble Gold Clusters in Nanosomes Displaying Robust Photoluminescence with Very Large Stokes Shift. *J. Colloid Interfaces Sci.* **2015**, *455*, 154–162. https://doi.org/10.1016/j.jcis.2015.05.042.

(54)   Lakowicz, J. R. *Principles of Fluorescence Spectroscopy*, 3rd ed.; Springer US, 2006. https://doi.org/10.1007/978-0-387-46312-4.

(55)   Zheng, J.; Nicovich, P. R.; Dickson, R. M. Highly Fluorescent Quantum Dots. *Annu. Rev. Phys. Chem.* **2007**, *58* (1), 409–431. https://doi.org/10.1146/annurev.physchem.58.032806.104546.

(56)   Han, Z.; Dong, X.-Y.; Luo, P.; Li, S.; Wang, Z.-Y.; Zang, S.-Q.; Mak, T. C. W. Ultrastable Atomically Precise Chiral Silver Clusters with More than 95% Quantum Efficiency. *Sci. Adv.* **2020**, *6* (6), 107–115. https://doi.org/10.1126/sciadv.aay0107.

(57)   Zhikun Wu; Jin, R. On the Ligand's Role in the Fluorescence of Gold Nanoclusters. *Nano Lett.* **2010**, *10* (7), 2568–2573. https://doi.org/10.1021/nl101225f.

(58)   Yang, T.; Peng, B.; Shan, B.; Zong, Y.; Jiang, J.; Wu, P. Origin of the Photoluminescence of Metal Nanoclusters : From Metal-Centered Emission to Ligand-Centered Emission. *Nanomaterials* **2020**, *10* (2), 261–285. https://doi.org/10.3390/nano10020261.

(59)   Janssens, T. V. W.; Clausen, B. S.; Hvolbæk, B.; Falsig, H.; Christensen, C. H.; Bligaard, T.; Nørskov, J. K. Insights into the Reactivity of Supported Au Nanoparticles: Combining Theory and Experiments. *Top. Catal.* **2007**, *44*, 15–26. https://doi.org/10.1007/s11244-007-0335-3.

(60)   Li, Z.; Ji, S.; Liu, Y.; Cao, X.; Tian, S.; Chen, Y.; Niu, Z.; Li, Y. Well-Defined Materials for Heterogeneous Catalysis: From Nanoparticles to Isolated Single-Atom Sites. *Chem. Rev.* **2020**, *120* (2), 623–682. https://doi.org/10.1021/acs.chemrev.9b00311.

(61)   Hvolbæk, B.; Janssens, T. V. W.; Clausen, B. S.; Falsig, H.; Christensen, C. H.; Nørskov, J. K. Catalytic Activity of Au Nanoparticles. *Nano Today* **2007**, *2* (4), 14–18.

https://doi.org/10.1016/S1748-0132(07)70113-5.

(62)   Somorjai, G. A.; McCrea, K. Roadmap for Catalysis Science in the 21st Century: A Personal View of Building the Future on Past and Present Accomplishments. *Appl. Catal. A Gen.* **2001**, *222*, 3–18. https://doi.org/10.1016/S0926-860X(01)00825-0.

(63)   Crampton, A. S.; Rötzer, M. D.; Ridge, C. J.; Schweinberger, F. F.; Heiz, U.; Yoon, B.; Landman, U. Structure Sensitivity in the Nonscalable Regime Explored via Catalysed Ethylene Hydrogenation on Supported Platinum Nanoclusters. *Nat. Commun.* **2015**, *7*, 10389–10401. https://doi.org/10.1038/ncomms10389.

(64)   Guo, L.; Du, P.; Fu, X.; Ma, C.; Zeng, J.; Si, R.; Huang, Y.; Jia, C. Contributions of Distinct Gold Species to Catalytic Reactivity for Carbon Monoxide Oxidation. *Nat. Commun.* **2016**, *7*, 1–8. https://doi.org/10.1038/ncomms13481.

(65)   Liu, L.; Meira, D. M.; Arenal, R.; Concepcion, P.; Puga, A. V.; Corma, A. Determination of the Evolution of Heterogeneous Single Metal Atoms and Nanoclusters under Reaction Conditions: Which Are the Working Catalytic Sites? *ACS Catal.* **2019**, *9* (12), 10626–10639. https://doi.org/10.1021/acscatal.9b04214.

(66)   Calle-Vallejo, F.; Pohl, M. D.; Reinisch, D.; Loffreda, D.; Sautet, P.; Bandarenka, A. S. Why Conclusions from Platinum Model Surfaces Do Not Necessarily Lead to Enhanced Nanoparticle Catalysts for the Oxygen Reduction Reaction. *Chem. Sci.* **2017**, *8*, 2283–2289. https://doi.org/10.1039/C6SC04788B.

(67)   Shimizu, K.; Miyamoto, Y.; Satsuma, A. Size- and Support-Dependent Silver Cluster Catalysis for Chemoselective Hydrogenation of Nitroaromatics. *J. Catal.* **2010**, *270* (1), 86–94. https://doi.org/10.1016/j.jcat.2009.12.009.

(68)   Chang, Z.; Jing, X.; He, C.; Liu, X.; Duan, C. Silver Clusters as Robust Nodes and π-Activation Sites for the Construction of Heterogeneous Catalysts for the Cycloaddition of Propargylamines. *ACS Catal.* **2018**, *8* (2), 1384–1391. https://doi.org/10.1021/acscatal.7b02844.

(69)   Boronat, M.; Garc, S. Enhanced Stability of Cu Clusters of Low Atomicity against Oxidation. Effect on the Catalytic Redox Process. *ACS Catal.* **2017**, *7* (5), 3560–3568. https://doi.org/10.1021/acscatal.7b00778.

(70)   Ndolomingo, M. J.; Bingwa, N.; Meijboom, R. Review of Supported Metal Nanoparticles : Synthesis Methodologies , Advantages and Application as Catalysts. *J. Mater. Sci.* **2020**, *55*, 6195–6241. https://doi.org/10.1007/s10853-020-04415-x.

(71)   Samantaray, M. K.; Elia, V. D.; Pump, E.; Falivene, L.; Harb, M.; Chikh, S. O.; Cavallo, L.; Basset, J. The Comparison between Single Atom Catalysis and Surface Organometallic Catalysis. *Chem. Rev.* **2020**, *120* (2), 734–813. https://doi.org/10.1021/acs.chemrev.9b00238.

(72)   Ulusal, F.; Erünal, E.; Güzel, B. Green Preparation of Pd Nanoparticles on SBA-15 via Supercritical Fluid Deposition and Application on Suzuki–Miyaura Cross-Coupling Reaction. *J. Nanoparticle Res.* **2018**, *20* (8), 219–232. https://doi.org/10.1007/s11051-018-4325-0.

(73)   Shultz, L. R.; Hu, L.; Preradovic, K.; Beazley, M. J.; Feng, X.; Jurca, T. A Broader-Scope Analysis of the Catalytic Reduction of Nitrophenols and Azo Dyes with Noble Metal Nanoparticles. *ChemCatChem* **2019**, *11* (11), 2590–2595. https://doi.org/10.1002/cctc.201900260.

(74)   Zhang, Z.; Luo, Y.; Guo, Y.; Shi, W.; Wang, W.; Zhang, B.; Zhang, R.; Bao, X.; Wu, S.; Cui, F. Pd and Pt Nanoparticles Supported on the Mesoporous Silica Molecular Sieve SBA-15 with Enhanced Activity and Stability in Catalytic Bromate Reduction. *Chem. Eng. J.* **2018**, *344*, 114–123. https://doi.org/10.1016/j.cej.2018.03.056.

(75)   Yang, Y.; Ochoa-Hernández, C.; De La Peña O'Shea, V. A.; Coronado, J. M.; Serrano, D. P. Ni2P/SBA-15 as a Hydrodeoxygenation Catalyst with Enhanced Selectivity for the Conversion of Methyl Oleate into n-Octadecane. *ACS Catal.* **2012**, *2* (4), 592–598. https://doi.org/10.1021/cs200659r.

(76)   Uson, L.; Hueso, J. L.; Sebastian, V.; Arenal, R.; Florea, I.; Irusta, S.; Arruebo, M.; Santamaria, J. In-Situ Preparation of Ultra-Small Pt Nanoparticles within Rod-Shaped Mesoporous Silica Particles: 3-D Tomography and Catalytic Oxidation of n-Hexane. *Catal. Commun.* **2017**, *100*, 93–97. https://doi.org/10.1016/j.catcom.2017.06.022.

(77)   Morales-Lara, F.; Abdelkader-Fernández, V. K.; Melguizo, M.; Turco, A.; Mazzotta, E.; Domingo-García, M.; López-Garzón, F. J.; Pérez-Mendoza, M. Ultra-Small Metal Nanoparticles Supported on Carbon Nanotubes through Surface Chelation and Hydrogen Plasma Reduction for Methanol Electro-Oxidation. *J. Mater. Chem. A* **2019**, *7* (42), 24502–24514. https://doi.org/10.1039/c9ta08424j.

(78)   Martinez, G.; Malumbres, A.; Lopez, A.; Mallada, R.; Hueso, J. L. Laser-Assisted Production of Carbon-Encapsulated Pt-Co Alloy Nanoparticles for Preferential Oxidation of Carbon Monoxide. *Front. Chem.* **2018**, *6*, 487–497. https://doi.org/10.3389/fchem.2018.00487.

(79)   Vajda, S.; White, M. G. Catalysis Applications of Size-Selected Cluster Deposition. *ACS Catal.* **2015**, *5* (12), 7152–7176. https://doi.org/10.1021/acscatal.5b01816.

(80)   Wu, Z.; Lanni, E.; Chen, W.; Bier, M. E.; Ly, D.; Jin, R. High Yield, Large Scale Synthesis of Thiolate-Protected Ag7 Clusters. *J. Am. Chem. Soc.* **2009**, *131* (46), 16672–16674. https://doi.org/10.1021/ja907627f.

(81)   Zeng, C.; Li, T.; Das, A.; Rosi, N. L.; Jin, R. Chiral Structure of Thiolate-Protected 28-Gold-Atom Nanocluster Determined by X-Ray Crystallography. *J. Am. Chem. Soc.* **2013**, *135* (27), 10011–10013. https://doi.org/10.1021/ja404058q |.

(82)   Nimmala, P. R.; Yoon, B.; Whetten, R. L.; Landman, U.; Dass, A. Au67(SR)35 Nanomolecules: Characteristic Size-Specific Optical, Electrochemical, Structural Properties and First-Principles Theoretical Analysis. *J. Phys. Chem. A* **2013**, *117* (2), 504–517. https://doi.org/10.1021/jp311491v.

(83)   Udayabhaskararao, T.; Bootharaju, M. S.; Pradeep, T. Thiolate-Protected Ag32 Clusters: Mass Spectral Studies of Composition and Insights into the Ag-Thiolate Structure from NMR. *Nanoscale* **2013**, *5* (19), 9404–9411. https://doi.org/10.1039/c3nr03463a.

(84)   Udaya Bhaskara Rao, T.; Pradeep, T. Luminescent Ag7 and Ag8 Clusters by Interfacial Synthesis. *Angew. Chemie - Int. Ed.* **2010**, *49* (23), 3925–3929. https://doi.org/10.1002/anie.200907120.

(85)   Chakraborty, I.; Pradeep, T. Atomically Precise Clusters of Noble Metals: Emerging Link between Atoms and Nanoparticles. *Chem. Rev.* **2017**, *117* (12), 8208–8271. https://doi.org/10.1021/acs.chemrev.6b00769.

(86)   Chong, H.; Zhu, M. Catalytic Reduction by Quasi-Homogeneous Gold Nanoclusters in the Liquid Phase. *ChemCatChem* **2015**, *7* (15), 2296–2304. https://doi.org/10.1002/cctc.201500247.

(87)   Huang, W.; Liu, J. H. C.; Alayoglu, P.; Li, Y.; Witham, C. A.; Tsung, C. K.; Toste, F. D.; Somorjai, G. A. Highly Active Heterogeneous Palladium Nanoparticle Catalysts for Homogeneous Electrophilic Reactions in Solution and the Utilization of a Continuous Flow Reactor. *J. Am. Chem. Soc.* **2010**, *132* (47), 16771–16773. https://doi.org/10.1021/ja108898t.

(88)   Thanh, N. T. K.; Maclean, N.; Mahiddine, S. Mechanisms of Nucleation and Growth of

144

Nanoparticles in Solution. *Chem. Rev.* **2014**, *114* (15), 7610–7630. https://doi.org/10.1021/cr400544s.

(89) Huang, H.; Toit, H. du; Besenhard, M. O.; Ben-Jaber, S.; Dobson, P.; Parkin, I.; Gavriilidis, A. Continuous Flow Synthesis of Ultrasmall Gold Nanoparticles in a Microreactor Using Trisodium Citrate and Their SERS Performance. *Chem. Eng. Sci.* **2018**, *189*, 422–430. https://doi.org/10.1016/j.ces.2018.06.050.

(90) Biswas, S.; Miller, J. T.; Li, Y.; Nandakumar, K.; Kumar, C. S. S. R. Developing a Millifluidic Platform for the Synthesis of Ultrasmall Nanoclusters: Ultrasmall Copper Nanoclusters as a Case Study. *Small* **2012**, *8* (5), 688–698. https://doi.org/10.1002/smll.201102100.

(91) Aiken III, J. D.; Finke, R. G. A Review of Modern Transition-Metal Nanoclusters: Their Synthesis, Characterization, and Applications in Catalysis. *J. Mol. Catal. A Chem.* **1999**, *145* (1–2), 1–44. https://doi.org/10.1016/S1381-1169(99)00098-9.

(92) Liu, L.; Lopez-Haro, M.; Lopes, C. W.; Li, C.; Concepcion, P.; Simonelli, L.; Calvino, J. J.; Corma, A. Regioselective Generation and Reactivity Control of Subnanometric Platinum Clusters in Zeolites for High-Temperature Catalysis. *Nat. Mater.* **2019**, *18* (8), 866–873. https://doi.org/10.1038/s41563-019-0412-6.

(93) Zhang, H.; Huang, X.; Li, L.; Zhang, G.; Hussain, I.; Li, Z.; Tan, B. Photoreductive Synthesis of Water-Soluble Fluorescent Metal Nanoclusters. *Chem. Commun.* **2012**, *48* (4), 567–569. https://doi.org/10.1039/c1cc16088e.

(94) Xu, H.; Suslick, K. S. Sonochemical Synthesis of Highly Fluorescent Ag Nanoclusters. *ACS Nano* **2010**, *4* (6), 3209–3214. https://doi.org/10.1021/nn100987k.

(95) Liu, S.; Lu, F.; Zhu, J.-J. Highly Fluorescent Ag Nanoclusters: Microwave-Assisted Green Synthesis and Cr3+ Sensing. *Chem. Commun.* **2011**, *47* (9), 2661–2663. https://doi.org/10.1039/c0cc04276e.

(96) Costandy, J. G.; Edgar, T. F.; Michael Baldea. Switching from Batch to Continuous Reactors Is a Trajectory Optimization Problem. *Ind. Eng. Chem. Res.* **2019**, *58* (30), 13718–13736. https://doi.org/10.1021/acs.iecr.9b01126.

(97) The, H. Le; Ta, B. Q.; Thanh, H. Le; Dong, T.; Thoi, T. N.; Karlsen, F. Geometric Effects on Mixing Performance in a Novel Passive Micromixer with Trapezoidal-Zigzag Channels. *J. Micromechanics Microengineering* **2015**, *25* (9), 094004–094015. https://doi.org/10.1088/0960-1317/25/9/094004.

(98) Afzal, A.; Kim, K. Y. Convergent-Divergent Micromixer Coupled with Pulsatile Flow. *Sensors Actuators, B Chem.* **2015**, *211*, 198–205. https://doi.org/10.1016/j.snb.2015.01.062.

(99) Lee, C. Y.; Chang, C. L.; Wang, Y. N.; Fu, L. M. Microfluidic Mixing: A Review. *Int. J. Mol. Sci.* **2011**, *12* (5), 3263–3287. https://doi.org/10.3390/ijms12053263.

(100) Sebastian, V.; Khan, S. A.; Kulkarni, A. A. Perspective Article: Flow Synthesis of Functional Materials. *J. Flow Chem.* **2017**, *7* (3–4), 96–105. https://doi.org/10.1556/1846.2017.00028.

(101) Luo, Z.; Castleman, A. W.; Khanna, S. N. Reactivity of Metal Clusters. *Chem. Rev.* **2016**, *116* (23), 14456–14492. https://doi.org/10.1021/acs.chemrev.6b00230.

(102) Sebastian, V. High and Efficient Production of Nanomaterials by Microfluidic Reactor Approaches. In *Advances in Microfluidics - New Applications in Biology, Energy, and Materials Sciences*; Yu, X.-Y., Ed.; IntechOpen, 2016. https://doi.org/10.5772/64347.

(103) David M., S.; Haben, P. M.; Novet, T. E.; Peterson, D. A.; Williams, G. M. Continuous Flow Reactor for the Synthesis of Nanoparticles. WO 2014/153266 A3, 2014.

(104) Feng, J.; Biskos, G.; Schmidt-Ott, A. Toward Industrial Scale Synthesis of Ultrapure Singlet Nanoparticles with Controllable Sizes in a Continuous Gas-Phase Process. *Sci. Rep.* **2015**, *5*, 15788–15797. https://doi.org/10.1038/srep15788.

(105) Krisztián, N.; Wootsch, A.; Groualle, M.; Otvös, Z.; Darvas, F. Instrument and Process for Nanoparticles Production in Continuous Flow Mode. WO2009/1334.18, 2009.

(106) Jähnisch, K.; Hessel, V.; Löwe, H.; Baerns, M. Chemistry in Microstructured Reactors. *Angew. Chemie - Int. Ed.* **2004**, *43* (4), 406–446. https://doi.org/10.1002/anie.200300577.

(107) Solorzano, I. O. De; Uson, L.; Miana, M.; Sebastian, V.; Arruebo, M. Continuous Synthesis of Drug-Loaded Nanoparticles Using Microchannel Emulsification and Numerical Modeling : Effect of Passive Mixing. *Int. J. Nanomedicine* **2016**, *11*, 3397–3416. https://doi.org/10.2147/IJN.S108812.

(108) Cabeza, V. S.; Kuhn, S.; Kulkarni, A. A.; Jensen, K. F. Size-Controlled Flow Synthesis of Gold Nanoparticles Using a Segmented Flow Microfluidic Platform. *Langmuir* **2012**, *28* (17), 7007–7013. https://doi.org/10.1021/la205131e.

(109) Nishioka, M.; Miyakawa, M.; Kataoka, H.; Koda, H.; Sato, K.; Suzuki, T. M. Continuous Synthesis of Monodispersed Silver Nanoparticles Using a Homogeneous Heating Microwave Reactor System. *Nanoscale* **2011**, *3* (6), 2621–2626. https://doi.org/10.1039/c1nr10199d.

(110) Estel, L.; Poux, M.; Benamara, N.; Polaert, I. Continuous Flow-Microwave Reactor: Where Are We? *Chem. Eng. Process. - Process Intensif.* **2017**, *113*, 56–64. https://doi.org/10.1016/j.cep.2016.09.022.

(111) Website. Percy Spencer Melts a Chocolate Bar, Invents the Microwave Oven Percy Spencer Melts a Chocolate Bar, Invents the Microwave Oven (accessed May 8, 2020).

(112) Horikoshi, S.; Schiffmann, R. F.; Fukushima, J.; Serpone, N. *Microwave Chemical and Materials Processing: A Tutorial*; Springer Nature Singapore Pte Ltd. 2018, 2017. https://doi.org/10.1007/978-981-10-6466-1.

(113) Chandrasekaran, S.; Ramanathan, S.; Basak, T. Microwave Material Processing—A Review. *AIChE J.* **2012**, *58* (2), 330–363. https://doi.org/10.1002/aic.12766.

(114) Horikoshi, S.; Serpone, N. *Microwaves in Catalysis - Methodology and Applications*; Wiley-VCH Verlag GmbH & Co. KGaA, Ed.; 2015. https://doi.org/10.1002/9783527688111.

(115) Saxena, V. K. K.; Chandra, U. Microwave Synthesis: A Physical Concept. In *Microwave Heating*; IntechOpen, 2011; pp 3–23. https://doi.org/10.5772/22888.

(116) Baxendale, I. R.; Hayward, J. J.; Ley, S. V. Microwave Reactions Under Continuous Flow Conditions. *Comb. Chem. High Throughput Screen.* **2007**, *10* (10), 802–836. https://doi.org/10.2174/138620707783220374.

(117) Horikoshi, S.; Sumi, T.; Serpone, N. A Hybrid Microreactor/Microwave High-Pressure Flow System of a Novel Concept Design and Its Application to the Synthesis of Silver Nanoparticles. *Chem. Eng. Process. Process Intensif.* **2013**, *73*, 59–66. https://doi.org/10.1016/j.cep.2013.07.009.

(118) Horikoshi, S.; Abe, H.; Torigoe, K.; Abe, M.; Serpone, N. Access to Small Size Distributions of Nanoparticles by Microwave-Assisted Synthesis. Formation of Ag Nanoparticles in Aqueous

Carboxymethylcellulose Solutions in Batch and Continuous-Flow Reactors. *Nanoscale* **2010**, *2* (8), 1441–1447. https://doi.org/10.1039/c0nr00141d.

(119)   Horikoshi, S.; Watanabe, T.; Narita, A.; Suzuki, Y.; Serpone, N. The Electromagnetic Wave Energy Effect(s) in Microwave-Assisted Organic Syntheses (MAOS). *Sci. Rep.* **2018**, *8* (1), 5151–5161. https://doi.org/10.1038/s41598-018-23465-5.

(120)   Dzido, G.; Markowski, P.; Małachowska-Jutsz, A.; Prusik, K.; Jarzębski, A. B. Rapid Continuous Microwave-Assisted Synthesis of Silver Nanoparticles to Achieve Very High Productivity and Full Yield: From Mechanistic Study to Optimal Fabrication Strategy. *J. Nanoparticle Res.* **2015**, *17* (27), 26–41. https://doi.org/10.1007/s11051-014-2843-y.

(121)   Manno, R.; Sebastian, V.; Mallada, R.; Santamaria, J. 110th Anniversary: Nucleation of Ag Nanoparticles in Helical Microfluidic Reactor. Comparison between Microwave and Conventional Heating. *Ind. Eng. Chem. Res.* **2019**, *58* (28), 12702–12711. https://doi.org/10.1021/acs.iecr.9b01460.

(122)   Sturm, G. S. J.; Van Braam Houckgeest, A. Q.; Verweij, M. D.; Van Gerven, T.; Stankiewicz, A. I.; Stefanidis, G. D. Exploration of Rectangular Waveguides as a Basis for Microwave Enhanced Continuous Flow Chemistries. *Chem. Eng. Sci.* **2013**, *89*, 196–205. https://doi.org/10.1016/j.ces.2012.11.039.

(123)   Wagner, J.; Köhler, J. M. Continuous Synthesis of Gold Nanoparticles in a Microreactor. *Nano Lett.* **2005**, *5* (4), 685–691. https://doi.org/10.1021/nl050097t.

(124)   Helmlinger, J.; Heise, M.; Heggen, M.; Epple, M.; Ruck, M.; Epple, M. A Rapid, High-Yield and Large-Scale Synthesis of Uniform Spherical Silver Nanoparticles by a Microwave-Assisted Polyol Process. *RSC Adv.* **2015**, *5* (112), 92144–92150. https://doi.org/10.1039/C5RA20446A.

(125)   Zhao, C.; He, L.; Zhang, S.; Middelberg, A. P. J. Nanoparticle Synthesis in Microreactors. *Chem. Eng. Sci.* **2011**, *66* (7), 1463–1479. https://doi.org/10.1016/j.ces.2010.08.039.

(126)   Martínez, G.; Sebastián, V.; Hueso, J. L. Alternative Methodologies for the Production of Nanomaterials Based on Microfluidics and Laser Pyrolysis Technologies. In *Manufacturing Nanostructures*; Ahmed, W., Ali, N., Eds.; One Central Press, 2015; p 417.

(127)   Sebastián, V.; Jensen, K. F. Nanoengineering a Library of Metallic Nanostructures Using a Single Micro Fluidic Reactor. *Nanoscale* **2016**, *8* (33), 15288–15295. https://doi.org/10.1039/c6nr04104c.

(128)   Makgwane, P. R.; Ray, S. S. Synthesis of Nanomaterials by Continuous-Flow Microfluidics : A Review. *J. Nanosci. Nanotechnol.* **2014**, *14* (2), 1338–1363. https://doi.org/10.1166/jnn.2014.9129.

(129)   Ma, J.; Lee, S. M.; Yi, C.; Li, C. Controllable Synthesis of Functional Nanoparticles by Microfluidic Platforms for Biomedical Applications – a Review. *Lab Chip* **2017**, *17*, 209–226. https://doi.org/10.1039/c6lc01049k.

(130)   Lu, M.; Ozcelik, A.; Grigsby, C. L.; Zhao, Y.; Guo, F.; Leong, K. W.; Tony. Microfluidic Hydrodynamic Focusing for Synthesis of Nanomaterials. *Nano Today* **2016**, *11* (6), 778–792. https://doi.org/10.1016/j.nantod.2016.10.006.

(131)   Song, Y.; Hormes, J.; Kumar, C. S. S. R. Microfluidic Synthesis of Nanomaterials. *Small* **2008**, *4* (6), 698–711. https://doi.org/10.1002/smll.200701029.

(132)   Tsuji, M.; Hashimoto, M.; Nishizawa, Y.; Kubokawa, M.; Tsuji, T. Microwave-Assisted

Synthesis of Metallic Nanostructures in Solution. *Chem. - A Eur. J.* **2005**, *11* (2), 440–452. https://doi.org/10.1002/chem.200400417.

(133) Gawande, M. B.; Shelke, S. N.; Zboril, R.; Varma, R. S. Microwave-Assisted Chemistry: Synthetic Applications for Rapid Assembly of Nanomaterials and Organics. *Acc. Chem. Res.* **2014**, *47* (4), 1338–1348. https://doi.org/10.1021/ar400309b.

(134) Gerbec, J. A.; Magana, D.; Washington, A.; Strouse, G. F. Microwave-Enhanced Reaction Rates for Nanoparticle Synthesis. *J. Am. Chem. Soc.* **2005**, *127* (45), 15791–15800. https://doi.org/10.1021/ja052463g.

(135) Gjuraj, E.; Kongoli, R.; Shore, G. Combination of Flow Reactors with Microwave-Assisted Synthesis: Smart Engineering Concept for Steering Synthetic Chemistry on the "Fast Lane." *Chem. Biochem. Eng. Q.* **2012**, *26* (3), 285–307.

(136) Glasnov, T. N.; Kappe, C. O. Microwave-Assisted Synthesis under Continuous-Flow Conditions. *Macromol. Rapid Commun.* **2007**, *28* (4), 395–410. https://doi.org/10.1002/marc.200600665.

(137) Dzido, G.; Jarzębski, A. B. Fabrication of Silver Nanoparticles in a Continuous Flow, Low Temperature Microwave-Assisted Polyol Process. *J. Nanoparticle Res.* **2011**, *13* (6), 2533–2541. https://doi.org/10.1007/s11051-010-0146-5.

(138) Nigar, H.; Julián, I.; Mallada, R.; Santamaría, J. Microwave-Assisted Catalytic Combustion for the Efficient Continuous Cleaning of VOC-Containing Air Streams. *Environ. Sci. Technol.* **2018**, *52* (10), 5892–5901. https://doi.org/10.1021/acs.est.8b00191.

(139) Nigar, H.; Sturm, G. S. J.; Garcia-Baños, B.; Peñaranda-Foix, F. L.; Catalá-Civera, J. M.; Mallada, R.; Stankiewicz, A.; Santamaría, J. Numerical Analysis of Microwave Heating Cavity: Combining Electromagnetic Energy, Heat Transfer and Fluid Dynamics for a NaY Zeolite Fixed-Bed. *Appl. Therm. Eng.* **2019**, *155*, 226–238. https://doi.org/10.1016/j.applthermaleng.2019.03.117.

(140) Yang, D. Design and Fabrication of an End-Launched Rectangular Waveguide Adapter Fed by a Coaxial Loop. *J. Inf. Commun. Converg. Eng.* **2012**, *10* (2), 103–107. https://doi.org/10.6109/jicce.2012.10.2.103.

(141) Horikoshi, S.; Serpone, N. *Microwaves in Nanoparticle Synthesis: Fundamentals and Applications*; Wiley-VCH, Ed.; 2013. https://doi.org/10.1002/9783527648122.

(142) Zhu, J.; Kuznetsov, A. V.; Sandeep, K. P. Mathematical Modeling of Continuous Flow Microwave Heating of Liquids. *Int. J. Therm. Sci.* **2007**, *46* (4), 328–341. https://doi.org/10.1016/j.ijthermalsci.2006.06.005.

(143) Khan, I. U.; Serra, C. A.; Anton, N.; Vandamme, T. F. Production of Nanoparticle Drug Delivery Systems with Microfluidics Tools. *Expert Opin. Drug Deliv.* **2015**, *12* (4), 547–562. https://doi.org/10.1517/17425247.2015.974547.

(144) Chen, H.; Meiners, J. C. Topologic Mixing on a Microfluidic Chip. *Appl. Phys. Lett.* **2004**, *84* (12), 2193–2195. https://doi.org/10.1063/1.1686895.

(145) Kumar, V.; Aggarwal, M.; Nigam, K. D. P. Mixing in Curved Tubes. *Chem. Eng. Sci.* **2006**, *61* (17), 5742–5753. https://doi.org/10.1016/j.ces.2006.04.040.

(146) Nivedita, N.; Ligrani, P.; Papautsky, I. Dean Flow Dynamics in Low-Aspect Ratio Spiral Microchannels. *Sci. Rep.* **2017**, *7*, 1–10. https://doi.org/10.1038/srep44072.

(147)   Tang, L.; Tang, Y.; Parameswaran, S. A Numerical Study of Flow Characteristics in a Helical Pipe. *Adv. Mech. Eng.* **2016**, *8* (7), 1–8. https://doi.org/10.1177/1687814016660242.

(148)   Fievet, F.; Ammar-Merah, S.; Brayner, R.; Chau, F.; Giraud, M.; Mammeri, F.; Peron, J.; Piquemal, J. Y.; Sicard, L.; Viau, G. The Polyol Process: A Unique Method for Easy Access to Metal Nanoparticles with Tailored Sizes, Shapes and Compositions. *Chem. Soc. Rev.* **2018**, *47* (14), 5187–5233. https://doi.org/10.1039/c7cs00777a.

(149)   Spivey, J. J.; Han, Y.-F. *Catalysis: Volume 29*; Royal Society of Chemistry, 2017.

(150)   Isobe, K. Oxidation of Ethylene Glycol and Glycolic Acid by Glycerol Oxidase. *Biosci. Biotechnol. Biochem.* **1995**, *59* (4), 576–581. https://doi.org/10.1271/bbb.59.576.

(151)   Baber, R.; Mazzei, L.; Thanh, N. T. K.; Gavriilidis, A. Synthesis of Silver Nanoparticles in a Microfluidic Coaxial Flow Reactor. *RSC Adv.* **2015**, *5* (116), 95585–95591. https://doi.org/10.1039/c5ra17466j.

(152)   Slistan-Grijalva, A.; Herrera-Ubina, R.; Silva-Rivas, J. F.; Ávalos-Borja, M.; Castillón-Barraza, F. F.; Posada-Amarillas, A. Classical Theoretical Characterization of the Surface Plasmon Absorption Band for Silver Spherical Nanoparticles Suspended in Water and Ethylene Glycol. *Physica* **2015**, *27* (1–2), 104–112. https://doi.org/10.1016/j.physe.2004.10.014.

(153)   Jiang, H.; Moon, K.; Zhang, Z.; Pothukuchi, S.; Wong, C. P. Variable Frequency Microwave Synthesis of Silver Nanoparticles. *J. Nanoparticle Res.* **2006**, *8* (1), 117–124. https://doi.org/10.1007/s11051-005-7522-6.

(154)   Baghbanzadeh, M.; Carbone, L.; Cozzoli, P. D.; Kappe, C. O. Microwave-Assisted Synthesis of Colloidal Inorganic Nanocrystals. *Angew. Chemie - Int. Ed.* **2011**, *50* (48), 11312–11359. https://doi.org/10.1002/anie.201101274.

(155)   Suchomel, P.; Kvitek, L.; Prucek, R.; Panacek, A.; Halder, A.; Vajda, S.; Zboril, R. Simple Size-Controlled Synthesis of Au Nanoparticles and Their Size-Dependent Catalytic Activity. *Sci. Rep.* **2018**, *8* (1), 1–11. https://doi.org/10.1038/s41598-018-22976-5.

(156)   Wu, Z.; Yang, S.; Wu, W. Shape Control of Inorganic Nanoparticles from Solution. *Nanoscale* **2016**, *8* (3), 1237–1259. https://doi.org/10.1039/c5nr07681a.

(157)   Calderón-Jiménez, B.; Johnson, M. E.; Montoro Bustos, A. R.; Murphy, K. E.; Winchester, M. R.; Baudrit, J. R. V. Silver Nanoparticles: Technological Advances, Societal Impacts, and Metrological Challenges. *Front. Chem.* **2017**, *5* (Feb), 1–26. https://doi.org/10.3389/fchem.2017.00006.

(158)   Becker, R.; Döring, W. Kinetische Behandlung Der Keimbildung in Übersättigten Dämpfen. *Ann. Phys.* **1935**, *416* (8), 719–752. https://doi.org/10.1002/andp.19354160806.

(159)   Polte, J. Fundamental Growth Principles of Colloidal Metal Nanoparticles - a New Perspective. *CrystEngComm* **2015**, *17* (36), 6809–6830. https://doi.org/10.1039/c5ce01014d.

(160)   Keating, M.; Chen, Y.; Larmour, I. A.; Faulds, K.; Graham, D. Growth and Surface-Enhanced Raman Scattering of Ag Nanoparticle Assembly in Agarose Gel. *Meas. Sci. Technol.* **2012**, *23* (8), 84006–840015. https://doi.org/10.1088/0957-0233/23/8/084006.

(161)   Burda, C.; Chen, X.; Narayanan, R.; El-Sayed, M. A. Chemistry and Properties of Nanocrystals of Different Shapes. *Chem. Rev.* **2005**, *105* (4), 1025–1102. https://doi.org/10.1021/cr030063a.

(162)   Belloni, J.; Mostafavi, M. Radiation Chemistry of Nanocolloids and Clusters. *Stud. Phys. Theor. Chem.* **2001**, *87*, 411–452. https://doi.org/10.1016/S0167-6881(01)80018-5.

(163)   Mostafavi, M.; Rey, G. R.; François, L.; Belloni, J. Transient and Stable Silver Clusters Induced by Radiolysis in Methanol. *J. Phys. Chem. A* **2002**, *106* (43), 10184–10194. https://doi.org/10.1021/jp014257a.

(164)   Remita, S.; Orts, J. M.; Feliu, J. M.; Mostafavi, M.; Delcourt, M. O. STM Identification of Silver Oligomer Clusters Prepared by Radiolysis in Aqueous Solution. *Chem. Phys. Lett.* **1994**, *218* (1,2), 115–121. https://doi.org/10.1016/0009-2614(93)E1451-L.

(165)   Tu, W.; Liu, H. Continuous Synthesis of Colloidal Metal Nanoclusters by Microwave Irradiation. *Chem. Mater.* **2000**, *12* (2), 564–567. https://doi.org/10.1021/cm990637l.

(166)   Díez, I.; Pusa, M.; Kulmala, S.; Jiang, H.; Walther, A.; Goldmann, A. S.; Müller, A. H. E.; Ikkala, O.; Ras, R. H. A. Color Tunability and Electrochemiluminescence of Silver Nanoclusters. *Angew. Chemie - Int. Ed.* **2009**, *48* (12), 2122–2125. https://doi.org/10.1002/anie.200806210.

(167)   Lai, Y. T.; Chen, T. C.; Lan, Y. K.; Chen, B. S.; You, J. H.; Yang, C. M.; Lai, N. C.; Wu, J. H.; Chen, C. S. Pt/SBA-15 as a Highly Efficient Catalyst for Catalytic Toluene Oxidation. *ACS Catal.* **2014**, *4* (11), 3824–3836. https://doi.org/10.1021/cs500733j.

(168)   Zhang, S.; Muratsugu, S.; Ishiguro, N.; Tada, M. Ceria-Doped Ni/SBA-16 Catalysts for Dry Reforming of Methane. *ACS Catal.* **2013**, *3* (8), 1885–1864. https://doi.org/10.1021/cs400159w.

(169)   Zuliani, A.; Ranjan, P.; Luque, R.; Van Der Eycken, E. V. Heterogeneously Catalyzed Synthesis of Imidazolones via Cycloisomerizations of Propargylic Ureas Using Ag and Au/Al SBA-15 Systems. *ACS Sustain. Chem. Eng.* **2019**, *7* (5), 5568–5575. https://doi.org/10.1021/acssuschemeng.9b00198.

(170)   Fan, H. T.; Liu, X. G.; Xing, X. J.; Li, B.; Wang, K.; Chen, S. T.; Wu, Z.; Qiu, D. F. Ordered Mesoporous Silica Cubic Particles Decorated with Silver Nanoparticles: A Highly Active and Recyclable Heterogeneous Catalyst for the Reduction of 4-Nitrophenol. *Dalt. Trans.* **2019**, *48* (8), 2692–2700. https://doi.org/10.1039/c8dt04663h.

(171)   Slowing, I. I.; Vivero-Escoto, J. L.; Wu, C. W.; Lin, V. S. Y. Mesoporous Silica Nanoparticles as Controlled Release Drug Delivery and Gene Transfection Carriers. *Adv. Drug Deliv. Rev.* **2008**, *60* (11), 1278–1288. https://doi.org/10.1016/j.addr.2008.03.012.

(172)   Li, Z.; Barnes, J. C.; Bosoy, A.; Stoddart, J. F.; Zink, J. I. Mesoporous Silica Nanoparticles in Biomedical Applications. *Chem. Soc. Rev.* **2012**, *41* (7), 2590–2605. https://doi.org/10.1039/c1cs15246g.

(173)   Argyo, C.; Weiss, V.; Bräuchle, C.; Bein, T. Multifunctional Mesoporous Silica Nanoparticles as a Universal Platform for Drug Delivery. *Chem. Mater.* **2014**, *26* (1), 435–451. https://doi.org/10.1021/cm402592t.

(174)   Mesoporous Silica Nanoparticles https://nanocomposix.com/pages/mesoporous-silica-nanoparticles#target (accessed Aug 17, 2020).

(175)   Larrea, A.; Eguizabal, A.; Sebastian, V. Gas-Directed Production of Noble Metal-Magnetic Heteronanostructures in Continuous Fashion: Application in Catalysis. *ACS Appl. Mater. Interfaces* **2019**, *11* (46), 43520–43532. https://doi.org/10.1021/acsami.9b15982.

(176)   Strachan, J.; Barnett, C.; Masters, A. F.; Maschmeyer, T. 4-Nitrophenol Reduction: Probing the Putative Mechanism of the Model Reaction. *ACS Catal.* **2020**, *10* (10), 5516–5521. https://doi.org/10.1021/acscatal.0c00725.

(177)   Johansson, E. M.; Ballem, M. A.; Córdoba, J. M.; Odén, M. Rapid Synthesis of SBA-15 Rods with Variable Lengths, Widths, and Tunable Large Pores. *Langmuir* **2011**, *27* (8), 4994–4999.

https://doi.org/10.1021/la104864d.

(178) Hoffmann, F.; Fröba, M. Vitalising Porous Inorganic Silica Networks with Organic Functions—PMOs and Related Hybrid Materials. *Chem. Soc. Rev.* **2011**, *40* (2), 608–620. https://doi.org/10.1039/c0cs00076k.

(179) Rivera-Muñoz, E. M.; Huirache-Acuña, R. Sol Gel-Derived SBA-16 Mesoporous Material. *Int. J. Mol. Sci.* **2010**, *11* (9), 3069–3086. https://doi.org/10.3390/ijms11093069.

(180) Johansson, E. M.; Córdoba, J. M.; Odén, M. The Effects on Pore Size and Particle Morphology of Heptane Additions to the Synthesis of Mesoporous Silica SBA-15. *Microporous Mesoporous Mater.* **2010**, *133* (1–3), 66–74. https://doi.org/10.1016/j.micromeso.2010.04.016.

(181) J.L. Blin; Imperór-Clerc, M. Mechanism of Self-Assembly in the Synthesis of Silica Mesoporous Materials: In Situ Studies by X-Ray and Neutron Scattering. *Chem. Soc. Rev.* **2013**, *42* (9), 4071–4082. https://doi.org/10.1039/C2CS35362H.

(182) Sturm, G. S. J.; Verweij, M. D.; Van Gerven, T.; Stankiewicz, A. I.; Stefanidis, G. D. On the Effect of Resonant Microwave Fields on Temperature Distribution in Time and Space. *Int. J. Heat Mass Transf.* **2012**, *55* (13–14), 3800–3811. https://doi.org/10.1016/j.ijheatmasstransfer.2012.02.065.

(183) Takesue, M.; Tomura, T.; Yamada, M.; Hata, K.; Kuwamoto, S.; Yonezawa, T. Size of Elementary Clusters and Process Period in Silver Nanoparticle Formation. *J. Am. Chem. Soc.* **2011**, *133* (36), 14164–14167. https://doi.org/10.1021/ja202815y.

(184) Naik, A. N.; Patra, S.; Sen, D.; Goswami, A. Evaluating the Mechanism of Nucleation and Growth of Silver Nanoparticles in a Polymer Membrane under Continuous Precursor Supply: Tuning of Multiple to Single Nucleation Pathway. *Phys. Chem. Chem. Phys.* **2019**, *21* (8), 4193–4199. https://doi.org/10.1039/c8cp06202a.

(185) Dutta, A.; Paul, A.; Chattopadhyay, A. The Effect of Temperature on the Aggregation Kinetics of Partially Bare Gold Nanoparticles. *RSC Adv.* **2016**, *6* (85), 82138–82149. https://doi.org/10.1039/c6ra17561a.

(186) Sergeev, B. M.; Lopatina, L. I.; Prusov, A. N.; Sergeev, G. B. Formation of Silver Clusters by Borohydride Reduction of AgNO3 in Polyacrylate Aqueous Solutions. *Colloid J.* **2005**, *67* (1), 72–78. https://doi.org/10.1007/s10595-005-0008-5.

(187) Dang, T. M. D.; Le, T. T. T.; Fribourg-Blanc, E.; Dang, M. C. The Influence of Solvents and Surfactants on the Preparation of Copper Nanoparticles by a Chemicalreduction Method. *Adv. Nat. Sci. Nanosci. Nanotechnol.* **2011**, *2* (2), 25004–25011. https://doi.org/10.1088/2043-6262/2/2/025004.

(188) Nikolovski, B. G.; Ilić, J. D.; Sovilj, M. N. How to Formulate a Stable and Monodisperse Water-in-Oil Nanoemulsion Containing Pumpkin Seed Oil: The Use of Multiobjective Optimization. *Brazilian J. Chem. Eng.* **2016**, *33* (4), 919–931. https://doi.org/10.1590/0104-6632.20160334s20140140.

(189) Reiss, H. The Growth of Uniform Colloidal Dispersions. *J. Chem. Phys.* **1951**, *19* (4), 482–487. https://doi.org/10.1063/1.1748251.

(190) Tu, W.; Liu, H. Rapid Synthesis of Nanoscale Colloidal Metal Clusters by Microwave Irradiation. *J. Mater. Chem.* **2000**, *10* (9), 2207–2211. https://doi.org/10.1039/b002232m.

(191) Polte, J.; Tuaev, X.; Wuithschick, M.; Fischer, A.; Thuenemann, A. F.; Rademann, K.; Kraehnert, R.; Emmerling, F. Formation Mechanism of Colloidal Silver Nanoparticles:

Analogies and Differences to the Growth of Gold Nanoparticles. *ACS Nano* **2012**, *6* (7), 5791–5802. https://doi.org/10.1021/nn301724z.

(192) Zhang, Z.; Su, T.; Zhang, S. Shape Effect on the Temperature Field during Microwave Heating Process. *J. Food Qual.* **2018**, 39–63. https://doi.org/10.1155/2018/9169875.

(193) Li, Y.; Liu, J. H.; Witham, C. A.; Huang, W.; Marcus, M. A.; Fakra, S. C.; Alayoglu, P.; Zhu, Z.; Thompson, C. M.; Arjun, A.; et al. A Pt-Cluster-Based Heterogeneous Catalyst for Homogeneous Catalytic Reactions : X-Ray Absorption Spectroscopy and Reaction Kinetic Studies of Their Activity and Stability against Leaching. *J. Am. Chem. Soc.* **2011**, *133* (34), 13527–13533. https://doi.org/10.1021/ja204191t.

(194) Muthu, K.; Priya, S. Green Synthesis, Characterization and Catalytic Activity of Silver Nanoparticles Using Cassia Auriculata Flower Extract Separated Fraction. *Spectrochim. Acta - Part A Mol. Biomol. Spectrosc.* **2017**, *179*, 66–72. https://doi.org/10.1016/j.saa.2017.02.024.

(195) Zhang, W.; Sun, Y.; Zhang, L. In Situ Synthesis of Monodisperse Silver Nanoparticles on Sulfhydryl-Functionalized Poly(Glycidyl Methacrylate) Microspheres for Catalytic Reduction of 4-Nitrophenol. *Ind. Eng. Chem. Res.* **2015**, *54* (25), 6480–6488. https://doi.org/10.1021/acs.iecr.5b01010.

(196) Murugadoss, A.; Chattopadhyay, A. A "green" Chitosan-Silver Nanoparticle Composite as a Heterogeneous as Well as Micro-Heterogeneous Catalyst. *Nanotechnology* **2008**, *19* (1), 15603–15612. https://doi.org/10.1088/0957-4484/19/01/015603.

(197) Zheng, Z.; Huang, Q.; Guan, H.; Liu, S. In Situ Synthesis of Silver Nanoparticles Dispersed or Wrapped by a Cordyceps Sinensis Exopolysaccharide in Water and Their Catalytic Activity. *RSC Adv.* **2015**, *5* (85), 69790–69799. https://doi.org/10.1039/c5ra09452f.

(198) Hsu, K. C.; Chen, D. H. Green Synthesis and Synergistic Catalytic Effect OfAg/Reduced Graphene Oxide Nanocomposite. *Nanoscale Res. Lett.* **2014**, *9* (1), 1–10. https://doi.org/10.1186/1556-276X-9-484.

(199) Naik, B.; Hazra, S.; Prasad, V. S.; Ghosh, N. N. Synthesis of Ag Nanoparticles within the Pores of SBA-15: An Efficient Catalyst for Reduction of 4-Nitrophenol. *Catal. Commun.* **2011**, *12* (12), 1104–1108. https://doi.org/10.1016/j.catcom.2011.03.028.

(200) Huo, H.; Jiang, Y.; Zhao, T.; Wang, Z.; Hu, Y.; Xu, X.; Lin, K. Quantitatively Loaded Ultra-Small Ag Nanoparticles on Molecularly Imprinted Mesoporous Silica for Highly Efficient Catalytic Reduction Process. *J. Mater. Sci.* **2020**, *55* (4), 1475–1488. https://doi.org/10.1007/s10853-019-04054-x.

(201) Crawley, M. L.; Trost, B. M. *Applications of Transition Metal Catalysis in Drug Discovery and Development: An Industrial Perspective*; Crawley, M. L., Trost, B. M., Eds.; Wiley-VCH Verlag GmbH & Co. KGaA, 2012. https://doi.org/10.1002/9781118309872.

(202) Dash, S.; Das, S.; Khan, M. I.; Sinha, S.; Das, B.; Jayabalan, R.; Parhi, P. K.; Tripathy, S. K. Sonochemically Synthesized Ag/CaCO3 Nanocomposites: A Highly Efficient Reusable Catalyst for Reduction of 4-Nitrophenol. *Mater. Chem. Phys.* **2018**, *220*, 409–416. https://doi.org/10.1016/j.matchemphys.2018.09.019.

(203) Tang, S.; Vongehr, S.; Meng, X. Carbon Spheres with Controllable Silver Nanoparticle Doping. *J. Phys. Chem. C* **2010**, *114* (2), 977–982. https://doi.org/10.1021/jp9102492.

(204) Dolatkhah, A.; Jani, P.; Wilson, L. D. Redox-Responsive Polymer Template as an Advanced Multifunctional Catalyst Support for Silver Nanoparticles. *Langmuir* **2018**, *34* (36), 10560–10568. https://doi.org/10.1021/acs.langmuir.8b02336.

(205) Zhao, S.; Duan, L.; Xiao, C.; Li, L.; Liao, F. Single Metal of Silver Nanoparticles in the Microemulsion for Recyclable Catalysis of 4-Nitrophenol Reduction. *J. Adv. Nanomater.* **2017**, *2* (1), 31–40. https://doi.org/10.22606/jan.2017.21004.

(206) Yang, F.; Wang, B.; Su, H.; Zhou, S.; Kong, Y. Facilely Self-Reduced Generation of Ag Nanowires in the Confined Reductive Siliceous Nanopores and Its Catalytic Reduction Property. *J. Alloys Compd.* **2017**, *719*, 30–41. https://doi.org/10.1016/j.jallcom.2017.05.160.

(207) Li, J.; Wang, Y.; Wang, M.; Wang, L.; Li, H. A Highly Robust and Reusable Polyimide-Supported Nanosilver Catalyst for the Reduction of 4-Nitrophenol. *J. Mater. Res.* **2015**, *30* (18), 2713–2721. https://doi.org/10.1557/jmr.2015.258.

(208) Sangili, A.; Annalakshmi, M.; Chen, S. M.; Balasubramanian, P.; Sundrarajan, M. Synthesis of Silver Nanoparticles Decorated on Core-Shell Structured Tannic Acid-Coated Iron Oxide Nanospheres for Excellent Electrochemical Detection and Efficient Catalytic Reduction of Hazardous 4-Nitrophenol. *Compos. Part B Eng.* **2019**, *162*, 33–42. https://doi.org/10.1016/j.compositesb.2018.10.084.

(209) Xu, J.; Zhou, T.; Jia, L.; Shen, X.; Li, X.; Li, H.; Xu, Z.; Cao, J. Generation and Thermally Adjustable Catalysis of Silver Nanoparticle Immobilized Temperature-Sensitive Nanocomposite. *J. Nanoparticle Res.* **2017**, *19* (3), 103–112. https://doi.org/10.1007/s11051-017-3769-y.

(210) Narayanan, R. K.; Devaki, S. J. Brawny Silver-Hydrogel Based Nanocatalyst for Reduction of Nitrophenols: Studies on Kinetics and Mechanism. *Ind. Eng. Chem. Res.* **2015**, *54* (4), 1197–1203. https://doi.org/10.1021/ie5038352.

(211) Baruah, B.; Gabriel, G. J.; Akbashev, M. J.; Booher, M. E. Facile Synthesis of Silver Nanoparticles Stabilized by Cationic Polynorbornenes and Their Catalytic Activity in 4-Nitrophenol Reduction. *Langmuir* **2013**, *29* (13), 4225–4234. https://doi.org/10.1021/la305068p.

(212) Ershov, B. G.; Janata, E.; Henglein, A. Growth of Silver Particles in Aqueous Solution : Long-Lived " Magic " Clusters and Ionic Strength Effects. *J. Phys. Chem. A* **1993**, *97* (2), 339–343. https://doi.org/10.1021/j100104a013.

(213) Wang, Q.; Lin, Y.; Liu, K. Role of Anions Associated with the Formation and Properties of Silver Clusters. *Acc. Chem. Res.* **2015**, *48* (6), 1570–1579. https://doi.org/10.1021/acs.accounts.5b00007.

(214) Jin, R.; Zhao, S.; Xing, Y.; Jin, R. All-Thiolate-Protected Silver and Silver-Rich Alloy Nanoclusters with Atomic Precision: Stable Sizes, Structural Characterization and Optical Properties. *CrystEngComm* **2016**, *18*, 3996–4005. https://doi.org/10.1039/C5CE02494C.

(215) Fang, G.; Bi, X. Silver-Catalysed Reactions of Alkynes: Recent Advances. *Chem. Soc. Rev.* **2015**, *44* (22), 8124–8173. https://doi.org/10.1039/c5cs00027k.

(216) Parker, E.; Leconte, N.; Godet, T.; Belmont, P. Silver-Catalyzed Furoquinolines Synthesis: From Nitrogen Effects to the Use of Silver Imidazolate Polymer as a New and Robust Silver Catalyst. *Chem. Commun.* **2011**, *47* (1), 343–345. https://doi.org/10.1039/c0cc02623a.

(217) Ranjan, P.; Ojeda, G. M.; Sharma, U. K.; Van der Eycken, E. V. Metal-Free Dearomatization: Direct Access to Spiroindol(En)Ines in Batch and Continuous-Flow. *Chem. - A Eur. J.* **2019**, *25* (10), 2442–2446. https://doi.org/10.1002/chem.201805945.

(218) Bantreil, X.; Bourderioux, A.; Mateo, P.; Hagerman, C. E.; Selkti, M.; Brachet, E.; Belmont, P. Phosphine-Triggered Selectivity Switch in Silver-Catalyzed o-Alkynylbenzohydroxamic Acid Cycloisomerizations. *Org. Lett.* **2016**, *18* (19), 4814–4817.

https://doi.org/10.1021/acs.orglett.6b02235.

(219) Ermolat'Ev, D. S.; Bariwal, J. B.; Steenackers, H. P. L.; De Keersmaecker, S. C. J.; Van Der Eycken, E. V. Concise and Diversity-Oriented Route toward Polysubstituted 2-Aminoimidazole Alkaloids and Their Analogues. *Angew. Chemie - Int. Ed.* **2010**, *49* (49), 9465–9468. https://doi.org/10.1002/anie.201004256.

(220) Sudrik, S. G.; Chaki, N. K.; Chavan, V. B.; Chavan, S. P.; Chavan, S. P.; Sonawane, H. R.; Vijayamohanan, K. Silver Nanocluster Redox-Couple-Promoted Nonclassical Electron Transfer: An Efficient Electrochemical Wolff Rearrangement of α-Diazoketones. *Chem. - A Eur. J.* **2006**, *12* (3), 859–864. https://doi.org/10.1002/chem.200500696.

(221) Zhao, J.; Nguyen, S. C.; Ye, R.; Ye, B.; Weller, H.; Somorjai, G. A.; Alivisatos, A. P.; Dean Toste, F. A Comparison of Photocatalytic Activities of Gold Nanoparticles Following Plasmonic and Interband Excitation and a Strategy for Harnessing Interband Hot Carriers for Solution Phase Photocatalysis. *ACS Cent. Sci.* **2017**, *3* (5), 482–488. https://doi.org/10.1021/acscentsci.7b00122.

(222) Gainer, M. J.; Bennett, N. R.; Takahashi, Y.; Looper, R. E. Regioselective Rhodium(II)-Catalyzed Hydroaminations of Propargylguanidines. *Angew. Chemie - Int. Ed.* **2011**, *50* (3), 684–687. https://doi.org/10.1002/anie.201006087.

(223) Lauder, K.; Toscani, A.; Scalacci, N.; Castagnolo, D. Synthesis and Reactivity of Propargylamines in Organic Chemistry. *Chem. Rev.* **2017**, *117* (24), 14091–14200. https://doi.org/10.1021/acs.chemrev.7b00343.

(224) Chen, Y.; Yang, T.; Pan, H.; Yuan, Y.; Chen, L.; Liu, M.; Zhang, K.; Zhang, S.; Wu, P.; Xu, J. Photoemission Mechanism of Water-Soluble Silver Nanoclusters: Ligand-to-Metal–Metal Charge Transfer vs Strong Coupling between Surface Plasmon and Emitters. *J. Am. Chem. Soc.* **2014**, *136* (5), 1686–1689. https://doi.org/10.1021/ja407911b.

(225) Ershov, B. G.; Henglein, A. Reduction of Ag+ on Polyacrylate Chains in Aqueous Solution. *J. Phys. Chem. B* **1998**, *102* (52), 10663–10666. https://doi.org/10.1021/jp981906i.

(226) Zhang, B. J.; Xu, S.; Kumacheva, E. Photogeneration of Fluorescent Silver Nanoclusters in Polymer Microgels. *Adv. Mater.* **2005**, *17* (19), 2336–2340. https://doi.org/10.1002/adma.200501062.

(227) Bootharaju, M. S.; Dey, R.; Gevers, L. E.; Hedhili, M. N.; Basset, J. M.; Bakr, O. M. A New Class of Atomically Precise, Hydride-Rich Silver Nanoclusters Co-Protected by Phosphines. *J. Am. Chem. Soc.* **2016**, *138* (42), 13770–13773. https://doi.org/10.1021/jacs.6b05482.

(228) Wu, P.-C.; Chen, C.-Y.; Chang, C.-W. The Fluorescence Quenching and the Aggregation Induced Emission Behaviours of the Silver Nanoclusters Labelled on Poly (Acrylic Acid-Co-Maleic Acid). *New J. Chem.* **2018**, *42* (5), 3459–3464. https://doi.org/10.1039/C7NJ04399F.

(229) Larrea, A.; Sebastian, V.; Ibarra, A.; Arruebo, M.; Santamaria, J. Gas Slug Microfluidics: A Unique Tool for Ultrafast, Highly Controlled Growth of Iron Oxide Nanostructures. *Chem. Mater.* **2015**, *27* (12), 4254–4260. https://doi.org/10.1021/acs.chemmater.5b00284.

(230) Peshkov, V. A.; Pereshivko, O. P.; Nechaev, A. A.; Peshkov, A. A.; Van Der Eycken, E. V. Reactions of Secondary Propargylamines with Heteroallenes for the Synthesis of Diverse Heterocycles. *Chem. Soc. Rev.* **2018**, *47* (11), 3861–3898. https://doi.org/10.1039/C7CS00065K.

(231) Witham, C. A.; Huang, W.; Tsung, C. K.; Kuhn, J. N.; Somorjai, G. A.; Toste, F. D. Converting Homogeneous to Heterogeneous in Electrophilic Catalysis Using Monodisperse Metal Nanoparticles. *Nat. Chem.* **2010**, *2* (1), 36–41. https://doi.org/10.1038/nchem.468.

(232) Ye, Y.; Fan, R. Silver-Catalyzed Synthesis of 4-Substituted Benzofurans via a Cascade Oxidative Coupling-Annulation Protocol. *Chem. Commun.* **2011**, *47* (19), 5626–5628. https://doi.org/10.1039/c1cc10137d.

(233) Blanc, A.; Bénéteau, V.; Weibel, J. M.; Pale, P. Silver & Gold-Catalyzed Routes to Furans and Benzofurans. *Org. Biomol. Chem.* **2016**, *14* (39), 9184–9205. https://doi.org/10.1039/c6ob01468b.

(234) He, D.; Garg, S.; Waite, T. D. H2O2-Mediated Oxidation of Zero-Valent Silver and Resultant Interactions among Silver Nanoparticles, Silver Ions, and Reactive Oxygen Species. *Langmuir* **2012**, *28* (27), 10266–10275. https://doi.org/10.1021/la300929g.

(235) Chen, C.-C.; Wu, H.-H.; Huang, H.-Y.; Liu, C.-W.; Chen, Y.-N. Synthesis of High Valence Silver-Loaded Mesoporous Silica with Strong Antibacterial Properties. *Int. J. Environ. Res. Public Health* **2016**, *13* (I), 99–113. https://doi.org/10.3390/ijerph13010099.

(236) He, Y.; Li, Z.; Tian, G.; Song, L.; Van Meervelt, L.; Van Der Eycken, E. V. Gold-Catalyzed Diastereoselective Domino Dearomatization/: Ipso -Cyclization/Aza-Michael Sequence: A Facile Access to Diverse Fused Azaspiro Tetracyclic Scaffolds. *Chem. Commun.* **2017**, *53* (48), 6413–6416. https://doi.org/10.1039/c7cc03152a.

(237) Soni, Y.; Kavya, I.; Ajithkumar, T. G.; Vinod, C. P. One Pot Ligand Exchange Method for a Highly Stable Au-SBA-15 Catalyst and Its Room Temperature CO Oxidation. *Chem. Commun.* **2018**, *54* (87), 12412–12415. https://doi.org/10.1039/C8CC06887A.

(238) García, C.; Pollitt, S.; van der Linden, M.; Truttmann, V.; Rameshan, C.; Rameshan, R.; Pittenauer, E.; Allmaier, G.; Kregsamer, P.; Stöger-Pollach, M.; et al. Support Effect on the Reactivity and Stability of Au25(SR)18 and Au144(SR)60 Nanoclusters in Liquid Phase Cyclohexane Oxidation. *Catal. Today* **2019**, *336*, 174–185. https://doi.org/10.1016/j.cattod.2018.12.013.

(239) Yuan, X.; Luo, Z.; Zhang, Q.; Zhang, X.; Zheng, Y.; Lee, J. Y.; Xie, J. Synthesis of Highly Fluorescent Metal (Ag, Au, Pt, and Cu) Nanoclusters by Electrostatically Induced Reversible Phase Transfer. *ACS Nano* **2011**, *5* (11), 8800–8808. https://doi.org/10.1021/nn202860s.

(240) Yang, Y.; Yao, Y.; Kline, D. J.; Li, T.; Ghildiyal, P.; Wang, H.; Hu, L.; Zachariah, M. R. Rapid Laser Pulse Synthesis of Supported Metal Nanoclusters with Kinetically Tunable Size and Surface Density for Electrocatalytic Hydrogen Evolution. *ACS Appl. Nano Mater.* **2020**, *3* (3), 2959–2968. https://doi.org/10.1021/acsanm.0c00238.

(241) Wei, H.; Huang, K.; Wang, D.; Zhang, R.; Ge, B.; Ma, J.; Wen, B.; Zhang, S.; Li, Q.; Lei, M.; et al. Iced Photochemical Reduction to Synthesize Atomically Dispersed Metals by Suppressing Nanocrystal Growth. *Nat. Commun.* **2017**, *8* (1), 1490–1498. https://doi.org/10.1038/s41467-017-01521-4.

(242) Santillán, J. M. J.; Muñetón Arboleda, D.; Muraca, D.; Schinca, D. C.; Scaffardi, L. B. Highly Fluorescent Few Atoms Silver Nanoclusters with Strong Photocatalytic Activity Synthesized by Ultrashort Light Pulses. *Sci. Rep.* **2020**, *10* (1), 1–13. https://doi.org/10.1038/s41598-020-64773-z.

(243) Ye, R.; Zhukhovitskiy, A.; Deraedt, C. V.; Toste, F. D.; Somorjai, G. A. Supported Dendrimer-Encapsulated Metal Clusters: Toward Heterogenizing Homogeneous Catalysts. *Acc. Chem. Res.* **2017**, *50* (8), 1894–1901. https://doi.org/10.1021/acs.accounts.7b00232.

(244) Arvela, R. K.; Leadbeater, N. E. Suzuki Coupling of Aryl Chlorides with Phenylboronic Acid in Water, Using Microwave Heating with Simultaneous Cooling. *Org. Lett.* **2005**, *7* (11), 2101–2104. https://doi.org/10.1021/ol0503384.

(245)   Horikoshi, S.; Ohmori, N.; Kajitani, M.; Serpone, N. Microwave-Enhanced Bromination of a Terminal Alkyne in Short Time at Ambient Temperature: Synthesis of Phenylacetylene Bromide. *J. Photochem. Photobiol. A Chem.* **2007**, *189* (2–3), 374–379. https://doi.org/10.1016/j.jphotochem.2007.02.029.

(246)   Leadbeater, N. E.; Pillsbury, S. J.; Shanahan, E.; Williams, V. A. An Assessment of the Technique of Simultaneous Cooling in Conjunction with Microwave Heating for Organic Synthesis. *Tetrahedron* **2005**, *61* (14), 3565–3585. https://doi.org/10.1016/j.tet.2005.01.105.

(247)   Website. Discover® CoolMate™ Low-Temperature Microwave Synthesis System https://edulab.unitn.it/nfs/Manualistica/Strumentazione_ OLDVersion/CEM - microwave synthesis/manuals/600180.pdf (accessed Sep 24, 2020).

(248)   Manno, R.; Ranjan, P.; Sebastian, V.; Mallada, R.; Irusta, S.; Sharma, U. K.; Van der Eycken, E. V.; Santamaria, J. Continuous Microwave-Assisted Synthesis of Silver Nanoclusters Confined in Mesoporous SBA-15: Application in Alkyne Cyclizations. *Chem. Mater.* **2020**, *32* (7), 2874–2883. https://doi.org/10.1021/acs.chemmater.9b04935.

(249)   Regali, F.; Liotta, L. F.; Venezia, A. M.; Montes, V.; Boutonnet, M.; Järås, S. Effect of Metal Loading on Activity, Selectivity and Deactivation Behavior of Pd/Silica-Alumina Catalysts in the Hydroconversion of n-Hexadecane. *Catal. Today* **2014**, *223*, 87–96. https://doi.org/10.1016/j.cattod.2013.08.028.

(250)   Dien, L. X.; Ishida, T.; Taketoshi, A.; Truong, D. Q.; Dang Chinh, H.; Honma, T.; Murayama, T.; Haruta, M. Supported Gold Cluster Catalysts Prepared by Solid Grinding Using a Non-Volatile Organogold Complex for Low-Temperature CO Oxidation and the Effect of Potassium on Gold Particle Size. *Appl. Catal. B Environ.* **2019**, *241*, 539–547. https://doi.org/10.1016/j.apcatb.2018.09.053.

(251)   Wang, N.; Sun, Q.; Yu, J. Ultrasmall Metal Nanoparticles Confined within Crystalline Nanoporous Materials : A Fascinating Class of Nanocatalysts. *Adv. Mater.* **2018**, *31* (1), 1803966–2803989. https://doi.org/10.1002/adma.201803966.

(252)   Cheng, N.; Zhang, L.; Doyle-Davis, K.; Sun, X. *Single-Atom Catalysts: From Design to Application*; Springer Singapore, 2019; Vol. 2. https://doi.org/10.1007/s41918-019-00050-6.

(253)   Cheng, X.; Wang, D.; Liu, J.; Kang, X.; Yan, H.; Wu, A.; Gu, Y.; Tian, C.; Fu, H. Ultra-Small Mo2N on SBA-15 as a Highly Efficient Promoter of Low-Loading Pd for Catalytic Hydrogenation. *Nanoscale* **2018**, *10* (47), 22348–22356. https://doi.org/10.1039/c8nr06916f.

(254)   Gryparis, C.; Efe, C.; Raptis, C.; Lykakis, I. N.; Stratakis, M. Cyclization of 1,6-Enynes Catalyzed by Gold Nanoparticles Supported on TiO 2: Significant Changes in Selectivity and Mechanism, as Compared to Homogeneous Au-Catalysis. *Org. Lett.* **2012**, *14* (12), 2956–2959. https://doi.org/10.1021/ol301212j.

(255)   Schröder, F.; Erdmann, N.; Noël, T.; Luque, R.; Van Der Eycken, E. V. Leaching-Free Supported Gold Nanoparticles Catalyzing Cycloisomerizations under Microflow Conditions. *Adv. Synth. Catal.* **2015**, *357* (14–15), 3141–3147. https://doi.org/10.1002/adsc.201500628.

(256)   Fang, J.; Li, J.; Zhang, B.; Yuan, X.; Asakura, H.; Tanaka, T.; Teramura, K.; Xie, J.; Yan, N. The Support Effect on the Size and Catalytic Activity of Thiolated Au25 Nanoclusters as Precatalysts. *Nanoscale* **2015**, *7* (14), 6325–6333. https://doi.org/10.1039/c5nr00549c.

(257)   Sekine, K.; Kobayashi, R.; Yamada, T. Silver-Catalyzed Three-Component Reaction of Propargylic Amines, Carbon Dioxide, and N-Iodosuccinimide for Stereoselective Preparation of (E)-Iodovinyloxazolidinones. *Chem. Lett.* **2015**, *44* (10), 1407–1409.

https://doi.org/10.1246/cl.150584.

(258) Yoshida, M.; Mizuguchi, T.; Shishido, K. Synthesis of Oxazolidinones by Efficient Fixation of Atmospheric CO 2 with Propargylic Amines by Using a Silver/1,8-Diazabicyclo[5.4.0] Undec-7-Ene (DBU) Dual-Catalyst System. *Chem. - A Eur. J.* **2012**, *18* (49), 15578–15581. https://doi.org/10.1002/chem.201203366.

(259) Islam, S. S.; Biswas, S.; Ali Molla, R.; Yasmin, N.; Islam, S. M. Green Synthesized AgNPs Embedded in COF: An Efficient Catalyst for the Synthesis of 2-Oxazolidinones and α-Alkylidene Cyclic Carbonates via CO2 Fixation. *ChemNanoMat* **2020**, *6* (9), 1386–1397. https://doi.org/10.1002/cnma.202000284.

(260) Ghosh, S.; Riyajuddin, S.; Sarkar, S.; Ghosh, K.; Islam, S. M. Pd NPs Decorated on POPs as Recyclable Catalysts for the Synthesis of 2-Oxazolidinones from Propargylic Amines via Atmospheric Cyclizative CO2 Incorporation. *ChemNanoMat* **2020**, *6* (1), 160–172. https://doi.org/10.1002/cnma.201900505.

(261) Khatun, R.; Biswas, S.; Biswas, I. H.; Riyajuddin, S.; Haque, N.; Ghosh, K.; Islam, S. M. Cu-NPs@COF: A Potential Heterogeneous Catalyst for CO2fixation to Produce 2-Oxazolidinones as Well as Benzimidazoles under Moderate Reaction Conditions. *J. CO2 Util.* **2020**, *40*, 101180–101191. https://doi.org/10.1016/j.jcou.2020.101180.

(262) Gao, H.; He, L.; Zhang, Y.; Zhang, S.; Wang, L. Facile Synthesis of Pt Nanoparticles Supported on Graphene/Vulcan XC-72 Carbon and Their Application for Methanol Oxidation. *Ionics (Kiel).* **2017**, *23* (2), 435–442. https://doi.org/10.1007/s11581-016-1861-4.

(263) El Khatib, K. M.; Abdel Hameed, R. M. Development of Cu2O/Carbon Vulcan XC-72 as Non-Enzymatic Sensor for Glucose Determination. *Biosens. Bioelectron.* **2011**, *26* (8), 3542–3548. https://doi.org/10.1016/j.bios.2011.01.042.

(264) Liu, J.; Zhao, Q.; Wu, C.; Wang, Y.; Wei, W.; Wang, X.; Yi, L. Performance Improvement of Activated Nanoporous Carbon Supported Gold Catalyst as an Anode for Direct Borohydride-Hydrogen Peroxide Fuel Cells. *RSC Adv.* **2014**, *4* (33), 17129–17135. https://doi.org/10.1039/c4ra01000k.

(265) Tang, J.; Bi, S.; Wang, X.; Hou, G.; Su, X.; Liu, C. Excellent Microwave Absorption of Carbon Black / Reduced Graphene Oxide Composite with Low Loading. *J. Mater. Sci.* **2019**, *54* (22), 13990–14001. https://doi.org/10.1007/s10853-019-03902-0.

(266) Kawasaki, H.; Kosaka, Y.; Myoujin, Y.; Narushima, T.; Yonezawa, T.; Arakawa, R. Microwave-Assisted Polyol Synthesis of Copper Nanocrystals without Using Additional Protective Agents. *Chem. Commun.* **2011**, *47*, 7740–7742. https://doi.org/10.1039/C1CC12346G.

(267) Vilar-Vidal, N.; Rivas, J.; López-Quintela, M. A. Size Dependent Catalytic Activity of Reusable Subnanometer Copper(0) Clusters. *ACS Catal.* **2012**, *2* (8), 1693–1697. https://doi.org/10.1021/cs300355n.

(268) Abiraman, T.; Rajavelu, K.; Rajakumar, P.; Balasubramanian, S. Sub 1 Nm Poly(Acrylic Acid)-Capped Copper Nanoparticles for the Synthesis of 1,2,3-Triazole Compounds. *ACS Omega* **2020**, *5* (14), 7815–7822. https://doi.org/10.1021/acsomega.9b03995.

(269) Pellarin, M.; Issa, I.; Langlois, C.; Lebeault, M. A.; Ramade, J.; Lermé, J.; Broyer, M.; Cottancin, E. Plasmon Spectroscopy and Chemical Structure of Small Bimetallic Cu(1-x)Agx Clusters. *J. Phys. Chem. C* **2015**, *119* (9), 5002–5012. https://doi.org/10.1021/jp511671m.

(270) Xu, S. L.; Shen, S. C.; Wei, Z. Y.; Zhao, S.; Zuo, L. J.; Chen, M. X.; Wang, L.; Ding, Y. W.; Chen, P.; Chu, S. Q.; et al. A Library of Carbon-Supported Ultrasmall Bimetallic Nanoparticles. *Nano*

Res. **2020**, *13* (10), 2735–2740. https://doi.org/10.1007/s12274-020-2920-8.

(271) Han, B.; Hou, X.; Xiang, R.; He, G. Synthesis of Highly Luminescent Cu/Ag Bimetal Nanoclusters and Their Application in a Temperature Sensor. *Anal. Methods* **2017**, *9* (27), 4028–4032. https://doi.org/10.1039/c7ay01164d.

(272) Yao, Y.; Huang, Z.; Li, T.; Wang, H.; Liu, Y.; Stein, H. S.; Mao, Y.; Gao, J.; Jiao, M.; Dong, Q.; et al. High-Throughput, Combinatorial Synthesis of Multimetallic Nanoclusters. *Proc. Natl. Acad. Sci. U. S. A.* **2020**, *117* (12), 6316–6322. https://doi.org/10.1073/pnas.1903721117.

(273) Chang, Z.; Huo, S.; Zhang, W.; Fang, J.; Wang, H. The Tunable and Highly Selective Reduction Products on Ag@Cu Bimetallic Catalysts Toward CO2 Electrochemical Reduction Reaction. *J. Phys. Chem. C* **2017**, *121* (21), 11368–11379. https://doi.org/10.1021/acs.jpcc.7b01586.

(274) Kang, X.; Wei, X.; Jin, S.; Yuan, Q.; Luan, X.; Pei, Y.; Wang, S.; Zhu, M. Rational Construction of a Library of M 29 Nanoclusters from Monometallic to Tetrametallic. *Proc. Natl. Acad. Sci. U. S. A.* **2019**, *116* (38), 18834–18840. https://doi.org/10.1073/pnas.1912719116.

(275) Zhang, B.; Wei, C. The Sensitive Detection of ATP and ADA Based on Turn-on Fluorescent Copper / Silver Nanoclusters. *Anal. Bioanal. Chem.* **2020**, *412*, 2529–2536. https://doi.org/10.1007/s00216-020-02476-0.

(276) Kim, N. R.; Shin, K.; Jung, I.; Shim, M.; Lee, H. M. Ag − Cu Bimetallic Nanoparticles with Enhanced Resistance to Oxidation : A Combined Experimental and Theoretical Study. *J. Phys. Chem. C* **2014**, *118* (45), 1721–1731. https://doi.org/10.1021/jp506069c.

(277) Li, N.; Liu, X. A Comparison of the Catalytic Efficiency of Copper-Based Bimetallic Nanoparticles in the Click Reactions. *J. Chem. Res.* **2020**, *44* (9–10), 566–570. https://doi.org/10.1177/1747519820912672.

(278) Shin, K.; Kim, D. H.; Yeo, S. C.; Lee, H. M. Structural Stability of AgCu Bimetallic Nanoparticles and Their Application as a Catalyst : A DFT Study. *Catal. Today* **2012**, *185* (1), 94–98. https://doi.org/10.1016/j.cattod.2011.09.022.

(279) Shin, K.; Kim, H.; Mo, H. Catalytic Characteristics of AgCu Bimetallic Nanoparticles in the Oxygen Reduction Reaction. *ChemSusChem* **2013**, *6* (6), 1044–1049. https://doi.org/10.1002/cssc.201201001.

(280) Liu, X.; Astruc, D. Atomically Precise Copper Nanoclusters and Their Applications. *Coord. Chem. Rev.* **2018**, *359*, 112–126. https://doi.org/10.1016/j.ccr.2018.01.001.

(281) Yuan, X.; Dou, X.; Zheng, K.; Xie, J. Recent Advances in the Synthesis and Applications of Ultrasmall Bimetallic Nanoclusters. *Part. Part. Syst. Charact.* **2015**, *32* (6), 613–629. https://doi.org/10.1002/ppsc.201400212.

(282) Peng, X.; Pan, Q.; Rempel, G. L. Bimetallic Dendrimer-Encapsulated Nanoparticles as Catalysts: A Review of the Research Advances. *Chem. Soc. Rev.* **2008**, *37* (8), 1619–1628. https://doi.org/10.1039/b716441f.

(283) Zhang, J.; Yuan, Y.; Wang, Y.; Sun, F.; Liang, G.; Jiang, Z.; Yu, S. H. Microwave-Assisted Synthesis of Photoluminescent Glutathione-Capped Au/Ag Nanoclusters: A Unique Sensor-on-a-Nanoparticle for Metal Ions, Anions, and Small Molecules. *Nano Res.* **2015**, *8* (7), 2329–2339. https://doi.org/10.1007/s12274-015-0743-9.

(284) Liu, H.; Zhang, X.; Wu, X.; Jiang, L.; Burda, C.; Zhu, J. J. Rapid Sonochemical Synthesis of Highly Luminescent Non-Toxic AuNCs and Au@AgNCs and Cu (II) Sensing. *Chem. Commun.*

2011, *47* (14), 4237–4239. https://doi.org/10.1039/c1cc00103e.

(285) Chen, W.; Lan, G.; Chang, H. Use of Fluorescent DNA-Templated Gold/Silver Nanoclusters for the Detection of Sulfide Ions. *Anal. Chem.* **2011**, *83* (24), 9450–9455. https://doi.org/10.1021/ac202162u.

(286) Sun, J.; Yang, F.; Zhao, D.; Chen, C.; Yang, X. Integrated Logic Gate for Fluorescence Turn-on Detection of Histidine and Cysteine Based on Ag/Au Bimetallic Nanoclusters-Cu2+ Ensemble. *ACS Appl. Mater. Interfaces* **2015**, *7* (12), 6860–6866. https://doi.org/10.1021/acsami.5b00434.

(287) Yu, Y.; Zhang, Q.; Yao, Q.; Xie, J.; Lee, J. Y. Guiding Principles in the Galvanic Replacement Reaction of an Underpotentially Deposited Metal Layer for Site-Selective Deposition and Shape and Size Control of Satellite Nanocrystals. *Chem. Mater.* **2013**, *25* (23), 4746–4756. https://doi.org/10.1021/cm402734r.

(288) Bhol, P.; Bhavya, M. B.; Swain, S.; Saxena, M.; Samal, A. K. Modern Chemical Routes for the Controlled Synthesis of Anisotropic Bimetallic Nanostructures and Their Application in Catalysis. *Front. Chem.* **2020**, *8*, 357–383. https://doi.org/10.3389/fchem.2020.00357.

(289) Santana, J. S.; Skrabalak, S. E. Continuous Flow Routes toward Designer Metal Nanocatalysts. *Adv. Energy Mater.* **2019**, *10* (11), 1902051–1902065. https://doi.org/10.1002/aenm.201902051.

(290) Cattaneo, S.; Bonincontro, D.; Bere, T.; Kiely, C. J.; Hutchings, G. J.; Dimitratos, N.; Albonetti, S. Continuous Flow Synthesis of Bimetallic AuPd Catalysts for the Selective Oxidation of 5-Hydroxymethylfurfural to 2,5-Furandicarboxylic Acid. *ChemNanoMat* **2020**, *6* (3), 420–426. https://doi.org/10.1002/cnma.201900704.

(291) Alexeev, O. S.; Gates, B. C. Supported Bimetallic Cluster Catalysts. *Ind. Eng. Chem. Res.* **2003**, *42* (8), 1571–1587. https://doi.org/10.1021/ie020351h.

(292) Laura, U.; Arruebo, M.; Sebastian, V. Towards the Continuous Production of Pt-Based Heterogeneous Catalysts Using Microfluidic Systems. *Dalt. Trans.* **2018**, *47* (5), 1693–1702. https://doi.org/10.1039/c7dt03360e.

(293) Matsuzawa, M.; Togashi, S.; Hasebe, S. Isothermal Reactor for Continuous Flow Microwave-Assisted Chemical Reaction. *J. Therm. Sci. Technol.* **2012**, *7* (1), 58–74. https://doi.org/10.1299/jtst.7.58.

(294) Zhang, L.; Lyng, J. G.; Brunton, N. P. The Effect of Fat , Water and Salt on the Thermal and Dielectric Properties of Meat Batter and Its Temperature Following Microwave or Radio Frequency Heating. *J. Food Eng.* **2007**, *80*, 142–151. https://doi.org/10.1016/j.jfoodeng.2006.05.016.

(295) Sakuma, H.; Ichiki, M. Electrical Conductivity of NaCl-H2O Fluid in the Crust. *J. Geophys. Res. Earth* **2016**, *121*, 577–594. https://doi.org/10.1002/2015JB012219.Received.

(296) Pande, S.; Weir, M. G.; Zaccheo, B. A.; Crooks, R. M. Synthesis , Characterization , and Electrocatalysis Using Pt and Pd Dendrimer-Encapsulated Nanoparticles Prepared by Galvanic Exchange. *New J. Chem.* **2011**, *35*, 2054–2060. https://doi.org/10.1039/c1nj20083f.

(297) Iatridi, Z.; Bokias, G.; Kallitsis, J. K. Physicochemical Study of the Complexation of Poly (Acrylic Acid) with Cu2+ Ions in Water. *Appl. Polym. Sci.* **2008**, *108* (2), 769–776. https://doi.org/10.1002/app.

(298) Gotoh, Y.; Ohkoshi, Y.; Nagura, M.; Akamatsu, K.; Deki, S. Preparation and Structure of Copper Nanoparticle/Poly(Acrylic Acid) Composite. *J. Mater. Chem.* **2000**, *10*, 2548–2552.

https://doi.org/10.1039/b003899g.

(299) Sree, M.; Bharati, S.; Chandu, B.; Rao, S. V. Explosives Sensing Using Ag – Cu Alloy Nanoparticles Synthesized by Femtosecond Laser Ablation and Irradiation. *RSC Adv.* **2019**, *9* (3), 1517–1525. https://doi.org/10.1039/c8ra08462a.

(300) Valodkar, M.; Modi, S.; Pal, A.; Thakore, S. Synthesis and Anti-Bacterial Activity of Cu , Ag and Cu – Ag Alloy Nanoparticles : A Green Approach. *Mater. Res. Bull.* **2011**, *46* (3), 384–389. https://doi.org/10.1016/j.materresbull.2010.12.001.

(301) Tsuji, M.; Hikino, S.; Tanabe, R.; Sano, Y. Synthesis of Bicompartmental Ag/Cu Nanoparticles Using a Two-Step Polyol Process. *Chem. Lett.* **2009**, *38* (8), 860–861. https://doi.org/10.1246/cl.2009.860.

(302) Liu, A.; Honma, I.; Ichihara, M.; Zhou, H. Poly(Acrylic Acid)-Wrapped Multi-Walled Carbon Nanotubes Composite Solubilization in Water: Definitive Spectroscopic Properties. *Nanotechnology* **2006**, *17* (12), 2845–2849. https://doi.org/10.1088/0957-4484/17/12/003.

(303) Deng, Y.; Sun, J.; Ni, X.; Yu, B. Tribological Properties of Hierarchical Structure Artificial Joints with Poly Acrylic Acid (AA) - Poly Acrylamide (AAm) Hydrogel and Ti6Al4V Substrate. *J. Polym. Res.* **2020**, *27* (6), 1–6. https://doi.org/10.1007/s10965-020-02143-z.

(304) Li, Y.; Wang, J.; Li, X.; Geng, D.; Li, R.; Sun, X. Superior Energy Capacity of Graphene Nanosheets for a Nonaqueous Lithium-Oxygen Battery. *Chem. Commun.* **2011**, *47* (33), 9438–9440. https://doi.org/10.1039/c1cc13464g.

(305) Ahmadi, E.; Zarghami, N.; Jafarabadi, M. A.; Alizadeh, L.; Khojastehfard, M.; Yamchi, M. R.; Salehi, R. Enhanced Anticancer Potency by Combination Chemotherapy of HT-29 Cells with Biodegradable, PH-Sensitive Nanoparticles for Co-Delivery of Hydroxytyrosol and Doxorubicin. *J. Drug Deliv. Sci. Technol.* **2019**, *51*, 721–735. https://doi.org/10.1016/j.jddst.2019.03.003.

(306) Liang, Y. N.; Hu, J.; Tam, M. K. C.; Xiao Hu. CuOx Nanotubes via an Unusual Complexation Induced Block Copolymer-like Self-Assembly of Poly(Acrylic Acid). *RSC Adv.* **2012**, *2*, 9531–9537. https://doi.org/10.1039/c2ra20951a.

(307) Ibrahim, I. R.; Matori, K. A.; Ismail, I.; Awang, Z.; Nor, S.; Rusly, A.; Nazlan, R.; Idris, F. M.; Misbah, M.; Zulkimi, M.; et al. A Study on Microwave Absorption Properties of Carbon Black and by Tuning the Matching-Absorbing Layer Structures. *Sci. Rep.* **2020**, *10*, 3135–3149. https://doi.org/10.1038/s41598-020-60107-1.

(308) Fahmy, A.; El-nasser, K. S.; Ali, I. O.; Salama, T. M.; Friedrich, J.; Fahmy, A.; El-nasser, K. S.; Ali, I. O.; Salama, T. M. Tuned Interactions of Silver Nanoparticles with ZSM-5 Zeolite by Adhesion-Promoting Poly (Acrylic Acid) Deposited by Electrospray Ionization (ESI). *J. Adhes. Sci. Technol.* **2017**, *4243*, 1–16. https://doi.org/10.1080/01694243.2017.1315910.

(309) Ezhova, A.; Huber, K. Contraction and Coagulation of Spherical Polyelectrolyte Brushes in the Presence of Ag+, Mg2+, and Ca2+ Cations. *Macromolecules* **2016**, *49*, 7460–7468. https://doi.org/10.1021/acs.macromol.6b01286.

(310) Rivas, L.; Pereira, E. D.; Moreno-villoslada, I. Water-Soluble Polymer – Metal Ion Interactions. *Prog. Polym. Sci.* **2003**, *28*, 173–208. https://doi.org/10.1016/S0079-6700(02)00028-X.

(311) Tao, S.; Yang, M.; Chen, H.; Ren, M.; Chen, G. Microfluidic Synthesis of Ag@Cu2O Core-Shell Nanoparticles with Enhanced Photocatalytic Activity. *J. Colloid Interface Sci.* **2017**, *486*, 16–26. https://doi.org/10.1016/j.jcis.2016.09.051.

(312) Purandare, P. S.; Lele, M. M.; Gupta, R. Parametric Analysis of Helical Coil Heat Exchanger. *Int. J. Eng. Res. Technol.* **2012**, *1* (8), 1–5.

(313) Andhare, A.; Kriplani, V. M.; Modak, J. P. Thermal Analysis of a Helical Coil Heat Exchanger. *Int. J. Innov. Res. Adv. Eng.* **2014**, *1* (12), 137–143.

(314) Andrzejczyk, R.; Muszyński, T. Performance Analyses of Helical Coil Heat Exchangers. the Effect of External Coil Surface Modification on Heat Exchanger Effectiveness. *Arch. Thermodyn.* **2016**, *37* (4), 137–159. https://doi.org/10.1515/aoter-2016-0032.

(315) Sobti, A.; Sehgal, R.; Wanchoo, R. K. Flow of Viscoelastic Fluid through a Helical Coil. *Chem. Biochem. Eng. Q.* **2017**, *31* (1), 11–20. https://doi.org/10.15255/cabeq.2015.2314.